HETEROGENEOUS ELECTRON TRANSFER OF SUPRAMOLECULAR ASSEMBLIES

by

Jianjun Wei

BS, East China University of Chemical Technology, 1992

ME, East China University of Science & Technology, 1995

Submitted to the Graduate Faculty of

Arts and Sciences in partial fulfillment

of the requirements for the degree of

Doctor of Philosophy

University of Pittsburgh

2004

UNIVERSITY OF PITTSBURGH

FACULTY OF ARTS AND SCIENCES

This dissertation was presented

by

Jianjun Wei

It was defended on

November 23, 2004

and approved by

Prof. Shigeru Amemiya

_____

Prof. Bruce A. Armitage

_____

Prof. Gilbert Walker

_____

Prof. David H. Waldeck

_____

Dissertation Director

HETEROGENEOUS ELECTRON TRANSFER OF SUPRAMOLECULAR ASSEMBLIES

Jianjun Wei, PhD

University of Pittsburgh, 2004

ABSTRACT

Heterogeneous electron transfer of protein, porphyrins through self-assembled monolayer (SAM) at gold electrodes was studied. The SAM was characterized by electrochemistry, thickness measurement, contact angle, scanning tunneling microscopy (STM) and others. The electron transfer rate constants of cytochrome c immobilized on a SAM by directly "wiring" its heme through a variety of nitrogen ligands (pyridine, imidazole or nitrilE) were measured by cyclic voltammetry. The electron transfer mechanism was explored by changing the distance between the electrode and protein, the composition of the SAM chains, the type of cytochrome c (horse heart cytochrome, rat cytochrome c and its mutants), and the conditions of electrolyte solutions. The results were compared to those of cytochrome c electrostatically adsorbed at carboxylic acid terminated SAMs, distinguishing the electron transfer mechanism and electron transfer pathways. A unified theoretical model, i.e. a gradual transition of the mechanism from a friction controlled reaction at short distance to tunneling controlled reaction at long distance, was applied to these "heme-wired" systems. In a study of photo-induced electron transfer of porphyrins through SAMs with chiral structure, an asymmetrical effect on the efficiency of electron transfer through these chiral chain structures was found. Induced circular dichroism of porphyrin aggregates, orbital angular momentum interaction in electronic coupling, are proposed as possible mechanisms for the asymmetry of electronic tunneling.

ACKNOWLEDGEMENTS

First of all, I would like to express my deeply sincere gratitude to Prof. David H. Waldeck for his excellent and invaluable guidance throughout my PhD. His keen interest in all my projects has inspired me in many ways. I really enjoyed working on the projects during the PhD under his guidance. I am so grateful that his door is always open for questions and discussions, and they were so helpful for me. I am thankful to him for his constant support and encouragement.

I am grateful to other professors in the Chemistry Department at Pittsburgh. Prof. Gilbert Walker, Prof. Eric Borget were members of my comprehensive committee; their scientific integrity and personal encouragement have been important for me to achieve the PhD program. I am enthusiastically looking forward to working with Prof. Walker as a postdoctoral research associate on a new scientific project. I appreciate Prof. Chris Schafmeister and his graduate student Greg Bird who provided the scaffold molecules in the chiral project. I would like to thank Prof. Butera, an expert of the UHV system, who introduced me to the vacuum realm and UHV based spectroscopy. In addition, I take this opportunity to thank my graduate course teachers, Prof. Peter Siska, Prof. Rob Coalson, Prof. Tara Meyer and Prof. Adrian Michael who brought me up to the level for the graduate research.

I would like to thank Dr. Haiying Liu who now is an assistant professor in chemistry at Michigan Technological University for his great support and fruitful collaboration in my cytochrome *c* project. He did a great job in synthesis and purification of functional-alkanthiols in

the lab. I am also grateful to him for his help during my stay in Pittsburgh since I came here in 2000. I gratefully thank Dr. Yufan He, as a former post-doctoral associate in this department, for his assistance and contributions on STM measurements. I am thankful to former group members, Dr. Hiromichi Yamamoto, Dr. Dimitri E. Khoshtariya and Dr. Andrew Napper for their help and many helpful discussions in the laboratory, especially for Hiro's instruction in SAM characterization and the UHV system operation and maintenance.

I also thank Min Liu, Palwinder Kaur, Hongjun Yue, Subhasis Chakrabarti and Amit Paul, who are the present members in this group, an "Asian group" except the boss. We have had a lot of entertainment over the years and I thank them for their help in different ways during the course of this work. In addition, I take this chance to thank all my friends I made here in Pittsburgh for their attention.

Finally, the extremely important support and encouragement are from my family here in Pittsburgh, my parents and parents-in-law in China. My daughter, Jeannette, born in March 2003 in Pittsburgh, is my pride. She grows so quick that now she can run around and give me fly kisses and hugs every day when I leave for work in the morning and go back home in the night. My wife, Li He, came here later 2000 and has not gone back to visit China eventhough her father got an operation for curing a carcinoma. This thesis could not have taken shape without her support. I am short of words in expressing my gratitude to my parents; they have been consistently supportive for my pursuits in study since I was a child, even though they only had 5 years school life. I would also dedicate this thesis to my younger brother, sister and other family members in China for their blessing and help in many ways.

TABLE OF CONTENTS

LIST OF TABLES

LIST OF FIGURES

CHAPTER 1 INTRODUCTION

AN OVERVIEW

Electron transfer (ET) plays key roles in a number of complex systems in nature, e.g., biological structures such as proteins, membranes and the photosynthetic reaction center. During aerobic respiration, cytochrome c, a small protein that is the only one from the electron transport system not in a complex, accepts electrons from complex III and shuttles them to complex IV which promotes four-electron reduction of O_2 to H_2O and pumps four protons across the inner mitochondrial membranes, producing a transmembrane potential that ultimately drives ATP synthesis. Photosynthesis, involving electron transfer and energy storage, is probably the most important reaction on earth. Electron transfer reactions are also centeral in the electrochemical corrosion process of metals. Understanding of electron transfer in such complex systems is an outstanding challenge, and it is critical for artificial reaction center design and the control of electron transfer reactions.

For the past 50 years, people have been conducting research on electron transfer, in both homogeneous and heterogeneous systems, and many of the molecular and bulk level electron transfer processes are known. Within a unifying framework of donor-bridge-acceptor electron transfer (in this donor-bridge-acceptor classification, a bridge may function as a spacer or a wire or a molecule, and the donor and/or acceptor may be a molecule or a solid electrode.), it is well known that the space between the electron donor and acceptor plays a very important role in determining the electron transfer reaction rate. In a coherent tunneling process, the electron

transfer rate has an exponential dependence on the separation of donor and acceptor, which can be commonly expressed as:

$$k_{ET} = k_0 \exp(-\beta d) \qquad 1\text{-}1$$

where d is the distance between electron donor and acceptor, and β is a decay factor which depends on the chemical composition/structure of the intervening media. For instance, β has value of about 1 $Å^{-1}$ for saturated carbon hydrogen chain, and β is reported to range from 0.3-0.8 $Å^{-1}$ for conjugated unsaturated chain. In each case, a large space separation results in a lower electron transfer rate constant.

Self-assembly technique has been widely used to control the molecular bridge length and regulate the separation space between a redox species and an electrode. A thiol molecule can covalently attach onto gold surfaces in solution and spontaneously form a self-assembled monolayer (SAM). A redox species can be in a bulk solution or absorbed at the SAM. By applying a voltage on a SAM modified gold electrode, the gold electrode can act as an electron donor or acceptor. When a negative voltage is applied, the Fermi level of electrons in gold has higher energy than the oxidized state of species, and the electrons transfer from the electrode (donor) to redox species (acceptor); whereas at positive voltage applied, the electrons transfer from reduced states of redox species to the gold electrode through SAM.

In this work, I describe the studies of electron transfer through molecular films. In this chapter, I provide a brief review of electron transfer theory, self-assembed monolayer formation, the electron transfer studies of cytochrome, and chirality effects on electron transfer. In Chapter 2 a new strategy to immobilize the redox protein cytochrome c by a nitrogen ligand (pyridine, imidazole or nitrile group) is demonstrated (Figure 1- 1). The ligands are imbedded in a monolayer film and provide a receptor, which displaces the methionine group, one of the axial

coordination groups of the heme in the center of cytochrome c, and binds the iron heme. Cytochrome c undergoes an electron transfer reaction directly from the heme through the SAM. This strategy, probably, provides a model to control the formal potential of metalloprotein on the surface, and to explore the fundamental kinetics of electron transfer in an integrated biological system in membrane. The immobilization is characterized by electrochemistry, scanning tunneling microscopy (STM), Surface Enhanced Raman Resonance spectroscopy (SERR). The details of this part can be found in Chapter 2 and Chapter 3.

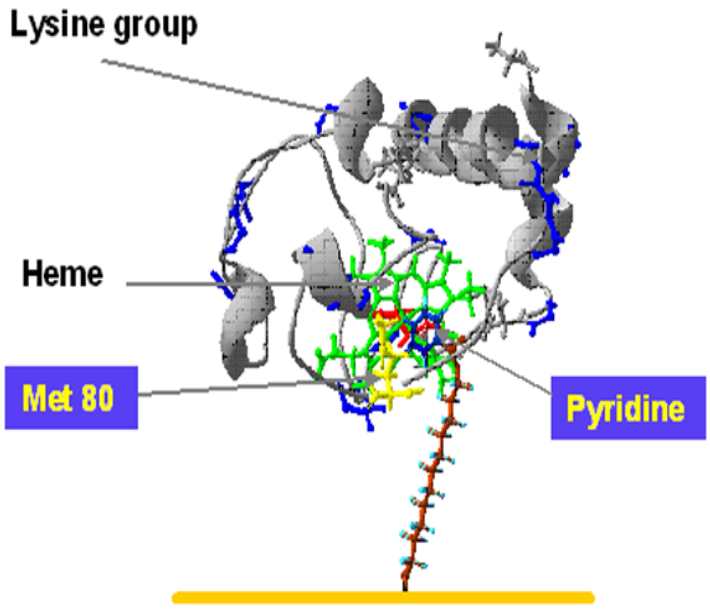

Figure 1- 1 A diagram of cytochrome c immobilization through ligand replacement at gold surface, the methionine (Met 80) is replaced by pyridine (receptor) in this picture. The alkane chain is attached to the gold surface through S-Au bond.

This strategy provides a model system to investigate aspects of electron transfer dynamics between biomolecules and metal electrodes. In Chapter 4 and Chapter 5, the electron transfer dynamics and mechanism of cytochrome c, immobilized on pyridine receptor, are

studied by changing the donor-acceptor space separation and reaction solvent conditions. Specifically, Chapter 4 focuses on electron transfer dynamics of cytochrome c by changing the distance separation; Chapter 5 addresses the electron transfer mechanisms by applying a unified model, adiabatic mechanism at short distance to nonadiabatic reaction at long distance separation. The change in reaction mechanism with distance reflects a gradual transition between the tunneling (long distance) and the solvent controlled (short distance) mechanisms. The ligand bound system is compared to the electrostatic adsorption system (Figure 1- 2).

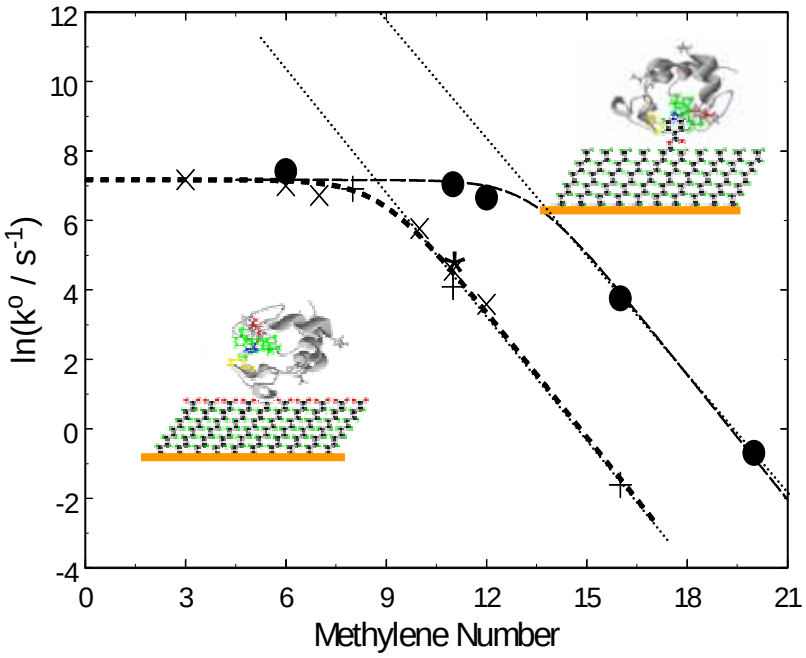

Figure 1- 2 A diagram of the change of electron transfer mechanism with distance for cytochrome c on pyridine SAM (right upper inserted) and carboxylic acid (left lower inserted). Carboxylic acid monolayer data are from Niki *et al.*[1 c,d](x), Bowden *et al.*[1 a,b](+), and this work(*); the pyridine terminated layers is shown as (●).The thin dased black curve and the thick dashed line show the distance dependence of the electron transfer of pyridine system and carboxylic acid system, respectively; the dotted lines show the predicted nonadiabatic electron transfer rate constant at shorter distance.

Chapter 6 probes the electron transfer pathway in the cytochrome c by comparing the native rat cytochrome c and its mutant, RC9-K13A, in which the lysine 13 group is replaced by an alanine amino acid. The change of the electron transfer rate constant for the mutant indicates

the different pathway of electron transfer pathways in the two systems. The direct 'link' to the protein's heme unit to the SAM can result in 'short-circuiting' the electron tunneling pathway.

Chapter 7 deals with the effects of chirality and electron spin polarization in the electron tunneling. A molecule of helical structure and terminated with a chromophore (porphyrin or coumarin) is prepared as a SAM at a gold surface. The photocurrent produced by irradiation with 435 nm light to the porphyrin terminated SAM has a noticeable asymmetry with different chiral linkers between the photoexcited acceptor and a gold electrode (donor). Figure 1- 3 shows the structure of designed chiral molecule which is used in this study.

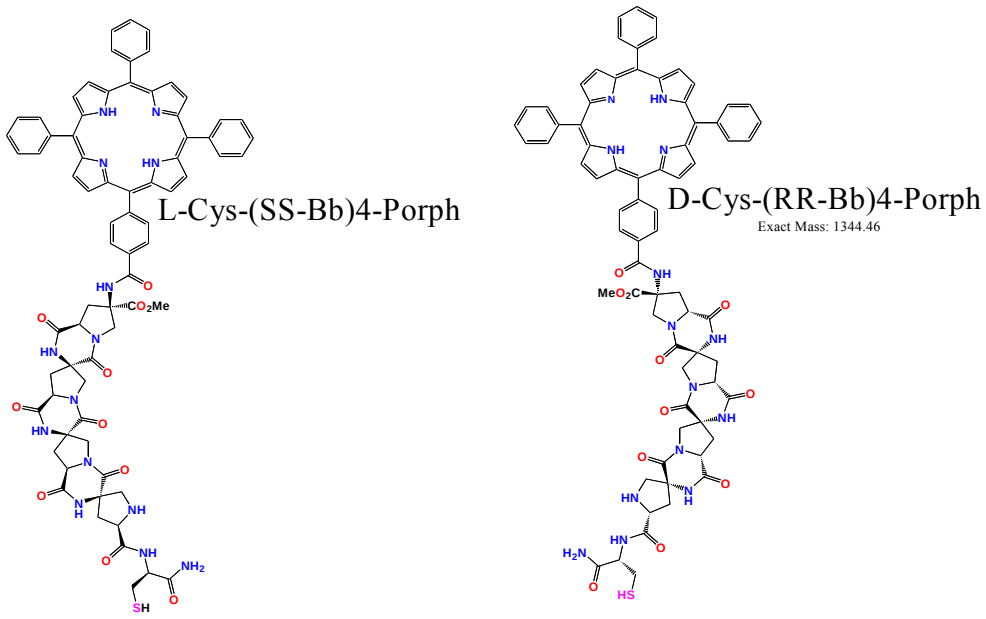

Figure 1- 3 Structure of a designed helical molecule terminated with a porphyrin, on the other side a cysteine is attached for SAM preparation on gold surface.

Chapter 8 summarizes all the electron transfer systems examined in this thesis work and provides a brief perspective comment on heterogeneous electron transfer.

1-1. A BRIEF REVIEW OF SELF-ASSEMBLED MONOLAYERS

Since research on self-assembled monolayers (SAMs) began in 1983, [2] SAMs have been extensively studied because of their potential benefits in various fields of research. A self-assembled monolayer (SAM) is a single molecular layer adsorbed spontaneously on a substrate (metal or semiconductor) via physical and/or chemical adhesion and is obtained by putting the substrate in a chemical solution or vapor. Langmuir-Blodgett (LB) and self-assembly in solution are the most common methods of preparation SAM. [3] To prepare a self-assembled alkanethiol monolayer on gold, the typical route is to incubate a clean gold surface in a very low concentration of alkanethiol ethanol or hexane solution, or some other organic solvent for a short time.

Figure 1- 4 illustrates the procedure of preparation for a self-assembled monolayer in solution. The growth kinetics and dynamics of SAMs in solution are still not very clear even though some researchers have been engaged in this study. The structure and growth of SAMs have been evaluated by many techniques, as outlined in a recent review article[4]. The kinetics of formation or desorption of molecules on the surface has been studied by using a quartz crystal microbalance,[5] electrochemistry,[6] spectroscopy [7] and so on. Experimental results[8] show that the chemisorption of the "headgroup" is the fastest step (a few minutes) of the self-assembly process, followed by a slower step, which lasts for several hours, to reach the final, stable structure. People have tried to understand the self-assembly process[8,9,10] and found that many factors can affect the growth rate of an alkanethiol SAM on various metal surfaces. In the initial phase, a longer chain length alkanethiol has a lower rate of growth than that of a shorter length chain because of the lower mobility of long chain molecules. The rate of growth increases with the concentration under low concentration conditions, and changes to be independent of

concentration at high concentrations. Solvent properties such as steric bulk, polarity, viscosity, and solubility for a given SAM molecule, are very important. In general, longer chain solvent molecules have a lower rate of chemisorption, and the growth rate is weakly temperature dependent in solution. A self-exchange reaction exists in the thiol solution and can be described by first order kinetics[11].

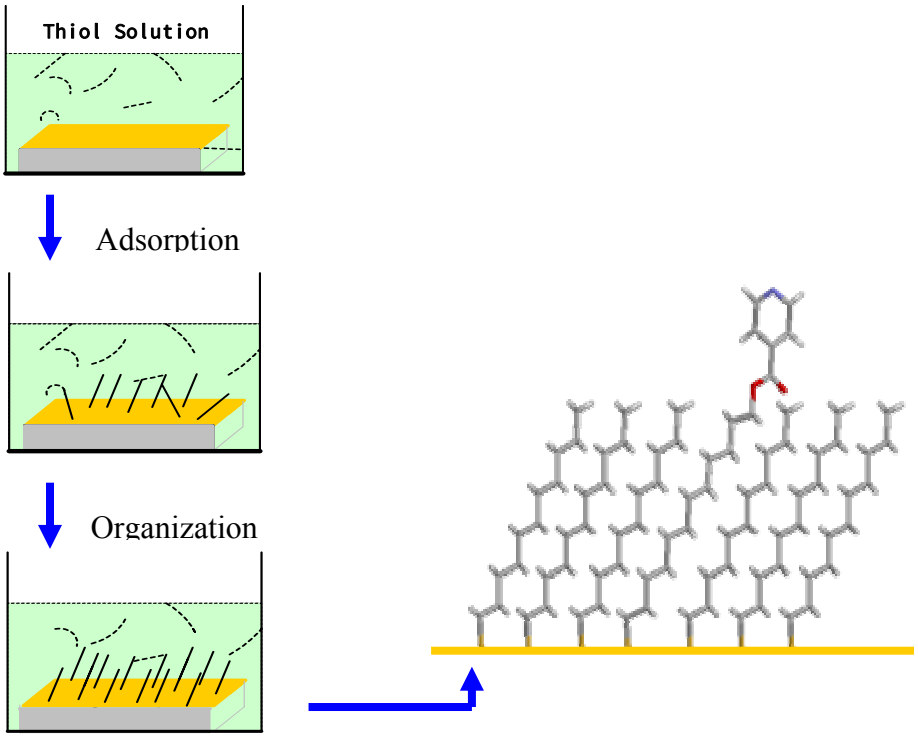

Figure 1- 4 A schematic of preparation of a SAM. The substrate, Au (gold), is immersed into an ethanol solution of the desired thiol(s). Initial adsorption is fast (seconds); then an organization phase follows which should be allowed to continue for >15 h for best results. A schematic of a fully assembled mixed SAM is shown to the right

SAMs based on thiols and related molecules on a substrate have many advantages. Thiols form a covalent bond readily with gold or other metals and the SAM is stable (estimated free energy about -51 KJ/mol at gold surfaces). By using a different monolayer composition and changing the end groups, the function (properties) of a SAM can be controlled[12]. It is possible to

fabricate a self-assembled monolayer which is insulating, or semi-conductive by controlling the structure and/or component of a SAM. Preparing mixed SAMs is another approach to get functional structures[3,9]. There are two common methods to prepare mixed SAMs: by immersing a gold substrate in a mixture of different molecules or by sequentially exposing the substrate to the different solution of thiols. Micro-contact printing (μCP), based on self-assembly technology, facilitates fabrication of molecular electronics as small as 1-2 nanometers that can switch, store and retrieve information[13]. In concept, the process of μCP is the same as the one that uses an inked stamp to print an address on an envelope or mark a date on a correspondence. The basic process of μCP is that an inked stamp is placed on a gold substrate under some controlled conditions, and SAMs are formed in the regions of contact between the stamp and surface.

A well ordered self-assembled monolayer on a substrate provides a highly oriented, compacted nanoscale structure with many potential applications, ranging from SAMs as the inert part in coatings to SAMs as active elements in sensors. In protective coatings, the SAM plays a role in preventing corrosion by blocking molecules access to a metal surface.[14] SAMs are used to adjust the wetting of a surface by changing the end-group (hydrophilic or hydrophobic). This property can be used in friction or lubrication control.[15] SAMs are promising in the context of microcontact printing (μCP)[16] and may be useful in microelectronics and micro-optical-electronics[17]. The electronic properties of SAMs can have a profound effect on the electron transfer of molecules, which is an aspect of molecular electronics. In the biomedical field, SAMs are used as an interface-layer to fabricate sensors or biosensors[18] and biomaterials can be immobilized on a SAM to mimic the interaction of biological interfaces[19].

1-2. UNDERLYING THEORY OF ELECTRON TRANSFER AND HETEROGENEOUS ELECTRON TRANSFER THROUGH SELF-ASSEMBLED MONOLAYERS

1-2-1. Classical Electron Transfer Theory

A large number of workers have developed for understanding of electron transfer through both theories and experiments. Marcus[20] introduced a model to describe electron transfer in the 1950's. This ET theory emerged as a view of intersecting parabolas in which the ET reaction activated state is reached at the crossing point, similar to the transition state reaction theory. An important contribution of Marcus' formulation is to connect electron transfer activation with fluctuations of electronic levels of the ET donor and acceptor, which are linearly coupled to a solvent thermal well characterized by Gaussian statistics. As shown in Figure 1- 5, the curvatures of the two parabolas are equal because of the Gaussian distribution of the energy fluctuations along the reaction coordinate (only shown in one dimension). The actual profile of reaction coordinates should include those coordinates involving vibrational coordinates of the reactant and products, as well as the orientational coordinates of the surrounding molecules. As a result, the potential energy of reactant-surroundings and product-surroundings should be a function of all of these nuclear coordinates and a multi-dimension potential energy surface.

Because the electrons are such light particles, compared to the nuclei, the electron transfer reaction obeys the Franck-Condon principle. The ET reaction happens only at or near a nuclear configuration in which the electronic energy of the reactant-surroundings is equal to that of product-surroundings. To realize the ET reaction, it is vital that there are thermal fluctuations of the reactant-surroundings energy surface through which reaction system can reach the intersection cross region. In a polar solvent, the solvent reorganization will happen as fluctuations in the orientation coordinates of the solvent molecule after the reaction.

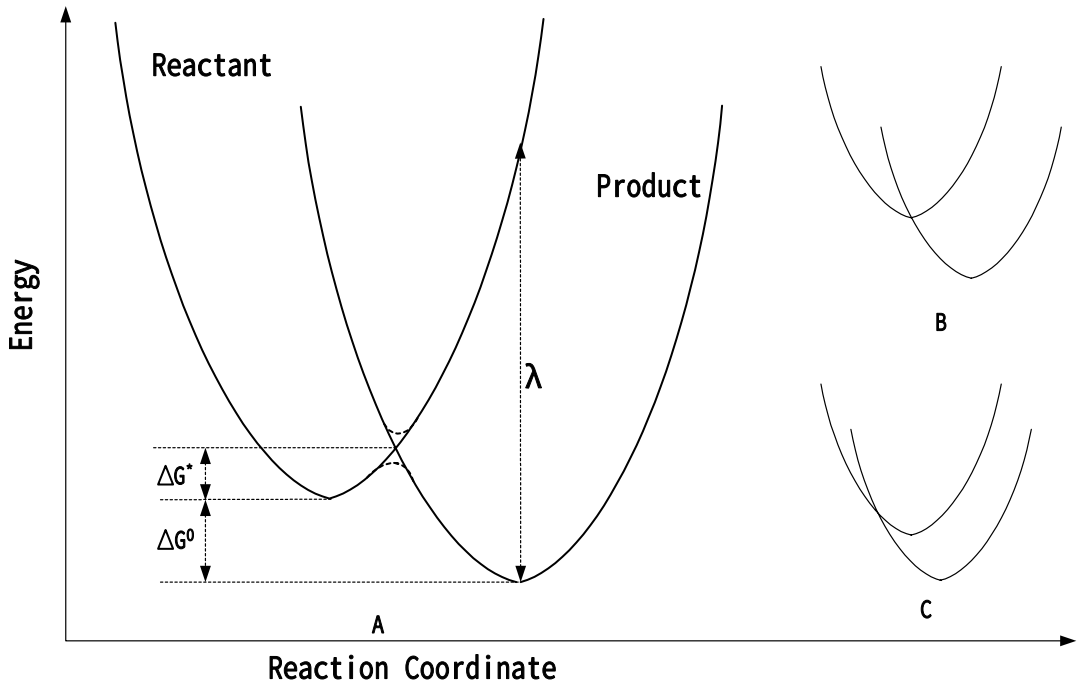

Figure 1- 5 A diagram of free energy-reaction coordinate curves for electron transfer in a nonadiabatic process (weak electronic coupling), in which ΔG^* is the activation free energy, and ΔG^0 is the reaction free energy which equals to the difference of reactant and the product energy, λ is the reorganization energy. The energy difference between the two dashed curves is equal to $2H_{if}$ where H_{if} is termed as the electronic coupling energy of the electronic states of donor and acceptor (R &P). A represents a reaction in normal region, B represents a reaction with maximum rate, C represents a reaction in inverted region

The electron transfer rate depends on not only the frequency of fluctuations for which the system reaches the cross point region, but also the probability that the reactant-surrounding nuclear configuration curve goes to that of product curve. The probability depends on many factors, for example, the strength of electronic coupling between the electronic orbital of donor and acceptor which depends on the distance of separation between the donor and acceptor. Assuming that the electronic coupling is small enough to be neglected in calculating the activation free energy for the electron transfer reaction, the rate constant can be expressed by the classical Marcus equation:

$$k_{ET} = A\exp\left(\frac{-\Delta G^*}{RT}\right) \qquad 1\text{-}2$$

$$A \propto \nu_n \kappa_{el} \qquad 1\text{-}3$$

$$\Delta G^* = \frac{(\lambda + \Delta G^0)^2}{4\lambda} \qquad 1\text{-}4$$

where ΔG^* is the free energy of activation which is related to reorganization energy λ (the work needed to bring reactant to the mean separation distance is not considered). The prefactor *A* represents a convolution of a suitable weighted frequency (ν_n) for crossing the intersection region and the transmission coefficient or averaged transition probability (κ_{el}) for electron transfer per passage of the system through the intersection region from reactant to product which has strong dependence on the electronic coupling of the reactants (donor and acceptor). For a reaction in which there is a substantial electronic coupling the transmission probability is close to 1 (so-called adiabatic reaction), whereas there is fairly small transmission probability for a weak electronic coupling reaction (nonadiabatic reaction), (*vide infra*).

The activation free energy relies on each vibration involved in the activation of the molecules and the solvent repolarization, namely, reorganization energy λ. Equation 1-2 to 1-4 predict an inverted region of the electron transfer reaction in which the rate constant decreases with increasing of exoergicity ΔG^0. In the limit where $\Delta G^0 + \lambda > 0$, the ΔG^* decreases as ΔG^0 increases negatively at a constant λ and the rate constant increases, is called the normal region. When $-\Delta G^0$ exceeds λ, ΔG^* begins to increase, which causes the rate constant to decrease; this region is called the inverted region. In view of the Figure 1- 5, the inverted region can be reached by lowering the product curve or raising the reactant curve. When the intersection crossing point reaches the minimum point of reactant curve, the reaction gets the maximum rate constant due to

zero barriers for the reaction (B in Figure 1- 5). Further negatively increasing the ΔG^0 will now raises the barrier, i.e. increasing ΔG^*, resulting in a so-called inverted region (C in Figure 1- 5).

The reorganization energy can be defined as the free energy needed to distort the atomic positions of the reactant and its solvation shell to the atomic positions of product and its solvation shell without allowing the electron transfer. The reorganization energy consists of the inner-shell normal mode vibrations of the reactant molecules (λ_i) from the equilibrium states and the change of outer-shell orientations of the surrounding solvent molecules (λ_o).

$$\lambda = \lambda_i + \lambda_o \qquad 1\text{-}5$$

The inner sphere contribution to the reorganization energy can be calculated from the changes in the bond lengths of the reactants,

$$\lambda_i = \sum_j \frac{f_j^r f_j^p}{f_j^r + f_j^p}\left(\Delta q_j\right) \qquad 1\text{-}6$$

in which f_j^r and f_j^p are respectively the jth normal mode force constant in the reactants and products, and Δq_j is the change in equilibrium value of the jth normal coordinate. The outer sphere reorganization energy contribution can be calculated in a dielectric continuum model,

$$\lambda_o = (\Delta e)^2\left[\frac{1}{2a_1} + \frac{1}{2a_2} - \frac{1}{r}\right]\left[\frac{1}{\varepsilon_{op}} - \frac{1}{\varepsilon_{st}}\right] \qquad 1\text{-}7$$

where Δe is the amount of charge transferred from donor to acceptor, a_1 and a_2 are the effective radii of the two reactants treated as spherical shapes, r is the reactants center to center separation distance, ε_{op} and ε_{st} are the optical and static dielectric constants of the solvent, respectively. From the equations, we can conclude that when the solvent molecules are nonpolar ($\varepsilon_{op} = \varepsilon_{st}$), the outer sphere solvent reorganization energy vanishes; the larger the radii of the reactants results in smaller the charge-solvent interaction and smaller λ_o.

1-2-2. Quantum Mechanical Aspects of Electron Transfer

Classical Marcus treatments of electron transfer have been intensely and successfully applied in strong electronic coupled electron transfer systems within the normal region to predict rate constants of electron transfer from experimental parameters. However, classical treatments of the problem do not include the nuclear tunneling through barrier which may occur, and is important in the inverted region. This effect causes the rate constant to decrease less in actual cases than that predicted by the equation in inverted region. Generally, the nuclear tunneling is treated by calculation of quantum mechanical[21] Franck-Condon factor or by semiclassical nuclear formulations[22]. In addition, the electronic barriers are usually neglected in classical Marcus theory so that the electronic transmission coefficient is close to one. However, weak electronic couplings result in less electronic transmission coefficient. In this case, the probability that the system undergoes a transition from the energy potential of reactants to that of products through a barrier will be determined by the overlap of nuclear and electronic wavefunction between initial reactant and final product states (solvent dynamics is neglected here). Quantum mechanical models have been established and continuing to be refined for probing the mechanisms of electron transfer kinetics and related chemical/biochemical processes.

For a nonadiabatic electron transfer reaction, a quantum-mechanical treatment based on Fermi golden rule has been developed by Levich and others.[23] In general conceptual terms, a transition rate depends upon the strength of the coupling between the initial and final state of a system and upon the number of ways the transition can happen (i.e., the density of the final states). There is a separation treatment of nuclear and electronic factors according to the time

scales of nuclear and electronic motions. In a simple way, the transition rate between two degenerate states is of the form known as *Fermi golden rule* expression:

$$k_{el} = \frac{2\pi}{h}\left|H_{if}\right|^2 FC \qquad 1\text{-}8$$

in which k_{el} is the rate that a system in an initial vibronic state will pass to a final vibronic state, H_{if} is the electronic coupling matrix element introduced earlier, *FC* is the Franck-Condon weighted density factor, which is proportional to the matrix element describing the overlap of nuclear wavefunctions between the initial and final thermally averaged vibronic states:

$$FC \propto \sum_v \sum_w \rho_v \left|\left\langle x_i \middle| x_f \right\rangle\right|^2 \delta\left(E_{iw} - E_{fw}\right) \qquad 1\text{-}9$$

in which x_i and x_f are the nuclear wavefunctions of w and v (*i* and *f* represent the vibrational levels of the initial and final states), ρ_v is the population density of vibrational level *v*, and δ (E_{iw}-E_{fw}) is the energy difference between these levels. Thus the transition is favored at the greatest overlap between the reactant and product large vibrational wavefunctions.

At low temperature, when the available thermal energy (k_BT) is unable to permit passage over the activation energy, the tunneling involved with nuclear vibration at high frequency becomes more important, resulting in a temperature-independent reaction. When temperature is raised so that $k_{BT}>h\nu_n$ (ν_n is nuclear vibration frequency), the high frequency vibrational modes are not significant, hence one can obtain a semiclassical version of the Marcus expression for reaction rate:

$$k_{el} = \frac{2\pi}{\hbar}\left|H_{if}\right|^2 \frac{1}{(4\pi\lambda k_B T)^{1/2}} \exp\left[\frac{-(\Delta G^0 + \lambda)^2}{4\lambda k_B T}\right] \qquad 1\text{-}10$$

When $-\Delta G^0 = \lambda$, the rate is predicted to reach a maximum, the same conclusion that is obtained on the basis of classical Marcus theory.

Another key parameter is the electronic coupling factor which can be better understood by applying a treatment called perturbation theory[21,24]. The perturbations (coupling) of electronic states of the reactants and products of reaction (Figure 1- 5 A) can be constructed based on the electronic Hamiltonian H_{el}:

$$H_{if} \equiv \langle \psi_i | H_{el} | \psi_f \rangle \equiv \int \psi_i^* H_{el} \psi_f \, d\tau \qquad 1\text{-}11$$

In the case of multidimensional configuration spaces, a more complex situation may arise. In the transition state model, the electron transfer occurs obeying the Franck-Condon principle, i.e no nuclear motions take place during the transfer. The product state is formed, and undergoes thermal equilibration with the surrounding medium. Hence, in general, the reaction coordinate has contributions from both the vibrational modes of the reactant and from the polarization models of the surrounding medium.

As the zero order states become close in energy they couple, the energies of the coordinate are shifted to new "perturbed" energies, shown as the dotted curve in Figure 1- 5 A. In the situation with weak perturbation, the potential energy surfaces do not shift signifcantly and the surfaces intersect; the reaction is nonadiabatic. When the magnitude of H_{if} increases because of strong perturbations between the zero-order states, the two curves do not cross and the electron transfer reaction is termed as adiabatic reaction, and occur on a single potential energy surface. A transition from the "nonadiabatic" to "adiabatic" limits occurs, depending on the strength of electronic coupling.

McConnell's superexchange model[25] based on a perturbation treatment provides one approach for calculating electronic coupling of donor-bridge-acceptor system. In this approach, one considers the m-bridge unit to be a single bridge possessing m locally excited states x_{j+1}, j=1

through m, x_1, x_{m+2} are reserved for the donor and acceptor states, respectively. In superexchange model, the electronic coupling arises from not only direct pathways, i.e. the nearest neighbor unit (tight-binding, $H_{j,j+1}$), but also the superposition of all possible m-th order pathways (a sum over all values of (m, H_{ij}). It has been known that the non-nearest-pathway interactions are important for long bridge systems. For a simple system with identical units in a long bridge, the superexchange model gives the electronic coupling as a function of the separation of electron donor and acceptor:

$$H_{if} = H_0 \exp\left[-\frac{\beta}{2}(d - d_0)\right] \qquad \text{1-12}$$

where H_0 is the electronic coupling at the closest separation d_0 and β is the exponential decay factor. This equation is comparable with equation 1-1. The electronic coupling in the superexchange picture has contribution from the electronic interactions via the LUMO and via the HOMO. In general, one must summarize pathways, and the coupling can be either negative or positive in a pathway. The total electronic coupling will be the sum of all interactions from each specific pathway.

1-2-3. Heterogeneous Electron Transfer through SAMs-A Semiclassical Approach

Electron transfer kinetics through SAM modified electrodes has been an active field of study for the past decade and continues to grow, largely because of the potential applications in molecular electronics and bioelectronics.[26] Considerable work has been performed on the mechanism of electron transfer through SAMs comprised of both conjugated and saturated components.[26, 27] Theoretical approaches to describing the heterogeneous electron transfer mechanism are available and continue to be refined.[28]

The heterogeneous electron transfer rate can be predicted by a semiclassical Marcus theory [20, 29] and verified experimentally[30]. A well-known result of Marcus theory is the parabolic dependence of the redox molecules free energy on the reaction coordinate, which produces a Gaussian density of electronic states distribution, and the introduction of reorganization energy, which has been developed and is suitable for the electron transfer reaction at the surface.

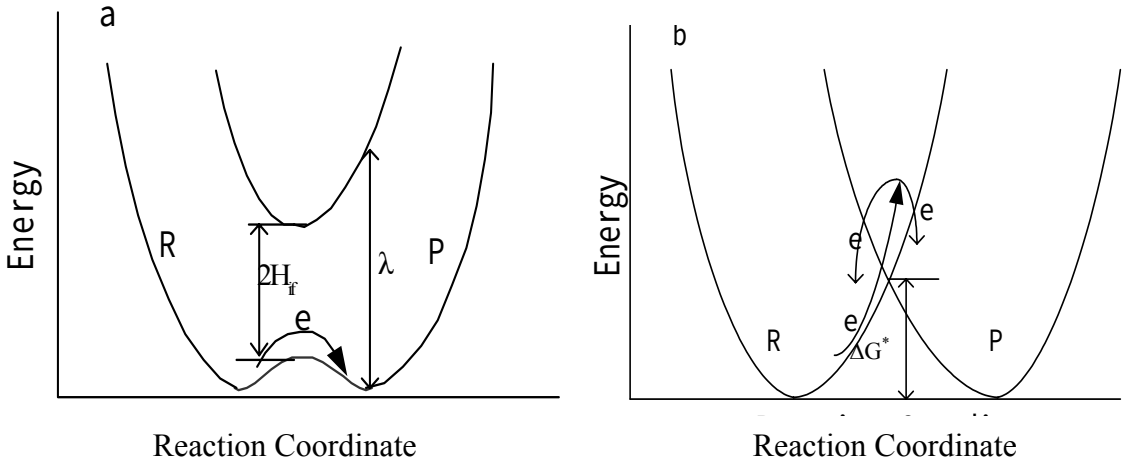

Figure 1- 6 Schematic diagram of free energy-reaction (for which the electrode potential E equals the formal potential $E^{0'}$ of redox group) coordinates profiles for symmetrical electron-transfer processes have a) strong (adiabatic) and b) weak (nonadiabatic) electronic matrix coupling element H_{if}.

The electron transfer reaction is treated within the Born-Oppenheimer approximation, which separates the electron dynamics from nuclear motion. This approximation is reasonable, because the tunneling of electrons between the electrode and redox centers occurs more rapidly than nuclear vibrations, rotations and translation[31].

Figure 1- 6 presents reaction coordinate diagrams for the redox reaction on the surface when the energy is set at the energy of formal potential for the redox species. The curvatures of two parabolas represent the redox potential change caused by a combination of nuclear motions such as vibration, internal rotations of reagents and solvent reorganization. The electron transfer takes place when the electronic states of the metal surface and redox molecules have the same energy. The electron tunneling probability at this resonance is quantified by the electronic coupling between the donor and acceptor orbitals, which is a very important factor for long-distance electron transfer. The strength of the electronic coupling (H_{if}) is dependent on the distance of redox molecule from the metal electrode. The probability (κ_{el}) of electron exchange in a pair of acceptor and donor varies from zero to unity and depends on the strength of the electronic coupling.

Electron transfer reactions are classified as being either “adiabatic” or “nonadiabatic” according to the strength of the coupling element $2H_{if}$. When $2H_{if} << k_BT$, the redox group will be thermally excited to the intersection point and continue along the upper curve, and have little probability of undergoing electron exchange (panel b of Figure 1-6). Hence, the system moves through the crossing region many times before the electron tunneling occurs. When the electronic coupling between the electrode and redox molecule becomes larger ($2H_{if} > k_BT$), electron transfer proceeds along the lower free energy curve with the flattened transition-state

region (panel b of Figure 1-6). In this case, the electron transfer rate is controlled by the nuclear motion needed to reach the transition state region, rather than the electron tunneling at this point.

Based on the dielectric continuum model, the reorganization energy for electron transfer reactions at SAM modified surface has been developed by Liu, et al[32] for electrode-SAM-redox interfaces. The solvent reorganization energy λ_s is given by the following equation;

$$\lambda_s = \left(\frac{1}{\varepsilon_I^{op}} - \frac{1}{\varepsilon_I^{st}}\right)\frac{(\Delta q)^2}{2a} - \left(\frac{\eta_{II,I}^{op}}{\varepsilon_I^{op}} - \frac{\eta_{II,I}^{st}}{\varepsilon_I^{st}}\right)\frac{(\Delta q)^2}{4d} + \sum_{n=1}^{\infty}\left\{\frac{\varepsilon_{II}^{op}\left(\eta_{II,I}^{op}\right)^{n-1}\left(\eta_{II,III}^{op}\right)^{n}}{\left(\varepsilon_{II}^{op}+\varepsilon_I^{op}\right)^2} - \frac{\varepsilon_{II}^{st}\left(\eta_{II,I}^{st}\right)^{n-1}\left(\eta_{II,III}^{st}\right)^{n}}{\left(\varepsilon_{II}^{st}+\varepsilon_I^{st}\right)^2}\right\}\frac{(\Delta q)^2}{d+nL} \qquad 1\text{-}13$$

$$\eta_{i,j} = \frac{\varepsilon_i - \varepsilon_j}{\varepsilon_i + \varepsilon_j} \qquad 1\text{-}14$$

where *a* is the cavity radius of the redox species, d is the distance from the redox species to the top of a film on the electrode (for adsorbed redox species, a=d), L is the film thickness, $\Delta q = \pm 1$ for a point charge. ε is the dielectric constant, where the superscripts of *op* and *st* mean optical and static, and the subscripts I, II, III mean the bulk solvent, the film, and the electrode, respectively. The parameters are set up, as follows:

$\varepsilon_I^{st} = 50$ or 120, $\varepsilon_I^{op} = 1{,}8$ $\varepsilon_{II}^{st} = \varepsilon_{II}^{op} = 2.25$, $\varepsilon_{III}^{st} = \varepsilon_{III}^{op} = \infty$.

We can write a general form for heterogeneous electron transfer reactions as

$$\text{Ox} + \text{electrode(e)} \longrightarrow \text{Red} \qquad 1\text{-}15$$

where Ox and Red refer to oxidized and reduced forms of redox couple. From the view of transition-state theory, the number of molecules at the transition state is the density of electronic-states at the at the transition state, controlled by the activation free energy ΔG_a^*. Assuming that

only electron transfer takes places from the Fermi level of the electrode, one can get the electron transfer rate constant, k_{et}

$$k_{et} = \kappa_{el} v_n \exp\left(\frac{-\Delta G_a^*}{RT}\right) \qquad 1\text{-}16$$

where R is the gas constant, ΔG_a^* is the activation free energy, k_{el} is the electronic transmission coefficient through *Landau-Zener* (cross) region, and v_n is the nuclear barrier-crossing frequency (or the frequency of passage of the reactant through the transition state), which is constituted from solvent repolarization and nuclear reorganization modes.

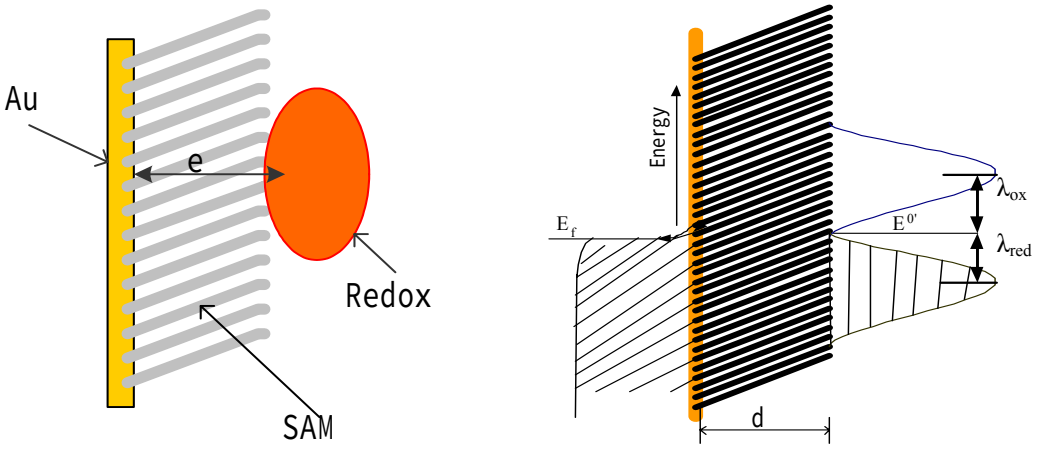

Figure 1- 7 a) A schematic diagram illustrates the physical structure of a SAM-modified device immobilizing redox molecules and electron transfer between the gold electrode and redox group. E_f is the Fermi level energy of gold electrodes; b) Density of electronic states representation of reaction coordinate diagrams. The abscissa plots the density of electronic states within the metal and reaction layer, and the ordinate plots the electronic energy level. The lined distribution represented filled electronics states

Figure 1- 7 a) displays a schematic diagram for the physical picture of a SAM on which a redox molecule is immobilized and electron exchange can occur between the electrode and redox species. Figure 1- 7 b) portrays an energy diagram for the interface. The potential of the

electrode is set at the formal potential of the redox couple ($E^{0'}$). The distribution of filled $d_e(\varepsilon)$ and unfilled $d_h(\varepsilon)$ electronic states in the metal is given by

$$d_e(\varepsilon) = \rho \cdot f(\varepsilon) \qquad 1\text{-}17$$

$$d_h(\varepsilon) = \rho \cdot [1 - f(\varepsilon)] \qquad 1\text{-}18$$

$$f(\varepsilon) = \frac{1}{1 + e^{-(\varepsilon_f - \varepsilon)/k_B T}} \qquad 1\text{-}19$$

where $f(\varepsilon)$ is Fermi distribution function with ε_f Fermi level energy, and ρ is the effective density of electronic states in the metal electrode. For Au and other metals, ρ is approximated as being constant over the energy range of interest. The distribution function of redox (donor/acceptor orbitals) groups on the electrode surface can be simply expressed as a Boltzmann distribution, assuming that all redox electronic states distribution is a time averaged distribution of a single redox species' instantaneous redox potential.

$$d_{ox/red}(\varepsilon) = N_{ox/red} C \exp\left(\frac{-\Delta G(\varepsilon)}{k_B T}\right) \qquad 1\text{-}20$$

in which $d_{ox/red}(\varepsilon)$ is the density of electronic states of Ox/Red (acceptor/donor orbitals) as functions of its energy ε, N is the number of Ox or Red groups on the surface, and C is a normalization constant which depends on the exact form of the free energy level *vs.* the reaction coordinate diagram. $\Delta G(\varepsilon)$ is the free energy function, and in the basis of Marcus theory, can be expressed as $\frac{(\varepsilon_F - \varepsilon + \eta - \lambda)^2}{4\pi\lambda k_B T}$ for the oxidant and $\frac{(\varepsilon_F - \varepsilon + \eta + \lambda)^2}{4\pi\lambda k_B T}$ for the reductant. In these expressions, η is the overpotential, T is the absolute temperature, and λ is the reorganization energy (see below). As discussed below, the electron exchange rate is

proportional to the overlap of filled electronic states of the metal electrode with the density of electronic states of the redox couple.

For a strongly adiabatic electron transfer process (Figure 1-6 a), κ_{el}=1, the strong electronic coupling between electrons in the electrode and redox (Red or Ox) state at the Fermi level will result in the oxidation or reduction of all the activated redox species. The electron transfer rate will occur primarily through electrode states near the Fermi level. The electron transfer rate can be approximated by the density of activated redox (Red or Ox) states.

$$k^{A}_{\mathrm{Re}d/Ox} = \nu_n d_{\mathrm{Re}d/Ox}(\varepsilon_f) = \nu_n N_{ox/red} C \exp\left(\frac{-\Delta G(\varepsilon_f)}{k_B T}\right) \qquad 1\text{-}21$$

The adiabatic standard heterogeneous rate constant at the formal potential of the redox couple (E=E$^{0'}$) is given by

$$k^{0}_{A} = \nu_n \cdot \left(\frac{\lambda}{\pi^3 RT}\right)^{1/2} \cdot \exp\left(-\Delta G_a^{*} \Big/ RT\right) \qquad 1\text{-}22$$

and ΔG_a^{*} is given by

$$\Delta G_a^{*} = \frac{\lambda}{4} - \left|H_{if}\right| \qquad 1\text{-}23$$

$|H_{if}|$ is half absolute value of electronic energy splitting of the system at the transition state, and λ is the reorganization energy.

For a nonadiabatic electron transfer process (Figure 1-6 b), the electron transfer rate constant can be expressed by the *Fermi Golden Rule*.

$$k_{et} = \frac{2\pi}{\hbar}\left|H_{if}\right|^2 (FC) \qquad 1\text{-}24$$

This equation describes the rate of a nonadiabatic transition between two states, with a coupling between the sites of magnitude, $|H_{if}|$. *FC* is the Franck-Condon weighted density of states and

accounts for the impact of nuclear coordinates on the electron-transfer rate. When $-\Delta G$ is smaller than the reorganization energy λ, the electron transfer reaction is in the normal region of Marcus theory, and high-frequency vibrational modes of the donor and acceptor are not a significant part of the reorganization. In this case, the *FC* item is given by

$$FC = \left(4\pi\lambda k_B T\right)^{-1/2} \exp\left(-\frac{(\lambda + \Delta G_a^{*})^2}{4\lambda k_B T}\right) \qquad 1\text{-}25$$

The electron transfer occurs not only near the Fermi level. One must integrate all the overlapped electron energies between the electrode and density of electronic state distribution, so that

$$k_{\mathrm{Red}}^{NA} = \frac{2\pi}{\hbar}|V|^2 \int_{-\infty}^{\infty} \rho \cdot f(\varepsilon) \cdot d_{ox}(\varepsilon) d\varepsilon \qquad 1\text{-}26$$

for reduction and

$$k_{Ox}^{NA} = \frac{2\pi}{\hbar}|V|^2 \int_{-\infty}^{\infty} \rho \cdot [1 - f(\varepsilon)] \cdot d_{\mathrm{Red}}(\varepsilon) d\varepsilon \qquad 1\text{-}27$$

for oxidation. Through this model, substituted Fermi function $f(\varepsilon)$, a general formalism has been developed for calculating the electron rate constant at an electrode using cyclic voltammetry (CV).[33]

$$k^{NA}{}_{red/ox} = \mu\rho k_B T \int_{-\infty}^{\infty} \frac{\exp\left\{-\left[x - \frac{\lambda \pm e\eta}{k_B T}\right]^2 \left(\frac{k_B T}{4\pi}\right)\right\}}{1 + \exp(x)} dx \qquad 1\text{-}28$$

where *e* is the charge on an electron, η is the overpotential, *x* is the electron energy relative to Fermi level ($x = (\varepsilon - \varepsilon_f)/k_B T$), and $\mu = (|H_{if}|^2 / h)\sqrt{4\pi^3 / \lambda k_B T}$ is a parameter for the distance dependence of the electronic coupling between the electrode and the redox sites. The coupling depends exponentially on distance, *d*, $\mu = \mu_0 \exp(-\beta d)$, β is the decay coefficient for

electronic tunneling, and μ_0 is the value of coupling constant at the closest distance from the electrode. The electron-transfer rate constants can be obtained by measuring the peak shift as a function of scan rate in cyclic voltammetry experiments[27a, 34]. Working curves of log(scan rate) versus peak position were generated for specific values of λ and T by a Mathcad program which numerically integrated the relevant equations. These working curves were used to fit the experimental data and obtain the standard rate constant, k^0, the rate constant at the point of formal potential (see Appendix for details).

1-3. ELECTRON TRANSFER STUDIES OF CYTOCHROME C

Cytochrome c plays an important role as a protein electron carrier in the cell biology of mitochondria for electron transport, oxidative phosphorylation and oxygen metabolism.[35] In the process, cytochrome c is reduced by an oxidized coenzyme Q, and coupling with a complex in membrane of mitochondrion, water is produced by oxidation of the cytochrome c by O_2. The reaction provides sufficient energy for synthesis of ATP (adenosine triphosphate) from ADP (adenosine diphosphate). Cytochromes facilitate electron transfer in respiration and photosynthesis by alternately binding to integral membrane proteins. So, understanding the correlation between structure and function, especially the electron transfer kinetics, is central to gaining insight into the roles of proteins in the body.

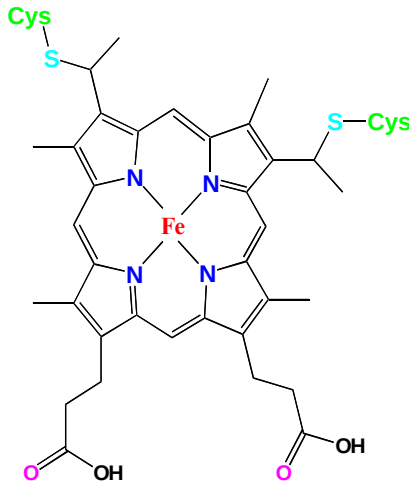

Figure 1- 8 The planar structure of the heme of cytochrome c

Cytochromes c's structure has been elucidated using a variety of methods[36, 37], such as x-ray diffraction techniques, dichroism, UV-vis spectroscopy, resonance Raman, mass spectrometry and nuclear magnetic resonance techniques (NMR) etc. Cytochrome c from horse heart, for instance, has been studied extensively both from structural and functional perspectives. Horse heart cytochrome c has a redox center which is a heme iron ligated by four nitrogen atoms

of the porphyrin ring, while a histidine (his-18) and a methionine (Met-80) serve as axial ligands.[38] There are 104 amino acids in horse heart cytochrome c which makes it a relatively simple and small metalloprotein. It is used widely to study the correlation between the function and structure of metal redox proteins. The redox center, iron heme, of cytochrome c is very important in respiration or photosynthesis. Figure 1- 8 shows the planar structure of the iron heme (axial ligation Met-80 and his-18 omitted). The formal potential of ferro/ferricytochrome c couple at pH 7 is 0.25~0.265 V vs NHE (standard hydrogen reference electrode).

Studying redox reactions and electron transport in cytochromes has been, and continues to be, an intense subject of study because of the importance of cytochromes in biological energy transduction processes. Because of limitations on the direct study in vivo, several model systems have been used to investigate the relationship of the structure and function in solution (homogeneous) and by immobilization on a surface (heterogeneous) (Figure 1- 9). For example, Sadegi S. J. et al [39a] report a model system to study the electrochemistry of interaction between two redox proteins, such as cytochrome c553 and cytochrome p450, by molecular "Lego", namely linking two proteins through an artificial peptide. Laser flash photolysis was used to get the intramolecular electron transfer rate constant in a buffer solution. Millett and coworkers [39b] studied the electron transfer interaction of yeast iso-1-cytochrome c with the high and low affinity binding sites on cytochrome c peroxidase compound using stopped-flow spectroscopy. Even though the homogeneous electron transfer model system is an important prototype for studying the kinetics of metalloproteins, it is meaningful to explore the biomolecular electron transfer mechanism using heterogeneous model systems, especially for long distance electron transfer reactions.

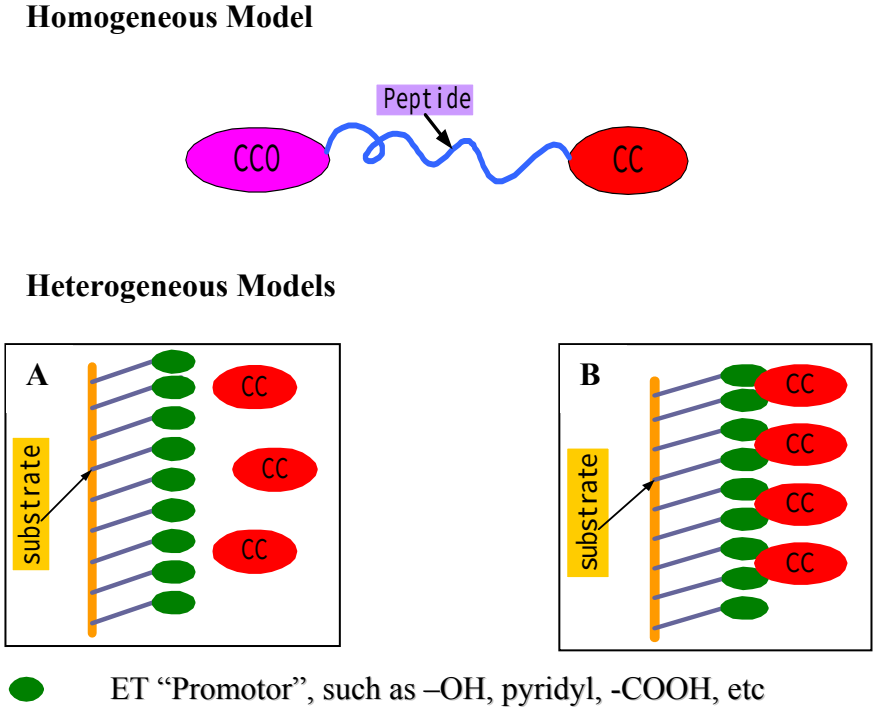

Figure 1- 9 A schematic diagram of models used in the electron transfer studies of cytochrome c. Homogeneous model represents that cytochrome c is linked through a molecular "Lego" (here a peptide) to another redox species, electron transfer reaction can be explored by spectroscopy. In heterogeneous models, A represents a model in which cytochrome c is freely diffusing in the solution and electron transfer through an ET "promoter" but without attachments; B represents a model in which cytochrome c molecules are adsorbed at the surface via "receptors"

Heterogeneous model systems enable a wide range of fundamental studies on electron transfer kinetics, bioelectronics, biosenors and so on.[40] Many researchers are engaged in heterogeneous electron transfer of cytochromes by modifying the electrodes because of the poor electroactivity of the protein at bare electrodes. Two model systems have been extensively used in electrochemistry through self-assembled monolayers. The first approach has the protein freely diffuse in the solution and operates under diffusion control [41] (Figure 1- 9 A). Disulfide, 1,2-bis(4-pyridyl) ethylene and bis(4-pyridyl) sulfide are the first molecules absorbed on gold electrodes that promote charge transfer reaction between the cytochromes and the electrodes.[41a, b] More recently, Miller and coworkers use self-assembled ω-hydroxythiol monolayers to

characterize the electron transfer rate between cytochrome c and an Au electrode; they determined the reorganization energy and the rate constant at different SAM thicknesses.[41d, e] However, recent research indicates that adsorption of cytochromes may take place even at bis(4-pyridyl) disulfide, 4-mercaptopyridine-modified gold electrodes or pure alkanethiol monolayers, previously considered as electrochemical non-adsorbing interface for metalloprotein.[42]

The second approach was first reported by the Bowden group[43] who controlled the reactivity by adsorbing cytochrome c through electrostatic association on carboxylic acid terminated monolayers (Figure 1- 9 B). This model system allows for the implementation of well-defined electrochemistry and electron transfer rate constant measurements as a function of film thickness. Niki and coworkers [44] investigated both long range and intermolecular electron transfer processes through the coupling between cytochrome c with carboxylic acid tethered alkanethiol SAMs. The effects of alkanethiol chain length, ionic strength, pH and viscosity of supporting electrolyte on electron transfer kinetics were examined. The voltammetric peak broadening [45] for such studies can display a significant degree of inhomogeneity, presumably a result of protein aggregation or a distribution of surface sites and geometries.

Most recently, pyridine-terminated SAMs with alkane chain length more than six methylenes were used to immobilize cytochrome c on gold electrodes. In these studies, a sufficient length of the methylene tether is needed for the pyridine group to penetrate into the cytochrome c and bind the heme.[46] The negative shift of the redox reaction's formal potential, compared to that observed on the carboxylic acid terminated films or cytochrome c in solution, demonstrates the strength of immobilization. It is known that the Met-80 axial ligand of native horse heart cytochrome c can be replaced by pyridine, imidazole and nitrile groups and their alkylated analogs. Figure 1- 10 displays the replacement reaction of Met-80 of the heme by

imidazole group, and Table 1-1 shows the formal potential of cytochrome c with different ligand hemes. Such replacements take place more favorably on oxidized states of cytochrome c, namely ferric-cytochrome c. In addition, the potential shift is expected to be affected by the solvent environment of the heme, conformational changes of the amino acid residues and, the steric changes of the protein.

Figure 1- 10 A scheme represents the reaction of Met-80 in heme of cytochrome c replaced by imidazole group

Table 1-1 Effects of the sixth ligand in low-spin metalloproteins reflected in redox potential shifts*

ligands	$E^{0'}$ (V vs. NHE)	ΔE (V)
His/Met-80	0.265	0.0
His/Pyridine	-0.029	-0.294
His/CN	-0.40	-0.665
His/Imidazole	-0.161	-0.426
His/1-MeIm	-0.094	-0.359
His/1-EtIm	-0.063	-0.327

* All data are cited from reference 38 p 276-277 and references therein; 1-MeIm is 1-methyl imidazole, 1-EtIm is 1- ethyl imidazole

In this thesis, a new strategy for cytochrome c immobilization at gold surfaces is decribed and applied to study the electron transfer of cytochrome c through SAMs. This approach, the

direct wiring the heme by a nitrogen ligand, provides a prototype to investigate many fundamentals of electron transfer kinetics of proteins, for instance electron transfer rate constant, electron transfer pathways, electronic coupling, the reorganization energy etc. Chapter 2 to Chapter 6 present the results of these studies.

1-4. ELECTRON SPIN POLARIZATION AND CHIRALITY EFFECTS IN ELECTRON TRANSFER

1-4-1. Electron Spin

An electron has a motion along its own axis which causes an angular momentum other than the orbital angular momentum from its circulation in space. This intrinsic angular momentum of the electron is termed as electron spin. Figure 1- 11 illustrates the electron intrinsic angular momentum which can be characterized only by a quantum number s=½. According to the quantized quantum momentum, the total electron spin angular momentum is:

$$S = [s(s+1)]^{1/2}\hbar = \frac{\sqrt{3}}{2}\hbar \qquad 1\text{-}29$$

This spin angular momentum is an intrinsic property of the electron and every electron has the same magnitude of spin angular momentum and can not be changed. The z-component of angular momentum is $S_z = m_s\hbar$ which is restricted to the 2s+1 values, i.e.

$$m_s = s, s-1, \ldots -s \qquad 1\text{-}30$$

The electron spin may only lie in two different orientations. As a charged particle, the magnetic momentum of individual electrons arising from its spin is $\mu_s = \frac{-e}{m_e} gS$, and the z-component of magnetic moment associated with the electron spin is $\mu_z = \frac{1}{2} g\mu_B$ in which $\mu_B = \frac{e\hbar}{2m_e}$ is termed as Bohr magneton. The electron spin magnetic moment is important in the spin-orbit interaction (spin-orbit coupling) which splits atomic energy levels and gives rise to fine structure in the spectra of atoms or molecules, dependent on the relative orientation of the spin and orbital magnetic moments. Taking the summation (vector) of z-component of orbital angular

momentum and spin angular momentum and all possible sums of their quantities, we will get quantum numbers for the angular momentum of the electron. $J_z=l_z+s_z$, j_z is half-integral only.

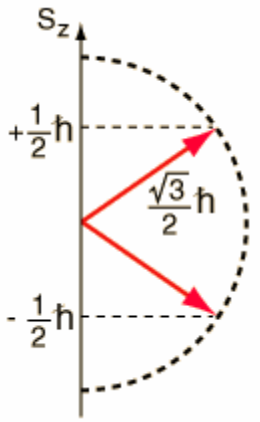

Figure 1- 11 An illustration of electron spin. The spin's "up" and "down" allows two electrons for each set of spatial quantum numbers (n, l, m_l)

1-4-2. Spin Polarization

Generally, spin polarization, a nonequilibrium spin (up or down) population of spin carriers, can be created through optical[47] or electrical injection[48]. To realize spin injection, an electrical current may be driven from a magnetic electrode in which electrons are spin polarized to a sample where a nonequilibrium spin population is accumulated. For optical injection, spin is polarized (oriented) through absorption of circular polarized light (right or left). Photons have quantum spin, but, the "spin axis" of a photon is always parallel to its direction of motion, pointing either forward or backward since photons travel at the speed c. These two states correspond to left-handed and right-handed photons. If electrons absorbed the angular momenta from the circular polarized light (with coherent spin, left or right), the electron orbital momenta will be directly oriented by light and the electron will be polarized through spin-orbit interaction.

The principle of electron spin polarization on semiconductor through circular polarized light will be illustrated by an example of GaAs below.

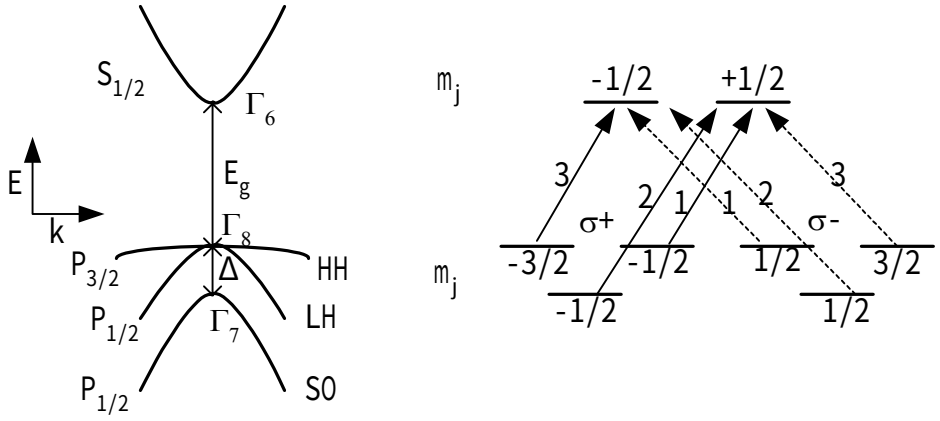

Figure 1- 12 Opitical spin polarization of semiconductor GaAs. On the left is the schematic band structure of GaAs at the center of the Brillouin zone showing the band gap energy, Eg=1.42 eV, and the spin-orbit splitting of the valence band, Δ=0.34 eV; Γ_6, Γ_7, Γ_8 are the corresponding symmetries at the k=0 point. On the right is a diagram of selection rules for interband transitions between the mj sublevels for circularly polarized light σ+ (solid line arrays) and σ-(dotted line arrays) (positive and negative helicity), with relative transition probabilities given by the numbers. HH and LH are the subbands at Γ_8 with angular monmentum 3/2 and 1/2, respectively.

The basic principle of optical spin polarization of GaAs is depicted in Figure 1- 12 in which the band structure of GaAs and the photoexcited spin-polarized electrons under irradiation with a circular polarized light (right or left) are illustrated. The probabilities (numbers along the arrows in Figure 1- 12) of the spin polarization are determined by the interaction of the angular and spin part of the wave function at subbands Γ with spherical harmonic operator corresponding to the (σ+ or σ-) optical transitions. The spin polarization of the excited electrons depends on the energy of incident light *hv*. If *hv* is between E_g and E_g+ **Δ**, only the electrons at subband Γ_8 can be excited. The relative densities of polarized spin of excited electron with σ+ light are 1 for parallel ($N\uparrow$) and 3 for antiparallel ($N\downarrow$) to the direction of light propagation. The spin polarization is defined as

$$P_n = \frac{N_\uparrow - N_\downarrow}{N_\uparrow + N_\downarrow} \qquad 1\text{-}31$$

For this example GaAs, one gets spin polarization P_n=(1-3)/(1+3)=-1/2 at the moment of light irradiation. The spin polarization is orientated against the direction of light propagation. If the light energy *hv* is equal to or greater than (E_g+**Δ)**, the electrons at spin-orbit split subband Γ_7 are involved in the electron transitions, no spin polarization occurs in the photoexcited electrons (P_n=0).

1-4-3. Electronic Excitation and Helicity of Porphyrins

Properties of porphyrins have been studied intensively[49] and refined continuously[50]. The theoretical models for electronic structure of the porphyrins has been developed and understood in terms of spectroscopies studies. The basic porphyrin ring has a sixteen-inner-member (atoms) "heart" with 18 π electrons, which are responsible for the porphyrin optical spectra. Based on the treatment of 16 atom cyclic polyene distorted by 4 pyrrole nitrogen atoms with simple extended Hückel molecular model, Gauterman and coworkers[51] have successfully, and the first time quantitatively, developed a 4-orbital model to describe the relative intensities of the two lowest energy $\pi \rightarrow \pi^*$ electronic transitions in porphyrin complexes. This model explained the absorption spectrum of porphyrin rings. The lowest energy excited singlet state from the electronic ground state Q(0,0) corresponds to the Q band between 500-650 nm, whereas the second excited singlet state from the ground state B(0,0) corresponds to the B bands (or Soret bands) between 380-420 nm. However, the change in porphyrin centers results in a variety in electronic and optical properties. Early studies[52] have found the two-banded (1Q,1B) visible spectrum observed from most metal or di-proton centered porphyrin complexes, distinctly different from four-banded (2Q, 2B) visible absorption spectrum in free base porphyrins, because

the centered two free base protons or metal center change the porphyrin ring symmetry from D_{2h} of free-base porphyrin to D_{4h}. A shoulder may show up on the high energy side (blue) of the Soret band due to one mode of vibrational excitiation B(1-0). Other bands with higher energy and much smaller intensities are present as N, L, M bands.

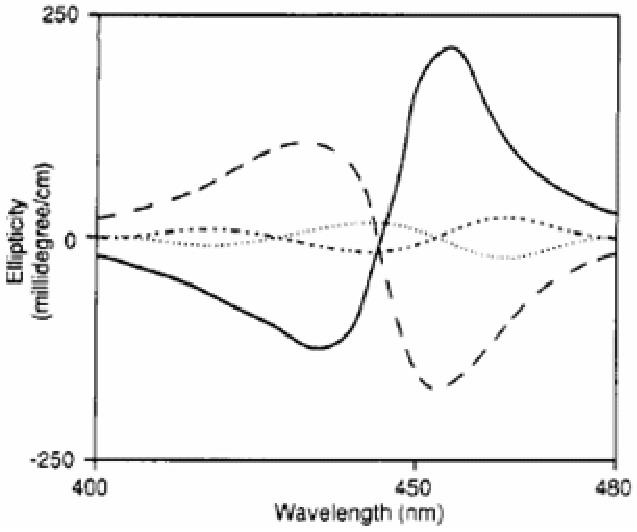

Figure 1- 13 An induced circular dichroism spectra of 5 uM free base porhyrin aggregate (trans-bis(N-methylpyridinium-4-yl)-diphenylporphine) in the presence of 50 uM polypeptides at pH4.5. Solid curve: poly-L-glutamate with 0.1 M NaCl, dashed curve: poly poly-D-glutamate with 0.1 M NaCl. (From ref 56a)

Light induced electron polarization in porphyrin complexes is one of the important optical properties, and has been widely studied by using time resolved electron paramagnetic resonance spectroscopy (EPR)[53], time dependent fluorescence anisotropy[50, 54], and circular dichroism[55,56]. In the early 1980's, Gibbs and coworkers[57] found large induced circular dichroism signals in the Soret (B) region of supramolecualr porphyrins-nucleic acid (DNA) structures. Later, the bisignates circular dichroism was observed in many bis-porphyrin derivatives[54b,55a] and peptide-porphyrin complexes or porphyrin aggregates[50a, 55b]. Figure 1- 13 shows an example of induced CD signals of free base porhyrin aggregates (*trans*-bis(N-methylpyridinium-4-yl)-

diphenylporphine) with presence of poly-Lglutamate or poly-D-glutamate peptide which was reported as helical structure[58]. The added NaCl generates porphyrin aggregates. Much weaker CD signal was observed from the porphyrin monomers in the solution (the dotted curve in Figure 1- 13, no NaCl is added)**.** The phases of induced CD of the porphyrins are reversed for the D verse L helical forms of the peptide, indicating the electronic helicity of excitation at the Soret region.

The electronic helicity can be ascribed to the long range coupling of transition dipole moments of porphyrin molecules (aggregate) orienting on the helical scaffold structure, where porphyrin monomer is not optically active. A model, so called exciton model, was first described by Kasha[59] for molecular aggregates, and later developed for porphyrin complex derivatives[55a ,60]. In this model, the B band is decribed as a combination of two mutually perpendicular oscillators, and they are considered degenerate in metal (or diprotonated) porphyrin (with D_{4h} symmetry) or free base porphyrin (D_{2h} symmetry). In other words, the Soret band (B band) of porphyrin monomer at Soret band consists of two components of absorption arising from B(0,0) and B(1,0). The B(0,0) is due to the excitation from ground state to the second excited singlet state whereas B(1,0), which is higher in energy, is due to the addition of one mode of vibrational excitation. So the single intense band at Soret band is a combination of both B(0,0) and B(1,0). These two B bands have polarizations perpendicular to each other. In the porphyrin aggregate, the exciton interaction gives rise to distinctive B bands (either split, or broadened single band, or with a shoulder depending on the electronic coupling between monomer second excited singlet states), they involve both B bands mentioned above. So the absorption bands have components arising from B(1,0) which is on the blue side (higher energy) and those arising from B(0,0) which is on the red side (low energy) of the aggregate absorption band. Also they have polarizations

perpendicular to each other and hence show opposite behaviour in CD experiments induced by chiral species.

As a summary, one can expect to obtain nonequilibrium electron spin (polarization) in the excitation at Soret band if a circular polarized light (left or right) illuminates to porphyrin complex with interporphyrin helicity.

1-4-4. The Interaction of Electron Helicity with Molecular Chirality

There is asymmetric interaction of chiral molecules with spin polarized electron helicity induced by polarized light. Hessler et al[61] unambiguously have observed the spin-dependent of electron beams transmitted (electron optic dichroism) with asymmetry factor of order 10^{-4} through metal-centered chiral molecules in a gas phase. In a photoemission experiment, Ray et al[62] have measured fairly larger asymmetry factor of 10^{-1} from multiple pure well-oriented chiral Langmuir-Blodgett films. Recently, Lischke and coworkers[63] have investigated asymmetry in a forward-backward angle-resolved photoelectron emission from unoriented chiral molecules induced by chircularly polarized light and shown asymmetry up to several percent which vary as a function of orbital binding energy. Other than the experimental studies, the corresponding theoretical developments have been evolved recently,[64] for the asymmetries in the collision of the polarized electron and chiral centers for both the oriented or unoriented molecules through electron scattering or photoemission.

General formulae allow people to disentangle the physical and orientational effects, which can provide a basis for the analysis of asymmetries in collisions between the electrons and oriented chiral molecules. For a given molecule system (M) (orientation defined by Euler angles $\alpha\beta\gamma$) with respect to the electron spin up ($\sigma+$) or spin down ($\sigma-$), the asymmetry factor in cross

section for elastic collisions between oriented molecules of definite handedness (M) and electrons of opposite spin polarization is defined as:

$$A = \frac{M(\sigma+) - M(\sigma-)}{M(\sigma+) + M(\sigma-)} \qquad 1\text{-}32$$

Whereas the asymmetry factor for collision between different isomers (molecular M and its optical enantiomer M') and electrons with definite helicity (spin up or down) is defined as:

$$\eta = \frac{M(\sigma+) - M'(\sigma+)}{M(\sigma+) + M'(\sigma+)} \qquad 1\text{-}33$$

In an unoriented molecule system, the two asymmetry factors should be basically the same due to the symmetry requirements. For oriented molecule systems, the A and η can be remarkably different and η can be much larger than A. Hessler results have provided the asymmetry A, while Ray et al have measured η.

Theoretical approach in terms of so-called "steric factors"[64c] has shown that the asymmetry *A* may depend on the molecular orientation during the elastic collision (electronic scattering) between electron helicity with the oriented chiral molecules, and the asymmetry factor can be one to two order larger than the unoriented chiral molecules[64b]. Figure 1- 14 provides an example of some numerical results for asymmetry factor A obtained through the theoretical approach. In this figure, α=β=0º, the C-Cl bond is parallel to the incoming beam axis. The molecule is rotated around z=Z, then the γ is changing, and A is shown as a function of γ. The results show that the left-handed electrons for M, the right-handed electrons for M' are scattered preferentially, and the asymmetry is about 1 order larger than the result from unoriented molecules. The studies on electron scattering in gas phase or electron photoemission through oriented chiral molecules both experimentally and theoretically have demonstrated that

the transmission efficiecy of electron through a target of chiral molecules may depend on the helicity of the electron (electron spin polarization or spin coherence). The larger asymmetry when the spin polarized electron transmits through oriented chiral molecules may result from the electron's wave function with many scattering chiral molecules in the organized structure.

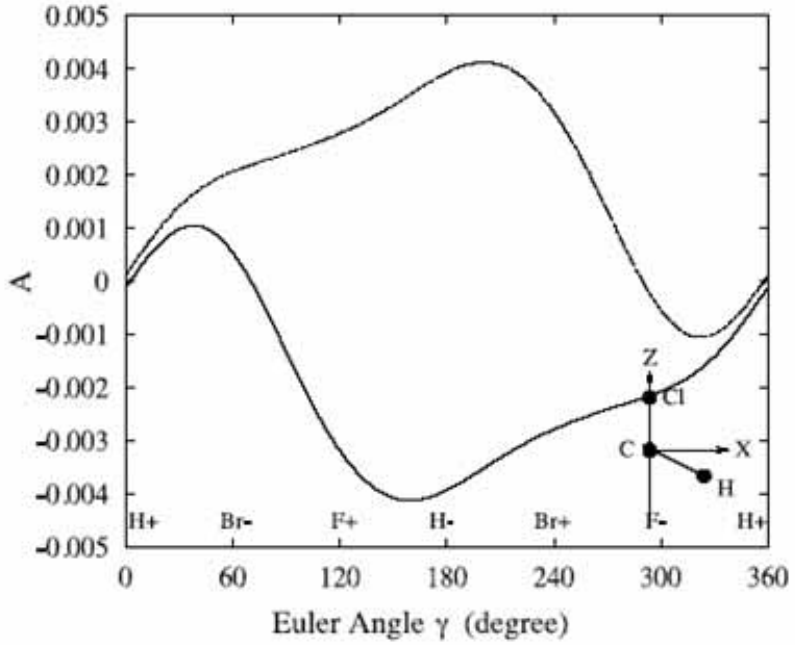

Figure 1- 14 A simulation of geometry dependent asymmetry A for CHBrClF in electron scattering. Electron energy 5.0 eV, α=0º, β=0º incoming electron bean orientation: θ=20º; Thick curve (negative A): molecule M, and thin curve: enantiomer M', from ref [64c].

Electron transfer through helical supramolecular structures has been intensely studied by using DNA[65,66] PNA (peptide nucleic acid)[67], poly peptide[68,69] polymers[70] or anologs, but the chirality effect has been investigated or exploited scarcely. Pujols-Ayala et al[69e] studied the role of peptide bond in electron transfer. Kimura group measured[69cd] the large dipole moment caused by helical peptide in the photoinduced electron transfer. Schenning and coworkers[70a] have realized well-defined chiral fibers incorporating donor and acceptor chromophores by self-assembly and measured the electron transfer rate constant, but no chiral effect was addressed.

Hence, a combinational study of chirality and electron helicity in electron transfer through helical structures would be of great interests in not only fundamentals of electron spin-chirality coupling or spin coherence transfer through supramolecules and biomolecules but also promising applications in the molecular recognition, chirality discrimination, quantum information processing and so on. In Chapter 7, the preliminary results of spin polarized electron transfer through self-assembled helical scaffold at gold surface are reported, including the scaffold monolayer preparation, characterization, asymmetry measurements and hypothesized mechanism of the coupling between electron helicity and molecular chirality.

BIBLIOGRAPHY

[1] a) Tarlow, M. J.; Bowden, F. F. . *Am. Chem. Soc*. **113**, 1847 (1991); b) Song, S.; Clark, R. A.; Bowden, F. F.; Tarlow, M. J. *J. Phys. Chem.* **1993**, *97*, 6564; c) Feng, Z. Q.; Imabayashi, S.; Kakuichi, T.; Niki, K. *Chem. Soc. Faraday Trans.* **1997**, *93*, 1367; d) Avila, A.; Gregory, B. W. ; Niki, K. ; Cotton, T. M. *J. Phys. Chem. B* **2000**, *104***,** 2759.

[2] Nuzzo, R. G.; Allara, D. L., *J. Am. Chem. Soc.*, **1983**, 105, 4481-4483.

[3] Finklea, H. O. Self-assembled monolayers on electrodes. In Robert A. Meyers (Ed.), *Encyclopedia of Analytical Chemistry* (2000). pp1-26. John Wiley & Sons Ltd, Chichester.

[4] Schreiber, F. *Progress in Surface Science,* **2000**, 65, pp151-256.

[5] Wink, T., Zuilen, S. J., Bult, A. and Bennekom, W. P.,. *Analyst*, **1997,** 122, 43-50.

[6] (a) Rubinstein, I.; Ron, H., *J. Am. Chem. Soc.*, **1998**, 120, 13444-13452; (b) Dia, P.; Jiang, D. et al, *J. Electroanal. Chem.* **1999**, 61-67.

[7] (a) Poirier, G. E.; Pylant, E. D., *Science*, 272 (1996), p 1145-1148; (b) Shon, Y. S.; Lee, T. R., *J. Phys. Chem. B*, 2000, 104, 8182-8191 (c) Shon, Y. S.; Lee, T. R., *J. Phys. Chem. B*, 2000, 104, 8192-8200.

[8] Bein, CD.; E. Barry Troughton, Tao, YT.; Evall, J.; Whitesides, GM.; Nuzzo; RG.; *J. Am. Chem. Soc.;* **1989**; *111*(1); 321-335

[9] Ulman, A. An Introduction to Ultrathin Organic Films, Academic Press, **1991**

[10] Porter, MD,; Bright, TB.; Allara, D.L.; *J. Am. Chem. Soc.;* **1987**; *109,*; 3559

[11] Schlenoff, J.B.; Li, M.; Ly, H. *J. Am. Chem. Soc.;* **1995**; *117,*; 12528-12536

[12] a) Laibinis, P.E.; Nuzzo, R. G.; Whitesides, G.M. *J. Phys. Chem.* **1992**, 96, 5097-5105; b) Bein, CD.; Whitesides, GM.; *J. Am. Chem. Soc.;* **1989**; *111*; 7155-7164-335

[13] Jortner, J. and Ratner, M. (Eds.) (1997) Molecular electronics. Malden, MA, Blackwell Science, Osney Mead, Oxford [England].

[14] Scherer, J.; Vogt, M.R., Magnussen, O.M.; Behm, R.J.; *Langmuir* 13 (1997) 7045.

[15] (a) Xiao, X.; Hu, J.; Charych, D.H.; Salmeron, M., *Langmuir* 12 (1996) 235. (b) Kim, H.I.; Graupe, M.; Oloba, O.; Koini, T.; Imaduddin, S.; Lee, T.R.; Perry, S.S.; *Langmuir* 15 (1999) 3179.

[16] Nuzzo. R. G. *Proc. Natl. Acad. Sci. USA*, 98(9), (2001) 4827-4829.

[17] Fendler, J. H., *Chemistry of Materials*, 13, (2001), pp 3196-3210.

[18] Wink, T., Zuilen, S. J., Bult, A. and Bennekom, W. P., *Analyst*, 122, (1997) pp 43-50.

[19] K.L. Prime, G.M. Whitesides, *Science* 252 (1991) 1164.

[20] a) Marcus, R. A. *J. Chem. Phys.* **1956**, 24, 966; b) Marcus, R. A. *Can. J. Chem.* **1959**, 37, 155.

[21] Newton, MD., *Chem. Rev.* **1991**, 767-792 and reference herein.

[22] Brunschwig, BS, Logan, J., Newton, MD., Sutin, N., *J. Am. Chem. Soc.* **1980**, 102, 5798-5809.

[23] a) Levich, VG., *Adv. Electrochem. Electrochem. Eng*. **1966**, 249; b) Kestner, NR.; Logan, J.; *J. Phys. Chem.* **1974**, 2148, c) Ulstrup, J.; Jortner, J.; *J. Phys. Chem.*, **1975**, 4358; d) Efrima, S.; Bixon, M. *Chem. Phys*. *1976*, 447; e) Van Duyne, RP.; Ficher, SF. *Chem. Phys.* **1974**, 5 183; f) Dogonadze, RR. Kuznetsov, AM.; Levich, VG. *Electrochim. Acta* **1968**, 13, 1025.

[24] (a) Dewar, M.J.S.; Dougherty, R. C. *The PMO Theory of Organic Chemistry*, Plenum, New York, **1975**. b) Sutin, N.; In *Bioorganic Chemistry*, Eichhorn, Eichhorn, G.L., Edt. American Elsevier, New York, **1973**.

[25] McConnell, H. M. *J. Chem. Phys.* **1961**, *35*, 508.

[26] (a) Chidsey, C. E. D *Science* **1991,** 251, 919; (b) Finklea, H. O. in: *Electroanalytical Chemistry* (A.J. Bard and I. Rubinstein, eds.); Marcel Dekker: New York, **1996,** 19, 109; (c) C. J. Miller, *Physical Methods in Electrochemistry*, I. Rubinstein, ed. (Wiley, NY, **1995**, 27. (d) Fendler, J. H., *Chemistry of Materials,* **2001,** 13, 3196-3210.

[27] (a) Napper, A. M.; Liu, HY; and Waldeck, D. H., *J. Phys. Chem.* B **2001**, 105, 7699-7707; (b) Sikes, H. D. Smalley, J. F.; Dudek, S. P.; Cook, A. R.; Newton, M. D.; Chidsey, C. E. D.; Feldberg, S. W. *Science,* **2001**, 291, 1519. (c) Stephen P. Dudek, Hadley D. Sikes, and Christopher E. D. Chidsey, *J. Am. Chem. Soc.* **2001**, 123, 8033-8038.

[28] (a) Weaver, M. J., *Chem. Rev.* **1992**, 92, 463-480; (b) Y. Fu, A. S. Cole, and T. W. Swaddle, *J. Am. Chem. Soc*. **1999,** 121, 10410.

[29] Marcus, R. A. *J. Chem. Phys*. **1965**, 43, 679.

[30] Closs, G. L.; Miller, J. R. *Science,* **1988**, 240, 440.

[31] Laviron, E., *J. Electroanal. Chem.*, **1979**, 101,19-28.

[32] Liu, Y.-P.; Newton, M. D. *J. Phys. Chem.* **1994**, *98*, 7162.

[33] (a) Weber, K., Creager, S. E., *Anal. Chem.* **1994**, 66, 3164-3172; (b) Tender, L., Carter, M. T., Murry, R. W., *Anal. Chem.* **1994**, 66, 3173.

[34] K. Weber and S. E Creager, *Anal. Chem*., **1994**, 66, 3164.

[35] Mathews, C. K.; Holde, K. E. van; Ahern, K. G., *Biochemistry* (Third edition), Book Addison Wesley Longman, p522-557

[36] (a) Scott, R. A.; Mauk, A. G., (Edt) *Cytochrome c*, A multidisciplinary approach, University Science Books, Sausalito, California p103-108; (b) Cinelli S, Spinozzi F, Itri R, Finet S, Carsughi F, Onori G, Mariani P., *Biophysical J.* 81 (6): 3522-3533, 2001; (c) Bushnell, G. W.; Louie, G. V.; Brayer GD, *J. Mol. Bio*., 214 (2): 585-595, (1990).

[37] (a) Bamford, V. A., Angove, H. C.; Seward, H. E.; Thomson, A. J.; Cole, J. A.; Butt J. N.; Hemmings, A. M.; Richardson, D. J., *Biochemistry* 41 (9): 2921-2931 (2002) (b) Banci, L., I. Bertini, M. Bruschi, P. Sompornpisut, P. Turano, *Proc. Natl. Acad. Sci. USA* 93: 14396-14400, (1996). (c) Grandori R., *Protein Science* 11 (3): p453-458 2002.

[38] Fedurco, M. *Coordination Chemistry Reviews*, 209 (2000) 263-331 and references therein.

[39] (a) Hazzard, J. T.; Govindaraj, S.; Poulos, T. L.; and Tollin, G., *J. of Biol. Chem.* 272 (12), pp. 7922–7926, 1997. (b) Mei, H.; Geren, L.; Miller, M. A.; Durham, B.; and Millett, F. *Biochemistry,* 41, 3968-3976, 2002.

[40] (a) Topoglidis, E.; Lutz, T.; Willis, R. L.; Barnett, C. J., Cass, A.; and Durrant, J. R. *Faraday Discuss.*116, p35-46, 2000; (b) Lowe, C. R., *Curr. Opin. in St. Bio*., 10 p428-434; (c) Ge, B.; Lisdat, F., *Analytic Chimica Acta* 454, p 53-64, 2002.

[41] (a) M.J. Eddowes, H.A.O. Hill, *J. Am. Chem. Soc.* 101 (1979) 4461. (b) I. Taniguchi, K. Toyosawa, H. Yamaguchi, K. Yasukouchi, *J. Chem. Soc. Chem. Commun.* (1982) 1032. (c) I. Taniguchi, S. Yoshimoto, K. Nishiyama, Chem. Lett. (1997) 353. (d) Samuel Terrettaz, Jun Cheng, and Cary J. Miller, *J. Am. Chem. Soc.* 1996, 118, 7857-7858. (e) J. Cheng, S. Terrettaz, J.I. Blankman, C.J. Miller, B. Dangi, R.D. Guiles, Isr. *J. Chem.* 37 (1997) 259.

[42] (a) E.P. Friis, J.E.T. Andersen, L.L. Madesn, P. Moller, R.J. Nichols, K.G. Olesen, J. Ulstrup, *Electrochim. Acta* 43 (1998) 2889. (b) Y. Maeda, H. Yamamoto, H. Kitano, *J. Phys. Chem.B*, 99 (1995) 4837.

[43] (a) Tarlov, M. J.; Bowden, E. F, *J. Am. Chem. Soc.* 1991, 113, 1847-1849 (b) Collinson, M.; Bosden, E. F.; Tarlov, M. J. *Langmuir*, 1992, 8, 1247; (c) Song, S. H.; Clark, R. A.; and Bowden, E. F, *J. Phys. Chem.* 1993, 97, 6564-6572

[44] (a) Feng, ZQ, Imabayashi, S., Kakiuchi, T., and Niki, K., *J. Chem. Soc. Faraday Trans.*, 1997, 93(7), 1367-1370; (b) Avila, A., Gregory. B. W., Niki, K., and Cotton, T. M., *J. Phys. Chem. B*, 2000, 104, 2759-2766.

[45] Clark, RA, and Bowden, E. *Langmuir* 1997, 13, 559-565.

[46] Yamamoto, H.; Liu, H.; Waldeck, D. H. *Chem. Comm*. 2001, 1032

[47] Meier, F.; Zakharchenya, B.P., **1984**, Eds., Optical Orientation (North-Holland, New York)

[48] Clark, W.G.; Feher, G., *Phys. Rev. Lett*. **1963**, 10, 134-138.

[49] The Porphyrin handbook, edited by Kadish, KM., Smith, KM., Guilard, R. , Academic press.

[50] a) Sriramakoti, A, PHD thesis, and reference herein, University Ordinances, 2002,; b) Pescitelli,G.; Gabriel, S,; Wang, YK.; Fleischhauer, J.; Woody, RW.; and Berova, N. *J. Am. Chem. Soc.* 2003, 125, 7613-7628. c) Guo, HW.; Jiang, JG.; Shi,YY.; Wang,YL; Liu, JN.; Dong, SJ. *J. Phys. Chem. B,* **2004**, *108,* 10185-10191

[51] Gouterman, M. J. In The Porphyrins, Dolphin, D. Edt.; Academic Press; New York, V0l 3, Part A Ch. 1, and reference therein;

[52] Dorough, G.D.; Miller, J. R.; Huennekens, F. M., *J. Am. Chem. Soc.* 1951. 73, 4315.

[53] a)Est, A.; Asano-Someda, M.; Ragogna, P.; Kaizu; Y. *J. Phys. Chem. A,* **2002**, 106, 8531-8542; b) Asano-Someda, M.; Est, A.; Kruger, U.; Stehlik, D.' Kaizu, Y.; Levanon, H., *J. Phys. Chem. A* **1999**, 103, 6704-6714; c) Carbonera, D.; Di Valentin, M., Corvaja, C.; Agostini, G.; Giacometti, G.; Liddell, PA.; Kuciauskas, D.; Moore, AL.; Moore, TA.; Gust, D.; *J. Am. Chem. Soc.* **1998,** *120,* 4398-4405; d) Berg, A.; Shuali, Z.; Levanon, H.; Wiehe, A.; Kurreck, H.; J. Phys. Chem. A **2001**, 105, 10060-10064; e) Fujisawa, J.; Ishii, K.; Ohba, Y.; Iwaizumi, M.; Yamauchi. S. *J. Phys. Chem.* **1995,** 99, 17082-17084; f) Wasielewski, MR.; Gaines, GL.; Wiederrecht, GP.; Svec, WA.; Niemczyk, MP, *J. Am. Chem. SOC.* **1993,**115**,** 10442-10443

[54] a) Shediac,R.; Gray, MHB.; Uyeda, HT.; Johnson, RC.; Hupp, JT.; Angiolillo, PJ.; Therien, MJ.; *J. Am. Chem. Soc.* **2000**, *122,* 7017-7033; b) Kumble, R.; Palese, S.; Lin, V. S.-Y.; Therien, M. J.; Hochstrasser, R. M. *J. Am. Chem. Soc.* **1998**, *120*, 11489-11498.

[55] a) Pescitelli, G.; Gabriel, S.; Wang,Y.; Fleischhauer, J.; Woody, RW.; Berova, N. *J. Am. Chem. Soc.* **2003**, 125, 7613-7628; b) Borovkov, V. V.; Lintuluoto, J. M.; Fujiki, M.; Inoue, Y. *J. Am. Chem. Soc.* **2000**, *122*, 4403-4407; (c) Borovkov, V. V.; Lintuluoto, J. M.; Sugeta, H.; Fujiki, M.; Arakawa, R.; Inoue, Y. *J. Am. Chem. Soc.* **2002**, *124*, 2993-3006. d) Lintuluoto, J. M.; Borovkov, V. V.; Inoue, Y. *J. Am. Chem. Soc.* **2002**, *124*, 13676-13677. Borovkov, V. V.; Lintuluoto, J. M.; Inoue, Y. *J. Phys. Chem. A* **2000**, *104*, 9213-9219. (e) Borovkov, V. V.; Lintuluoto, J. M.; Inoue, Y. *Org. Lett.* **2000**, *2*, 1565-1568, f) Borovkov, V. V.; Lintuluoto, J. M.; Inoue, Y. *J. Am. Chem. Soc.* **2001**, *123*, 2979-2989.

[56] a) Pasternack, RF.; Giannetto, A.; Pagano, P.; Gibbs, EJ. *J. Am. Chem. Soc.* **1991,** 113**,** 7799-7800; b) Ogoshi, H.; Mizutani, T. *Acc. Chem. Res.* **1998**, *31*, 81-89. c) Ogoshi, H.; Mizutani, T.; Hayashi, T.; Kuroda, Y. In *The Porphyrin Handbook*;Kadish, K. M., Smith, K. M., Guilard, R., Eds.; Academic Press: San Diego,2000; Vol. 6, pp 280-340. d) Weiss, J. *J. Inclusion Phenom. Macrocyclic Chem.* **2001**, *40*, 1-22. e) Kurtan, T.; Nesnas, N.; Koehn, F. E.; Li, Y.-Q.; Nakanishi, K.; Berova, N.*J. Am. Chem. Soc.* **2001**, 123, 5974-5982

[57] a) Gibbs, E. J.; Tinoco, I., Jr.; Maestre, M.; Ellinas, P. A,; Pasternack, R. F. *Biochem. Biophys.* Res. Commun. **1988**, *157,*350. b) Gibbs, E. J.; Maurer, M. C.; Zhang, J. H.; Reiff, W. M.; Hill, D. T.; Malicka-Blaszkiewicz, M.: McKinnie, R. E.; Liu, H. Q.; Pasternack, R. F. *J.* Inorg. *Biochrm.* **1988**, *32,* 39. c) Pasternack, R. F.; Brigandi, R. A,; Abrams, M. J.; Williams, A. P.; Gibbs, E. *J. Inorg. Chem.* **1990**, *29,* 4483.

[58] a) Doty, P.; Wada, **A,;** Yang, J. T.; Blout, E. R. *J. Polym. Sci.* **1957**,23, 851. b) Idelson. M.; Blout, E. R., *J. Am. Chem. Soc.* **1958,** 80, 4631. (c) Stryer, **L.;** Blout, E. R. *J. Am. Chem. Soc.* **1961,** 83, 1411.

[59] Kasha, M. *Radiat. Res.* **1963**, *20*, 55-70

[60] a) Osuka, A.;Maruyama, K. *J. Am. Chem. Soc.* **1988**, *110*, 4454-4456. b) Ohno, O.; Ishikawa, N.; Matsuzawa, H.; Kaizu, Y.; Kobayashi, H. *J. Phys. Chem.* **1989**, *93*, 1713-1718. c) Eriksson, S.; Kaellebring, B.; Larsson, S.; Maartensson, J.; Wennerstroem, O. *Chem. Phys.* **1990**, *146*, 165-177. d) Tran-Thi, T. H.; Lipskier, J. F.; Maillard, P.; Momenteau, M.; Lopez- Castillo, J. M.; Jay-Gerin, J. P. *J. Phys. Chem.* **1992**, *96*, 1073-1082. e) Munro, O. Q.; Marques, H. M. *Inorg. Chem.* **1996**, *35*, 3768-3779.

[61] a) Mayer, S.; Kessler, J., *Phys. Rev. Lett.*, **1995**, 74, 4803-4806, b) Mayer, S.; Nolting, C.; Kessler, J., *J. Phys.* B: At. Mol. Opt. Phys. **1996**, 29,3497-3511.

[62] Ray, K.; Ananthavel, S. P.; Waldeck, D. H. and R. Naaman*, Science* **1999** 283, 814.

[63] a) Lischke, T.; Bowering, N.; Schmidtke, B.; Muller, N.; Khalil, T.; Heinzmann, U., *Phys. Rev.* A, 2004, 70, 022507. b) Bowering, N., Lischke, T., Schmidtke, B., Muller, N., Khalil, T., Heinzmann, U., *Phys. Rev. Lett.*, **2001**, 86, 1187-1190,

[64] a) Blum K. and Thompson, D. G. *Adv. At. Mol. Opt. Phys*. **1997,** 38, 39; b) Smith, I M.; Busalla, A.; Thompson, D. G.; Blum K.;*J. Phys. B:* At. Mol. Opt. Phys. **1998,** 31, 4039; c)Musigmann, M.; Busalla, A.; Blum K.; Thompson, D. G. *J. Phys. B:* At. Mol. Opt. Phys. **1999,** 32, 4117-4128; d) Musigmann, M.; Blum K.; Thompson, D. G. *J. Phys. B:* At. Mol. Opt. Phys. **2001,** 34, 2679-2696; e) Musigmann, M.; Busalla, A.; Blum K.; Thompson, D. G. *J. Phys. B*: At. Mol. Opt. Phys. **2001,** 32, L79-L85;

[65] a) Kelley, SO.; Jackson, NM.; Hill, MG.; and Barton, JK. *Angew. Chem. Int. Ed.* **1999**, 38, 941. b) Giese, B.; Wessely, S.; Spormann, M.; Lindemann, U.; Meggers, E.; and Michel-Beyerle, ME.; *Angew. Chem. Int. Ed.* **1999**, 38, 996. c) Harriman, A., *Angew. Chem. Int. Ed.* **1999**, 38, 945; d) Grinstaff, MA. *Angew. Chem. Int. Ed.* **1999**, 38, 3629.

[66] a) Long,YT.; Li, CZ.; Sutherland, TC.; Chahma, M.; Lee,JS.; Kraatz, HB.; *J. Am. Chem. Soc.* **2003,** 125, 8724-8725; b) Li, C.-Z.; Long, Y.-T.; Kraatz, H.-B.; Lee, J. S.; *J. Phys. Chem. B. ;* **2003**; *107*(10); 2291-2296. c) Long, Y.-T.; Li, C.-Z.; Sutherland, T. C.; Kraatz, H.-B.; Lee, J. S.; *Anal. Chem.;* **2004**; *76*(14); 4059-4065. d) Breeger, S.; Hennecke, U.; Carell, T.; *J. Am. Chem. Soc.;***2004**; *126*(5); 1302-1303.

[67] Cichon, M. K.; Haas, C. H.; Grolle, F.; Mees, A.; Carell, T.; *J. Am. Chem. Soc.;* **2002**; *124*(47); 13984-13985.

[68] a) Sakamoto, M.; Ueno, A.; and Mihara, H.; *Chem. Commun.*, **2000**, 1741–1742; b) Niwa,M.; Morikawa, M.; and Higashi, N.*; Angew. Chem. Int. Ed.* **2000**, 39, 960. c) Huang, CY.; He, S.; DeGrado, WF.; McCafferty,DG.; Gai, F., *J. Am. Chem. Soc.* **2002,** 124, 12674-12675

[69] a) Yanagisawa, K.; Morita, T.; Kimura, S.; *J. Am. Chem. Soc.;* **2004**; *126*(40); 12780-12781. b) Kitagawa, K.; Morita, T.; Kimura, S.; *J. Phys. Chem. B. ;* **2004**; *108*(39); 15090-15095. c) Morita, M.; Kimura, T.; *J. Am. Chem. Soc.;* **2003**; *125*(29); 8732-8733. d) Morita, T.; Kimura, S.; Kobayashi, S.; Imanishi, Y.; *J. Am. Chem. Soc.;* **2000**; *122*(12); 2850-2859. e) Pujols-Ayala, I.; Sacksteder, C. A.; Barry, B. A.; *J. Am. Chem. Soc.;* **2003**; *125*(25); 7536-7538.

[70] a) Schenning, A. P. H. J.; v. Herrikhuyzen, J.; Jonkheijm, P.; Chen, Z.; Wurthner, F.; Meijer, E. W.;. *J. Am. Chem. Soc.* **2002,** 124, 10252-10253. b) Schenning, A. P. H. J.; Peeters, E.; Meijer, E. W.; *J. Am. Chem. Soc.;* **(Article); 2000**; *122*(18); 4489-4495.

CHAPTER 2 DIRECT WIRING OF CYTOCHROME C'S HEME UNIT TO AN ELECTRODE: AN ELECTROCHEMICAL STUDY[§]

A novel strategy for the immobilization of cytochrome c on the surface of chemically modified electrodes is demonstrated and used to investigate the protein's electron transfer kinetics. Mixed monolayer films of alkanethiols and ω-terminated alkanethiols (terminated with pyridine, imidazole or nitrile groups that are able to ligate with the heme) are used to adsorb cytochrome c to the surface of gold electrodes. The use of mixed films, as opposed to pure films, allows the concentration of adsorbed cytochrome c to remain dilute and ensures a higher degree of homogeneity in their environment. The adsorbed protein is studied using electrochemical methods and scanning tunneling microscopy.

2-1 INTRODUCTION

Electron transfer reactions play a central role in biological processes, for example photosynthesis and respiration. In addition, electron transfer processes are central to the development and operation of many biosensors and biocatalytic devices. Our understanding of electron transfer in proteins has seen great strides in recent years for both unimolecular and bimolecular processes. With the recent growth of methods to control and manipulate the surface chemistry of electrodes, heterogeneous electron transfer with biomolecules (proteins, nucleotides, etc.) should see a similar development. This work describes a strategy for immobilizing

[§] This work has been published as Wei, JJ; Liu, HY; Dick, AR; He, HY; Waldeck, DH. "Direct Wiring of Cytochrome c's Heme Unit to an Electrode: Electrochemical Studies", *J. Am. Chem. Soc.,* **2002**, 124, 9591-9599

biomolecules on a chemically modified electrode through a specific interaction that provides some selectivity for the biomolecule's orientation on the surface. This strategy is realized for the binding of cytochrome c to the surface of chemically modified Au electrodes and should enable a range of fundamental studies on the electron transfer kinetics.

A number of workers [1,2,3] have investigated the electron transfer mechanism of cytochrome c on electrodes. The earliest studies were reported for electrodes modified with a redox mediator through which the electrode reduces or oxidizes the cytochrome c. Much of this early work focused on finding systems in which the electron transfer is facile and preventing decomposition of the protein on the electrode. More recently Miller [4] used hydroxyl terminated alkanethiols to coat the surface of Au electrodes and found that the electron transfer rate constant could be controlled by changing the thickness of the monolayer film, however he did not immobilize the protein on the surface. Workers [2,3] have immobilized cytochrome c by electrostatic association of carboxylic acid terminated alkanethiol monolayer films with the positively charged outer surface of the protein. These systems allow for the implementation of well-defined electrochemistry and electron transfer rate constant measurements as a function of the film thickness. However, the voltammograms obtained from such studies can display a significant degree of inhomogeneity, presumably a result of protein aggregation or a distribution of surface sites and geometries.

Most recently cytochrome c was immobilized on the surface of pure monolayers of pyridine-terminated alkanethiols that had alkane chain lengths of more than six methylenes [5]. For chain lengths below six methylenes no immobilization was observed. Presumably, the length requirement results from the need for the cytochrome to partially penetrate the film so that the pyridine moiety can interact with the heme. A large negative shift in the apparent redox

potential, compared to that observed on the carboxylic acid terminated films, was identified. Although the immobilization was robust, the electrochemical response was not very reversible, making these systems unsuitable for detailed studies of the electron transfer mechanism.

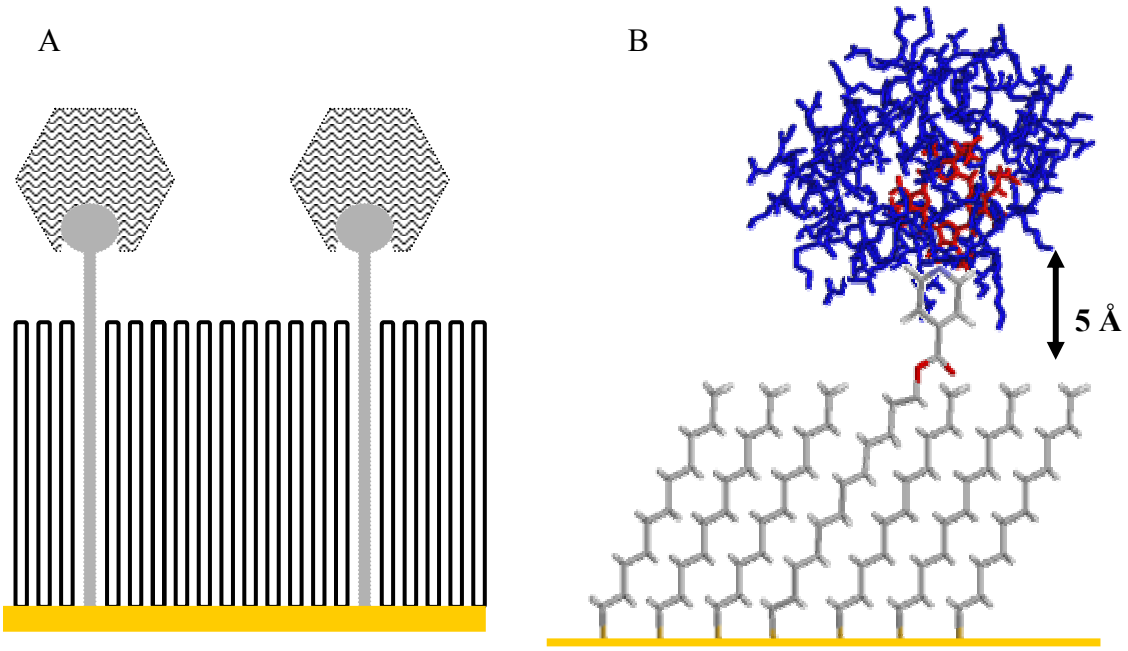

Figure 2- 1 The schematic diagram in panel A illustrates the strategy for immobilizing a molecule on the monolayer surface through a specific binding event. The drawing in panel B illustrates the realization of this approach for immobilizing cytochrome c on the suface.

This work demonstrates the ability to create mixed monolayer films that associate with a specific part of the protein and allow electron transfer to its redox center. Figure 2- 1 illustrates the design of the monolayer system (Panel A) and its realization for the pyridine/cytochrome c system (Panel B). By creating mixed films of pyridine alkanethiols in a diluent of shorter chain alkanethiols, cytochrome c can be immobilized on the surface by association of the functionalized longer chain thiols with the heme of the cytochrome. The immobilization is achieved by an alkanethiol that is terminated with a functionality that can bind to the heme of the

cytochrome, in particular pyridine and imidazole were found to interact strongly, and nitrile terminated chains more weakly. Chart 2-1 shows the materials used to create these three mixed film systems. The immobilization is demonstrated by electrochemical voltammetry measurements and STM imaging of the surfaces. We further show that the voltammograms are close to ideal, which indicates well-defined sites on the surface of the electrode, allowing the electron transfer kinetics to be characterized electrochemically. This strategy for immobilization should be applicable to many systems and should allow the use of electrochemical methods to address important issues in protein electron transfer; *e.g.,* developing structure-function relationships for the reorganization energy, quantifying the relationship between the electronic coupling and the electron transfer mechanism, and others.

CHART 2-1

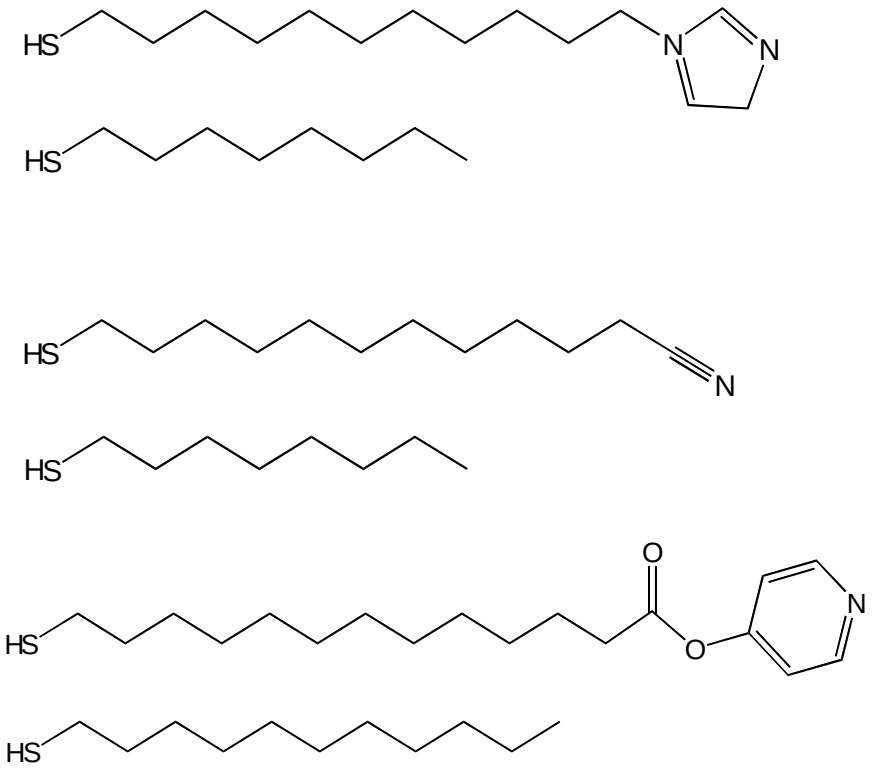

2-2 EXPERIMENTAL SECTION

Reagents and Materials: Water for experiments was purified by using a Barnstead-Nanopure system and had a resistivity of 18 MΩ-cm. 1,2-Dicyclohexylcarbodiimide, or DCC, (99%) was purchased from Alfa Aesar. 1-Octanethiol (98.5+%), 1-hexadecanethiol, and 1-undecanethiol (98+%) were purchased from Aldrich and used without further purification. Imidazole (99%), 11-bromo-1-undecanol (98%), 12-mercapto-1-dodecanol (98+%), methanolic iodine (99%), sodium bisulfite (99%), thiourea (99+%, A.C.S. reagent), K_2CO_3 (99+%, A.C.S. reagent), NaOH (97%) and $MgSO_4$ (99%) were purchased from Aldrich. Absolute ethanol was purchased from Pharmco Products, Inc.

Cytochrome c (Sigma C 7752, from horse heart, minimum 95% based on molecular weight 12384) was purified using a cation exchange column (CM-52, carboxymethyl-cellulose from Whatman). The purification was carried out in a cold room at 5°C, by the reported method.[6] 30 mg of cytochrome c was dissolved in 2 ml of 50 mM phosphate buffer solution at pH 7 (25 mM Na_2HPO_4 and 25 mM NaH_2PO_4). A small amount of $K_3Fe(CN)_6$ was added to the solution to oxidize the protein. This solution was placed onto a 1.5 cm diameter by 30 cm long column containing carboxymethyl cellulose (Whatman, CM-52) that was pretreated with 25 mM of the phosphate buffer. The protein was eluted with 50, 60, 70, and 80 mM phosphate buffer in a stepwise manner. The center of the last separated portion was collected. The phosphate buffer was removed from the protein using an ultrafiltration membrane (Millipore, YM10) under positive pressure. The cytochrome c aqueous solution was quickly frozen at –80 °C, and dried in vacuum. The purified cytochrome c was stored in a freezer with dry ice under an argon atmosphere until use.

Electrode Preparation: A gold wire (0.5 mm dia.,99.99%) was cleaned by reflux in nitric acid (68-70%) at 130°C for overnight, and then washed with deionized water. The tip of the gold wire was heated to form a ball *ca*. 0.06-0.15 cm^2 surface area. The gold ball was reheated in the flame until glowing and then quenched in deionized water. This annealing process was performed a few times to make a smooth gold ball. The exposed Au wire was sealed in a glass capillary tube, and the Au ball tip was annealed and cooled down in a high purity stream of Argon gas.

Chemically modified electrodes were prepared by immersion in an ethanol solution that contained 1 mM of 1-(11-mercaptoundecyl) imidazole and 1-octanethiol (the mole ratio of 1-(11-mercaptoundecyl) imidazole to 1-octanethiol was 1:9). The electrode remained in this solution for 1-2 days to form the mixed SAM. The electrode was taken out from the solution; first rinsed with absolute ethanol, then rinsed with the supporting buffer solution (20 mM phosphate buffer pH 7) and finally dried with a stream of dry argon gas. At this stage the electrode was used to perform characterization studies of its capacitance and voltammetric response in the buffer solution. After this characterization, the electrode was immersed in a 100 μM cytochrome c solution (purged with argon gas) for 30 to 60 minutes in order to immobilize the cytochrome on the SAM coated electrode. These electrodes were immediately used in voltammetry studies.

After the measurements, the monolayer film was removed from the electrode by immersing it in a "piranha" solution (a mixture of 30% H_2O_2 and 98% H_2SO_4 in a 1:3 volume ratio) for 20 sec. The surface area of the electrode was then determined by performing voltammetry in a 0.5 M KCl solution that contained 1mM $K_3[Fe(CN)_6]$ and 1mM $K_4[Fe(CN)_6]$. The peak current in this measurement displayed a linear relation with the square root of the scan rate [7].

The same procedure was used to prepare the pyridine and nitrile terminated thiol monolayers. For the pyridine-terminated films the 1mM thiol solution was composed of a 1:9 mixture of 1-(12-mercaptododecyl)pyridine and 1-undecanethiol, and for the nitrile-terminated films the 1 mM thiol solution was composed of 1-(11-mercaptoundecyl)nitrile and 1-ocatecanthiol. For the control study in which the diluent film blocked adsorption, the SAM was comprised of 1-(12-mercaptodecyl)pyridine and 1-hexadecanethiol.

Electrochemical measurements: Cyclic voltammetry on the immobilized cytochrome c was carried out with an EG&G PAR-283 potentiostat, which was controlled by a Pentium computer running ver. 4.3 of PARC Model 270 software and a GPIB board. The three electrode cell was composed of a platinum spiral counter electrode, an Ag/AgCl (3 M NaCl) reference electrode, and the SAM coated Au as a working electrode. The voltammetry measurements were performed in 20 mM phosphate buffer solution (pH of 7.0) under an argon atmosphere.

Impedance measurements (EIS) were performed using a VoltaLab PGZ407 universal potentiostat to determine the capacitance of the mixed SAMs before immobilization of the cytochrome c. The experiments were performed with a three electrode cell and a 20mM phosphate buffer solution (pH of 7.0).

STM Measurements: For the STM studies a Au(111) facet of a single crystalline bead (prepared by the Clavilier's method [8]) was used as the substrate. It was cleaned by immersion in hot piranha solution (1:3 H_2O_2 and H_2SO_4) for 1 hour, followed by immersion in hot HNO_3 for 30 minutes. After each step the sample was rinsed by ultrasonication in ultrapure water (>18.2 MΩ-cm) from a Barnstead, Nanopure Infinity system. The crystal was hydrogen flame annealed,

and allowed to cool down to room temperature in air. The preparation of mixed SAMs of 1-(12-mercaptodecyl) pyridine and 1-undecanethiol (1:9 mole ratio) on the Au (111) bead for STM was the same as the SAM's prepared for electrochemical experiments. Two beads were put into the solution mixture for two to three days. One bead was rinsed with ethanol and then directly used for STM experiments, while the other bead was placed in a solution of cytochrome c (100 μM) for 30-60 minutes to immobilize the protein. This bead was rinsed with supporting buffer solution before being analyzed by STM. The STM images were obtained with a PicoScan STM system (Molecular Imaging). STM tips were cut by using 0.25 mm diameter Pt-Ir wires (Goodfellow). All the STM images were obtained under constant current mode at 50-100pA and a tip-sample bias of 0.8-1.0V.

1. Synthesis of 1-(1-mercaptoundecyl)imidazole: The 1-(11-mercaptoundecyl) imidazole was prepared in the following manner. Imidazole (1.453 g, 21.316 mmol) and 11-bromo-1-undecanol (5.355 g, 21.316 mmol) were added together in 50 mL of dry DMF under argon atmosphere. K_2CO_3 (5.898 g, 42.676 mmol) was added to the mixed solution and stirred for 24 hours at room temperature. The resulting mixture was poured into iced water and extracted with methylene chloride (350 mL) to remove DMF. The solution was dried with $MgSO_4$, filtered, concentrated and purified by column chromatography (silica gel, chloroform) to obtain 1-(11-hydroxundecyl) imidazole. 1H NMR (300 MHz) $CDCl_3$: 7.503 (s, 1H); 7.064 (s, 1H); 6.911 (s, 1H); 3.933 (t, J= 7.08, 2H); 3.64 (t, J= 6.89, 2H); 1.772 (m, 2H); 1.561 (m, 2H); 1.267 (broad, 14 H). The 1-(11-hydroxyundecyl)imidazole (3.259, 12.83 mmol) and thiourea (2.930g, 38.492 mmol) were added to 35 mL of hydrobromic acid (48%) and refluxed for a day. The mixture was neutralized with K_2CO_3, then NaOH was added (1.539 g, 38.492 mmol), and the solution was

refluxed in an argon atmosphere for 8 hours. The resulting solution was cooled down to room temperature, poured into ice water and extracted with methylene chloride. The solution was dried with $MgSO_4$, filtered, concentrated and purified by column chromatography (silica gel, chloroform) to obtain 1-(11-mercaptoundecyl) imidazole. 1H NMR (300 MHz) $CDCl_3$: 7.490 (s, 1H); 7.066 (s, 1H); 6.905 (s, 1H); 3.924 (t, J= 7.13, 2H); 2.522 (q, J=7.47, 2H); 1.769 (m, 2H); 1.605 (m, 2H); 1.392-1.264 (broad, 15 H). EI-HRMS: Calcd. 254.18167, ($C_{14}H_{26}N_2S$), Found 254.18215.

2. Synthesis of Bis[12-((pyridinylcarbonyl)oxy)dodecyl]disulfide

a. Bis(12-hydroxyododecyl)disulfide: 12-Mercapto-1-dodecanol (10 mmol) was dissolved in 50 mL methanol and titrated with 0.5 M methanolic iodine until the reaction solution turned from colorless to a persistent yellow. The reaction was quenched with 10% sodium bisulfite to a colorless solution. The resulting mixture was dissolved in distilled water and extracted with CH_2Cl_2. The solvent was removed under vacuum. Purification of the resulting crude disulfide was performed by flash chromatography (CH_3Cl) to obtain the disulfide as a white solid. ^1H NMR (300 MHz) $CDCl_3$: δ 3.651 (q, J= 6.36, 4H); 2.689 (t, J= 7.34, 4H); 1.654 (m, 4H); 1.570 (m, 4H); 1.379-1.255 (m, 32H).

b. Bis[12-((pyridinylcarbonyl)oxy)dodecyl]disulfide: 1,2-dicyclohexylcarbodiimide (DCC) (0.603 g, 2.92 mmol) was added to 20 mL of dichloromethane solution of bis(12-hydroxydodecyl)disulfide (0.55 g, 1.33 mmol), isonicotic acid (0.327 g, 2.66 mmol) and 4-dimethylaminopyridine (32 mg, 0.266 mmol) at 0 ^oC. After one hour, the solution was allowed to warm to room temperature and stirring was continued for 4 days. After removal of the precipitated dicyclohexylurea (DCU) by filtration, the solvent was removed under reduced

pressure to yield a crude solid. The solid was recrystallized with ethanol to yield a white powder product. ^{1}H NMR (300 MHz) $CDCl_3$: δ 8.799 (s, 4H); 7.910 (d, J= 4.83, 4H); 4.369 (t, J= 6.60, 4H); 2.685 (t, J= 7.29, 4H); 1.766 (m, 4H), 1.676 (m, 4H); 1.378-1.287 (m, 32H). EI-HRMS: Calculated to be 644.370, ($C_{36}H_{56}N_2O_4S_2$), and found to be 644.368.

3. Synthesis of 12-mercapto-dodecanenitrile

a. 12-hydroxy-dodecanenitrile: 11-bromo-undecanol (4.00g, 15.923 mmol) and sodium cyanide (1.528 g, 31.84 mmol) were added to 30 mL of DMSO solution and stirred at 80 ^{o}C for two days. The resulting solution was extracted with methylene chloride and washed with a large amount of water to remove DMSO. The combined organic layers were washed, dried, and concentrated at reduced pressure. The crude product that resulted from evaporation of solvent was purified by column chromatography (methylene chloride) to obtain 12-hydroxy-dodecanenitrile. H NMR δ ($CDCl_3$): 3.626 (t, J= 6.60 Hz, 2H), 2.332 (t, J= 7.02 Hz, 2H), 1.650 (m, 2H), 1.558 (m, 2H), 1.435 (m, 2H), 1.281-1.208 (broad, 12H).

b. 12-Bromdodecanenitrile: 12-hydroxy-dodecanenitrile (1.20 g, 6.09 mmol) was dissolved in 30 mL of dry ethyl ether and cooled down to –10 ^{o}C. Subsequently, 0.6 mL of PBr_3 was added to the solution and stirred at room temperature for three days. The resulting solution was washed with 0.1 M Na_2CO_3 solution and pure water and extracted with ethyl ether. The combined organic layers were washed, dried, and concentrated at reduced pressure. The crude product that resulted from evaporation of solvent was purified by column chromatography (methylene chloride) to obtain 12-bromodecanenitrile. H NMR δ ($CDCl_3$): 3.409(t, J= 6.81 Hz, 2H), 2.337 (t, J= 7.10 Hz, 2H), 1.630 (m, 2H), 1.417 (m, 2H), 1.342 (m, 2H), 1.225-1.207 (broad, 12H).

c. 12-mercapto-dodecanenitrile: 12-mercapto-dodecanenitrile was prepared according to a literature procedure [9]. 11-bromo-undecanenitrile (1.079 g, 3.978 mmol) and thiourea (0.899 g, 11.812 mmol) were added to 50 mL of dry ethanol and refluxed overnight under N_2 atmosphere. The solvent was removed at reduced pressure. 50 mL of water containing KOH (0.662 g, 11.81 mmol) was added and refluxed for 6 hours. The resulting solution was cooled down to room temperature and extracted with methylene chloride and washed with water. The combined organic layers were washed, dried, and concentrated at reduced pressure. The crude product that resulted from evaporation of solvent was purified by column chromatography (methylene chloride) to obtain 12-mercapto-dodecannitrile. H NMR δ ($CDCl_3$): 2.516 (q, J= 7.41 Hz, 2H), 2.332 (t, J= 7.08 Hz, 2H), 1.674 (m, 4H), 1.459-1.276 (broad, 17H). EI-HRMS: Calcd. 213.1551 for $C_{12}H_{23}NS$ and Exptl 213.1542.

2-3 RESULTS

Structural Characterization: The thickness of the monolayer films was assessed through capacitance studies. AC impedance measurements were used to characterize the capacitance of the monolayer films, and the area of the electrode was determined in the manner described in the experimental section. For the pyridine system (dodecylpyridine and undecane) an average capacitance of 1.34 $\mu F/cm^2$ was found and for the imidazole system (undecylpyridine and octane) an average capacitance of 1.96 $\mu F/cm^2$ was found. Using a parallel plate model for the monolayer film one obtains a thickness of 15 Å for the pyridine-terminated system and 10.5 Å for the imidazole terminated system [10]. These distances are in reasonable agreement with expectation. Because the pyridine-terminated film consists mostly of undecanethiol and a small fraction of pyridine terminated material, the capacitance measurement should yield a film

thickness that is similar to that expected for undecanethiol, perhaps slightly thicker. If one assumes that the alkanethiol chains are tilted at 30 degrees from the surface normal [11], one obtains a thickness of 12.3 Å for an undecanethiol film. A corresponding analysis for the imidazole terminated films, mostly composed of octanethiol, yields a film thickness of 9.0 Å.

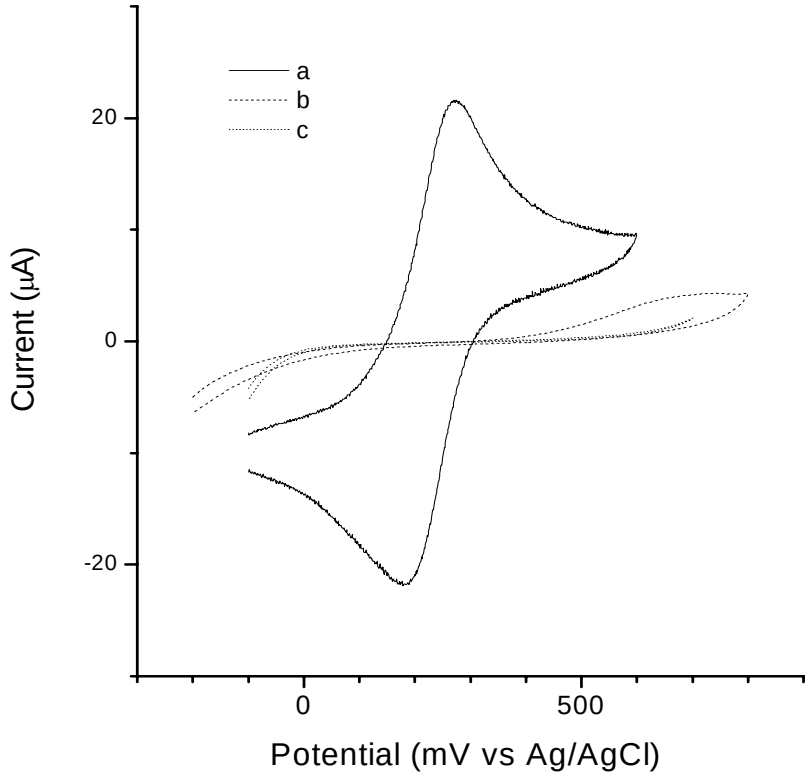

Figure 2- 2 Voltammograms are shown for three different electrodes in contact with an equimolar $Fe(CN)_6^{3-/4-}$ solution (solid line is bare electrode; dashed line is imidazole mixed film electrode; dotted line is pyridine mixed film electrode).

Figure 2- 2 illustrates the good blocking behavior observed for the mixed monolayer films. The three voltammograms in this figure were taken with the same redox solution (1 mM $[Fe(CN)_6]^{3-}/[Fe(CN)_6]^{4-}$ in 0.5 M KCl) and the same parameters (cell geometry and 100 mV/s scan rate). The bare Au electrode shows a well defined faradaic response (solid curve, a). In contrast, the voltammograms for the octanethiol and imidazole alkanethiol films (dashed curve, b)

and the undecanethiol and pyridine-alkanethiol films (dotted curve, c) show the blocking behavior that is commonly found for insulating alkanethiol coated electrodes [12]. The blocking behavior indicates that the films are compact and inhibit penetration of the ferricyanide and ferrocyanide redox species. Because of the much larger size of a cytochrome c, compared to ferricyanide and ferrocyanide, one expects no significant influence of defect sites on the observed faradaic current.

Scanning tunneling microscopy studies were used to characterize the films. Figure 2-3A shows STM images of a pyridine terminated alkanethiol film to which cytochrome c had been immobilized. The bright spots show positions on the surface where the protein is adsorbed. The feature that is analyzed here occupies an area of about 15 nm^2 and a height of 0.7 to 0.9 nm. Although a bit larger than the cross-sectional area expected for individual cyctochrome c molecules (7 to 8 nm^2), this size is consistent with that expected for a protein [13]. A range of feature sizes, somewhat smaller than that shown and significantly larger ones, can be identified on the surface, however. An analysis of the image in Figure 2-3A indicates a surface coverage of about 2.5%. It should be emphasized that the distribution of protein on the surface is not uniform; both regions with higher density of protein and with lower density of protein were readily identifiable.

Figure 2- 3B shows images of a monolayer film with no adsorbed protein (the scale is expanded over that shown in Figure 2-3A). Different regions are also evident in this image. Areas of depression (dark regions) are typically of dimension 20 to 30 Å across. Such structures represent depressions in the film that are associated with defects in the underlying Au surface and have been commonly observed for alkanethiol films on gold electrodes [14]. Although these features are interpreted as defects in the underlying gold, they are still coated with alkanethiol.

In addition to this structure, elevated regions are also visible. These elevated regions, which are not present in pure alkanethiol monolayer films, correspond to 3% to 4% of the total area and are assigned to the pyridine-terminated thiols. The vertical/height length scale shown here for the images is compressed over the actual physical height. The reason for this artificial compression when observing alkanethiols is discussed elsewhere[15]. It is evident from the image that the pyridine is not uniformly distributed throughout the film. The degree of 'phase segregation' and its dependence on preparation and solvent conditions has not yet been investigated.

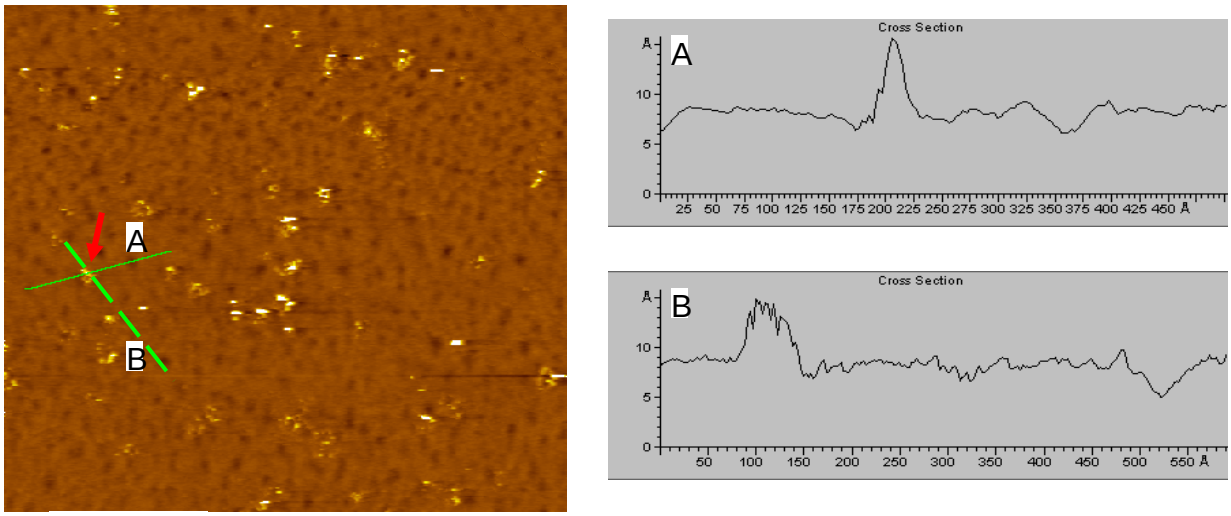

Panel A

Panel B

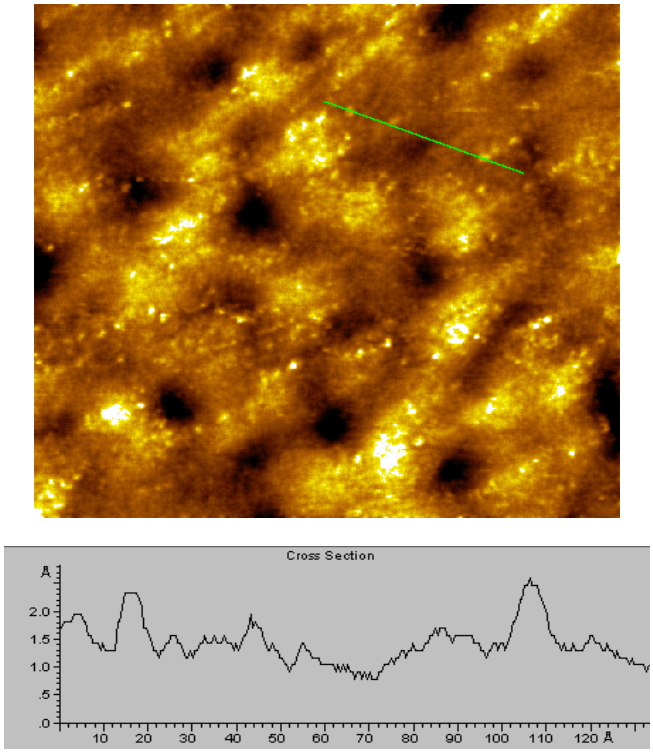

Figure 2- 3 Panel A shows a topographic image for an electrode that has cytochrome c immobilized on the surface. A cross-section through one of the features is shown for two different directions. The image size is 188 nm x 188 nm, the bias voltage is 0.5 V, and the current set point is 25 pA. Panel B shows an image for a pyridine-coated electrode with no cytochrome c adsorbed on the surface. The image size is 36.5 nm x 36.5 nm, the bias is 0.8 V, and the current set point is 0.1 nA.

Electrochemical Characterization: Cyclic voltammetry was performed on mixed monolayer films consisting of approximately 95% alkanethiol and 5% of an alkanethiol chain that was functionalized with either pyridine, imidazole or nitrile [16]. These SAM coated electrodes were incubated in a solution of cytochrome c for 30 to 60 minutes before being placed in a phosphate buffer solution at pH=7.0. When the functionalized alkanethiol chain was longer than the alkanethiol diluent, cytochrome c was immobilized on the electrode surface. When the alkanethiol diluent was longer than the functionalized chain, the cytochrome c did not adsorb to the film. This conclusion was deduced from the inability to observe a faradaic current in the mixed films when the diluent alkanethiol had a chain length comparable to that of the ω-terminated thiol.

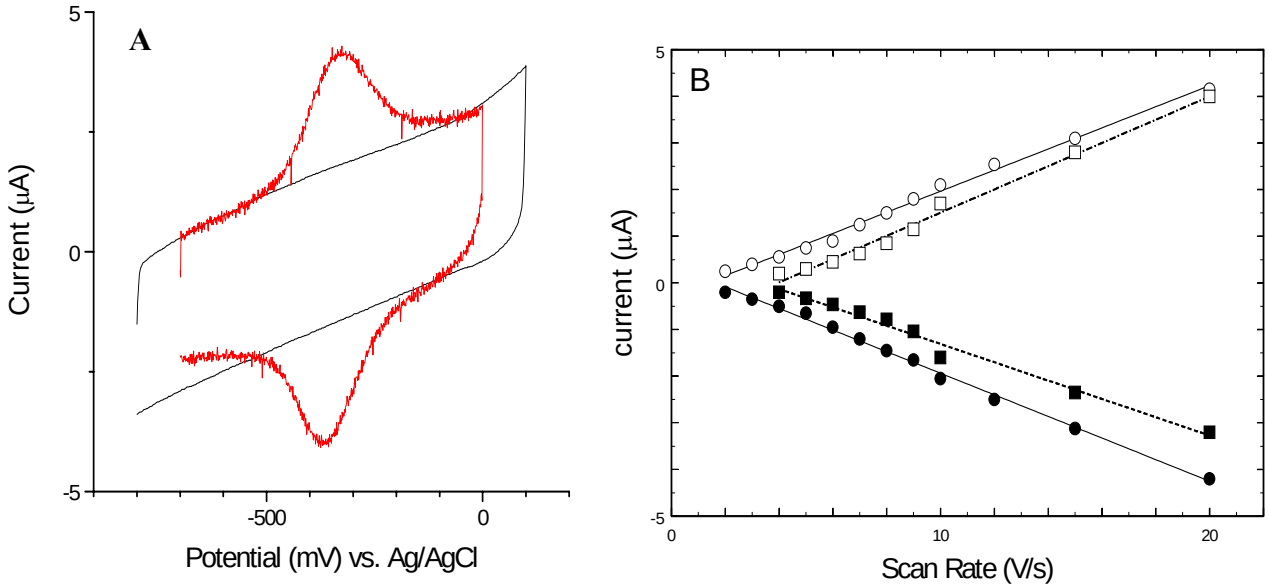

Figure 2- 4 Panel A shows voltammograms for the imidazole films in which the surface has been exposed to cytochrome c ((red curve) and not been exposed to cytochrome c (black curve). Panel B shows the linear dependence of the peak current on the voltage scan rate (imidazole is circles and pyridine is squares). The filled symbols are for the reduction wave, and the empty symbols are for the oxidation wave.

The electrochemical response was used to demonstrate that the cytochrome was immobilized on the surface of the monolayer film. Figure 2- 4A shows voltammograms obtained for the imidazole systems both with and without incubating the electrode in the cytochrome solution. In every case, when a monolayer coated electrode was placed directly in the electrochemical cell containing only the buffer solution (not exposed to cytochrome c), the voltammogram displayed no faradaic response. Subsequently, this same electrode was treated with cytochrome c, rinsed, and placed in the buffer solution (see Experimental Section for details). In each case a well-defined faradaic response was observed for the electrodes that were incubated in the cytochrome c solution. The same behavior was observed for the mixed films that were functionalized with pyridine, and voltammograms of this sort were shown for pyridine-terminated films earlier .

In addition to the incubation studies, the peak current i_p was measured as a function of the voltage scan rate for electrodes coated with cytochrome and was found to exhibit a linear dependence, which is consistent with immobilization of the cytochrome on the surface. These data are presented for both pyridine and imidazole in panel B of Figure 2- 4. For a redox couple that is immobilized on the electrode surface, the peak current is given by

$$i_p = \frac{n^2 F^2}{4RT} v N \qquad 2\text{-}1$$

where n is the number of electrons transferred, F is Faraday's constant, v is the voltage scan rate and N is the number of redox active sites on the surface. For the imidazole system the slope of this linear dependence, with n=1, gives a surface coverage of $2.0 \pm 0.1 \times 10^{12}$ cm^{-2} (or 3.3 picomol/cm^2), and for the pyridine system it gives $1.5 \pm 0.1 \times 10^{12}$ cm^{-2} (or 2.5 picomol/cm^2). The method for determining the electrode areas is described in the experimental section. The surface coverage of cytochrome was also determined by integrating the oxidation peak of the

voltammograms. This procedure generated coverages that ranged from 2 to 6 picomol/cm^2. Using the coverage of 1.5 x 10^{12} cm^{-2} on pyridine terminated films, one calculates an average area per cytochrome c molecule of 67 nm^2, which is about ten times the cross-sectional area of a cytochrome c molecule. Although these data do not quantify the homogeneity of the protein's distribution on the surface, they indicate that the average distance between protein molecules is high. This average coverage of 10% is significantly larger than that obtained from the image in Figure 2- 3A. In part this difference can be accounted for by the limited sampling in the STM image and by differences in the preparation and incubation of the monolayer films (see Experimental section).

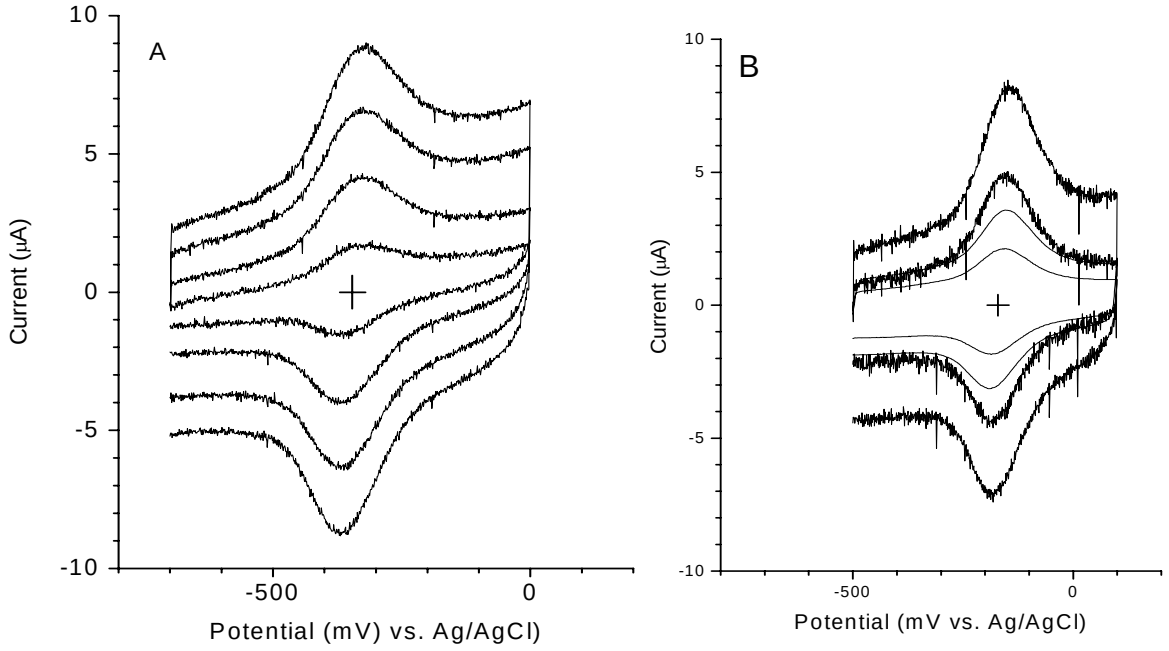

Figure 2- 5 Voltammograms are shown for cytochrome c immobilized on the surface of mixed monolayer films containing imidazole functionalities (panel A) and pyridine functionalities (panel B). The scan rates for these voltammograms are 20 V/s, 15 V/s, 10 V/s and 6 V/s.

The voltammograms of the imidazole and pyridine mixed films at some selected voltage scan rates are presented in Figure 2- 5. These data display well-defined peaks and show a small shift of the peak separation with the scan rate. This dependence can be used to analyze the electron transfer rate constant, see below. It is evident that the noise level for the pyridine-terminated films (panel B) is higher than for the imidazole-terminated films (panel A). In order to obtain better defined peaks for the pyridine films at the slower scan rates a filter (the time constant of the filter is 590 Hz) was used in the data collection. The use of a filter accounts for the difference in noise level between the slower scan rate curves and the higher scan rate curves, for which no filter was employed, in panel B. Table 2-1 reports the full width at half maximum (ΔE) of the reduction peak for the adsorbed cytochrome and is close to the ideal value for a fully reversible system of 91 mV. The peak widths for the mixed films are similar to that for dilute films of cytochrome c on carboxylic acid terminated alkanethiols and indicate a high degree of homogeneity for the mixed systems. By contrast, an earlier study, which immobilized cytochrome c on pure layers of pyridine terminated alkanethiols, displayed significant broadening of the voltammograms and a large asymmetry between the oxidation and reduction response . For the electrodes where the cytochrome is freely diffusing, the difference between the voltammogram's peak potential and the potential at half height is reported in Table 2-1. In this latter case the ideal value should be 56 mV. The voltammograms for the nitrile films were significantly noisier than those shown here and for this reason the rest of the study focuses on the pyridine and imidazole mixed films.

Table 2-1 Electrochemical parameters for different electrode/cytochrome systems.

System	$E^{0'}$ (mV)	ΔE (mV)	Scan Rate (V/s)
$HOC(CH_2)_6S$ [a]	44 ± 2	58	0.2
$PyCO_2(CH_2)_2S$ [a]	5	56	0.2
$HOOC(CH_2)_{10}S$	12 ± 3	99	0.6
$PyCO_2(CH_2)_{12}S/C_{11}H_{21}S$	-172 ± 10	108	1.0
$Im(CH_2)_{11}S/C_8H_{15}S$	-346 ± 20	117	1.0
$NC(CH_2)_{11}S/C_8H_{15}S$	-415 ± 20	132	8.0

a. In this system the cytochrome c is not immobilized on the electrode surface but is in solution at a concentration of 50 μM.

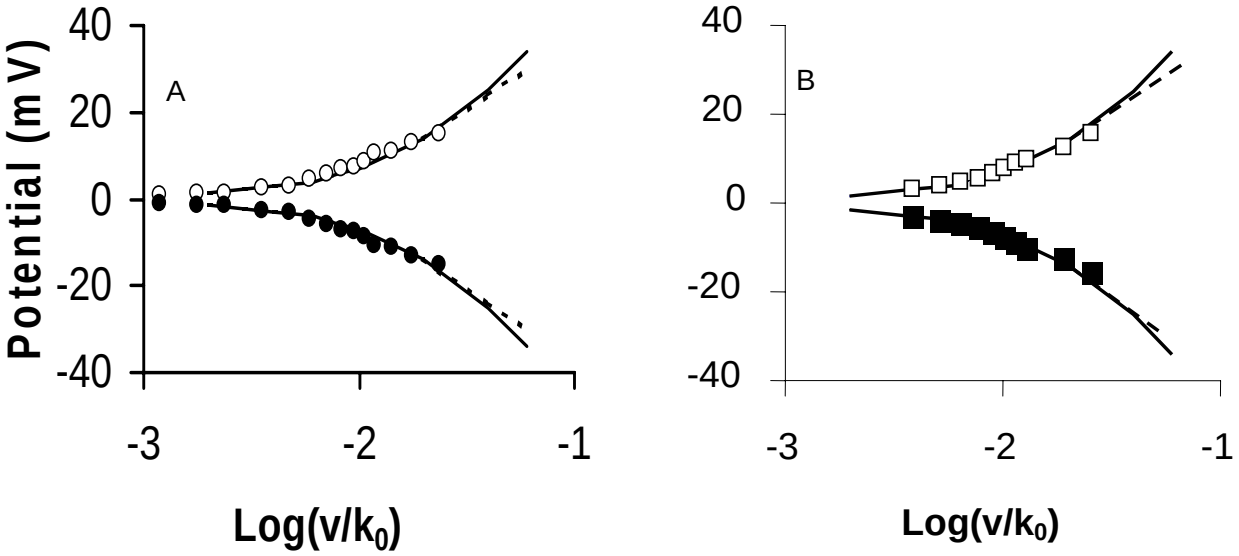

Figure 2- 6 The dependence of the peak potential on the scan rate is shown for the imidazole system (Panel A) and the pyridine system (Panel B). The symbols follow the convention of Figure 2- 4. Fits of the data to Marcus theory predictions are also shown for two different reorganization energies (0.8 eV is the solid line and 0.9 eV is the dashed line)

Table 2-1 also provides data on the apparent formal potentials for a number of different systems. For $S(CH_2)_2$-Py monolayers and hydroxy terminated monolayers to which the

cytochrome does not adsorb, the reported formal potentials are 5 mV and 44 mV versus Ag/AgCl, respectively. For carboxylic acid terminated monolayers to which the cytochrome is immobilized by electrostatic binding to the protein exterior, the apparent formal potential is 12 mV versus Ag/AgCl, intermediate between those found for the nonadsorbed protein. In contrast, for the mixed monolayer films, which are composed of pyridine, imidazole and nitrile functionalities that can interact with the cytochrome's heme, a significant negative shift of the redox potential is observed, ranging from –172 mV for the pyridine system to –415 mV for the nitrile system. This shift in the redox potential is consistent with those found in homogeneous solution studies of cytochrome c when the ligands pyridine, imidazole, and nitrile are present[17]. Spectroscopic studies have shown that the pyridine, imidazole and nitrile functionalities can bind to the redox center of the cytochrome in free solution[18]. Consequently the negative shift in redox potential indicates an interaction between the terminal functionality of the layer and the cytochrome's heme.

The dependence of the reduction (or oxidation) peak's position on the voltage scan rate can be used to characterize the electron transfer rate constant[19]. This method was used to determine rate constants for the cytochrome c immobilized on the pyridine and imidazole terminated films. Figure 2- 6 shows a plot of the peak separation versus the voltage scan rate for each system, along with the best fit to the classical Marcus theory for the electron transfer rate constant. The theoretical curves are shown for two different reorganization energies, 0.8 and 0.9 eV . This procedure provides standard rate constants (k^0) of 780 s^{-1} for the pyridine-terminated layer (electron transfer through a C12 chain) and 850 s^{-1} for the imidazole terminated layer (electron transfer through a C11 chain). These rate constants are quite high (peak voltage shifts are small) and one must be concerned about possible contributions from iR drop to the observed

peak shifts [7,20]. To this end, the impedance of the electrochemical cell was measured to have a resistance of 300 to 500 Ω, which leads to a shift of less than 2mV at the highest currents. Attempts to analyze for the iR drop by changing the electrolyte concentration were not successful because concentrations above 50 mM buffer caused desorption of the cytochrome c from the electrode film.

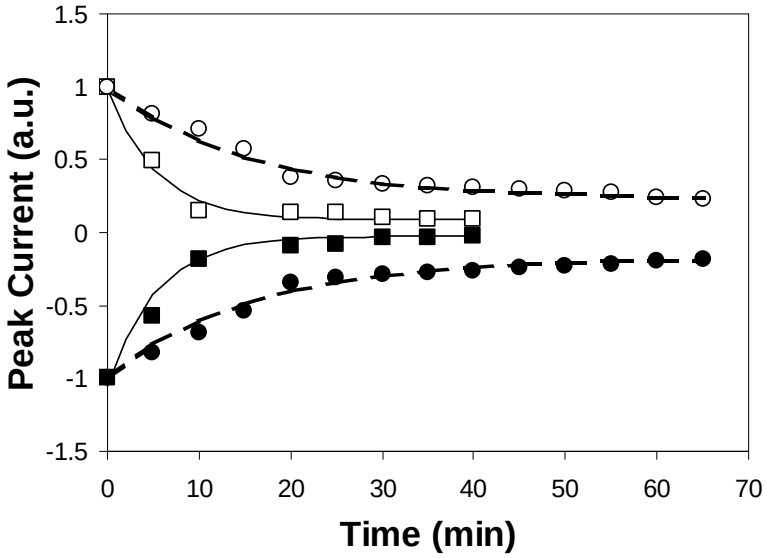

Figure 2- 7 Time profiles for the surface concentration of immobilized cytochrome c are shown for both the pyridine terminated films and the imidazole terminated films. The symbol convention is the same as Figure 2- 6.

Association Strength: The strength of association and stability of the adsorbed cytochrome c films was assessed by monitoring the desorption kinetics. In this procedure the coated film was placed in the solution, and within a few seconds (<10 s) a voltammogram was initiated with a scan rate of 20 V/s. Voltammograms were run at subsequent time points until the peak current was found to stabilize. Because the peak current is proportional to the amount of cytochrome adsorbed on the surface, this procedure generates a profile of the adsorbed species concentration as a function of time. Figure 2- 7 shows these concentration profiles for both the

imidazole and the pyridine-terminated films. The desorption kinetics can be modeled by considering that the system evolves toward an equilibrium of the following type:

$$S\text{-}H_2O \; + \; \text{Cyt.C} \; \underset{k}{\overset{k'}{\rightleftarrows}} \; H_2O \; + \; S-Cyt.C \qquad 2\text{-}2$$

where S-H_2O represents a solvated surface binding site, Cyt. C represents a cytochrome c molecule in solution, and S-Cyt. C represents a surface bound cytochrome c. The rate constant k' characterizes the binding to surface sites and the rate constant k characterizes the dissociation of the cytochrome from the binding site. Under the initial condition that all the cytochrome c is bound to the surface, one finds that the concentration of the surface adsorbed cytochrome θ(t) evolves according to

$$\frac{\theta(t)}{\theta(0)} = f + (1-f)\exp\left(-(k+\kappa')t\right) \qquad 2\text{-}3$$

where κ' is given by k'·[Cyt. C], θ(t) is the coverage at time t, and f is the ratio κ'/(θ(0)(κ'+k)). For the pyridine-terminated layer the decay constant is $2.5\text{x}10^{-3}$ s^{-1} and f is 0.14 ± 0.03, whereas the imidazole-terminated layer has a decay constant of $1.0\text{x}10^{-3}$ s^{-1} and f of 0.35 ± 0.04. The faster decay rate and the lower final value for the pyridine film indicates that its adsorption constant is smaller than that of the imidazole film; that is, the imidazole has a stronger association with the cytochrome than does the pyridine. If one assumes that θ(0)=1, the fitting parameters give rate constants of k = $2.2\text{x}10^{-3}$ s^{-1} and κ' = $3.5\text{x}10^{-4}$ s^{-1} for pyridine, and k = $6.5\text{x}10^{-4}$ s^{-1} and κ' = $3.5\text{x}10^{-4}$ s^{-1} for imidazole. The effective association rate constant κ' appears to be the same for both systems, suggesting that the association is diffusion limited. In contrast, the dissociation rate constants are different from one another, with the imidazole system being almost three times smaller than that of the pyridine system.

2-4 DISCUSSION AND CONCLUSION

The immobilization of the cytochrome c on functionalized monolayer films is demonstrated through a combination of electrochemical and structural probes. By combining ω-terminated pyridine or imidazole alkanethiols with an alkanethiol diluent it is possible to immobilize cytochrome c onto electrode surfaces through the interaction of the pyridine, or imidazole, with the heme of the cytochrome. The immobilization is demonstrated by the electrochemical observation that the peak current of the voltammogram grows linearly with the voltage scan rate and that the faradaic response is observed for the cytochrome c treated electrodes when they are immersed in the buffer solution. Complimentary studies used scanning tunneling microscopy to observe the presence of nanometer scale objects on the surface of the monolayer film after they were treated in a solution containing cytochrome c. The lateral scale of the objects is similar to that expected for protein adsorption.

Previous work reported the immobilization of cytochrome c on the surface of pure monolayers of pyridinalalkanethiol. That work demonstrated the immobilization in a similar manner, however the electrochemistry was not representative of a homogeneous distribution of redox sites. The pure monolayer films contained relatively broad peak widths (160 mV to 190 mV) and displayed asymmetric redox kinetics. In particular, the oxidation was found to be much faster than the rate constant for reduction. This observation was believed to reflect a change in the redox active sites after oxidation - associated with the degree, or strength, of interaction between the cytochrome and the pyridine. In contrast, the mixed monolayer systems show much narrower widths for the redox peaks (see Table 2-1) and yield similar rate constants for the reduction and oxidation waves. This indicates a much more uniform distribution of sites on the surface and not profound changes in binding geometry upon electron transfer.

The immobilization strategy utilized here is different than that used to immobilize the cytochrome c on the surfaces of –COOH terminated alkanethiol monolayers. In that case one observes similar widths for the voltammetric peaks, but the redox potential observed on the COOH layers are much more positive than those found for the mixed monolayer films (seeTable 2-1). The large difference in observed redox potential indicates that the nature of the immobilization is different in the two cases. The pyridine and imidazole terminated films have redox potentials that are shifted negative of that found for cytochrome c in free solution and is similar to the shift observed when cytochrome c/pyridine complexes are studied in free solution. In contrast, the COOH terminated layer has a redox potential that is similar to that observed for cytochrome c in solution. These findings are consistent with the immobilization of cytochrome c on COOH terminated films by adsorption on the protein's periphery whereas the pyridine and imidazole terminated layers interact with the heme of the cytochrome.

The desorption of cytochrome c from the layer was monitored voltammetrically for both the pyridine-terminated layers and the imidazole-terminated layers. It was found that the dissociation of the cytochrome from the imidazole films is about three times slower than that from the pyridine terminated films. This finding is consistent with a stronger interaction between the heme and the imidazole than with the heme and pyridine .

Finally, the electron transfer rate constants were measured for the cytochrome c on the surface. For the imidazole system the rate constant was found to be 850 s^{-1} through a C11 methylene chain and 780 s^{-1} through a C12 methylene chain. These rate constants are comparable to rate constants observed for electron transfer through C6 methylene chains of carboxylic acid terminated layers. Detailed studies of the carboxylic acid terminated films have identified an electron transfer rate constant that is independent of distance for methylene chain

lengths of C6 and shorter. The difference in length associated with C6 and C11 can be converted to a distance. If one takes the C-C bond length to be 1.5 Å and the alkane chains to be tilted at 30 degrees from the surface normal, one finds a distance of 5.5 Å. This value is in reasonable agreement with the distance from the end of the COOH terminated layer through the cytochrome c outer surface to the redox active heme, a tunneling distance of 5 to 6 Å, which is consistent with the COOH binding electrostatically to the cytochrome's outer surface. For the COOH terminated monolayers, it has been reported that the cytochrome displays a tunneling dependence for methylene chain lengths of C9 and longer [2,3]. For the current system, one might expect that the range of distances, for which the electron transfer rate constant is distance independent, would be extended if the recognition element (pyridine, imidazole) binds to the heme of the protein rather than its outer surface. For longer methylene chains, one expects to observe a distance dependence for the electron transfer rates. Preliminary studies show that this is so, and this effect is being investigated further[21].

The ability to adsorb the redox active cytochrome c to the surface of SAM coated gold electrodes in a restricted geometry has been demonstrated. These systems provide a model system to investigate aspects of electron transfer dynamics between biomolecules and metal electrodes.

BIBLIOGRAPHY

[1] a) Lewis, N.S.; Wrighton, M. S. *Science* **1981**, *211*, 944; b) Armstrong, F. A.; Hill, H. A. O.; Walton, N. J. *Acc. Chem. Res.* **1988**, *21*, 407

[2] a) Feng, Z. Q.; Imabayashi, S.; Kakiuchi, T.; Niki, K. *J. Chem. Soc. Faraday Trans.* **1997**, *93*,1 367; b) Avilla, A.; Gregory, B. W.; Niki, K.; Cotton, T. M. *J. Phys. Chem. B* **2000***, 104*, 2759.

[3] a) Tarlov, M. J.; Bowden, E. F. *J. Am. Chem. Soc.* **1991**, *113*, 1847; b) Collinson, M.; Bosden, E. F.; Tarlov, M. J. *Langmuir*, **1992**, *8*, 1247; c) Song, S.; Clark, R. A.; Bowden, E. F.; Tarlov, M. J. *J. Phys. Chem***. 1993**, *97*, 6564.

[4] Terrettaz, S.; Cheng, J.; Miller, C. J.; Guiles, R. D. *J. Am. Chem. Soc*. **1996***, 118*, 7857.

[5] Yamamoto, H.; Liu, Haiying; Waldeck, D. H. *Chem. Comm.* **2001**, 1032.

[6] Brutigan, D.L.; Ferguson, S.; Margoliash, E. *Methods in Enzymology*; Fleischer, S. and Packer, L Ed.; Academic Press, New York, 1978,Vol. LIII, pp. 131-132.

[7] Sawyer, D. T.; Sobkowiak, A.; Roberts, Jr. J. L. *Experimental Electrochemistry for Chemists;* (Wiley New York, **1995**), 74-75. The diffusion constant of $Fe(CN)_6^{3-/4-}$ is assumed to be 7.63×10^{-6} cm^2/sec.

[8] Clavilier, J. *J. .Electroanal.Chem*., **1980**. *107*, 205.

[9] Napper, A. M.; Liu, H.; Waldeck, D.H.; *J. Phys. Chem. B* **2001,** *105,* 7699.

[10] This calculation assumes a parallel plate model for the capacitance of the film (C= ε (area)/(thickness)) and takes the alkanethiol dielectric constant ε to be 2.6.

[11] a) Ulman, A. *Chem Rev.* **1996**, *96*, 1533; b) Schreiber, F. *Prog. Surf. Sci*. **2000**, *65*, 151

[12] a) Miller, C.J. *Physical Electrochemistry: Principles, Methods, and Applications* Rubinstein, I, ed. (Marcel Dekker, Inc., New York, **1995**) 27; b) Finklea, H.O.; *Electroanalytical Chemistry*; Bard, A. J., Rubinstein, I. eds. *19* (Marcel Dekker, New York, **1996**) 109; c) Khoshtariya, D.E.; Dolidze, T.D.; Zusman, L.D.; Waldeck, D.H. *J. Phys. Chem.* **2001,** *105* 1818.

[13] *Cytochrome C: A Multidisciplinary Approach*, Scott, R.A.; Mauk, A. G. eds. (University Science Books, Sausalito, **1996**).

[14] Poirier, G. E. *Chem. Rev.* **1997**, *97*, 1117

[15] a) Weiss, P. S.; Bumm, L.A.; Dunbar, T.D.; Burgin, T.P.; Tour, J.M.; Allara, D.L. *Ann. N. Y. Acad. Sci.* **1998**, *852*, 145; b) Gorman, C.B.; Carrol, R.L.; He, Y.; Tian, F.; Fuierer, R. *Langmuir* **2000**,*16*, 6312.

[16] Although the deposition solution contained a 9:1 ratio of thiol species, the STM studies indicate that the composition of the film deviates from this ratio significantly.

[17] See Table 1 of Fedurco, M. *Coord. Chem. Rev*. **2000**, *209*, 263, and references therein.

[18] a) Spiro, T. G.; Li, X.Y. *Resonance Raman Spectra of Heme and Metalloproteins in Biological Applications of Raman spectroscopy*; (Wiley, NY, **1988)** *3*, 1; b) Hirota, S. Ogura, T.; Shingawa, I. K.;Yoshikawa, S.; Kitagawa, T. *J. Phys. Chem.* **1996**, *100*, 15274; c) Yeh, S. R.; Rousseau, D. L. *J. Biol. Chem.* **1999**, *274*, 17853; d) Smith, M.; Mclendon, G. *J. Am. Chem. Soc.* **1981**, *103*, 4912; e) Ferrer, J. C.; Gullemette, J. G.; Bogumil, R.; Inglis, S. C.; Smith, M.; Mauk, A. G. *J. Am. Chem. Soc.* **1993**, *115*, 7507; f) Liu, G.; Chen, Y. Tang. W. *J. Chem. Soc., Dalton Trans.,* **1997**, 795.

[19] a) Napper, A. M.; Liu, H.; Waldeck, D.H. *J. Phys. Chem. B* **2001**, *105*, 7699; b) Tender, L.; Carter, M.T.; Murray, R. W. *Anal. Chem.* **1994**, *66*, 3173; b) Weber, K.; Creager, S. E. *Anal. Chem.* **1994**, *66*, 3166; c) Honeychurch, M. J. *Langmuir* **1999**, *15*, 5158.

[20] Bard, A. J.; Faulkner, L.R. *Electrochemical Methods* (Wiley, New York, **1980**).

[21] Wei, J.; Liu, H.-Y., Khoshtariya, D.E.; Yamamoto, H.; Dick, A.; Waldeck, D. H. *Angewandte Chem.,* **2002**, *41*, 4700.

CHAPTER 3 SERR AND ELECTROCHEMICAL STUDY OF CYTOCHROME C BOUND ON ELECTRODES THROUGH COORDINATION WITH PYRIDINYL-TERMINATED SAMS**

Cytochrome c (Cyt-c) is immobilised on Ag and Au electrodes coated with self-assembled monolayers (SAM), comprised of pyridine-terminated alkanethiols and a shorter chain diluent thiol. Surface enhanced resonance Raman (SERR) spectroscopy of coated Ag electrodes reveals that the adsorbed Cyt-c forms a potential-dependent coordination equilibrium with a predominant five-coordinated high spin (5cHS) state in the reduced form and six-coordinated low spin (6cLS) state prevailing in the oxidised form. In the oxidized species, the native Met-80 ligand of the heme is replaced by a pyridinyl residue of the bifunctional thiols that according to earlier scanning tunnelling microscopy form islands in the hydrophobic monolayer. The redox potentials derived from the SERR band intensities are estimated to be -0.24 and -0.18 V (vs. AgCl) for the 6cLS and 5cHS states, respectively, and lie in the range of the midpoint potential determined for Cyt-c on coated Au electrodes by cyclic voltammetry. Whereas in the latter case, a nearly ideal Nernstian behaviour for a one-electron couple was observed, the SERR spectroscopic analysis yields ca. 0.4 for the number of transferred electrons for each spin state. This discrepancy is mainly attributed to a distribution of substates of the immobilised protein in both the 6cLS and 5cHS forms, as indicated by substantial band broadening in the SERR spectra. These substates may arise from different orientations and heme pocket structures and exhibit

** Murgida, DH.*, Hildebrandt, P., Wei, JJ.; He, YF.; Liu,. HY.; Waldeck, DH.*, "SERR and Electrochemical Study of Cytochrome c Bound on Electrodes through Coordination with Pyridinyl-terminated SAMs"; *J. Phys. Chem. B*, **2004**, 108, 2261

different redox properties. Whereas SERR spectroscopy probes all adsorbed Cyt-c species including those that are largely redox-inactive, CV measurements reflect only the substates for which the heterogeneous electron transfer is faster than the scan rate.

3-1 INTRODUCTION

In the past few years, redox proteins adsorbed on electrodes have gained increasing attention both in physico-chemical and biophysical studies. [1,2] In a practical sense, immobilised proteins represent key elements for bioelectronic devices with potential applications in biotechnology and nanotechnology. To fully exploit the functional properties of proteins and enzymes and to allow for rational design of tailor-made devices, detailed knowledge of the mechanism and dynamics of the interfacial processes, specifically heterogeneous electron transfer (ET) reactions, is required. In a fundamental sense, deeper insight into the underlying redox chemistry may contribute to a better understanding of the molecular processes of membrane-bound and membrane-associated proteins under physiological conditions.

In this respect, cytochrome *c* (Cyt-*c*) represents an ideal model protein inasmuch as its three-dimensional structure is well characterized,[3] and a large body of experimental data has been accumulated on its homogeneous and heterogeneous electron transfer reactions.[4,5,6,7,8,9,10,11] This heme protein offers the particular advantage that it can be immobilised on electrodes in a well-defined manner using quite different strategies. Because of its high molecular dipole moment and the clustering of cationic lysine residues on the front surface of the protein, Cyt-*c* binds electrostatically to anionic electrode surfaces in a largely uniform orientation. Such surfaces can be provided either by chemisorption of anions on electrode surfaces[11,12] or, more elegantly, by depositing self-assembled monolayers (SAM) of bifunctional thiols that carry

negatively charged headgroups (carboxylate[7,8] or phosphate [13]). Alternatively, covalent attachment can be achieved by chemical cross-linking to the lysine residues on the front surface of the protein, however the resultant orientational distribution of the bound proteins appears to be more heterogeneous than in the case of electrostatic binding.[8b] Also the immobilization via hydrophobic interactions has been shown on electrodes covered with SAMs of alkanethiols. In this case, the protein is bound via a (partial) insertion of the hydrophobic amino acid segment 80 – 85 into the monolayer. Finally, it is also possible to attach the protein via direct coordination to the heme, by using SAMs of thiols that carry a headgroup such as pyridinyl that can effectively compete with the native Met-80 ligand for the axial coordination site of the heme.

In these systems, the immobilised Cyt-*c* displays quite different redox properties with substantial variations in the redox potentials and the electron transfer kinetics. For a comprehensive understanding of these processes, however, it is necessary to analyse how the variations in the thermodynamic and kinetic properties are related to the molecular structure of the immobilised protein. Surface enhanced resonance Raman (SERR) spectroscopy can provide such information since this technique selectively probes the redox sites, i.e., the heme group of the immobilised proteins, and allows monitoring of potential-dependent changes in the molecular structure.[14] By combining this technique with the potential-jump method, it is possible to study the electron transfer dynamics of the immobilised species and gain valuable insight into the molecular mechanism of the interfacial redox process. Previous studies applied this approach to electrostatically, hydrophobically, and covalently bound Cyt-*c*,[8b] the present work is dedicated to the analysis of the redox process of Cyt-*c* directly linked to an electrode via axial coordination of a pyridinyl residue. In addition to electrochemical techniques and scanning tunnelling microscopy (STM), which have been used in previous studies, we have employed SERR

spectroscopy for a comprehensive analysis of the thermodynamic and structural aspects of the redox behavior of the bound Cyt-*c*.

3-2 MATERIALS AND METHODS

Chemicals. Bis[11-((4-pyridinylcarbonyl)oxy)undecyl]disulfide (C11py) and Bis[12-((pyridinylcarbonyl)oxy)dodecyl]disulfide (C12py) were prepared in the manner described previously.[9c,d] Horse heart cytochrome c (Sigma, type VI) was chromatographically purified according to previously published procedures.[9c,d,15] The 11-mercapto-1-undecanol (97%), 1-octanethiol (98.5+%), 1-hexadecanethiol, and 1-undecanethiol (98+%) were purchased from Aldrich and used without further purification. Absolute ethanol was purchased from Pharmco Products, Inc.; water for experiments was purified by using a Barnstead-Nanopure system and had a resistivity of 18 MΩ-cm.

SERR Electrode Preparation: Silver electrodes were electrochemically roughened as described before[16] and then immersed in ethanolic solutions of 1:9 mixtures of a pyridinyl terminated alkanethiol and a diluent alkanethiol (1 mM total) for a period of 1-3 days to create mixed self-assembled monolayers (SAM). For 1:9 mixtures of 4-pyridinyl-CO_2-$(CH_2)_{11}$-SH / 1-octanethiol or 4-pyridinyl-CO_2-$(CH_2)_{11}$-SH / 1-decanethiol the SAMs are denoted as Py-H, while SAMs obtained with 1:9 mixtures of 4-pyridinyl-CO_2-$(CH_2)_{12}$-SH / 11-mercapto-1-undecanol are denoted as Py-OH. After rinsing with ethanol and drying under an Ar stream, electrodes were immersed in the electrochemical cell containing ca. 0.5 μM Cyt-*c* in a 20 mM phosphate buffer at pH 7.0. The protein was allowed to adsorb for 60 min. at open circuit and under purging with Ar.

Gold electrode preparation: For cyclic voltammetry (CV) studies, the gold (99.99% Aldrich) electrodes were prepared in the same procedure as before[9c] with a tip of exposed area 0.06-0.12 cm^2. For the STM studies, an Au(111) facet of a single crystalline bead (prepared by Clavilier's method[17]) was used as the substrate and cleaned thoroughly before SAM preparation. The SAM preparation on gold electrodes, for both the cyclic voltammetry and the STM measurements, proceeded in the same way as that on the silver electrodes. The electrodes were rinsed with ethanol and dried under an Ar gas stream.

Cyclic voltammetry Cyclic voltammetry on the immobilized Cyt-*c* was carried out with an EG&G PAR-283 potentiostat, which was controlled by a Pentium computer running ver. 4.3 of PARC Model 270 software and a GPIB board. The three electrode cell had a platinum spiral counter electrode, an Ag/AgCl (3 M NaCl) reference electrode, and the surface modified working electrode. The voltammetry measurements were performed in 20 mM phosphate buffer solution (pH of 7.0) under an argon atmosphere. After measurement, the SAM on the gold bead was removed by immersing it in a "piranha" solution (a mixture of 30% H_2O_2 and 98% H_2SO_4 in a 1:3 volume ratio) for 20 sec. The bead area was determined by running voltammetry in a 0.5 M KCl solution that contained 1mM $K_3[Fe(CN)_6]$ and 1mM $K_4[Fe(CN)_6]$. [9c,18]

The capacitance of the SAM was estimated from the charging current of the voltammograms during the cyclic voltammetry measurement.

$$\frac{dQ}{dt} = C\frac{dV}{dt} \qquad \text{i. e.} \qquad i = Cv \qquad 3\text{-}1$$

where Q is the charge, C is the capacitance, V is the potential of a parallel plate capacitor, i is the charging current, and v is the voltage scan rate. The voltammograms give average capacitances of 1.2 $\mu F/cm^2$ for 1-day-electrode and 1.22 $\mu F/cm^2$ for 3-day-electrode, corresponding to the film thickness 16.8 Å and 16.5 Å, respectively.[19] Of course, such a simple model does not adequately

describe electrochemical interfaces.[20] However, given this caveat it is apparent that the film thickness is very close to that expected from simple bond length calculations.

SERR measurements: SERR spectra were measured with the 413-nm excitation line of a Kr^+-laser (Coherent Innova 302) using a spectrograph (U1000, ISA) equipped with a liquid nitrogen cooled CCD camera. The spectral resolution was 4 cm^{-1} and the step width (increment per data point) was 0.53 cm^{-1}. Accumulation times of the spectra were 10-40 seconds. The laser beam (*ca.* 60 mW) was focused onto the surface of a rotating Ag electrode in a home-built thermostated electrochemical cell, which permits temperature control within ± 0.1 °C. The SAM-modified Ag electrode was in contact with a solution containing the supporting electrolyte (20 mM potassium phosphate buffer at pH = 7) and *ca.* 0.5 μM Cyt-*c*. All potentials refer to the Ag/AgCl electrode. Measurements were performed under continuous purging with argon. Stationary spectra were measured at several potentials between +0.1 V and –0.6 V.

STM Measurements: The STM images were obtained with a Nano IIIA STM system (Digital Instruments). STM tips were cut by using 0.25 mm diameter Pt-Ir wires (Goodfellow). All the STM images were obtained in air under constant current mode at 50-100 pA and a tip-sample bias of 0.8-1.0 V. Two different sample preparations of the ω-hydroxyalkanethiol mixture (C12py/C11OH) are presented. They differ by the exposure time, 1 day versus 3 days, of the electrode to the solution mixture of alkanethiols. The measurements were reproduced twice.

3-3 RESULTS

Cyt-*c* was adsorbed on Ag electrodes that were coated with SAMs of Py-H. By using SERR spectroscopy, the redox equilibria and the heme pocket structure of the adsorbed protein were probed as a function of the electrode potential. The spectra were measured in the high frequency region between *ca.* 1300 and 1700 cm^{-1} to probe the ν_3 and ν_4 vibrational modes. These modes provide sensitive markers for the coordination, spin, and redox state of the heme iron. Visual inspection of the spectra measured at two extreme potentials, 0.1 V and –0.5 V, at which the sample is expected to be nearly fully oxidised and fully reduced respectively, indicates the coexistence of two different Cyt-*c* species at each potential (Figure 3- **1**). At 0.1 V, the ν_3 region displays a peak at 1504 cm^{-1}, which is typical for a six-coordinate low-spin oxidised ($6cLS^{Ox}$) heme, and a shoulder at *ca.* 1491 cm^{-1} characteristic of a five-coordinate high-spin oxidised ($5cHS^{Ox}$) heme. In addition, the ν_4 band is centered at *ca.* 1373 cm^{-1}, which is also indicative of a $6cLS^{Ox}$ heme. A simple band fitting analysis shows that, on the low frequency side, this peak deviates from a single Lorentzian bandshape, indicating the superposition by at least one further band at slightly lower frequencies expected for a $5cHS^{Ox}$ heme. At –0.5 V the situation is reversed, such that the ν_4 band is found at *ca.* 1354 cm^{-1}, a position typical for $5cHS^{Red}$ hemes, and the deviation from the Lorentzian shape is now observed on the high frequency side, i.e. in the region expected for a $6cLS^{Red}$ form. Additionally, the ν_3 region exhibits two weaker bands at 1467 cm^{-1} and 1491 cm^{-1} that are clear indications for $5cHS^{Red}$ and $6cLS^{Red}$ Cyt-*c*, respectively. Also evident in Figure 3- 1 are bands centered around 1590 cm^{-1}, however these are not very reliable markers and are not discussed. Thus, the potential-dependence of the shape and position of the ν_3 and ν_4 bands suggest a conformational

equilibrium of the adsorbed protein that is dominated by a 6cLS and a 5cHS form in the oxidised and in the reduced state, respectively.

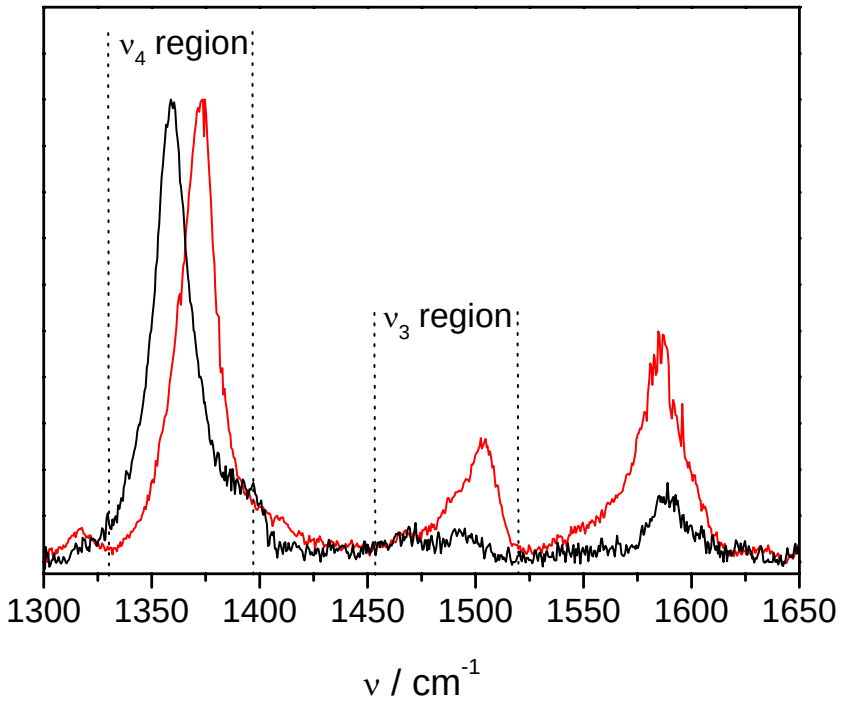

Figure 3- 1 SERR spectra of Cyt-c adsorbed to a Py-H coated Ag electrode at -0.5 V (black) and 0.1 V (red).

SERR spectra measured as a function of the electrode potential between –0.6 V and 0.1 V in 50 mV steps (data not shown) display a gradual transition between the two extreme cases represented in Figure 3- 1. A sound quantitative analysis of the coupled redox and conformational equilibria requires knowledge of the component spectra for the four species that are involved, *i.e.,* $6cLS^{Red}$, $6cLS^{Ox}$, $5cHS^{Red}$, and $5cHS^{Ox}$. Since these species cannot be prepared in a pure form, their component spectra are not known *a priori*. Rather, they must be determined iteratively, in a manner described previously.[21] The resonance Raman (RR) and SERR spectra of native and non-native 6cLS and 5cHS species of Cyt-*c*, which were analysed in

detail previously, were chosen as an initial set of spectra. The spectral parameters (positions, bandwidths, and relative intensities) for each redox and coordination state ($6cLS^{Red}$, $6cLS^{Ox}$, $5cHS^{Red}$ and $5cHS^{Ox}$) were varied iteratively to obtain a consistent fit to all the experimental data by using only the relative contributions of the individual species as adjustable parameters (Figure 3- 2, Table 3-1). Figure 3- 3 shows the relative contributions of the different species to the spectra, as a function of electrode potential. At very negative potentials the spectra are dominated by the $5cHS^{Red}$ component but at positive values the $6cLS^{Ox}$ form becomes the most intense one, confirming the idea of a redox state dependent coordination equilibrium for the adsorbed protein.

Table 3-1 Frequencies and band widths (in parentheses) of the SERR marker bands ν_3 and ν_4 of the various Cyt-*c* species.

Species	ν_3 / cm^{-1}	ν_4 / cm^{-1}
$6cLS^{Red}$ (Py-H)[a]	1493.6 (14.4)	1362.5 (16.4)
$6cLS^{Ox}$ (Py-H)[a]	1504.2 (11.7)	1373.9 (14.1)
$5cHS^{Red}$ (Py-H)[a]	1467.8 (14.4)	1357.6 (17.4)
$5cHS^{Ox}$ (Py-H)[a]	1492.0 (16.6)	1368.5 (16.9)
$6cLS^{Red}$ (B1)[b]	1490.7 (13.1)	1360.2 (9.5)
$6cLS^{Ox}$ (B1)[b]	1501.1 (11.9)	1371.0 (15.2)
$6cLS^{Red}$ (B2)[c]	1492.5 (13.5)	1359.0 (12.0)
$6cLS^{Ox}$ (B2)[c]	1503.0 (12.3)	1373.0 (15.9)
$5cHS^{Red}$ (B2)[c]	1471.0 (15.0)	1353.0 (12.5)
$5cHS^{Ox}$ (B2)[c]	1489.0 (14.5)	1369.0 (12.7)

[a]Cyt-*c* species on Py-H coated electrodes (this work).
[b]B1 refers to the native protein.
[c]B2 denotes the non-native conformational states obtained upon electrostatic or hydrophobic interactions.

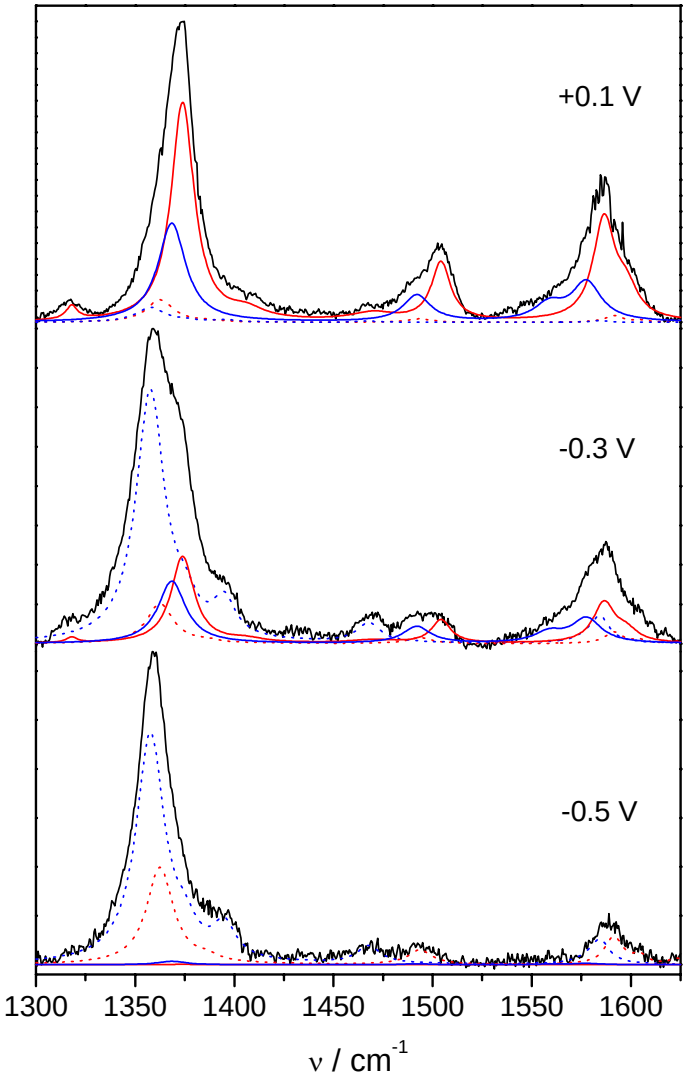

Figure 3- 2 Experimental SERR spectra of Cyt-c adsorbed on Py-H coated electrodes at different potentials. The component spectra of the various species are given by different lineshapes and colours. Blue solid: 5cHSOx; blue dotted: 5cHSRed; red solid: 6cLSOx; red dotted: 6cLSRed (cf. Table 3-1).

The relative spectral contributions are proportional to the relative concentrations of the different species, however, the respective proportionality factors which are unknown, are likely to be different. Therefore, the data in Figure 3- 3 represent only semi-quantitative potential-dependencies of the populations of the various Cyt-*c* species. Nevertheless, it can be concluded

that the adsorbed Cyt-*c* forms a potential-dependent conformational equilibrium that is dominated by a $5cHS^{Red}$ species at negative values and a $6cLS^{Ox}$ one at positive potentials.

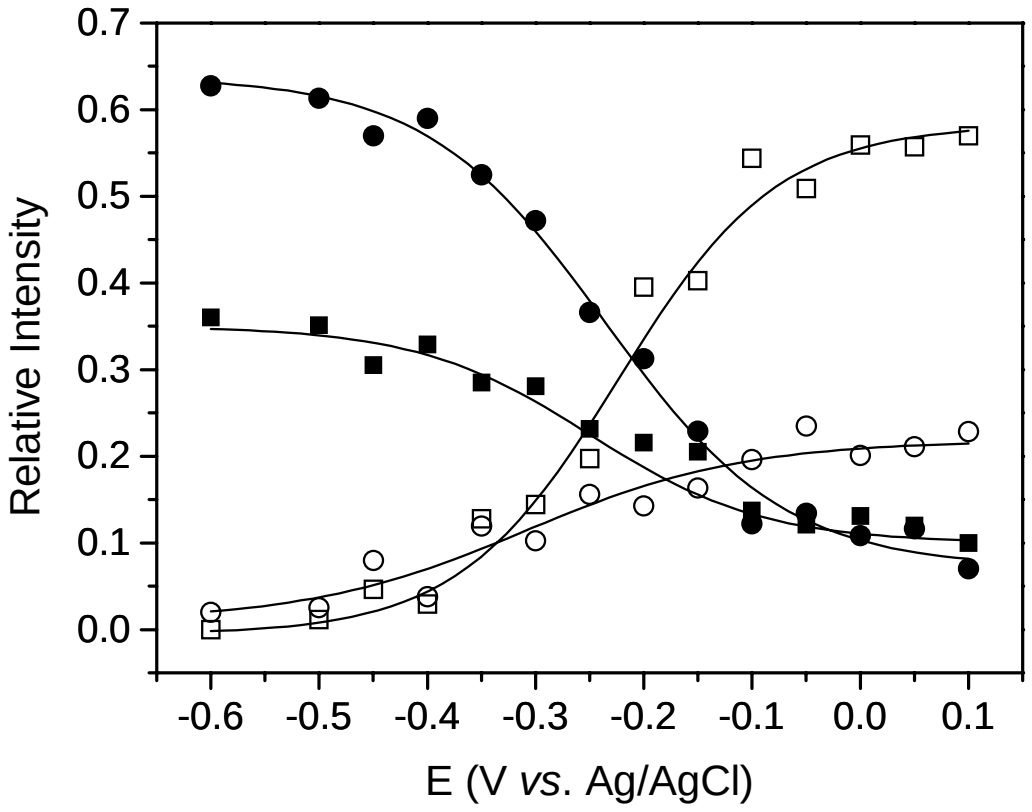

Figure 3- 3 Potential-dependent distribution of species of Cyt-*c* adsorbed on Py-H coated electrodes expressed in relative intensities. Solid squares: $6cLS^{Red}$; hollow squares: $6cLS^{Ox}$; solid circles: $5cHS^{Red}$; hollow circles: $5cHS^{Ox}$.

In another series of experiments, the alkyl-terminated diluent thiols in the mixed monolayer films were replaced by hydroxyl-terminated thiols. Earlier work has shown that Cyt-*c* does not directly adsorb to hydroxyl-terminated layers,[8c,22] whereas it does adsorb to alkyl-terminated layers. The Py-OH monolayers were characterised by cyclic voltammetry, STM, and SERR spectroscopy. These measurements indicate a very poor adsorption of Cyt-*c* to the surface. From the SERR measurements on Ag/Py-OH (Figure 3- 4) the coverage is estimated to be *ca.*

2% of that obtained on Py-H monolayers. The low signal-to-noise ratio of the SERR spectra under these conditions impedes any further analysis.

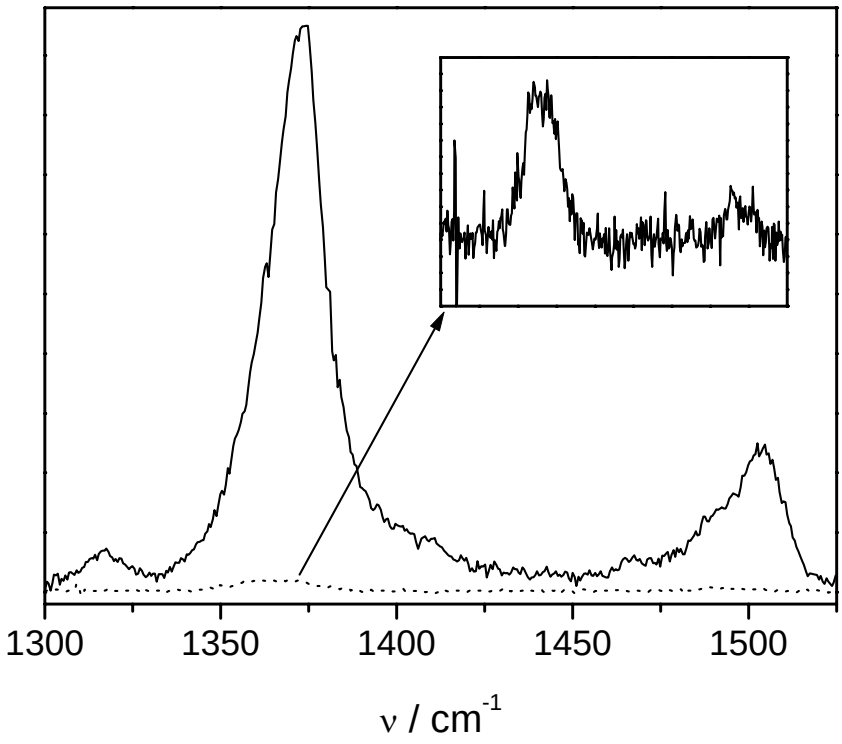

Figure 3- 4 SERR spectra of Cyt-*c* adsorbed on Py-H (solid line) and Py-OH (dotted line and inset) monolayers measured under identical conditions.

Cyclic voltammetry and STM measurements were performed for two different preparations of the hydroxyl-terminated electrodes. The two preparations differed by the exposure time of the electrode to the deposition solution (1 part pyridine-terminated alkanethiol and 9 parts hydroxyl-terminated thiol), for 1 day (1-day-electrode) and 3 days (3-day-electrode). The two voltammograms in Figure 3- 5 were obtained after these electrodes had been incubated in a Cyt-*c* solution for 40 minutes, then washed and studied in a buffer solution. The flatter curve was obtained from the 3-day-electrode and the other curve, with a pronounced faradaic current,

resulted from the 1-day-electrode. The lack of significant faradaic current from the 3-day-electrode illustrates that little or no Cyt-*c* is adsorbed on the electrode, whereas the 1-day-electrode shows a weak faradaic response. The full width at half maximum of the reduction peak for the 1-day electrode is 88 mV. Analysis of the reduction peak gives a Cyt-*c* coverage of 0.21 picomol/cm^2, from both the peak current and the peak charge integral.[23] This coverage is 8-9% of that for the Py-H system reported previously.[9c]

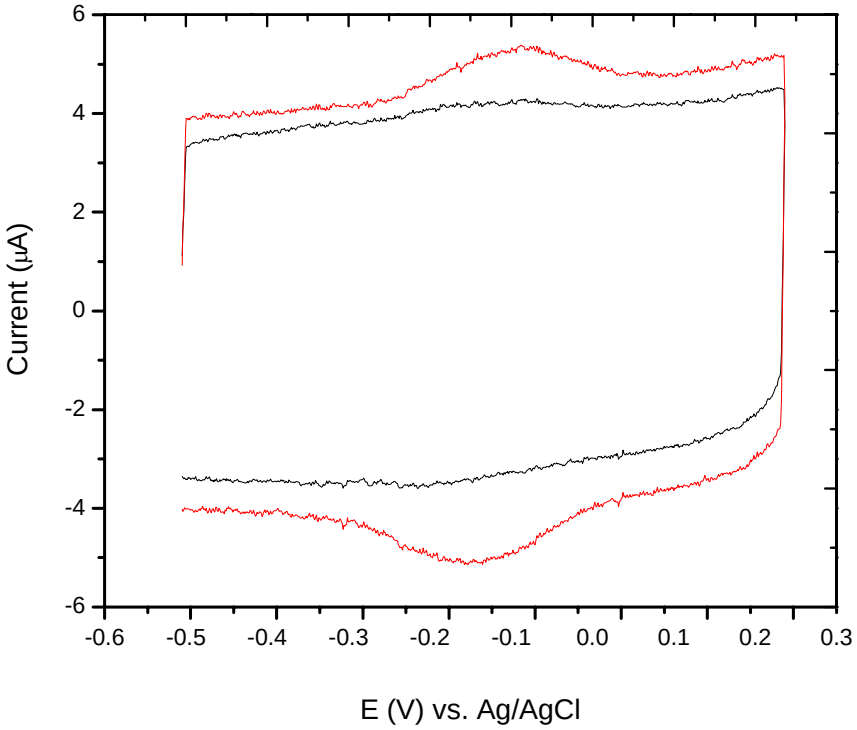

Figure 3- 5 Cyclic voltammograms of Cyt-*c* immobilized on a gold electrode coated with a Py-OH self-assembled monolayer. The two curves are the response from the electrode incubated in Py-OH ethanol solution for 3 days (black) and 1 day (red) at a scan rate of 30 V/sec in a buffer solution at pH 7.

STM images of these two electrode preparations are shown in Figure 3- 6. Panel A shows images for the 3-day preparation, and Panel B shows images for the 1-day preparation. The primary difference to note between these two images is the presence of bright spots

(elevated regions) on the images for the 1-day-electrode preparation (panel B). The cross-section shown below Figure 3- 6B intersects three of the elevated spots in the image, for which the heights range from 3 to 5 Å. The height difference is in reasonable agreement with the 6 Å expected for these hydroxy-terminated and pyridine-terminated thiols from simple bond length estimates.[24] These elevated regions are similar to those observed previously for Py-H/alkanethiol mixed systems.[9c] An analysis of this image indicates that the elevated regions occupy 1.5% to 2% of the total area.[25]

In contrast to the 1-day-electrode, the images of the 3-day-electrode (Figure 3- 6A) do not display elevated regions. This result suggests that prolonged exposure of the electrode to the thiol solution leads to the formation of a nearly pure hydroxyl-terminated thiol monolayer, to the exclusion of the pyridine-terminated thiol. This finding is substantiated by the failure to observe faradaic current or a SERRs signal on the 3-day electrodes.

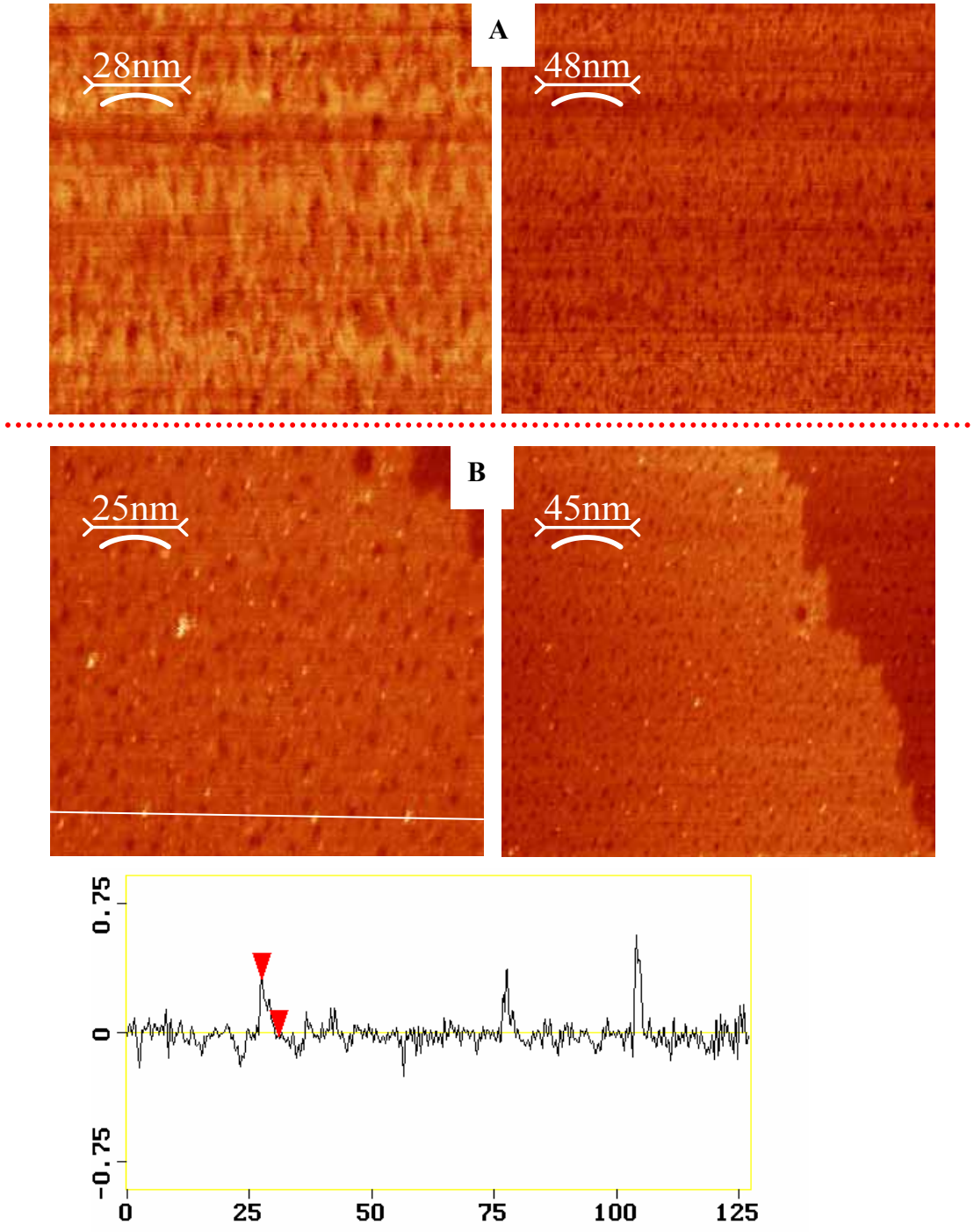

Figure 3- 6 STM images of a gold electrode incubated in an ethanolic Py-OH solution (1:9 molar ratio of C12py and C11OH) for 3 days (A) and for 1 day (B)

3-4 DISCUSSION

Conformational equilibria. The potential-dependent SERR measurements of Cyt-*c* adsorbed on Py-H-coated Ag electrodes clearly indicates a redox-coupled conformational equilibrium between two forms of the adsorbed protein that are assigned to 6cLS heme and 5cHS heme configurations (Figure 3- 3). Figure 3- 7 shows a square reaction scheme that can account for these observations.

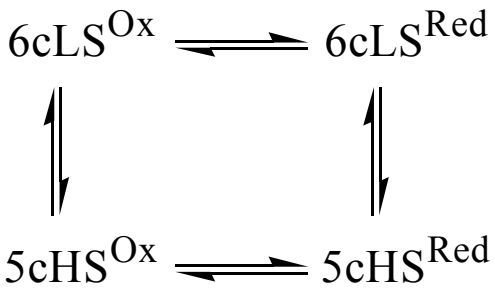

Figure 3- 7 Redox and conformational equilibria of Cyt-c adsorbed to Py-H coated electrodes.

Previous SERR and RR studies in our group have shown that when Cyt-*c* is electrostatically adsorbed to negatively charged model systems, *e.g.* Ag electrodes coated with ω-carboxyl alkanethiols, the native protein (B1) is in equilibrium with a new conformational state B2.[8c,11,12] The formation of the B2 state is induced by the local electrostatic field at the binding domain. This field arises from the array of negative charges on the SAM surface interacting with the positively charged lysine groups on the surface of Cyt-*c* and by the external field caused by the polarization of the metal electrode and the potential drop across the SAM. The main structural difference between the B2 conformational state and the native protein is the lack of the ligand Met-80 at the sixth axial position of the heme Fe. The axial position can either

remain vacant, yielding a 5cHS heme, or be occupied by His-33 to form a new 6cLS configuration.

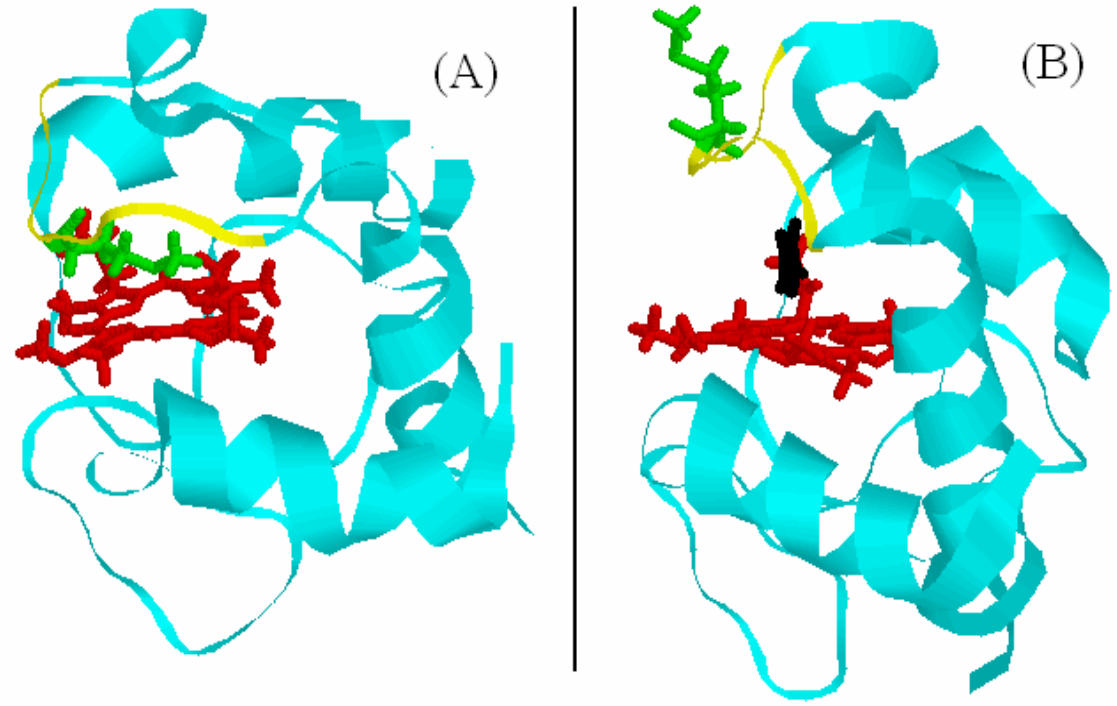

Figure 3- 8 Solution structures of ferric Cyt-c (A; PDB-1AKK) and the complex with imidazole (B; PDB-1F17). Red: heme; green: Met-80; yellow: peptide segment 77-85, black: imidazole. [30]

Recently, we reported the immobilisation of Cyt-*c* on Ag electrodes coated with hydrophobic SAMs. In this case, binding occurs via the hydrophobic patch, which includes the surface residues I85, G84, A83, F82 and I81. This patch is located in the center of the ring of lysine residues, in close vicinity to the partially exposed heme edge (Figure 3- 8A). In this case, the driving force for adsorption is the entropy gained by minimizing the solvent-exposed hydrophobic area. The interactions between the hydrophobic peptide segment and the SAM are hypothesized to induce the rupture of the Fe-Met-80 bond, which leads to a 5cHS heme and subsequently to a new 6cLS form, in which His-33 is likely the sixth ligand. Although the

mechanisms are totally different, both electrostatic and hydrophobic interactions between the SAM and the front face of Cyt-*c* induce conformational equilibria that, with respect to the spin- and coordination state of the heme, are similar to those found for Cyt-*c* bound to Py-H monolayers. In this sense, the adsorption properties of the different systems are similar.

Characterisation of the Py-H mixed monolayers on Au by STM and cyclic voltammetry[9c] showed that the pyridinyl head groups constitute 1-4 % of the modified Au surface. Thus, *a priori*, one cannot discard the possibility that Cyt-*c* binds to Py-H coated electrodes via the hydrophobic region of the SAM, that is, without the involvement of the pyridinyl head groups. However, several observations indicate that adsorption through hydrophobic binding may hold, if at all, only for a very small fraction of the adsorbed Cyt-*c* molecules. In earlier work, the Au bead electrodes coated with only alkanethiol did not reveal any obvious Faradaic current, whereas the mixed films display a strong Faradaic signal. In addition, the apparent redox potential was shifted about 170 mV negative of that for the native form. This redox potential corresponds well to that found in solution for pyridine coordinated to Cyt-*c*'s heme with a largely preserved protein secondary structure.[26]

The most compelling evidence for ligation of Cyt-*c* with the pyridine head group, rather than the alkanethiol diluent, comes from the SERR spectra. The SERR spectra show that the conformational equilibrium on the Py-H films is shifted significantly from that on pure alkanethiol films. For Cyt-*c* adsorbed on purely hydrophobic alkanethiol monolayers, the conformational equilibrium of the oxidised protein is completely shifted towards the B2 forms (6cLS and 5cHS), whereas in the reduced state only the native 6cLS form (B1) is detected. In contrast, on Py-H monolayers ferrous Cyt-*c* mainly exists in the 5cHS form. In addition, the component spectra that are determined for the different redox and ligation states of Cyt-*c*

immobilised on Py-H monolayers differ from the so-called B1 and B2 forms. Specifically, the bands ν_3 and ν_4 of the 6cLS form are shifted to higher wavenumbers with respect to the corresponding modes of the B1 and B2 states and also show some differences in relative intensities both in the reduced and oxidised state (Figure 3- 9, Table 3-1). In addition, the 6cLS component exhibits significant spectral differences with respect to the alkaline forms of the protein.[27] These differences suggest that the sixth ligand cannot be assigned to Met-80 (B1), His-33 (B2), or a lysine residue (alkaline form). Instead, the 6cLS species in both redox states most likely corresponds to the pyridinyl-coordinated heme. Also the 5cHS form exhibits spectral differences with respect to the B2 5cHS species on pure hydrophobic monolayers, especially for the ν_3 band (Table 3-1). This comparison further indicates that at least the major fraction of the 5cHS species does not result from proteins immobilised on the hydrophobic regions of the Py-H SAMs.

The specific interactions of the protein with the Py-H monolayers and the differences with respect to purely hydrophobic or electrostatic adsorption are reflected in the width of the band ν_4, which is an indicator of the flexibility or stability of the heme pocket. In native Cyt-*c*, the ν_4 bandwidth of the ferric form is broader by 60 % than that of the more stable ferrous form. Also in the non-native 6cLS conformations that are induced by purely hydrophobic or electrostatic interactions of the protein with appropriate model systems, the ν_4 band envelopes of the oxidised forms are always broader by at least 20% than those of the reduced forms. In contrast, for Cyt-*c* adsorbed to Py-H monolayers the ν_4 band of the 6cLS form is narrower by 20% in the oxidized state than in the reduced state, indicating that the heme pocket stability is reversed. This observation can be attributed to the higher stability of the pyridine-Cyt-*c* complex

in the ferric state compared to the ferrous state. On the other hand, in the 5cHS conformation, the bandwidth of ν_4 does not change significantly with the oxidation state, as expected.

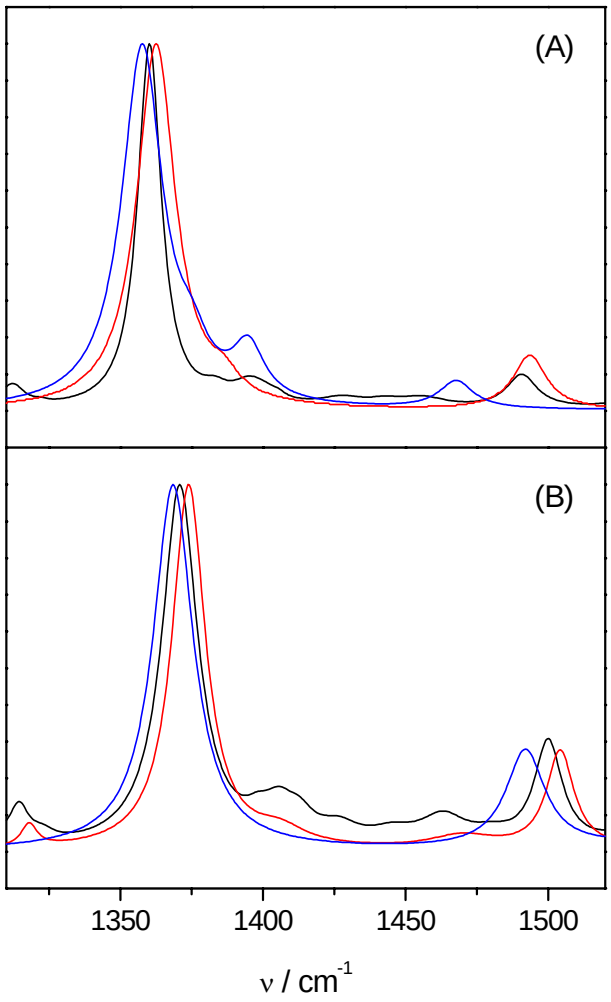

Figure 3- 9 Component spectra of different species of ferrous (A) and ferric (B) Cyt-*c*. Black: native protein (B1); red: 6cLS form on Py-H monolayers; blue: 5cHS form on Py-H

Upon substitution of Met-80 by an external ligand the entire loop 77-85 is shifted away from the heme such that Met-80 points away from the protein interior, as shown in Figure 3- 8B for the NMR structure of imidazole complex of Cyt-*c* in solution. Thus, the hydrophobic segment 80-85 becomes more flexible and solvent exposed. In the 6cLS form of Cyt-*c* bound to

Py-H SAM the pyridinyl group serves as the external ligand, and it is likely that the displaced peptide segment 80 – 85 interacts with the hydrophobic chains of the monolayer, stabilising the complex. This interpretation is consistent with the drastically weaker adsorption of Cyt-*c* on SAMs of mixed pyridinyl/hydroxyl-terminated thiols (Figure 3- 4), even though the pyridinyl coverage on the film is similar (within a factor of two). The hydrophobic interactions should persist when the coordinative pyridinyl-iron bond is broken in the 5cHS form. Furthermore, it is likely that the pyridinyl group remains in the heme pocket and prevents the Met-80 from rebinding to the ferrous heme, in contrast to the case of Cyt-*c* immobilised on purely hydrophobic monolayers. This scenario explains why the native B1 form is recovered for the reduced state at hydrophobic electrodes, but not for the Py-H coated electrodes. In addition, these conclusions are in agreement with the apparent increase in the 6cLS/5cHS equilibrium constant by a factor of *ca* 5 (Figure 3- 3) from the reduced (-0.6 V) to the oxidised (0.1 V) couple, which is consistent with the larger affinity of exogenous N-ligands for the ferric form of Cyt-*c*.

A related scenario has been observed for the formation of the bis-His complex of Cyt-*c* upon SDS binding in solution. At submicellar concentrations, SDS molecules interact with the hydrophobic patch of the protein and destabilise the heme pocket, such that complete complexation with His-33 is achieved for ferric cytochrome *c* whereas in the reduced protein the 5cHS state is stabilised under the same conditions.

Redox equilibria. The redox equilibria for both individual redox couples in Figure 3- 7 can be analysed according to the Nernst equation

$$E = E^0 - \frac{RT}{nF}\ln\left(\frac{I_{\mathrm{Red}} f_{\mathrm{Red}}}{I_{Ox} f_{Ox}}\right) \qquad 3\text{- }1$$

where I and f_i represent the absolute intensities and the inverse relative SERR cross-sections respectively. Since the f_i factors are unknown, the determination of the apparent redox potentials was based only on the relative SERR intensities, *i.e.* assuming $f_{Red} = f_{Ox}$. The Nernst plots show clear deviations from linearity, especially at high potentials, and an apparently linear region around the zero point of the ordinates, *i.e.* in the vicinity of the apparent redox potential, as shown in Figure 3- 10 for the 6cLS redox couple. Restricting the analysis to this linear region, apparent redox potentials of –0.24 V and –0.18 V are obtained for the 6cLS and 5cHS forms, respectively. The values for n were found to be only *ca.* 0.4 in each case. Both redox potentials are more positive than those found for the state B2 induced upon electrostatic adsorption (*ca.* -0.38 and -0.43 V).[11] Such positive shifts may reflect interactions between the hydrophobic chains in the Py-H monolayer and the peptide segment 80-85, which is likely to restrict solvent accessibility to the heme. Taking into account the uncertainty associated with the assumption $f_{red}=f_{ox}$, the apparent redox potential for the 6cLS couple determined by SERR spectroscopy is similar to that the midpoint potential derived from CV and both values exhibit comparable negative shifts with respect to the redox potential of the native protein in solution. Note that for both methods the values are more consistent with that found in solution for pyridine ligated to the heme iron with the protein in a largely preserved secondary structure (*ca.* -0.17 V)[26] than with the denatured pyridine/cytochrome *c* complex (*ca.* -0.33 V).[26]

The square reaction scheme in Figure 3- 7 provides a first approximation that accounts for the four spectroscopically distinguishable species. The underlying assumptions in this model are that the four cytochrome *c* species are electroactive and have a well-defined and potential-independent orientation with respect to the electrode, such that the system can be described with

only two redox potentials. The broadening of the SERR bands, which is especially evident for the reduced forms of 5cHS and 6cLS (see Table 3-1), suggests a distribution of substates. These substates are not distinguishable on the level of the present SERR spectra and may only differ with respect to the orientation of the protein relative to the SAM surface, which in turn affects the solvent accessibility of the heme and could lead to a distribution of redox potentials. In addition, a subset of orientations may be unfavourable for electron transfer and those species do not participate in the redox process. As in the case of Cyt-*c* electrostatically adsorbed to carboxyl-terminated SAMs, the orientational distribution might be potential-dependent, which could explain the deviations from an ideal Nernstian behaviour at extreme electrode potentials. In fact, the experimental data in Figure 3- 10 can be simulated by a Gaussian distribution of redox potentials centered at ca. –0.24 V plus a fraction of redox inactive 6cLS ferrous Cyt-*c*.

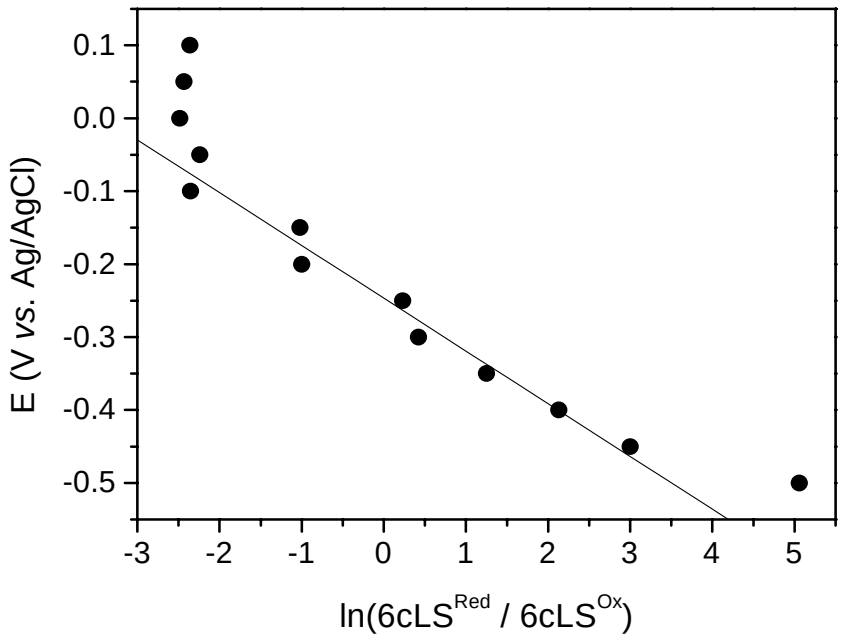

Figure 3- 10 Nernstian plot for the 6cLS couple of Cyt-*c* adsorbed on Py-H monolayers. Further details are given in the text.

Thus, for Cyt-*c* adsorbed to Py-H coated Ag electrodes, stationary SERR measurements clearly show the existence of two redox couples (6cLS and 5cHS) with non-ideal electrochemical response. On the other hand, CV experiments performed on the same system but using Au electrodes show only one redox couple ascribed to the Py-coordinated heme (6cLS) and a nearly ideal electrochemical response for scan rates faster than 1 V/s.[9b,c] In previous work, the standard heterogeneous electron transfer rate constant of Cyt-*c* on Py-H films was determined by measuring the peak potential separation as a function of the voltage scan rate.[9b,c] That analysis gave a rate constant of 780 (±40) s^{-1}. The voltammogram in Figure 3- 5 for Cyt-*c* adsorbed on the same tether but with a hydroxyl diluent, to eliminate partial unfolding from hydrophobic interactions and eliminate direct hydrophobically adsorbed protein, gives a rate constant of 760 s^{-1}. The correspondence in these rate constants suggest that the electron transfer rate is controlled by the coordination with the heme through the pyridinyl tether and that partial unfolding of the protein's hydrophobic region has little effect.

These apparent contradictions between SERR and CV results can be rationalised in terms of structural differences of the SAMs on the two different metals and kinetic arguments based on the square reaction scheme in Figure 3- 7. Previous studies have shown that alkanethiols form more densely packed SAMs on Ag than on Au, as is reflected for example in a higher resistance to ion transport.[28] Therefore, one should expect a smaller amount of 5cHS species on Py-H coated Au electrodes compared to the more hydrophobic preparations on Ag. If in addition, the rate constants for the 6cLS to 5cHS conformational transitions and the heterogeneous electron transfer rate constant for the 5cHS species are much smaller than the scan rate, then the

electrochemical response should be largely dominated by the 6cLS redox couple. For scan rates faster than 1 V/s, rate constants smaller than 0.7 s^{-1} can fulfil these conditions.

Time-resolved SERR measurements of Cyt-*c* adsorbed on Ag electrodes coated with ω-carboxyl alkanethiols show that the B1-to-B2 transition is at least three orders of magnitude slower than the heterogeneous electron transfer of the B1 species.[29] On the other hand, in the electron-tunnelling regime, the heterogeneous electron transfer rate constant of Cyt-*c* electrostatically adsorbed on carboxyl-terminated SAMs is ca. 200 times smaller than that of the directly linked heme on Py-H monolayers of comparable length.[30b] The reason for such a difference is the stronger electronic coupling in the second case. One could expect an even more dramatic difference between the 6cLS and 5cHS forms on Py-H SAMs since the orientation of the latter species is certainly not optimised for electron transfer.

3-5 CONCLUSIONS

1. The SERR spectra demonstrate that the redox center of cytochrome *c* can be directly linked to a silver electrode by coating the metal surface with mixed SAMs of Py-H, in which the pyridinyl head groups are able to substitute for the natural axial ligand Met-80. The concomitant displacement of the peptide segment 80-85 from the heme pocket further stabilizes the complex via hydrophobic interactions with the alkyl-terminated thiols.

2. In line with the redox-dependent binding constant of the pyridinyl residue to the heme, this complex is more stable in the ferric than in the ferrous form leading to a redox dependent spin and coordination equilibrium.

3. In both the 6cLS and the 5cHS states, the protein is most likely not adsorbed in a uniform orientation with respect to the plane of the electrode, but rather exists in a distribution of orientations (substates) that correspond to a distribution of redox potentials. This distribution can account for the non-Nernstian behavior observed in the SERR spectroscopic analysis of Cyt-*c* on the coated Ag electrode.

4. The CV data reveals a nearly ideal Nernstian behaviour for Cyt-*c* immobilised on a coated Au electrode. This discrepancy may be rationalised in terms of a fraction of the adsorbed proteins with very slow ET kinetics that does not contribute to the CV signals but is probed in the SERR experiments.

BIBLIOGRAPHY

[1] *Electroanalytical Methods for Biological Material*; Brajter-Toth, A., Chambers, J. Q., Eds.; Marcel Dekker, Inc.: New York, 2002

[2] Willner, I.; Katz, E. *Angew. Chem. Int. Ed.* **2000**, *39*, 1180-1218.

[3] (a) *Cytochrome c-A Multidisciplinary Approach*; Scott, R. A.; Mauk, A. G., Eds.; University Science Books: Sausalito, California, 1995. (b) Moore, G. R.; Pettigrew, G. W. *Cytochromes c: Evolutionary, Structural and Physicochemical Aspects*; Springer: New York, 1990.

[4] (a) Casimiro, D. R.; Richards, J. H.; Winkler, J. R.; Gray, H. B. *J. Phys. Chem.* **1993**, *97*, 13073-13077. (b) Luo, J.; Reddy, K. B.; Salameh, A. S.; Wishart, J. F.; Isied, S. S. *Inorg. Chem.* **2000**, *39*, 2321-2329. (c) Mines, G. A.; Bjerrum, M. J.; Hill, M. G.; Casimiro, D. R.; Chang, I. J.; Winkler, J. R.; Gray, H. B. *J. Am. Chem. Soc.* **1996**, *118*, 1961-1965. (d) Winkler, J. R.; Di Bilio, A. J.; Farrow, N. A.; Richards, J. H.; Gray, H. B. *Pure Appl. Chem.* **1999**, *71*, 1753-1764.

[5] (a) Harris, M. R.; Davis, D. J.; Durham, B.; Millett, F. *BBA-Bioenergetics* **1997**, *1319*, 147-154. (b) Mclendon, G. *Acc. Chem. Res.* **1988**, *21*, 160-167. (c) Mei, H. K.; Wang, K. F.; Peffer, N.; Weatherly, G.; Cohen, D. S.; Miller, M.; Pielak, G.; Durham, B.; Millett, F. *Biochemistry* **1999**, *38*, 6846-6854. (d) Pletneva, E. V.; Fulton, D. B.; Kohzuma, T.; Kostic, N. M. *J. Am. Chem. Soc.* **2000**, *122*, 1034-1046.

[6] (a) Armstrong, F. A.; Hill, H. A. O.; Walton, N. J. *Acc. Chem. Res.* **1988**, *21*, 407-413. (b) Lewis, N. S.; Wrighton, M. S. *Science* **1981**, *211*, 944-947.

[7] (a) Avila, A.; Gregory, B. W.; Niki, K.; Cotton, T. M. *J. Phys. Chem. B* **2000**, *104*, 2759-2766. (b) Feng, Z. Q.; Imabayashi, S.; Kakiuchi, T.; Niki, K. *J. Chem. Soc., Faraday Trans.* **1997**, *93*, 1367-1370. (c) Song, S.; Clark, R. A.; Bowden, E. F.; Tarlov, M. J. *J. Phys. Chem.* **1993**, *97*, 6564-6572. (d) Tarlov, M. J.; Bowden, E. F. *J. Am. Chem. Soc.* **1991**, *113*, 1847-1849.

[8] (a) Murgida, D. H.; Hildebrandt, P. *Angew. Chem. Int. Ed.* **2001**, *40*, 728-731.(b) Murgida, D. H.; Hildebrandt, P. *J. Mol. Struct.* **2001**, *565*, 97-100. (c) Murgida, D. H.; Hildebrandt, P. *J. Phys. Chem. B* **2001**, *105*, 1578-1586. (d) Murgida, D. H.; Hildebrandt, P. *J. Am. Chem. Soc.* **2001**, *123*, 4062-4068. (e) Murgida, D. H.; Hildebrandt, P. *J. Phys. Chem. B* **2002**, *106*, 12814-12819.

[9] (a) Liu, H. Y.; Yamamoto, H.; Wei, J. J.; Waldeck, D. H. *Langmuir* **2003**, *19*, 2378-2387. (b) Wei, J. J.; Liu, H. Y.; Khoshtariya, D. E.; Yamamoto, H.; Dick, A.; Waldeck, D. H. *Angew. Chem. Int. Ed.* **2002**, *41*, 4700-4703. (c) Wei, J. J.; Liu, H. Y.; Dick, A. R.; Yamamoto, H.; He, Y. F.; Waldeck, D. H. *J. Am. Chem. Soc.* **2002**, *124*, 9591-9599. (d) Yamamoto, H.; Liu, H. Y.; Waldeck, D. H. *Chem. Commun.* **2001**, 1032-1033.

[10] Rivas, L.; Murgida, D. H.; Hildebrandt, P. *J. Phys. Chem. B* **2002**, *106*, 4823-4830.

[11] Wackerbarth, H.; Murgida, D. H.; Oellerich, S.; Dopner, S.; Rivas, L.; Hildebrandt, P. *J. Mol. Struct.* **2001**, *563*, 51-59.

[12] Oellerich, S.; Wackerbarth, H.; Hildebrandt, P. *J. Phys. Chem. B* **2002**, *106*, 6566-6580.

[13] Murgida, D. H.; Hildebrandt, P.; Smith, A. Unpublished results.

[14] Kneipp, K.; Kneipp, H.; Itzkan, I.; Dasari, R. R.; Feld, M. S. *J. Phy. Condens. Matter* **2002**, *14*, R597-R624.

[15] Brutigan, D. L.; Ferguson, S.; Margoliash, E. *Methods in Enzymology*; Fleischer, S; Packer, L., Eds.; Academic Press: New York,1978, Vol. 53, pp. 131-132.

[16] Wackerbarth, H.; Klar, U.; Gunther, W.; Hildebrandt, P. *Appl. Spectrosc.* **1999**, *53*, 283-291.

[17] Clavilier, J.; Faure, R.; Guinet, G.; Durand, R. *J. Electroanal. Chem.* **1980**, 107, 205-209.

[18] Sawyer, D. T.; Sobkowiak, A.; Roberts, J. L., Jr. *Experimental Electrochemistry for Chemists*; Wiley: New York, 1995; pp 74-75. The diffusion constant of $Fe(CN)_6^{3-/4-}$ is assumed to be 7.63 x 10^{-6} cm^2/sec.

[19] This calculation assumes a parallel plate model for the capacitance of the film ($C = ee_0/d$) and takes the alkanethiol dielectric constant e to be 2.6.

[20] (a) Andreu, R.; Fawcett, W. R. *J. Phys. Chem.* **1994**, *98*, 12753-12758. (b) Porter, M. D.; Bright, T. B.; Allara, D. L.; Chidsey, C. E. D. *J. Am. Chem. Soc.* **1987**, *109*, 3559-3568.

[21] Dopner, S.; Hildebrandt, P.; Mauk, A. G.; Lenk, H.; Stempfle, W. *Spectrochim. Acta Part A-Mol. Biomol. Spectrosc.* **1996**, *52*, 573-584.

[22] Terrettaz, S.; Cheng, J.; Miller, C. J. *J. Am. Chem. Soc.* **1996**, *118*, 7857-7858.

[23] The reduction was taken to be reversible. For a description of such an analysis see Bard, A. J.; Faulkner, L. R. *Electrochemical Methods*; Wiley: New York, 1996.

[24] a) Weiss, P. S.; Bumm, L.A.; Dunbar, T.D.; Burgin, T.P.; Tour, J.M.; Allara,D.L. Ann. N. Y. Acad. Sci. **1998**, *852*, 145; b)Gorman, C.B.; Carrol, R.L.; He, Y.; Tian, F.; Fuierer, R. Langmuir **2000**, *16*, 6312.

[25] Assigning these elevated structures to pyridine-terminated thiols, yields a pyridine coverage of about 13 pmol/cm^2, assuming a coverage of 700 pmol/cm^2 for a compact alkanethiol monolayer on Au(111).[a,b] A comparison of this pyridine coverage estimate to the electrochemically determined Cyt-*c* coverage, indicates a pyridinyl/Cyt-*c* ratio of about sixty. a) Finklea, H. O. in *Electroanalytical Chemistry*; Bard, A. J., Ed.; Marcel Dekker: New York, 1996; pp 109-335; b) Walczak, M. M.; Popenoe, D. D.; Deinhammer, R. S.; Lamp, B. D.; Chung, C. K.; Porter, M. D. *Langmuir* **1991**, *7*, 2687-2693.

[26] Fan, C. H.; Gillespie, B.; Wang, G. M.; Heeger, A. J.; Plaxco, K. W. *J. Phys. Chem. B* **2002**, *106*, 11375-11383.

[27] Dopner, S.; Hildebrandt, P.; Rosell, F. I.; Mauk, A. G. *J. Am. Chem. Soc.* **1998**, *120*, 11246-11255.

[28] (a) Laibinis, P. E.; Whitesides, G. M.; Allara, D. L.; Tao, Y. T.; Parikh, A. N.; Nuzzo, R. G. *J. Am. Chem. Soc.* **1991**, *113*, 7152-7167. (b) Walczak, M. M.; Chung, C. K.; Stole, S. M.; Widrig, C. A.; Porter, M. D. *J. Am. Chem. Soc.* **1991**, *113*, 2370-2378.

[29] Murgida, D. H.; di Paolo, R; Hildebrandt, P. Unpublished results.

[30] a) Cytochrome c: PDB 1AKK. Primary citation: Banci, L., Bertini, I., Gray, H. B., Luchinat, C., Reddig, T., Rosato, A., Turano, P. *Biochemistry* **1997**, 36, 9867 ; b) Complex with imidazole: PDB 1FI7, Primary

citation: Banci, L., Bertini, I., Liu, G. H., Reddig, T., Tang, W. X., Wu, Y. B., Yao, Y., Zhu, D. X. *J. Biol. Inorg. Chem*. **2001**, 6, 628.

CHAPTER 4 ELECTRON TRANSFER DYNAMICS OF CYTOCHROME C: A CHANGE IN THE REACTION MECHANISM WITH DISTANCE[††]

A novel strategy to immobilize cytochrome c on SAM coated gold electrodes, by directly linking a pyridinalalkanethiol to the protein's redox active heme unit, and studies the electron transfer mechanism by changing the distance between the surface and the protein. Comparison of the kinetic data for this system with earlier data on COOH terminated SAMs requires a change in electron transfer mechanism with distance from the electrode surface that does not involve large-amplitude conformational rearrangement.

4-1 INTRODUCTION

Redox processes are ubiquitous in nature, and the understanding of electron transfer in complex systems; e.g., biological structures such as proteins, membranes, and the photosynthetic reaction center, is an outstanding challenge. This work provides new results on the electron transfer dynamics of the protein cytochrome c as a function of distance from a metal electrode. Comparison of this distance dependence with previous studies indicates that a conformationally gated mechanism involving a large amplitude protein motion is not operative, but a change in the electron transfer mechanism occurs and is linked to the protein environment.

The redox protein cytochrome c is very well characterized and numerous studies of its electron transfer have been performed, both homogeneous and heterogeneous.[1] A number of

[††] This work was published as Wei, JJ**;** Liu, HY; Khoshtariyaa, DE.; Yamamoto, H.; Waldeck, DH; "Electron Transfer Dynamics of Cytochrome C. A Change in the Reaction Mechanism with Distance. ," *Angew. Chem. Int. Ed.*, **2002**, 41 (24): 4700-4703.

workers have immobilized cytochrome c on gold electrodes that are coated with a self-assembled monolayer (SAM) of–S–$(CH_2)_{n-1}$–COOH, presumably by binding to the protein's lysine groups.[2] By changing the length of the alkane chain the electronic coupling strength between the electrode and the protein can be varied. At large SAM thickness the electron transfer rate constant declines exponentially with distance (electron tunneling mechanism), but at short thickness it is distance independent, hence there is a change in the rate limiting step, the mechanism of reaction. More recently mixed monolayer films of pyridine-terminated alkanethiols embedded in an alkanethiol diluent have been used to directly tether the heme to the surface.[3] This strategy for immobilization (see Fig 1) should eliminate large-amplitude conformational motion of the protein on the surface of the SAM as a gating mechanism for the electron transfer, because the heme is directly linked to the alkanethiol tunneling barrier.

4-2 RESULTS AND DISCUSSION

The immobilization of the cytochrome on the film has been demonstrated through electrochemical control experiments and by direct imaging using STM.[3b] The primary evidence for binding near the heme is the negative shift of the redox potential, as compared to that in solution, and the differential adsorption strength for different functional endgroups (nitriles, imidazole and pyridinal).[3b] The electron transfer rate constant between the Au electrode and the cytochrome c were determined using cyclic voltammetry.[3b] The composition of the mixed films (given in Table 4-1) consists of 3-4% pyridine terminated chains in a diluent of alkane-terminated chains, and the coverage of cytochrome corresponds to about 10% of the pyridine sites, less than 1% overall. The nearly ideal quality of the voltammograms stands in strong contrast to that reported with pure layers of pyridine-terminated alkanes,[3a] for which the

voltammetry showed severe asymmetry in the redox rates and significant inhomogeneity. The homogeneous behavior of the voltammetry that is observed on the mixed films indicates that the protein does not denature.[4] Spectroscopic studies are underway to characterize the adsorbed cytochrome and will be reported elsewhere.

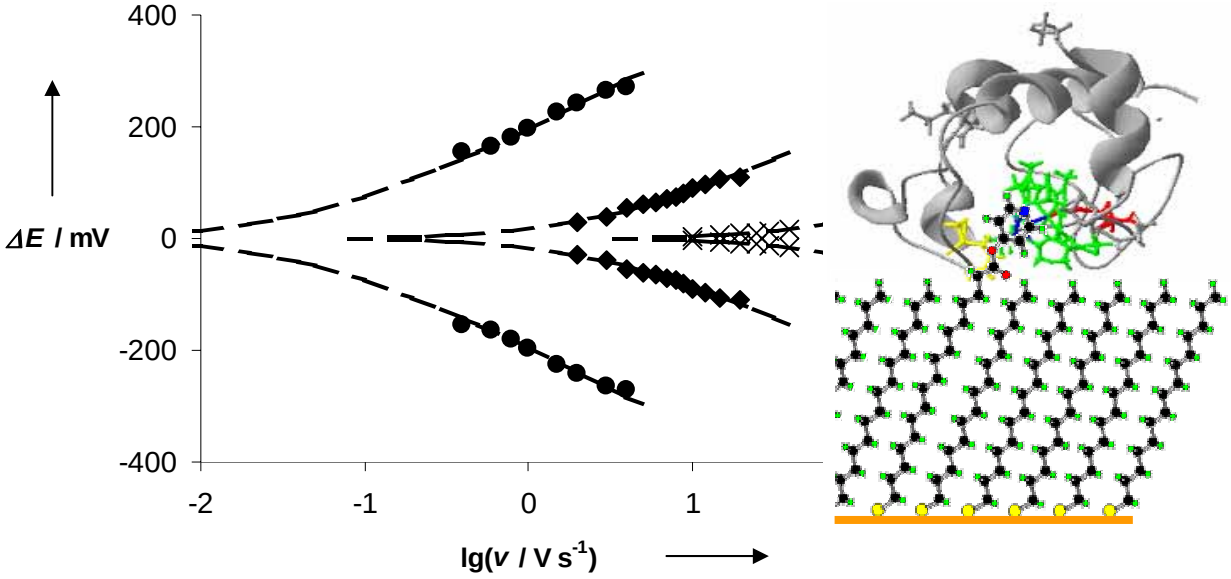

Figure 4- 1 The dependence of the peak separation E on the voltage scan rate v is shown for pyridine-terminated chains having lengths of twenty methylenes (circles), sixteen methylenes (diamonds), and six methylenes (x). In each case the data is fit to the Marcus model with a reorganization energy of 0.8 eV. A schematic diagram of the cytochrome immobilization strategy is shown on the right.

Figure 4- 1 shows the dependence of the voltammetric peak positions on the voltage scan rate for three different systems. The shift of the peak position with voltage scan rate is used to quantify the standard electron transfer rate constant k^{0}.[5] The eicosanethiol (C20) chain has the slowest k^{0}; its peaks move apart at lower scan rates than the other data, which are for shorter methylene chain lengths (C16 and C6). The dashed curves in this figure show the best fit to the Marcus theory model with a reorganization energy λ_o of 0.8 eV for each of the systems. Because

the data do not extend to high overpotentials, the fits are not very sensitive to the value of the reorganization energy, e.g., λ_o = 0.5 eV gives similar quality fits and a k^0 that only differs by a few percent from those in Table 4-1.

The thickness dependence of k^0 is summarized in Table 4-1 and plotted in Figure 4- 2, along with earlier data for cytochrome c adsorbed on –COOH terminated SAMs. At large thickness, both data sets display an exponential dependence on distance. For nonadiabatic electron transfer, k^0 is proportional to the electronic coupling squared; i.e.,

$$k_{NA}^{0} \propto \left|H_{if}\right|^2 = \left|H_{if}^{0}\right|^2, \exp\left(-\beta R_e\right) \qquad 4\text{-}1$$

where $|H_{if}^{0}|$ is the electronic coupling matrix element at the minimum donor-acceptor separation distance and β is a characteristic decay factor.[6,7] The two data sets (COOH and pyridinal SAMs) should have the same distance dependence in the nonadiabatic ('tunneling') regime since the distance is being changed by the number of methylene units in the tether for both cases. A best fit to the rate data at long distance gives a β of 1.22 per CH_2 for the COOH SAMs and 1.19 per CH_2 for the pyridinal SAMs. Although the slopes are similar, the absolute value of the rate constant is significantly larger (at a given methylene number) for the pyridine-terminated tethers, indicating a larger tunneling probability (electronic coupling).

Table 4-1 Rate constant data for cytochrome c immobilized on pyridinal-alkanethiols.[8]

system	k^0 (Hz)	# trials
C6py/C5	1670± 60	2
C11py/C10	1150± 80	5
C12py/C11	783 ± 36	3
C16py/C15	43 ± 10	7
C20py/C19	0.50±0.06	3
C22py/C21	0.032 ±0.026	2

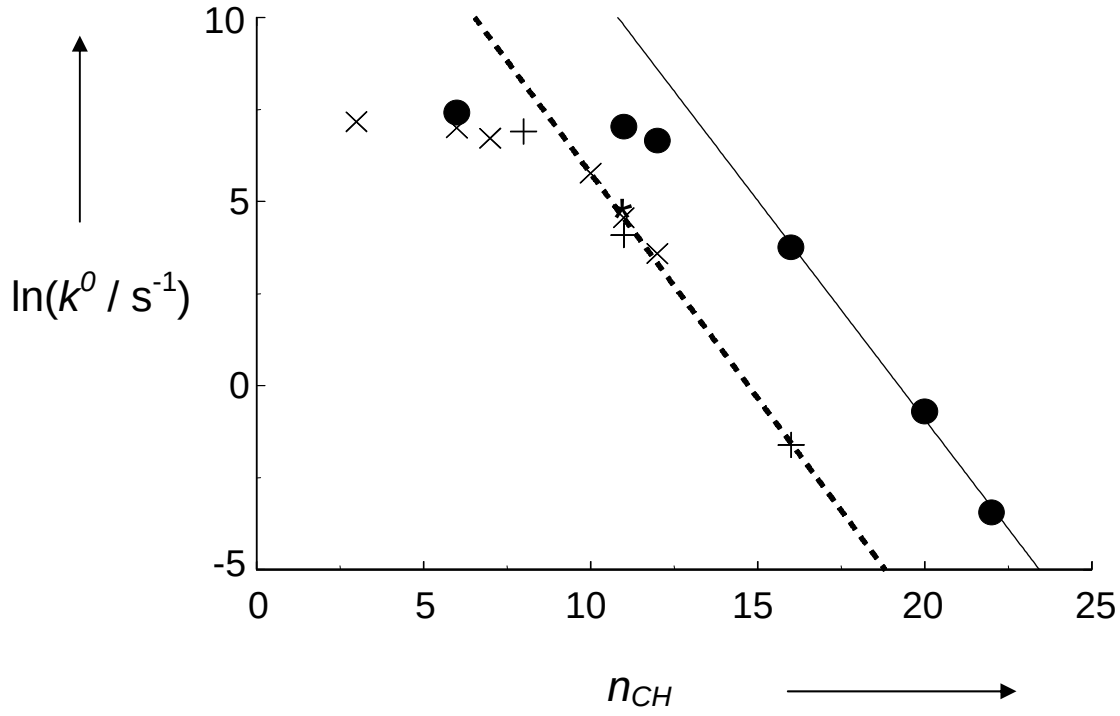

Figure 4- 2 The graph plots k^0 versus methylene number for cytochrome c on SAM coated gold electrodes (x from [2c,d], + [2a,b], and * this work for COOH and for pyridine terminated layers). The lines are fits to Eqn 4-1.

Both data sets show a plateau region at short donor-acceptor separations; however the plateau region for the pyridine-terminated SAMs extends to larger film thicknesses (about 12 methylenes). The maximum rate constants for both film types are similar (the hexyl chains have a rate constant of about 1100 Hz for the COOH terminated SAMs and about 1700 Hz for the pyridine terminated SAMs) and display plateau behavior. Previous workers[2] explained the plateau behavior as resulting from a change in the rate-determining step from electron tunneling at large distances to conformational rearrangement of the protein-SAM system to a redox-active state at short thickness; analogous to the conformationally gated mechanism used to describe protein-protein electron transfer. Because the pyridine binds near the heme, the conformationally gated mechanism would need to involve local changes near the redox center, rather than large-amplitude motion of the protein. In addition, the ac impedance and cyclic voltammetry data indicate a typical charge-transfer step[2,5] and do not support a more complex mechanism involving a conformational step. Direct spectroscopic detection of redox species immobilized on the carboxylic acid terminated SAMs[9] support the view that the conformational changes are small. In summary, the mode of binding restricts the type of conformational change that can be linked to the electron transfer process at short distances, implying that large amplitude motion of the protein is not involved.

Hildebrandt[9] observed a significant deuterium isotope effect for the electron transfer rate constant on thin (C2 and C3) films and suggested that proton transfer may be coupled to the electron transfer or rearrangement of the hydrogen bonded network in the protein may constitute a rate limiting step. In addition, he observed a thickness dependence for the isotope effect and postulated that the mechanism change is modulated by the applied electric field. The influence of a D_2O buffer on the electron transfer rate constant was evaluated for the C16 and C11

pyridinal systems. For the C16-pyridinyl tether the rate constant was 50 Hz, which is very similar to that observed in the H_2O buffer. For the C11-pyridinyl tether the rate constant was 900 Hz, which is a factor of 0.78 smaller than that found in the H_2O buffer. These findings are consistent with those of Hildebrandt.

The large difference in the extent of the plateau region and the higher electron transfer rates for the pyridine system (see Figure 4- 2) are consistent with a larger electronic coupling for the pyridine immobilized cytochrome c than for the carboxylate. The enhanced electronic coupling suggests that the change in electron transfer mechanism may be linked to the change in electronic coupling with distance from the electrode. In the adiabatic, or strong coupling, regime the rate constant k_A^0 does not display an exponential distance dependence, but does depend on the polarization relaxation in the medium.[10] In the simple limit

$$k_A^0 = \frac{1}{\tau_{eff}} \sqrt{\frac{\lambda_o}{\pi^3 RT}} \exp\left(-\frac{\Delta G_a^*}{RT} \right) \qquad 4\text{-}2$$

where the activation free energy is given by

$$\Delta G_a^* = \frac{\lambda_o}{4} - |H| \qquad 4\text{-}3$$

when the reaction free energy is zero. The reorganization energy λ_o is difficult to calculate since it depends in a detailed manner on the protein structure,[11a] the SAM coated electrode[11b] and the solvent. The characteristic polarization relaxation time τ_{eff} measures the time-scale for the response of the surrounding medium (the solvent molecules, protein interior, etc.[10]) to the change in the charge distribution, associated with the electron transfer, and will depend on detailed properties of the SAM associated protein. A simple approximation treats this relaxation time as the longitudinal dielectric relaxation, which in a Debye dielectric continuum model is given by

$$\tau_{eff} \approx \tau_L = \left(\frac{\varepsilon_\infty}{\varepsilon_s} \right) \frac{3 \eta V_m}{RT} \qquad 4\text{-}4$$

where τ_L is the longitudinal relaxation time of the solvent polarization, η is the solvent shear viscosity, V_m is the molar volume, ε_s is the static dielectric constant, and ε_∞ is the high frequency dielectric constant. Hence, the experimental signature for electron transfer in the adiabatic limit is a friction dependent rate constant,[12] and the rate constant for the cytochrome c in the plateau region displays a viscosity dependence.[2d,13] This model is also consistent with the D_2O findings since the D_2O 'hydrated' protein would have a different relaxation than the H_2O hydrated protein and D_2O has a slower dielectric relaxation time than H_2O. Although the pyridinyl system has a larger rate constant in the plateau region than that of the COOH system, their similarity suggests that the activation free energies in the two cases are similar despite the different manner of protein immobilization. This observation requires that any significant changes in the reorganization energy between the two systems must be compensated for by changes in the polarization relaxation time and the electronic coupling magnitude, which also modifies the relaxation time.[10,12] Because the current method does not provide a precise measurement of λ_o, a more detailed study of this correspondence is being pursued.

4-3 CONCLUSION

This work demonstrates how a new strategy for immobilizing cytochrome c on electrode surfaces, which directly tethers the redox active site to the metal electrode, can be used to explore the change in electron transfer mechanism with distance between the protein and the electrode. The distance was changed through the variation of the methylene chain length in the tether, but differs from earlier studies by the nature of the SAM cytochrome interaction. The difference in binding modes provides a stronger electronic coupling for the pyridinal systems than for the COOH system and changes the SAM thickness at which the onset of a plateau (distance independent rate constant) is observed. This circumstance also causes different rate constants in the tunneling regime for the two different binding modes (but same methylene chain number). These findings indicate that the electron transfer at short distance need not be linked to a large-amplitude conformational change of the protein with respect to the electrode surface. A change in the electron transfer mechanism that arises from the enhanced electronic coupling at short distance is also consistent with the observations.

BIBLIOGRAPHY

[1] a) Fedurco, M. *Coord. Chem. Rev.* **2000,** *209*, 263; b) R. A. Scott, *Cytochrome C: A Multidisciplinary Approach*, R. A. Scott and A. G. Mauk; ed. (University Science Books, Sausalito, **1996**) 515.

[2] a) Tarlow, M. J.;, and Bowden, F. F., *J. Am. Chem. Soc*. **1991,** *113*, 1847; b) Song, S.; Clark, R. A.; Bowden, F. F.;, Tarlow, M. J. *J., Phys. Chem.* **1993**, *97*, 6564; c) Feng, Z. Q.; Imabayashi, S.; Kakuichi, T.; and Niki, K. *Chem. Soc. Faraday Trans.* **1997**, *93*, 1367; d) Avila, A.; Gregory, B. W.; Niki, K.; and Cotton, T. M. *J. Phys. Chem. B* **2000**, *104,* 2759.

[3] a) Yamamoto, H.; Liu, H.; Waldeck, D. H. *Chem Comm*, **2001**, 1032; b) Wei, J., Yamamoto, H.; Liu, H.; Dick, A.; He, Y. and Waldeck, D. H. *J. Am. Chem. Soc.* **2002**, *124*, 9591.

[4] a) Armstrong, F. A.; *J. Chem. Soc. Dalton Trans.* **2002**, 661; b) Earlier work that immobilized cytochrome c onto pure films of pyridine-terminated alkanes showed asymmetric redox kinetics and inhomogeneity in the redox potential (see 3a).

[5] a) Napper, A. M.; Liu, H.; Waldeck, D. H. *J. Phys. Chem. B* **2001**, *105*, 7699; b) Tender, L.; Carter, M. T.; Murray, R. W. *Anal. Chem.* **1994**, *66*, 3173. c) Weber, K.; Creager, S. E. *Anal. Chem.* **1994**, *66*, 3166. d) Honeychurch, M. J. *Langmuir* **1999**, *15*, 5158.

[6] H. O. Finklea, in: *Electroanalytical Chemistry* (A.J. Bard and I. Rubinstein, eds.); Marcel Dekker: New York, **1996,** *19,* 109.

[7] W. B. Curry, M. D. Grabe, I. V. Kurnikov, S. S. Skourtis, D. N. Beratan, J. J. Regan, A. J. A. Aquino, P. Beroza, and J. N. Onuchic, *J. Bioenerg. and Biomembranes* **1995,** *27*, 285.

[8] The reported error is two standard deviations. In each case the SAM is a pyridine-terminated alkanethiol (e.g., C6py has six CH_2s) immersed in an alkanethiol diluent. See 3b for details on film composition and characterization.

[9] D. H. Murgida and P. Hildebrandt, *J. Am. Chem.Soc.* **2001**, *123*, 4062.

[10] a) L.D Zusman. *Z. Phys. Chem*. **1994,** *186,* 1; b) J. N. Onuchic, D. N. Beratan and J. J. Hopfield *J. Phys Chem.* **1986,** *90*, 3707.

[11] a) I. Muegge I, P. X. Qi, A. J. Wand, Z. T. Chu, Warshel A, *J. Phys. Chem. B.* **1997**, *101* 825; b) Y. P. Liu, M. D. Newton, *J. Phys. Chem.* **1994**, *98*, 7162.

[12] a) D. E. Khoshtariya, T. D. Dolidze, L. D. Zusman, and D. H. Waldeck *J. Phys. Chem. A* **2001**, *105*, 1818; b) M. J. Weaver, *Chem. Rev*., **1992**, *92*, 463.

[13] J. J. Wei, H. Liu, and D. H. Waldeck, unpublished results.

CHAPTER 5 THE CHARGE TRANSFER MECHANISM FOR CYTOCHROME C ADSORBED ON NANOMETER THICK FILMS: DISTINGUISHING FRICTIONAL CONTROL FROM CONFORMATIONAL GATING[‡‡]

Using nanometer thick tunneling barriers with specifically attached cytochrome c, the electron transfer rate constant was studied as a function of the SAM composition (alkane versus terthiophene), the ω-terminating group type (pyridine, imidazole, nitrile), and the solution viscosity. At large electrode-reactant separations the pyridine-terminated alkanethiols exhibit an exponential decline of the rate constant with increasing electron transfer distance. At short separations, a plateau behavior, analogous to systems involving -COOH terminal groups to which cytochrome c can be attached electrostatically, is observed. The dependence of the rate constant in the plateau region on system properties is investigated. The rate constant is insensitive to the mode of attachment to the surface, but displays a significant viscosity dependence, change with spacer composition (alkane versus terthiophene), and nature of the solvent (H_2O versus D_2O). Based on these findings and others, the conclusion is drawn that the charge-transfer rate constant at short distance is determined by polarization relaxation processes in the structure, rather than the electron tunneling probability or large-amplitude conformational rearrangement (gating). The transition in reaction mechanism with distance reflects a gradual transition between the nonadiabatic (tunneling) and adiabatic (frictional) mechanisms. This conclusion is consistent with data from a number of other sources, as well.

[‡‡] This work was published as Khoshtariya, DE.; Wei, JJ.; Liu, HY.; Yue, HJ., and Waldeck, DH., "The Charge-Transfer Mechanism for Cytochrome C Adsorbed on Nanometer Thick Films. Distinguishing Frictional Control from Conformational Gating" *J. Amer. Chem. Soc.*, **2003**, 125, 7704-7714.

5-1 INTRODUCTION

Because of their diversity and rich behavior, the kinetics and mechanism of biochemical charge-transfer processes are often difficult to identify, and many aspects of a protein's microscopic mechanism remain unclear because of the complex and inhomogeneous character of biomolecular systems. Nevertheless experimental and theoretical studies have shown that elementary electron transfer events involving redox-active proteins can be understood in the light of contemporary theoretical models for molecular charge-transfer reactions. Cytochrome c is a small, 'model', redox protein[1] with a well-known molecular structure, and numerous studies of its electron transfer rate have been performed, both homogeneous[2,3] and heterogeneous.[4,5]

A large number of studies have compared cytochrome c's electron transfer kinetics with contemporary theoretical models. The nonadiabatic (tunneling) charge transfer mechanism[6] predicts the exponential decay of the charge-transfer rate constant with the electron transfer distance R_e,

$$k_{et} \propto \exp\left[-\beta\left(R_e - R_o\right)\right] \qquad 5\text{-}1$$

where R_o is a minimal electron donor-acceptor distance and β is a decay parameter whose value depends on the intervening atomic and molecular structure.[7] The observation of an exponential distance dependence for a given reaction series provides strong evidence for the nonadiabatic (tunneling) mechanism. The exponential dependence arises from the dependence of the rate constant on the electronic coupling |H| between the electron donor and acceptor

$$k_{et} \propto |H|^2 \qquad 5\text{-}2$$

and the exponential decrease of the exchange interaction that causes $|H|$, such that

$$|H| = H^0 \exp\left[-\frac{\beta}{2}(R_e - R_o)\right] \qquad 5\text{-}3$$

where H^0 the value of $|H|$ at the minimum distance R_o. The same model predicts an activation free energy for the rate constant,

$$k_{et} \propto \exp\left[-\frac{\Delta G_a}{RT}\right] \qquad 5\text{-}4$$

that depends quadratically on the reaction free energy ΔG_o, namely

$$\Delta G_a = \frac{(\lambda - \Delta G_o)^2}{4\lambda} - |H| \qquad 5\text{-}5$$

Assuming that the reorganization free energy, λ, is constant within a reaction series, a bell-shaped dependence of $\log(k_{et})$ *vs.* ΔG_0 should be observed, at least for "homogeneous" unimolecular rate constants (for electrode processes Eqn 5-5 is approximately valid within the range of $|\Delta G_O| \leq \lambda$, *vide infra*[8]).

An alternative description of the electron transfer rate constant is required when the electronic interaction between the electron donor and electron acceptor is large enough and is referred to as the adiabatic limit. In this limit, the rate constant is no longer controlled by the magnitude of the electronic coupling, but rather by the frictional coupling between the changing charge distribution of the reactants and the polarization of the surrounding medium. This frictional coupling is most often characterized by a characteristic relaxation time of the medium τ_s or a viscosity η for the medium. Phenomenological and theoretical models, based on the Kramers theory[9], have been used to treat the reaction rate constant in this limit. When the frictional coupling to the medium is very strong the rate constant decreases as $1/\tau_s$ or $1/\eta$. Empirically a power law form is often found to describe the friction dependence of the rate constant; e.g.,

$$k_{et} \propto \eta^{-\gamma} \qquad 5\text{-}6$$

where γ is an "empirical" parameter with typical values within the range $0 < \gamma \leq 1$.[10]

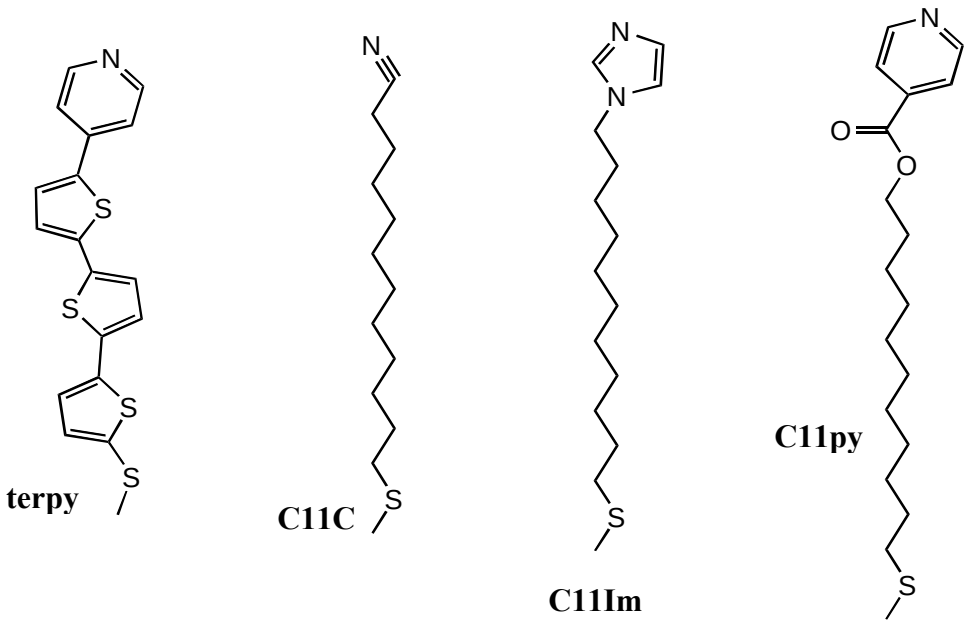

Chart 5-1 Molecular structures are shown for the different receptor-based tethering molecules.

The electron transfer kinetics of cytochrome c in "homogeneous" systems, including bimolecular reactions of the protein with natural or artificial counterparts and unimolecular reactions of an unnatural cytochrome that has low-molecular weight redox partners covalently attached, have been performed. Although these studies have provided a wealth of information and indicate biases toward one or more of the characteristic features quantified by Eqns. 5-1,5-5, or 5-6, they do not probe the dependence of the intrinsic charge-transfer mechanism on the reaction conditions. Except for a few reports (*vide infra*), these studies do not explore the possible change in the mechanism from the nonadiabatic limit to the adiabatic limit. This deficiency reflects the difficulty in varying the fundamental parameters, R_e, $|V|$, and ΔG_0 in an independent and quantifiable manner. Heterogeneous bioelectrochemical systems, in which cytochrome c or other redox proteins exchange electrons with a metal electrode by tunneling

through insulating self-assembled monolayer (SAM) films promises to allow such studies.[4,5,11] Electrochemical methods are well proven for the determination of rate constants and intrinsic mechanisms in chemical studies.[10,12]

The present work is an extension of earlier studies from this group that probes the electron transfer kinetics of cytochrome c that is linked to nanometer thick monolayer films by direct binding with the protein's heme unit.[5,11] This report presents new data on the viscosity dependence and deuterium isotope dependence of the electron transfer rate constant for the systems described earlier and presents data for new types of tethers, including a conjugated linker. In addition to these new data, a comprehensive and self-consistent analysis of the results is presented. In particular, the data show a clear change in the reaction mechanism with distance of the protein from the electrode, and the analysis compares the description by a unified charge-transfer theory with that by a conformational gating model.

5-2 EXPERIMENTAL SECTION

Reagents and Materials. Water for the experiments was purified by using a Barnstead-Nanopure system and had a resistivity of 18 MΩ cm. 1,3-Dicyclohexylcarbodiimide, or DCC, (99%) was purchased from Alfa Aesar. All mercaptoalkanes were purchased from Aldrich and used without further purification. Imidazole (99%), 6-Mercapto-1-hexanol, 11-bromo-1-undecanol (98%), 12-mercapto-1-dodecanol (98+%), 1-nonadecanol, isonicotinic acid (99%), docosanedioic acid (85%), methanolic iodine (99%), sodium bisulfite (99%), thiourea (99+%, A.C.S. reagent), K_2CO_3 (99+%, A.C.S. reagent), NaOH (97%), and $MgSO_4$ (99%) were purchased from Aldrich. 4-Pyridinecarbaldehyde and 2-bromothiophene, 4-bromopyridine Anhydrous *N*,*N*-dimethylformamide (DMF) were bought from Fluka. Absolute ethanol was

purchased from Pharmcoproducts, Inc., Dextrose ((+)-D-glucose anhydrous, 99%) was purchased from Sigma.

CytC (Sigma C 7752, from horse heart, minimum 95% based on molecular weight 12 384) was purified using a cation exchange column (CM-52, carboxymethyl-cellulose from Whatman) in a manner described previously. The purified cytochrome *c* was stored under an argon atmosphere in a freezer with dry ice until use.

The solution used in the voltammetry study was 20 mM sodium phosphate buffer solution at pH 7. The viscosity of the solutions was varied by using glucose concentrations of 0, 200 g/L, 400 g/L. The solution viscosities were measured to be 0.98 cP, 1.76 cP, and 3.88 cP respectively. The measurements were performed at room temperature with an Ubbelohde viscometer.

***Electrode Preparation*:** More details of preparation and characterization of the gold electrode can be found elsewhere. Only a brief outline of the procedure is given here. A gold wire (0.5 mm diameter, 99.99%) was cleaned by reflux in nitric acid (68-70%) at 130 °C overnight and then was washed with deionized water. The tip of the gold wire was heated and annealed in a gas flame to form a ball of about 0.06-0.12 cm^2 surface area. Chemically modified electrodes were prepared by immersion in an ethanol or THF solution that contained 1 mM of -$S(CH_2)_nOOC(C_5H_4N)$ and -$S(CH2)_{n-2}CH_3$ (the mole ratio of -$S(CH_2)_nOOC(C_5H_4N)$ to -$S(CH_2)_{n-2}CH_3$ was 1:9). The electrode remained in this solution for 1 day to form the mixed SAM. The electrode was taken out from the solution, first rinsed with absolute ethanol (or THF), then rinsed with the supporting buffer solution (20 mM phosphate buffer pH 7), and finally dried by a stream of argon gas. The electrode was characterized, as previously, [11] and then immersed in a 100 μM

cytochrome *c* solution (purged with argon gas) for 30 to 60 min in order to immobilize the cytochrome on the SAM-coated electrode. These electrodes were immediately used in voltammetry studies.

***Electrochemical Measurements*:** Electrochemical measurements were performed by using an EG&G PAR-283 potentiostat controlled by a PC computer running version 4.3 of PARC's 270 software and a GPIB board. The three-electrode cell was composed of a platinum spiral counter electrode, an Ag/AgCl (3 M NaCl) reference electrode, and the SAM-coated Au as a working electrode. The voltammetry measurements were performed in 20 mM phosphate buffer solution (pH of 7.0) at different viscosities under an argon atmosphere. To study the isotope effects, the SAM modified gold electrodes were incubated in cytochrome c D_2O buffer solution to immobilize protein, then measured in both D_2O and H_2O buffer solution.

Material Preparation: Pyridine, imidazole, nitrile terminated disulfide derivatives, 2-(4-pyridine-5-terthiophene-thiol), nonadecanethiol and heneicosanethiol were prepared according to literature procedures.[11,13] ^{1}H NMR spectra were obtained at 300 MHz and the coupling constant is reported in Hz.

1. Preparation of disulfides.

Bis(6-hydroxyhexanyl) disulfide: 6-Mercapto-1-hexanol (6.0 g, 44.696 mmol) was dissolved in 10 mL methanol and titrated with 0.5 M methanolic iodine until the reaction turned from colorless to a persistent yellow. The reaction was quenched with 10% sodium bisulfite to a colorless solution. The resulting mixture was dissolved in distilled water and extracted with CH_2Cl_2, and the solvent was removed under vacuum. Purification of the resulting crude disulfide

was performed by flash chromatography (CH_3Cl) to afford the disulfide (5.35 g) as a white solid in 90% yield. ^{1}H NMR (300 MHz) $CDCl_3$: δ 3.649 (t, J= 6.435, 4H); 2.690 (t, J= 7.275, 4H); 1.703 (m, 4H); 1.584 (m, 4H); 1.510-1.375 (m, 8H).

Bis(11-hydroxyundecyl) disulfide: ^{1}H NMR (300 MHz) $CDCl_3$: δ 3.651 (q, J= 6.18, 4H); 2.689 (t, J= 7.34, 4H); 1.679 (m, 4H); 1.579 (m, 4H), 1.379-1.290 (broad, 28 H).

Bis(16-hydroxyhexadecyl)disulfide: 16-Mercapto-hexadecanol was prepared by reducing 16-mercaptohexadecanoic acid in ethyl ether using $LiAlH_4$. Diluted NaOH solution was used to quench the reaction. The resulting solution was dissolved in 0.2 M HCl and extracted with CH_2Cl_2. The solvent was removed under vacuum. Purification of the resulting crude 16-mercapto-hexadecanol was performed by flash chromatography (CH_3Cl). ^{1}H NMR (300 MHz) $CDCl_3$: δ 3.646 (t,J= 6.615, 2H); 2.527 (q, J= 7.34, 2H); 1.603 (m, 6H); 1.327 (broad, 23H); Bis(16-hydroxyhexadecyl)disulfide is insoluble in common solvents, such as CH_2Cl_2, and NMR data were not obtained.

Bis(20-hydroxyeicosyl)disulfide and *Bis(22-hydroxydocosyl)disulfide* were prepared through the same procedures as preparation of *Bis(16-hydroxyhexadecyldisulfide).*

2. Preparation of pyridine derivatives.

Bis[6-((pyridinylcarbonyl)oxy)hexanyl]disulfide: 1,3-dicyclohexylcarbodiimide (DCC) (4.13 g, 20.02 mmol) was added to 20 mL of dichloromethane solution of bis(6-hydroxyhexanyl) disulfide (2.42 g, 9.10 mmol), isonicotic acid (2.24 g, 18.20 mmol) and 4-dimethylaminopyridine (0.22 g, 1.82 mmol) at 0 ^{o}C. After one hour, the solution was allowed to warm to room temperature and stirring was continued for 4 days. After removal of the precipitated dicyclohexylurea (DCU) by filtration, the solvent was removed under reduced pressure to yield a

crude solid. The solid was recrystallized with ethanol and chromatographed on silica gel (60-200 mesh) with ethyl acetate. Evaporation of the solvent yielded the disulfide as 3.45 g of a white solid. ^{1}H NMR (300 MHz) $CDCl_3$: δ 8.789 (d, J= 5.97, 4H); 7.849 (d, J= 5.97, 4H); 4.362 (t, J= 6.615, 4H); 2.695 (t, J= 7.215, 4H); 1.802 (m, 4H), 1.723 (m, 4H); 1.488-1.453 (m, 8H).

Bis[11-((4-methyl-4-pyridinylcarbony)oxy)undecyl]disulfide, diiodides: Bis[11-((4-pyridinylcarbonyl)oxy)undecyl]disulfide was refluxed with an excess of iodomethane in ethanol for 24 hours under nitrogen. The solution was cooled to room temperature and the precipitate that formed was filtered and recrystallized in ethanol and acetone three times. A brown solid was obtained. ^{1}H NMR (300 MHz) $CDCl_3$: δ 9.501 (d, J= 6.54, 4H); 8.515 (d, J= 6.46, 4H); 4.834 (s, 6H); 4.449 (t, J= 6.614, 4H); 2.694 (t, J= 7.301, 4H); 1.818 (m, 4H); 1.678 (m, 8H); 1.476-1.216 (broad, 24H).

Bis[11-((4-pyridinylcarbonyl)oxy)undecyl]disulfide: ^{1}H NMR (300 MHz) $CDCl_3$: δ 8.810 (s, 4H); 7.901(d, J= 5.73, 4H); 4.367 (t, J= 6.63, 4H); 2.684 (t, J=7.32, 4H); 1.789 (m, 4H); 1.675 (m, 4H); 1.43-1.29 (broad, 28H). EI-HRMS: Calcd. 616.3385 ($C_{34}H_{52}N_2O_4S_2$), found 616.3369.

Bis[16-((4-pyridinylcarbony)oxy)hexadecyl]disulfide: ^{1}H NMR (300 MHz) $CDCl_3$: δ 8.889 (s, 4H); 7.869 (d, J= 5.46, 4H); 4.359 (t, J= 6.705, 4H); 2.683 (t, J= 7.36, 4H); 1.781 (m, 8H); 1.673 (m, 4H); 1.43-1.29 (broad, 44H). EI-HRMS: Calcd. 756.4896 ($C_{44}H_{72}N_2O_4S_2$), Found 756.4934.

Bis[22-((4-pyridinylcarbony)oxy)docosyl)disulfide: ^{1}H NMR (300 MHz) $CDCl_3$: δ 8.789 (d, J=5.52, 4H); 7.857 (d, J= 5.76, 4H); 4.358 (t, J= 6.66, 4H); 2.685 (t, J= 7.37, 4H); 1.784 (m, 4H); 1.694 (m, 4H); 1.26 (broad, 72H).

2-(4-pyridine-5-terthiophene-thiol): ^{1}H NMR (300 MHz) $CDCl_3$: δ 8.593-8.455 (m, 2H); 7.43 (d, J=3.87, 2H); 7.321-7.305 (m, 2H); 7.196-7.180 (m, 2H); 7.153-7.126 (m, 1H); 7.083-7.016 (m, 2H), $C_{17}H_{11}NS_4$.

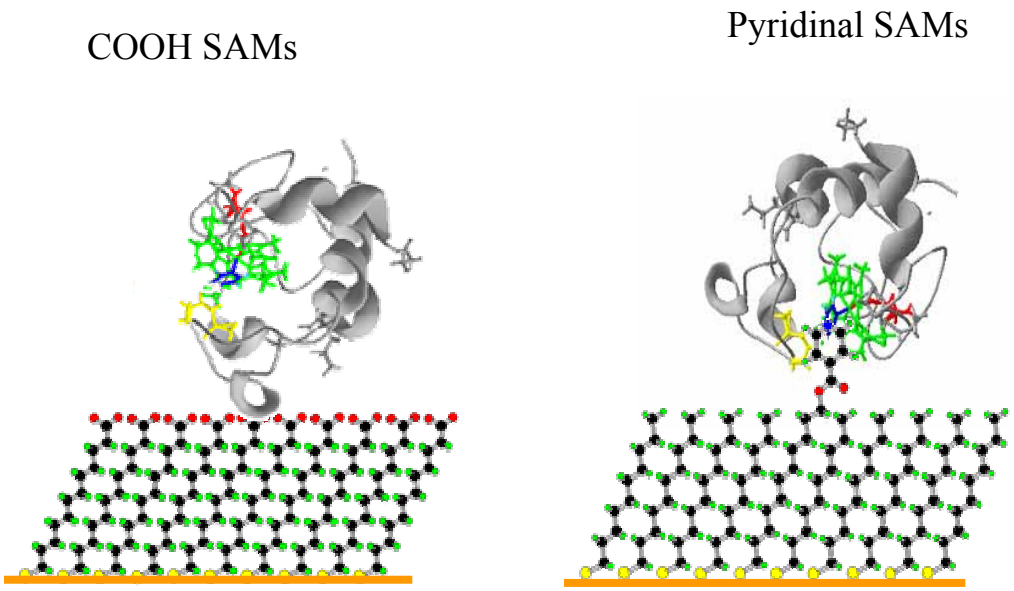

Figure 5- 1 This schematic drawing shows the adsorption of the cytochrome c to the surface of self-assembled monolayer films through two different binding motifs: A) electrostatic attraction between carboxylate groups on the SAM and the protein's positive lysine groups and B) coordination of a receptor group (pyridine) in the SAM with the heme of the protein.

5-3 RESULTS

Two different strategies have been used to adsorb cytochrome c onto the surface of nanometer thick insulating films on metal electrodes (see Figure 5- 1). The first method uses carboxylate terminated SAMs that bind the protein electrostatically, since it is positively charged (panel A). It is believed that the ionized lysines on the surface of the cytochrome interact with the carboxylate groups. The second method uses SAMs that are terminated with nitrogen containing head groups that can bind to the heme unit of the protein (panel B). The first method has the advantage of providing a better mimic of the in vivo environment of cytochrome c and the disadvantage of not controlling the position of the cytochrome with respect to the electrode in a well defined manner. The second method provides better control of the cytochrome c orientation on the surface, but requires the receptor group on the SAM to displace an axial ligand from the heme, thereby causing partial unfolding. The second method is exploited here, but comparisons are drawn with the work of others using the first method.

The standard rate constants for electron transfer between the SAM coated Au electrode and the attached cytochrome c were determined through the evaluation of cyclic voltammetry data, a standard procedure. Representative Voltammograms for these systems have been reported.[5,11] In brief, the dependence of the observed peak potential for the faradaic current is measured as function of the voltage scan rate.[14] Quantitative analysis of this dependence provides the standard heterogeneous electron transfer rate constant, which is the heterogeneous electron transfer rate constant at a reaction free energy of zero. Plots of the peak position as a function of scan rate have been reported for the alkylpyridine systems, already. This method is limited in its time resolution by the RC characteristics of the electrode. With the small diameter (1 to 2 mm) gold ball electrodes used in this work, rate constants up to about 10,000 Hz can be

measured. The standard heterogeneous rate constants k^0_{et} for the different systems are summarized in Table 5-1 through Table 5-3.

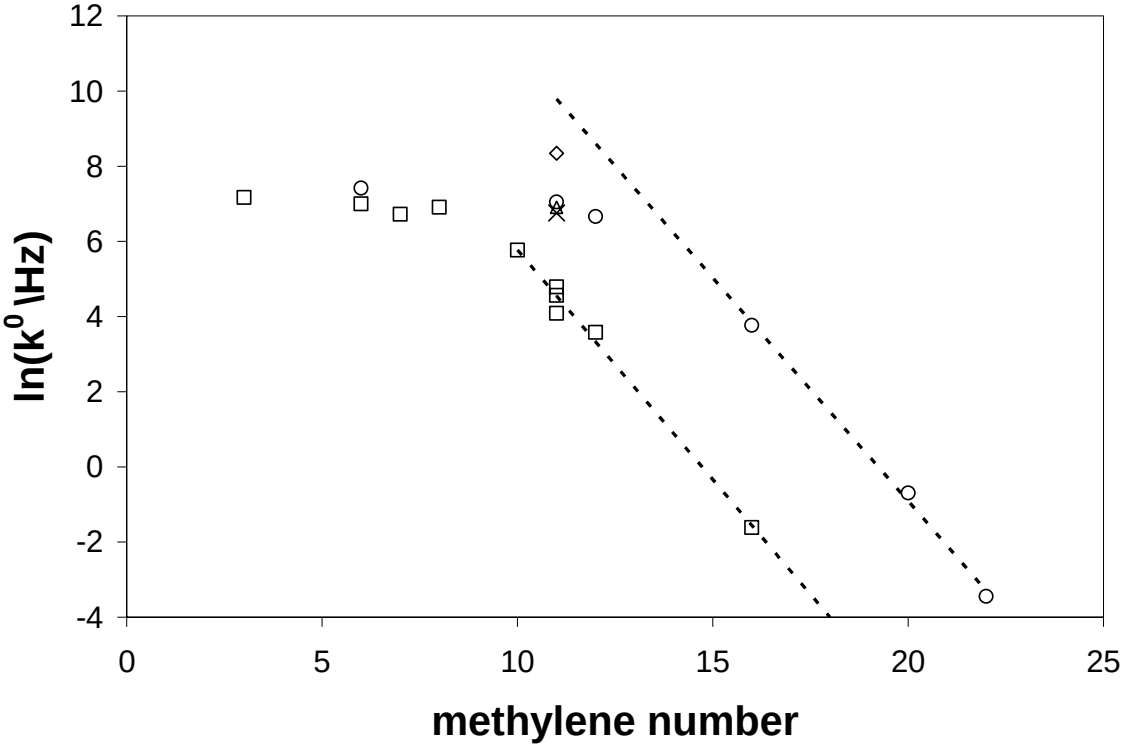

Figure 5- 2 This diagram plots the apparent standard electron transfer rate constants for the different systems. The data for systems bound through coordination with the heme are represented by circles for pyridine, X for imidazole, triangle for CN, and diamond for terthiophene. The squares are the data for electrostatic adsorption on COOH. The dashed lines are fits to the nonadiabatic model at large layer thickness.

In Figure 5- 2, the measured heterogeneous rate constant is plotted as a function of the methylene number of the tethering group for the different SAMs studied here and for the -COOH terminated SAMs of Niki. At large electrode-reactant separations, the pyridine terminated alkanes and the COOH terminated SAMs display an exponential dependence on the charge-transfer distance, Eqns 1 and 3 with a decay constant of about one per methylene. This decay constant is similar to that found in other tunneling studies with saturated hydrocarbons. This behavior at large distance is a signature for nonadiabatic electron transfer. Both data sets show a

plateau region at short donor-acceptor separations, however the plateau region spans to larger film thicknesses for the pyridinyl systems. Although the behavior is qualitatively similar for these two systems, the maximum rate constants differ by about a factor of two and the rate constants in the pyridine-bound systems are consistently higher than those for the electrostatically bound system.

The figure also shows new data on the cytochrome c adsorbed through three other tethers in the region of the plateau. In two of these systems the receptor group has been modified from a pyridine to an imidazole and a nitrile unit and contains a C11 tether. These head groups cause a quite different apparent redox potential but have a minor effect on the standard electron transfer rate constant. The shift in the apparent redox potential is consistent with solution studies of cytochrome c's redox potential shift when it binds small ligands. In particular, the immobilized cytochrome c studies give -172 mV for the pyridine head group, whereas a cytochrome c solution with pyridine added has a -294 mV shift.[1a,15a] The imidazole tether causes an apparent redox potential of -346 mV and the nitrile causes -415 mV, which should be compared to -426 mV and -665 mV for cytochrome c solutions containing imidazole and cyanide, respectively.[1a,15b,c] The addition of an exogenous ligand to the solution may cause a conformational change in the protein that might contribute to the redox potential shift, or it may ligate to the heme and cause a shift in the redox potential. A recent study by Fan etal.[15a] distinguishes these two contributions for the case of pyridine and finds that the heme bound pyridine has a redox potential of -161 mV, and that the larger negative redox potential of -294 mV should be associated with a non-native protein conformation. Their findings corroborate the view of cytochrome c adsorption that is illustrated in Fig 1, in which the cytochrome c binds to the pyridine in a native-like conformation rather than a denatured form. Despite these large

changes in the apparent redox potentials, the standard electron transfer rate constants for the three C11 systems lie within 10% of each other (see Table 5-1). The other tether is a terthiophene oligomer with a pyridinyl head unit. It displays an apparent redox potential that is similar to that found for the alkylpyridine systems but the rate constant shows a factor of four increase (see Table 5-1). For these systems the head groups change the apparent redox potential and the nature of the linker changes the observed rate constants.

Table 5-1 Rate constant data for cytochrome c immobilized on different mixed SAMs.[a]

System	k^0 (Hz)	E^0 (mV)	#Trials	System	k^0 (Hz)	E^0 (mV)	#Trials
C6py/C5	1580	-175	6	C11CN/C8	1000	-415	2
C11py/C10	1150	-168	14	C11Im/C8	860	-346	4
C12py/C11	785	-172	4	Terpy/C7	4200	-188	2
C16py/C15	52	-158	12				
C20py/C19	0.50	-156	3				
C22py/C20	0.032	-145	2				

a) In each case the diluent SAM is an alkanethiol and the measurement is made in aqueous buffer. The data are the average of experimental results obtained on different days with different electrode preparations.

Table 5-2. Rate constants of immobilized cytochrome c for different solution viscosities.[a]

	η=0.98 cP		η=1.76 cP		η=3.88 cP	
System	#Runs	k^0 (Hz)	#Runs	k^0 (Hz)	#Runs	k^0 (Hz)
C6py/C5	3	1512	4	1050	3	670
C11py/C10	2	1155	5	990	4	780
C16py/C15	2	60	2	60	2	61

a) Data are only obtained from the viscosity measurement, which may be not identical to the average data of all measurements, provided Table 5-1.

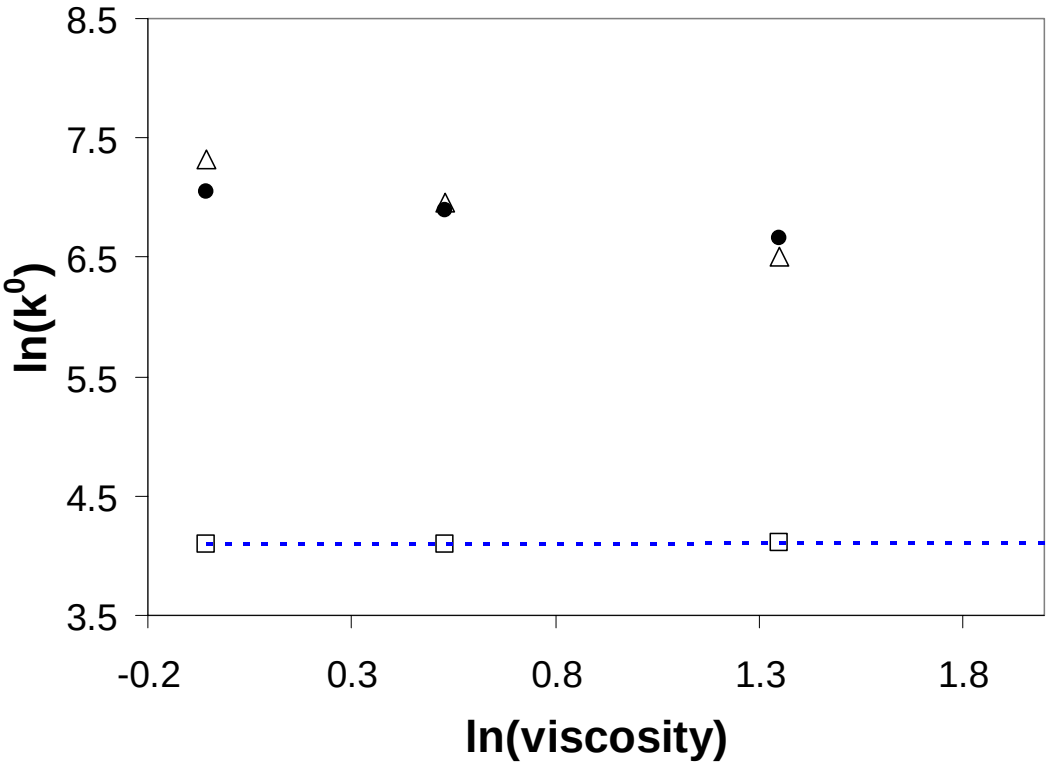

Figure 5- 3 The viscosity dependences of the observed electron transfer rate constant are shown for three different alkanethiol chain lengths: the triangles are C6, the circles are C11, and the squares are C16. The dashed line has zero slope.

Figure 5- 3 presents the dependence of k_{et}^{0} on the solution viscosity, varied by addition of glucose, for the C6Py, C11Py and C16Py SAM systems. Fits of the data to the power law form of Eqn 6 gives γ values of 0.58 for C6Py, 0.28 for C11Py, and ≈ 0 for C16Py. The dependence on the viscosity correlates with the chain length of the alkane linker. The viscosity dependence is seen in the plateau region of the distance dependence, whereas the rate constant is independent of the viscosity in the large distance regime. The viscosity independence of the rate constant for the C16Py system is consistent with the nonadiabatic mechanism being operative in this regime and demonstrates that the experimental procedure for changing the viscosity is not causing some other change in the protein or its adsorbed state. The "maximal" value of $\gamma \approx 0.58$ found for the

plateau region is typical for viscosity dependent protein processes and small molecule reactions.[16] Although the rate constants for C11Py and C6Py are very similar, the viscosity dependence for the C6Py system is significantly steeper than that found for the C11Py system. The observation of a viscosity dependence for the electron transfer rate constant was observed previously for cytochrome c adsorbed electrostatically to carboxylic-acid terminated films[4d] and for the $Fe(CN)_6^{3-/4-}$ couple in contact with very thin alkane based monolayer films.[17] Clearly a viscosity linked process becomes important in the plateau region of the data in Figure 5- 2 and demonstrates a change in the mechanism of the electron transfer reaction with distance.[18]

Table 5-3 D_2O dependence of the rate constant data for immobilized cytochrome c.[a]

C11py/C10			C16py/C15		
Cell	Incubant	k^0 (Hz)	Cell	Incubant	k^0 (Hz)
H_2O	H_2O	1140	H_2O	H_2O	58
D_2O	H_2O	1100	D_2O	H_2O	
H_2O	D_2O	890	H_2O	D_2O	
D_2O	D_2O	879	D_2O	D_2O	55

a) Data are only obtained from the isotopic measurements and may not be identical to the average data of all measurements, provided in Table 5-1.

Table 5-3 provides data that displays a shift in the electron transfer rate constant for cytochrome c when it has been exposed to heavy water.[19] These experiments show that long time exposure (*ca* 30 minutes or more) of the protein to D_2O changes the observed electron transfer rate constant in the plateau region of Figure 5- 2. If a C11Py/C10 coated electrode is placed in a D_2O buffer solution containing cytochrome c and allowed to incubate to form the adsorbed state of the protein, the measured standard electron transfer rate constant decreases by 30%. This decrease is independent of whether the measurement in the electrochemical cell occurs with H_2O buffer or D_2O buffer. The typical time that the electrode is in the electrochemical cell is less than ten minutes. These results suggest that water present in the

protein acts to modulate the electron transfer rate constant in the plateau region. In contrast the C16Py/C15 coated electrodes do not display a dependence on D_2O versus H_2O and demonstrate that the modification of the 'normal' buffer solution with D_2O does not impact the adsorbed state of the protein.

The results that are presented and summarized here cannot be explained in terms of the nonadiabatic electron transfer model (Eqns 1 and 2) over the whole range of systems. For methylene chains longer than dodecane, the standard electron transfer rate constant declines exponentially with increasing alkane chain length, does not display a viscosity dependence, and does not change with the use of D_2O buffer. These observations are consistent with the nonadiabatic electron transfer mechanism. Further, they demonstrate that the method for changing the viscosity and the use of D_2O do not change the adsorption state of the protein. Although the electron transfer rate constant is well described by the nonadiabatic model at large distances, the reaction mechanism must change for shorter distances because the rate constant is no longer decaying exponentially with distance, displays a viscosity dependence, and depends on the use of D_2O versus H_2O. The nature of the reaction mechanism at short distances and the thickness at which the mechanism changes are discussed below.

5-4 DISCUSSION

Tunneling mechanism at large n and the role of binding mode. From Figure 5- 2 one can see that at large electrode-cytochrome c separations the data for SAM films that are terminated with pyridinyl moieties show a trend similar to that of the -COOH terminated films, but the onset of the exponential decline (set by Eqns 5-1 and 5-2) occurs at larger film thicknesses (*ca.* 12 methylenes). The steepness of the decline is similar for the two systems, 1.19 per CH_2 for the

pyridinal SAMs and 1.22 per CH_2 for the COOH SAMs, and agrees with the fall off found for tunneling through saturated hydrocarbons. This shift can be understood by considering the different binding modes of cytochrome on the two film types. The COOH terminated groups electrostatically bind the cytochrome by its lysine groups and the pyridine-terminated alkanethiols bind through ligation with the heme group.[20] Inspection of Figure 5- 2 shows that a shift of the COOH rate constants by about four methylene groups to the right would cause a good correspondence between the two data sets.

This correspondence can be quantified more fully by estimating the physical distance between the electrode surface and the heme unit of the protein. Consider the pyridine unit to coordinate at the heme and assume it contributes little to the effective charge-transfer distance because of its π-conjugated nature.[21] The "effective" donor-acceptor separation d between the metal surface and the heme, upon the variation of the SAM thickness, can be estimated according to

$$d = 1.90 + 1.12\ n\ (Å) \qquad 5\text{-}7$$

where n is the number of methylenes in the alkane chain and 1.90 Å accounts for the S atom radius of the thiol.[22] A similar analysis for cytochrome c adsorbed on the COOH terminated films requires that the tunneling pathway from the outer layer of the SAM through the protein exterior and into the heme unit be identified. Because of the possibility that the cytochrome can be oriented in a number of different ways on the surface, one should more formally consider a distance distribution. Recent work by Niki[23] implies that the electron tunneling occurs mostly through the lysine 13 which lies near the heme unit. Using the cytochrome c crystal structure, one can estimate a physical, 'through-space', distance of 5.8 A from the lysine to the heme and a 'through-bond' distance of about 20 A. These considerations of the actual physical distance

between the electrode and the heme lead to a much better correspondence between the two data sets. Figure 5- 5 presents the dependence of heterogeneous rate constant for the pyridinyl systems as a function of the charge-transfer distance, estimated through Eqn 5-7, and for the COOH systems with a 5 Å shift to account for the extra tunneling distance from the SAM edge through the protein matrix.

Friction-control vs. conformational gating. Previous workers[4d,23] have explained the distance independent behavior of the charge-transfer rate constant in the plateau region, for the case of -COOH terminated SAMs, as resulting from a change in the rate-determining step. In particular, the charge transfer occurs by the nonadiabatic (tunneling) mechanism and is gated by a conformational rearrangement to a precursor state that is electroactive. This mechanism is similar to the conformationally-gated mechanism that has been used to describe electron transfer processes involving a range of processes with cytochrome c's.[3b24] For the COOH terminated SAMs this may correspond to the diffusive tumbling of the cytochrome c on the surface to an orientation in which the protein's heme is closest to the surface and electron transfer occurs rapidly. Such a scenario is not consistent with the data for the pyridine terminated chains, which show a similar distance dependence but do not involve reorientation of the protein on the SAM surface.

A number of results do not support simple conformational gating of the heterogeneous electron transfer on SAM coated Au electrodes. First, the electrochemical data, ac impedance and cyclic voltammetry, indicate a simple charge-transfer step. For example, the peak potential's shift with voltage scan rate and symmetry of the oxidation and reduction waves suggest a simple electrochemical reaction, rather than a mechanism involving a pre-equilibrium. Second, the observation of similar limiting values of rate constants for the different monolayer films, which

have two very different binding modes of cytochrome c, suggests that the electron transfer is not preceded by the large-scale protein-SAM structural rearrangement (conformationally-gated). Third, the dependence of the electron transfer rate constant on the amount of D_2O in the adsorbed protein, rather than D_2O in the solution, for the pyridine system is not consistent with large scale motion of the protein on the surface of the film. Fourth, the larger rate constant that is found for the conjugated terthiophene tether cannot be explained by a conformational gating mechanism. These observations indicate that conformational gating is not controlling the electron transfer rate constant for the pyridine terminated SAMs, but it does not discount this mechanism for the COOH terminated SAMs nor does it discount small amplitude conformational changes that may be linked to the electron transfer coordinate.

In contrast, an adiabatic charge-transfer mechanism for the charge transfer kinetics in the plateau region is consistent with the findings. In particular, the viscosity dependence of the rate and the D_2O effects can be understood through consideration of frictional coupling in the adiabatic mechanism, whereas the higher electron transfer rate for the conjugated linker can be rationalized through the effect of the electronic coupling on the activation barrier for the reaction (Eqn 5-5). Below, comparisons of electron transfer rates in many different cytochrome c systems as a function of free energy are presented and show a Marcus bell-shaped behavior. The electrochemical rate data appear to follow this Marcus free energy dependence. This observation can be understood by using the adiabatic charge transfer mechanism in the plateau region, but not by consideration of a conformationally gated electron transfer.[1a,3a,25] Comprehensive models that account for the transition between the nonadiabatic and adiabatic limits are available, so it is interesting to compare these models with the data and see if reasonable parameter values are

obtained. Before drawing these comparisons however, the electrochemical data is compared with other literature data on cytochrome c in homogeneous solutions.

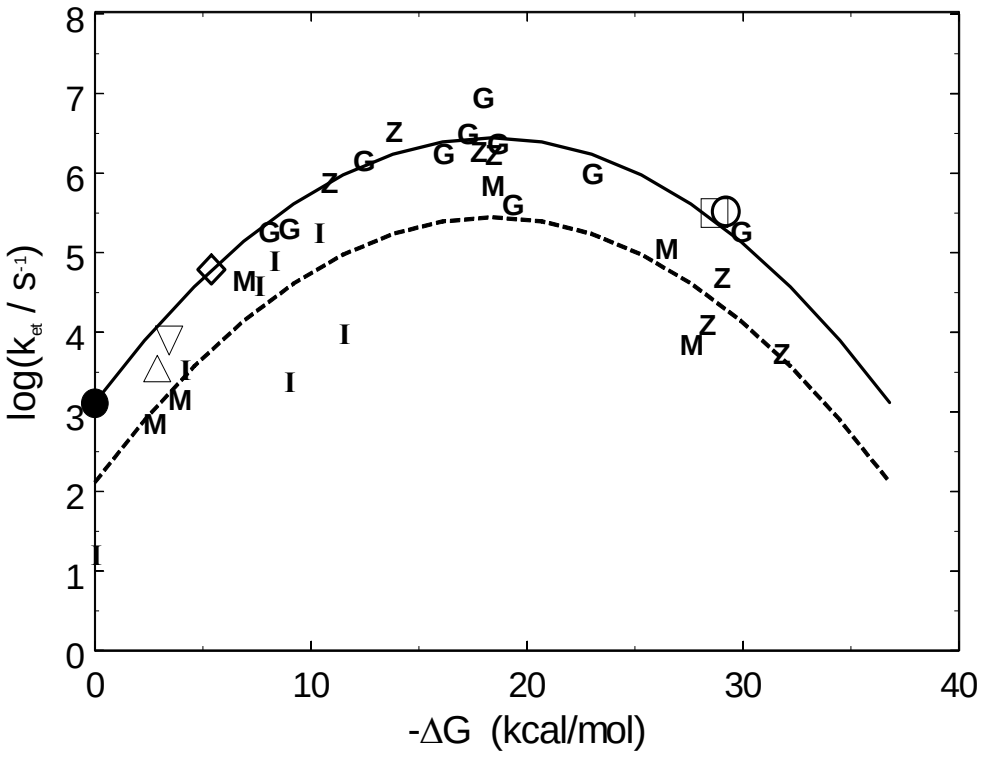

Figure 5- 4 This Marcus plot shows the free energy dependence of cytochrome c's electron transfer rate constant from a number of different studies, mostly homogeneous solution -the data are from Gray *et al.* [G][2d] for Ru-modified cytochrome c; Zhou *et al.* [2b][Z] for cytochrome c/uroporphyrin complexes; McLendon[3a] for interprotein system cytochrome c/cytochrome b_5 [M]; and Isied et al[2e] for Ru- modified cytochrome c [I]. The open symbols ([◊[3c]], [▽[3f]], [□[3b]], [Δ[3d]], [○[3e]]) correspond to rate constants that exhibit a dependence on the external solution viscosity. The filled circle shows the electrochemical electron transfer rate at short distances (plateau region), which also displays a viscosity dependence.[4d] The solid curve shows the free energy dependence expected from the Marcus model, and the dashed curve is the same model shifted down by a factor of ten.

Comparison of homogeneous and electrochemical kinetics. Figure 5- 4 plots electron transfer rate constants as a function of ΔG_0 for many different systems involving cytochrome c (including the "limiting" electrochemical value, k_{el}^0). These data include "unimolecular" systems, in which a redox center is covalently attached to the cytochrome c, and bimolecular

systems. Because they have a well-defined metal-to-metal separation distance, the unimolecular systems can be compared with the electrochemical data in more detail (*vide infra*). The rate constants fall surprisingly well on a bell-shaped curve that is generated by fitting the rate data for a series of ruthenium-modified cytochrome c's. The kinetic data that are plotted with open symbols (cytochrome c/P870 in Rb. Sphaerodis,[3f] cytochrome c/Ru(II)bpy,[3b] cytochrome c/radical cation in cytochrome c peroxidase,[3c] zinc cytochrome c/bean plastocyanin,[3d] and cytochrome c/fern plastocyanin[e] complexes) exhibit a dependence on the external solution viscosity. The electrochemical rate constant (filled circle) measured at $\Delta G_0=0$ shows a thousand-fold reduction from the maximum rate constant but lies on the same curve. The observed free energy dependence of the rate data and the viscosity-sensitive behavior for some of them (Figure 5- 4) indicate that the electron transfer belongs either to the totally adiabatic (friction controlled), or, at least, to the intermediate (or mixed, *vide infra*) kinetic regimes, rather than corresponding to a conformationally-gated mechanism.[25d]

The data in Figure 5- 4 and the general correspondence with the reaction free energy reflects the importance of the activation free energy on the reaction rate constant. The large scatter in the rate data is to be expected since the data correspond to cytochrome c in such different environments. The peak of the curve corresponds to the reaction free energy magnitude that matches the reorganization energy so that the reaction rate is at a maximum. The dashed line in the figure was obtained by shifting the solid curve down by an order of magnitude. The data show that the free energy and reorganization energy determine the rate constant to within an order of magnitude or so. These data give a reorganization energy for the cytochrome c of 0.8 eV. Although the reorganization energy depends on both partners in a redox reaction, these data suggest that the protein dominates the contribution and is fairly consistent between systems. For

the electrochemical studies, the kinetic data probe the reorganization energy through the dependence of k_{et} on ΔG_0 (*i.e.* the overpotential $e\xi$) by way of Eqn 8,

$$k_{et} \propto \int_{-\infty}^{\infty} f(\varepsilon) \ \exp\left[-\frac{\left(e\xi \ + \ \varepsilon_F - \varepsilon \ \pm \ \lambda\right)^2}{4\lambda \ \ RT} \right] d\varepsilon \qquad 5\text{-}8$$

where $f(\varepsilon)$ is the Fermi-Dirac distribution function and ε_F is the Fermi energy. When $|\Delta G_0| \leq \lambda$, the electrochemical data coincides with the solid curve in Figure 5- 4.[26a]

A number of experimental and theoretical studies[26,27] report the reorganization energy of cytochrome c and they range in value from 0.8 eV to 0.4eV for the protein in solution. What portion reflects an intrinsic protein component and what portion reflects the environment or redox partner has been addressed through theoretical studies. These studies find that the inner-sphere (heme) contribution to the reorganization energy is about 0.1 eV, the protein's 'outer sphere' (interior) contribution is about 0.45 eV, and the solvent's contribution is about 0.25 eV. The reasonable characterization of the rate data with a single reorganization energy and the theoretical studies imply that the reorganization energy, although the solvent affects it, is primarily determined by the protein environment.

A unified model for the electron transfer: Theoretical work[28] that accounts for both the tunneling (distance-controlled, Eqn 5-1) and friction controlled (viscosity dependent, Eqn 5-6) charge-transfer mechanisms and a gradual turnover between them are available. Adapting the unified expression for the unimolecular rate constant to an electrode process at ΔG_0, one finds

$$k_{et}^{o} = \frac{|H|^2}{\hbar} \frac{\rho_m}{1+g} \sqrt{\frac{\pi^3 RT}{\lambda_o}} \exp\left(-\Delta G_a \big/ RT \right) \qquad 5\text{-}9$$

in which ρ_m is the density of electronic states in the electrode, and the adiabaticity parameter g is given by

$$g = \frac{\pi^3 \, RT \, |H|^2 \, \rho_m \, \tau_{eff}}{\hbar \, \lambda_o} \qquad 5\text{-}10$$

g acts as a control parameter; the reaction mechanism is nonadiabatic when g<<1, yielding the equation

$$k_{NA}^o = \frac{|H|^2}{\hbar} \rho_m \sqrt{\frac{\pi^3 RT}{\lambda_o}} \exp\left(-\Delta G_a / RT\right) \qquad 5\text{-}11$$

For long range electron transfer in biological systems, the weak coupling or nonadiabatic regime, in which the process is viewed as a tunneling ("quantum friction") mechanism, is used for both homogeneous and heterogeneous electron transfer reactions. The mechanism is adiabatic when g>>1, yielding the expression

$$k_A^o = \frac{1}{\tau_{eff}} \sqrt{\frac{\lambda_o}{\pi^3 RT}} \exp\left(-\Delta G_a / RT\right) \qquad 5\text{-}12$$

where the characteristic time τ_{eff} is related to relaxation processes of the solvent molecules, protein interior, etc. In the approximation of a dielectric continuum and a Debye-type dielectric response, one finds that

$$\tau_{eff} \approx \tau_L = \left(\frac{\varepsilon_\infty}{\varepsilon_s}\right) \frac{3 \eta V_m}{R T} \qquad 5\text{-}13$$

where τ_L is the longitudinal relaxation time of the solvent polarization and η is the solvent shear viscosity.[28a] The other parameters are the molar volume V_m, the static dielectric constant ε_S, and the high frequency dielectric constant ε_∞. For the case of more complex environments τ_{eff} might be associated with some conformational or molecular rearrangement that is coupled to the

electron transfer. The strong coupling, or adiabatic regime, is often used to describe short-range electron transfer and is viewed as solvent controlled (overdamped) motion in a single electronic state (sometimes called the "friction mechanism"). The experimental signature for electron transfer in this regime is a friction (or viscosity) dependent rate constant, often characterized by the power law form, Eqn 5-6, as mentioned in the introductory section. To summarize, the nonadiabatic electron transfer mechanism displays an exponential distance dependence and viscosity independence, whereas the adiabatic mechanism displays a viscosity dependence but no distance dependence.

Eqn 5-10 reveals that the electron transfer mechanism depends on the value of $|V|^2$ compared to the other parameters τ_{eff} and λ_o. Recent work studying the electron exchange of the $Fe(CN)_6^{3-/4-}$ redox couple with alkanethiol coated gold electrodes observed the transition from the adiabatic to nonadiabatic regime with the increasing thickness of the electron tunneling barrier. For this redox couple the transition between the nonadiabatic and adiabatic mechanisms occurred at an electron exchange distance of *ca* 8-9 Å (distance for g=1) and a relaxation time of about 50 ps in an 11 cP aqueous electrolyte solution; of course, the actual value depends on the particulars of the system under study. For electron transfer processes in highly structured media with long relaxation times τ_{eff} and small reorganization energies λ_o, *e.g.* a protein, the transition from the adiabatic regime to the nonadiabatic regime should occur at much smaller values of |H|, which may correspond to relatively long distances.

The distance-dependence of the electron transfer rate constant for cytochrome c can be quantitatively compared to Eqn 5-9. In order to perform the analysis for a wider range of data (the unimolecular data of Gray and the electrochemical data), the observed electron transfer rate constants were converted to their maximum (optimal) values k_{max} by rearrangement of Eqn 5-9,

$$k_{\max} \equiv k_{et}^{o} \exp\left(\Delta G_a / RT\right) = \frac{|H|^2}{\hbar} \frac{\rho_m}{1+g} \sqrt{\frac{\pi^3 RT}{\lambda_o}} \qquad 5\text{-}14$$

This transformation removes the activation barrier from the considerations and allows the dynamical part of the rate constant to be studied. This procedure requires accurate knowledge of the activation energy, however. The data in Figure 5- 5 show this transformation if the same reorganization energy 0.8 eV, as suggested by the Figure 5- 4, is used for the three data sets.

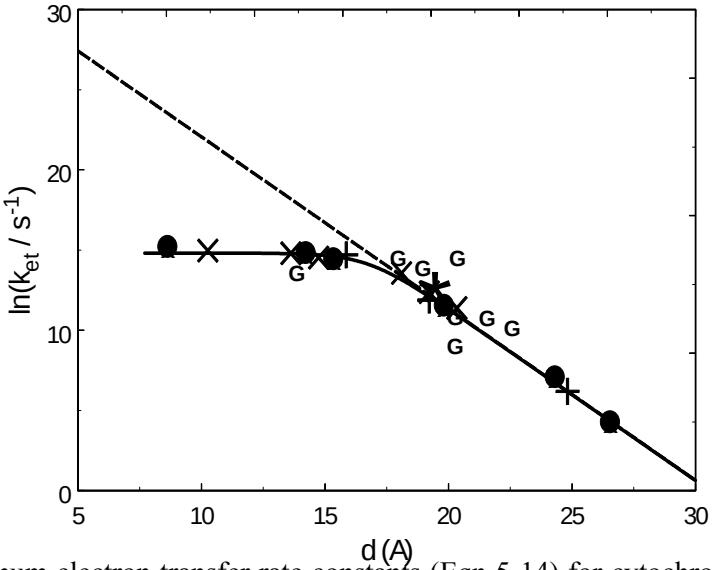

Figure 5- 5 The maximum electron transfer rate constants (Eqn 5-14) for cytochrome c from Figure 5- 2 are plotted as a function of the electron transfer distance. A constant distance of 5 Å has been added to the electrochemical data on the carboxylic acid terminated films (x -Niki *et al.*[4c,d]; + -Bowden *et al.*[4a,b]; * this work) so that they coincide with the data on pyridine terminated layers (●) and the data of Gray *et al.* (G).[2c] The solid black curves are fits to Eqn 5-14, and the dashed line shows the predicted nonadiabatic electron transfer rate constant at shorter distance.

Given this assumption about the reorganization energy, Figure 5- 5 plots the distance dependence of k_{max} for the two electrochemical systems and the homogeneous studies as a function of the distance between the redox active heme of the cytochrome and the electron donor, gold electrode and ruthenium moiety. The •'s correspond to the rate constants of the pyridine

terminated SAMs and the G's correspond to the unimolecular rate constant data of Gray. The data for the COOH terminated SAMs (x,*,+) did not show a good correspondence with the other two data sets unless the electron transfer distance was increased by 5 Å, as discussed with regard to Eqn 5-7. This shift, to account for the extra tunneling distance, provides excellent correspondence among the three data sets. The solid black curve in Figure 5- 5 shows a fit to Eqn 5-14, which describes the transition between electron transfer regimes. The dashed line corresponds to an extrapolation of the nonadiabatic rate constant back toward short distances. Although the good correspondence between Eqn 5-14 and the data is compelling, it is important to assess the values of the parameters in the model and their reasonableness.

Fitting of the rate constant data in the different regimes allows the adiabaticity parameter g to be evaluated. By fitting the electron transfer rate constants at large distances to the nonadiabatic model, one can define the parameters that describe the nonadiabatic rate. Using a reorganization energy of 0.8 eV and a density of states for the Au electrode[8b] of 0.28 eV^{-1}, one finds an electronic coupling between the Au electrode and cytochrome c of 0.17cm^{-1} at 17 Å and a β of 1.07/Å. These parameters can then be used to predict what the nonadiabatic rate constant would be at shorter distances. In the plateau region of the kinetics, the fit of the data to the adiabatic model requires that the characteristic relaxation time for the protein's polarization response τ_{eff} be 188 ns. This relaxation time is unusually long for a pure liquid solvent response, however the protein provides a highly structured solvation environment and its polarization relaxation should be slower than that of a simple redox system. Using Eqn 5-14 it is then possible to extract the adiabaticity parameter g, which controls the transition between regimes. Figure 5- 6 plots 1+g as a function of distance between the redox sites, i.e., the heme and the electrode. The horizontal dashed line shows the location of g=1 and marks the transition

between regimes, which occurs between 16 and 17 Å. At large distances g goes asymptotically to zero and at short distances it increases exponentially. This analysis requires that the electron transfer mechanism for cytochrome c lie in the strong to intermediate regimes at distances up to 17 Å.

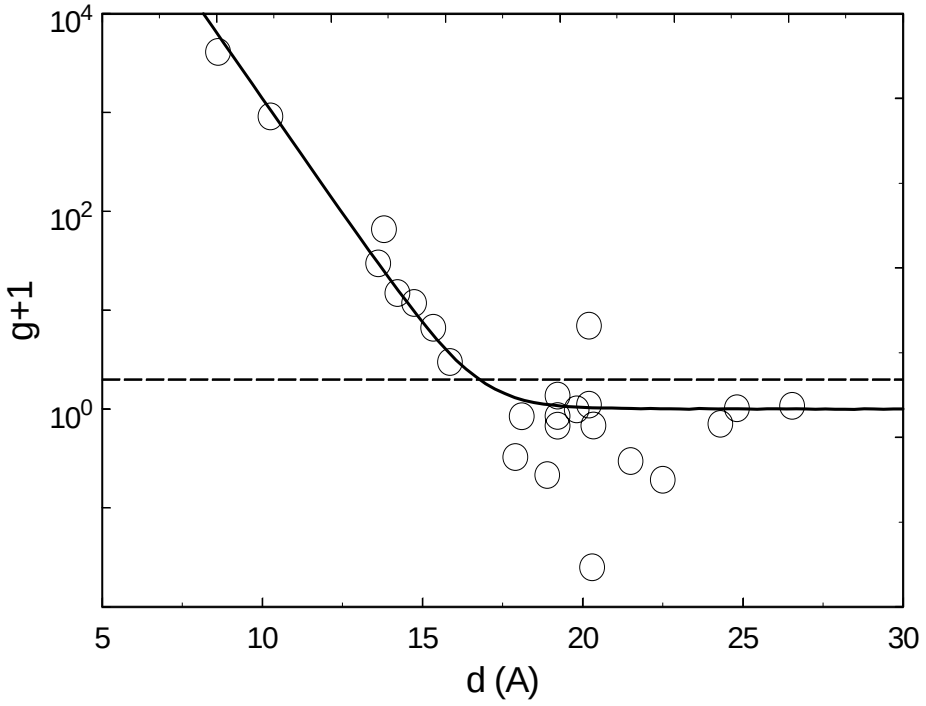

Figure 5- 6 The logarithm of the ratio of the calculated nonadiabatic (simple linear extrapolation, Figure 5- 5) to the experimental rate constants, $k_{NA}/k_{EXP} = 1+g$, are plotted *versus* the effective charge transfer distance for the cytochrome c system. The solid curve represents the best fit, Eqns 5-9 and 5-10. The horizontal dashed line shows the case of g=1.

Is such a long polarization relaxation time reasonable? Most direct studies of solvation relaxation times have been performed for small organic molecules in neat polar liquids and have rapid relaxation times, ranging from a few hundred femtoseconds in acetonitrile to a few hundred picoseconds in n-decanol.[29a] In more highly structured solvents, such as 1,3-butanediol and alcohol glasses, the solvation times can be in the regime of a few nanoseconds. However, relaxation times as low as 10^{-4} - 10^{-8} s have been reported for the myoglobin heme pocket, even

at room temperature (see [30,31]). Compared to these values the 188 ns time required by this analysis seems reasonable for the protein interior. For this timescale to be physically reasonable, the polarization response must involve some sort of quasi-diffusional conformational motion in the protein. It is worth mentioning that this 188 ns time lies close to the low-frequency edge for the actual conformation fluctuation spectrum of native cytochrome c and near the upper bound for helix-coil transitions of peptide chains.[32] Other conformational changes that accompany the redox reaction,[27,33,34] including a shift of interglobular "catalytic water", may contribute to the frictional coupling. Alternatively, it may be that proton transfer is linked to the electron transfer coordinate.[35] Certainly, the D_2O studies would be consistent with a reaction coordinate that involved water(s) in the protein or proton transfer. The results are also consistent with the finding that electron transfer in cytochrome c can be used to trigger the folding/unfolding of the protein, and they suggest that this process is associated with a conformational change in the protein that modifies the polarization along the redox reaction coordinate. The unified model of Eqn 5-14 is able to describe the distance dependent rate constants with an effective polarization relaxation time of 150 to 200 ns.

Included in this study is the linking of the protein to the gold electrode through a terthiophene tether that is terminated with a pyridine unit. In this case a substantial increase of the rate constant is observed, almost four-fold, while the formal redox potential remains the same as for the alkane analogue. In the adiabatic charge transfer picture, this increase can be understood as a decrease in the activation barrier to the electron transfer that arises from an increased electronic coupling strength (see Eqn 5-5). This observation is not consistent with a conformational gating model since the pyridine group, which is the portion of the tether that interacts directly with the protein, is the same for the alkane and terthiophene tethers. Using the

same parameters for the electron transfer as described above, these data indicate that the electronic coupling must change by 0.03 eV (*ca* 250 cm^{-1}) for a fourfold increase in the rate constant. Given the small value for the electronic coupling through the alkane tether, one can assign the change in electronic coupling strength to the terthiophene-linked protein. By comparison with other studies of conjugated molecular wires, one estimates an electronic coupling for a conjugated, n=12 tether to be 100 to 1000 times larger than that for an equivalent length alkane chain. This increase is in agreement with the value found below for the alkane tethered pyridine case (*vide infra*). Within the nonadiabatic (tunneling) picture, this coupling corresponds to a 10^4 to 10^6 increase in the charge transfer rate constant (see eq 5-1), which is clearly not found. This rate constant for the terthiophene linker can be rationalized by a rate-determining charge-transfer step that operates through an adiabatic mechanism, rather than a nonadiabatic mechanism.

Comparison with other redox protein systems: Only a few reports plot the biological electron transfer data for comparable donor-acceptor distances below 10-15 Å, where one expects a transition from the nonadiabatic to adiabatic mechanism. These studies include primary electron transfer steps in photosynthetic reaction centers,[36,30] and recent data on azurin that is adsorbed to a SAM coated gold electrode.[37] The azurin data displays behavior similar to that found in cytochrome c, a plateau region for thin SAM films. The authors of that report restricted their discussion to the gated mechanism, which is not appropriate for the current system, for the reasons outlined above. Whether the electron transfer involving cytochrome c in the reaction centers occurs by the adiabatic mechanism is not clear. Indeed, these natural systems may display a large degree of inhomogeneity (see ref 30,36). The kinetics for some of the electron transfer processes is clearly not exponential and this behavior has been explained by

a broad distribution of nonadiabatic electron transfer rates and by a mixed adiabatic/nonadiabatic model.[30,36] It may be that intramolecular quantum degrees of freedom contribute significantly to the reorganization energy for some of the primary electron transfer steps in the photosynthetic reaction center, and this could modify the onset of the nonadiabatic to adiabatic mechanism change. In terms of the classical model used above, the quantum degrees of freedom act to renormalize the electronic matrix element |H| and shift the onset of the frictional regime to smaller donor-acceptor distances. Such a condition may be crucial for the primary steps in photosynthesis and could result from the special evolutionary design. A manifestation of kinetically coupled quantum modes, a significant inner sphere reorganization contribution, causes a distortion of the bell-shaped free energy plot, Figure 5- 5, on the side of highly negative free energy gaps. No such distortion is evident in Figure 5- 5 and indicates a minor role for high frequency vibrational modes in the cytochrome electron transfer, in agreement with the results of reference.

5-5 CONCLUSIONS

Conventional electrochemical techniques were applied to the electron transfer of cytochrome c protein immobilized on the surface of SAM modified electrodes. Chemical control of the adsorption allowed the accurate determination of heterogeneous unimolecular rate constants for the electron exchange between the SAM-modified metal electrode and the cytochrome c. This approach allowed the charge-transfer rate constant's dependence on distance, solution viscosity, and other parameters to be studied in detail. The data display a change in the electron transfer mechanism with the distance from the electrode and the rate constant's dependence on viscosity and chemical composition of the SAM was studied in each regime. Analysis of these and published kinetic data for cytochrome c with a unified model for cytochrome c's redox kinetics is presented and suggests that the electron transfer occurs very close to, or in, the intermediate (still viscosity-sensitive) regime at physiologically significant distances, ca 17 Å. This conclusion requires that the electron transfer event be coupled to a polarization response of the medium (the protein interior and its environment, including the protein/water boundary hydrogen-bonded network) with an unusually long characteristic relaxation time of a few hundred nanoseconds. The detailed features of this response and its molecular character remain unclear, but it may involve a conformational motion that is linked to the polarization response along the electron transfer reaction coordinate. Under such conditions the transformation from adiabatic to nonadiabatic regimes can occur at large electron transfer distances, *ca* 17 Å or more.

What advantage arises from an adiabatic (friction controlled) electron transfer mechanism for cytochrome c? It may be that the multiple functions of cytochrome c require external regulatory tools of mechanism switching that can be implemented through specific protein-

protein interactions. In particular, because the reaction occurs in the frictional or intermediate electron transfer regime the strong dependence of the rate constant on the donor-acceptor distance is prevented and acts as a 'throttle' for the reaction. Whether these findings arise from the particular construction of cytochrome c and are associated with its special role as a redox protein in living cells, or whether it is more generally operative in biological systems remains an open question.

Supplemental Information

The Impact of Ionic Strength on the Measured Rate Constant

To address the importance of iR drop on the measured standard heterogeneous rate constant, experiments were performed at a range of solution ionic strengths for the C5/C6-Py system. This system was studied because it had the highest rate constant of the alkyl tethered systems and should be most susceptible to problems with the iR drop artifact. Data were collected for buffer solution concentrations ranging from 20 mM to 200 mM buffer solution and at different viscosities. The data in the graph show the trend in the rate constant with ionic strength in the aqueous buffer solution. The data in the table show the extreme rate constants at three different viscosities.

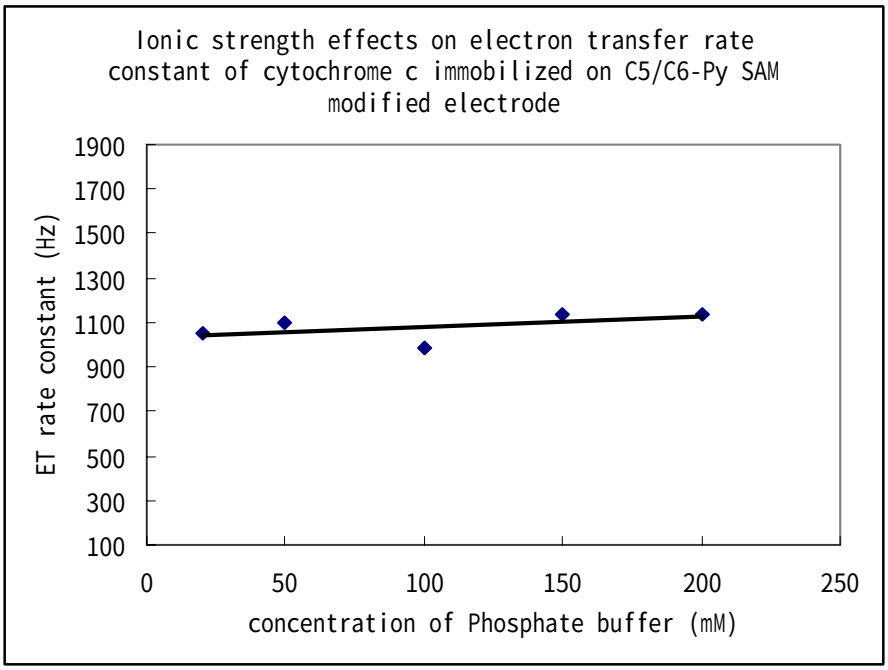

Solutions of different viscosity	**k (Hz) 20 mM buffer**	**k (Hz) 200 mM buffer**
0 g/L glucose	1513	1720
200 g/L glucose	1050	1140
400 g/L glucose	672	815

The SAM modified electrodes were incubated in 20 mM buffer solution with 50-100 μM cytochrome c and run cyclic voltammetry in different ionic strength solution by changing the concentration of phosphate buffer at pH 7. The viscosities of the solution were altered by adding 200 g/L or 400 g/L glucose.

BIBLIOGRAPHY

[1] a) Fedurco, M. *Coord. Chem. Rev.* **2000,** *209*, 263; b) Scott, R. A. *Cytochrome C: A Multidisciplinary Approach*, R. A. Scott and A. G. Mauk, ed. (University Science Books, Sausalito, **1996**) 515.

[2] a) Meade, T. J. ; Gray, H. B.; Winkler, J. R. *J. Am. Chem. Soc*. **1989,** *111*, 4353; b) Zhou, J. S.; Rodgers, M. A. J. *J. Am. Chem. Soc.* **1991,** *113*, 7728; c) Casimiro, D. R.; Richards, J. H.; Winkler, J. R.; Gray, H B. *J. Phys. Chem.* **1993**, *97*, 13073; d) Mines, G. A.; Bjerrum, M. J.; Hill, M. G.; Casimiro, D. R.; Chang, I.-J.; Winkler, J. R.; Gray, H. B. *J. Am. Chem. Soc*. **1961,** *118,* 1961; e) Luo, J.; Reddy, K. B.; Salameh, A. S.; Wishart, J.F.; Isied, S. S. *Inorg. Chem.* 2000, *39*, 2321.

[3] a) McLendon, G. *Acc. Chem. Res.* **1998**, *21*, 160; b) Harris, M. R.; Davis, D. J.; Durham, B.; Millett, F. *Biochim. Biophys. Acta* **1997,** *1319*, 147; c) Mei, H.; Wang, K.; Peffer, N.; Weatherly, G.; Cohen, D. S.; Miller, M.; Pielak, G.; Durham, B.; Millett, F. *Biochemistry* 1999, *38*, 6846; d) Ivković-Jensen, M. M.; Kostić, N. M. *Biochemistry* **1997***, 36*, 8135; e) Pletneva, E. V.; Fulton, D. B.; Kohzuma, T.; Kostić, N. M. *J. Am. Chem. Soc.* **2000**, *122*, 1034; f) Overfield, R.E.; Wraight, C.A.; DeVault, D. *FEBS Lett*, **1979,** *105*, 137.

[4] a) Tarlow, M. J.; Bowden, F. F. . *Am. Chem. Soc*. **113**, 1847 (1991); b) Song, S.; Clark, R. A.; Bowden, F. F.; Tarlow, M. J. *J. Phys. Chem.* **1993**, *97*, 6564; c) Feng, Z. Q.; Imabayashi, S.; Kakuichi, T.; Niki, K. *Chem. Soc. Faraday Trans.* **1997**, *93*, 1367; d) Avila, A.; Gregory, B. W. ; Niki, K. ; Cotton, T. M. *J. Phys. Chem. B* **2000**, *104***,** 2759.

[5] Wei, J.; Liu,H; Khoshtariya, D.E.; Yamamoto, H.; Dick, A.; Waldeck, D. H. *Ang. Chem. Int. Ed.* **2002**, *41*, 4700.

[6] a) Barbara, P. F.; Meyer, T. J.; Ratner, M. A. *J. Phys. Chem*. **1996,** *100*, 13148; b) Curry, W. B.; Grabe, M. D.; Kurnikov, I. V.; Skourtis, S. S.; Beratan, D. N. ; Regan, J. J.; Aquino, A. J. A. ; Beroza, P. ; Onuchic, J. N. *J. Bioenerg. and Biomembranes* **1995,** *27*, 285; c) Closs, G. L.; Miller, J. R. *Science* **1998**, *240*, 440.

[7] Beratan, D. N.; Betts, J. N.; Onuchic, J. N. *Science* **1991**, *252*, 1285.

[8] a) Finklea, H. O. in: *Electroanalytical Chemistry* (Bard, A.J. ; Rubinstein, I. eds.); Marcel Dekker: New York, **1996***, 19,* 109; b) Chidsey, C. E. D. *Science* **1991**, *251*, 919; c) Miller, C. J. *Physical Methods in Electrochemistry*, I. Rubinstein, ed. (Wiley, NY, **1995**) 27.

[9] Kramers, H. A. *Physica* **1940**, *7*, 284.

[10] a) Weaver, M. J.; McManis, G. E. *Acc. Chem. Res*. **1990**, *23*, 294; b) Weaver, M. J. *Chem. Rev*., **1992**, *92*, 463; c) Fawcett, W. R.; Opallo, M. *Angew. Chem. Int. Ed. Engl*. **1994**, *33*, 2131; d) Williams, M. E.; Crooker, J. C.; Pyati, R.; Lyons, L. J.; Murray, R. W. *J. Am. Chem. Soc*., **1997,** *119,* 10249; e) Fu, Y. ; Cole, A. S.; Swaddle, T. W. *J. Am. Chem. Soc*. **1999***, 121*, 10410; f) Khoshtariya, D. E.; Dolidze, T. D.; Krulic, D.; Fatouros, N.; Devilliers, D. *J. Phys. Chem. B* **1998***, 102,* 7800.

[11] a) Wei, J.; Liu, H.; Dick, A. R.; Yamamoto, H.; He, Y.; Waldeck, D. H.; *J. Am. Chem. Soc.;* **2002**; *124*; 9591; b) Yamamoto, H.; Liu, H.; Waldeck, D. H. *Chem Comm* **2001,** 1032.

[12] Bard, A. J.; Faulkner, L. R. *Electrochemical Methods* Wiley, New York, **1980**.

[13] a) Hu, J.; Fox, M.; *J. Org. Chem*.; **1999**; *64*; 4959; b) Abbotto, A.; Bradamante, S.; Facchetti, A.; Pagani, G.; *J. Org. Chem*.; **1997**; *62*; 5755.

[14] a) Napper, A. M.; Liu, H.; Waldeck, D. H. *J. Phys. Chem. B* **2001**, *105*, 7699; b)Tender, L.; Carter, M. T.; Murray, R. W. *Anal. Chem.* **1994**, *66*, 3173; c) Weber, K.; Creager, S. E. *Anal. Chem.* **1994**, *66*, 3166; d) Honeychurch, M. J. *Langmuir* **1999**, *15*, 5158.

[15] a) Fan, C.; Gillespie, B.; Wang, G.; Heeger, A. J.; Plaxco, K. W. *J. Phys. Chem. B* **2002**, ASAP; b) Battistuzzi, G.; Borsari, M.; Cowan, J A.; Ranieri, A.; Sola, M. *J. Am. Chem. Soc.* **2002**, *124*, 5315; c) Battistuzzi, G.; Borsari, M.; Ranieri, A.; Sola, M. *J. Am. Chem. Soc.* **2002**, *124*, 26.

[16] a) Waldeck, D. H. *Chem. Rev.* **1991**, *91*, 415; b) Fayer, M. D. *Ann. Rev. Phys. Chem.* **2001**, *52*, 315; c) Frauenfelder, H.; Wolynes, P.G.; Austin, R.H. *Rev. Mod. Phys.* **1999**, *71*, S419.

[17] Khoshtariya, D. E.; Dolidze, T. D.; Zusman, L. D.; Waldeck, D. H. *J. Phys. Chem. A* **2001**, *105,* 1818.

[18] A viscosity-dependent rate constant may occur when the barrier-crossing process has a dissipative nature - experiences frictional coupling with the medium (solvent). For the case of "full" solute-solvent coupling $\gamma \rightarrow 1$, the Smoluchowski limit. Deviation from this limit may be caused by weak, or intermediate, solute-solvent coupling, or a change toward a weaker electronic coupling, as discussed later.

[19] Some of these data were reported in reference 5.

[20] Murgida, D.; Hildebrandt, P.; Liu, H.; Wei, J. and Waldeck, D. H.; in preparation.

[21] a) Sikes, H. D.; Smalley, J. F.; Dudek, S. P.; Cook, A. R.; Newton, M. D.; Chidsey. C. E. D.; Feldberg, S. W. *Science* **2001***, 291*, 1519; b) Creager, S.; Yu, C.J.; Bamdad, C.; O'Connor, S.; Maclean, T.; Lam, E.; Chong, Y.; Olsen, G. T.; Luo, J.; Gozin, M.; Kayyem, J. F. *J. Am. Chem. Soc.* **1999***, 121,* 1059.

[22] Liu, Y.-P.; Newton, M. D. *J. Phys. Chem.* **1994,** *98,* 7162.

[23] Niki, K.; Sprinkle ,J.R.; Margoliash, E. *Bioelectrochemistry* **2002**, *55*, 37.

[24] a) Engstrom G.; Xiao K.H.; Yu C.A.; Yu L.; Durham B.; Millett F. *J. Biol. Chem.* **2002**, *277*, 31072; b) Sharp R.E.; Chapman S.K. Biochim. *Biophys. Acta – Protein Struc and Molec. Enzym.* **1992**, *1432* ,143. c) Canters, G. W. Dennison, C. *Biochimie* **1995**, *77*, 506.

[25] a) McLendon, G.; Pardue, K.; Bak, P. *J. Am. Chem. Soc*. **1987***, 109,* 7540; b) Graige, M. S.; Feher, G.; Okamura, M. Y. *Proc. Natl. Acad. Sci. USA* **1998**, *95*, 11679; c) Davidson, V. *Biochemistry*, **2000**, *39,* 4924; d) Davidson, V. *Acc. Chem. Res*. **2000***, 33,* 87.

[26] a) Terrettaz, S.; Cheung, J.; Miller, C. J. *J. Am. Chem. Soc.* **1996**, *118*, 7857; b) Winkler, J. R.; DiBilio, A. J.; Farrow, N. A.; Richards, J. H.; Gray, H. B. *Pure Appl Chem.* **1999**, *71*, 1753; c) Legrand, N.; Bondon, A.; Simonneaux, G. *Inorg. Chem.* **1996**, *35,* 1627.

[27] a) Miyashita, O.; Go, N. *J. Phys. Chem. B* **2000**, *104*, 7516; b) Sigfridsson, E.; Olsson, M. H. M.; Ryde U. *J. Phys. Chem. B* **2001**, *105*, 5546; c) Basu, G.; Kitao, A. Kuki, A.; Go, N. *J. Phys. Chem. B* **1998**,

102, 2085; d) Muegge, I.; Qi, P. X.; Wand, A. J.; Chu, Z. T.; Warshel, A. *J. Phys. Chem. B* **1997**, *101*, 825.

[28] a) Zusman, L.D *Z. Phys. Chem*. **1994***, 186,* 1; b) Beratan, D. N.; Onuchic, J. N. *J. Chem. Phys* **1988,** *89*, 6195;c) Onuchic, J. N. Beratan, D. N.; Hopfield, J. J. *J. Phys. Chem.* **1986**, *90*, 3707.

[29] a) Maroncelli, M. *J. Mol. Liq.* **1993**, *57*, 1; b) Nandi, N.; Bhattacharyya, K.; Bagchi, B. *Chem. Rev.* **2000**, *100*, 2013.

[30] Kotelnikov, A. I.; Ortega, J. M.; Medvedev, E. S.; Psikha, B. L.; Garcia, D.; Mathis, P. *Bioelectrochemistry* **2002**, *56*, 3.

[31] a) Bashkin, J. S.; McLendon, G.; Mukamel, S.; Marohn, J. *J. Phys. Chem.* **1990**, *94*, 4757; b) Pierce, D. W.; Boxer, S. G. *J. Phys. Chem.* **1992**, *96*, 5560; c) Beece, D.; Eisenstein, L.; Frauenfelder, H.; Good, D,; Marden, M. C.; Reinisch, L.; Reynolds, A. H.; Sorensen, L.B.; Yue, K. T. *Biochemistry* **1980**, *19*, 5147.

[32] Eaton, W. A.; Munoz, V.; Thompson, P. A.; Henry, E. R.; Hofrichter, J. *Acc. Chem. Res.* **1998***, 21,* 745.

[33] a) Banci, L.; Bertini, I.; Gray, H. B.; Luchinat, C.; Reddig, T.; Rosato, A.; Turano, P. *Biochemistry* **1997***, 36,* 9867; b) Qi, P. X.; Beckman, R. A. ; Wand, A. J. *Biochemistry* **1996**, *35,* 12275; c) Moss, D.; Nabedryk, E.; Breton, J.; Mantele, W. *Eur. J. Biochem.* **1990**, *187*, 565; d) Yuan, X.; Sun, S.; Hawkridge, F. M.; Chlebowski, J. F.; Taniguchi, I. *J. Am. Chem. Soc.* **1990**, *112*, 5380; e) Cohen, D. S.; Pielak, G. J. *J. Am. Chem. Soc.* **1995**, *117*, 1675.

[34] a) Bertini, I; Hajieva, P.; Luchinat, C.; Nerinovski, K. *J. Am. Chem. Soc.* **2001**, *123*, 12925; b) Bertini, I; Huber, J. G.; Luchinat, C.; Piccioli, M. *J. Magn. Res.* **2000**, *147*, 1; c) Qi, P. X.; Urbauer, J. L.; Fuentes, E. J.; Leopold, M.F.; Wand, A. *J. Struc. Biol.* **1994**, *1*, 378; d) Bertini, I.; Dalvit, C.; Huber, J. G.; Luchinat, C.; Piccioli, M. *FEBS Lett.* **1997***, 415,* 45.

[35] Murgida, D. H.; Hildebrandt, P. *J. Am. Chem. Soc.* **2001**, *123*, 4062.

[36] a) McMahon, B. H.; Muller, J. D.; Wraight, C. A.; Nienhaus, G. Ulrich; *Biophys. J* **1998**, *74*, 2567.; b) Nonella, M.; Schulten, K. *J. Chem. Phys*. **1991**, *95*, 2059.

[37] a) Chi, Q.; Zhang, J.; Andersen, J.E.T.; Ulstrup, J. *J. Phys. Chem. B* **2001**, *105*, 4669; b) Zhang, J.; Chi, Q.; Kuznetsov, A.M.; Hansen, A.G.; Wackerbarth,H.; Christensen, H. E. M.; Andersen, J. E. T. ; Ulstrup, J. *J. Phys. Chem. B* **2002**, *106*, 1131.

CHAPTER 6 PROBING ELECTRON TUNNELING PATHWAYS: ELECTROCHEMICAL STUDY OF RAT HEART CYTOCHROME C AND ITS MUTANT ON PYRIDINE-TERMINATED SAMS[§§]

The electron transfer rates between gold electrodes and adsorbed cytochromes are compared for native cytochrome *c* and its mutant (K13A), using two different immobilization strategies. A recent study by Niki showed that the electron transfer rate for a particular mutant cytochrome *c* (K13A) is orders of magnitude slower than the native form, when electrostatically adsorbed on SAM coated gold electrodes. The current study directly 'links' the protein's heme unit to the SAM, thereby 'short-circuiting' the electron tunneling pathway. These findings demonstrate that the immobilization strategy can modify the electron transfer rate by changing the tunneling pathway.

6-1 INTRODUCTION

The ability to self-assemble chemically well-defined monolayer films on electrode surfaces has enabled electrochemical studies of biological molecules and promises to enable the investigation of redox-coupled, biological machines. Current applications are limited by the electrical communication between the biological macromolecule and the electrode, however.[1] A number of different strategies have been employed, such as facilitators, redox mediators, direct covalent linkage of the protein or enzyme to the electrode, and protein adsorption. Nevertheless, the

[§§] This work has been published as Wei, JJ; Liu, HY, Niki, K.; Margoliash, K.; Waldeck*, DH, Probing electron transfer pathway of cytochrome c and its mutant immobilized at surface. *J. Phys. Chem. B*, **2004**, 108; 16912-16917.

control variables for electronic communication through monolayer films have not been clearly delineated. This work describes fundamental studies of the protein cytochrome *c* when it is adsorbed to monolayer coated electrodes. A comparison of the new results reported here with earlier findings support the electron tunneling pathway recently identified by Niki *et al*[2] for cytochrome *c*.

The fundamental understanding of electron tunneling in organic and biological molecules has been developed over the past fifteen years through a series of well-defined studies in homogeneous solutions. These studies have established that structural features of a molecule play an important role in determining electron tunneling rates. From studies in unimolecular organic supramolecules (comprised of a donor unit, an acceptor unit, and a bridging unit), it is clear that the placement and connectivity of atoms determines the magnitude of the electronic coupling between donor and acceptor groups.[3] For linear systems the tunneling probability density flows mostly through the covalent linkages, whereas for systems with a molecular cleft the preferred tunneling pathway(s) can proceed through noncovalent contacts.[4] Early work in proteins made either simplified assumptions about the importance of covalent linkages, 'the pathway model'[5], or totally ignored covalent linkages.[6] Over time these two, seemingly divergent, descriptions have evolved and were recently shown to be mathematically isomorphic.[5a]

With regard to a quantitative understanding of the electron tunneling mechanism, the understanding of heterogeneous electron transfer reactions lags behind that of intramolecular and intermolecular electron transfer reactions. Because the transferring electron proceeds from a delocalized state to a localized one (or vice versa) and a continuum of electrode states are available, one might expect the electron tunneling probability at electrodes to differ from that

between two localized molecular states. Recent work on simple redox couples has demonstrated that through bond electron tunneling dominates in some cases,[7] but in other cases tunneling via nonbonded contacts can be dominant.[8] The recent work of Niki et al has studied different mutants of cytochrome *c,* which were electrostatically adsorbed to carboxylate surfaces, and found an unusual sensitivity to the presence of the protein's lysine 13 amino acid. The current work addresses whether this sensitivity arises from changes in the tunneling pathway for the adsorbed protein or from changes in the energetics of the protein.

Niki's recent study replaces the lysine units on the surface of the cytochrome *c* and studies the electron transfer rate under conditions where the protein is electrostatically adsorbed to the surface. Their work shows that replacement of the lysine-13 with an alanine changes the electron transfer rate by five orders of magnitude. When studying a related cytochrome mutant, which swaps the lysine 13 with a glutamic acid (at position 90) that is adjacent on the protein surface, they observed a similar decrease in rate constant. Because the electrostatic binding should be similar for this latter mutant and the native system, this result suggests that the adsorption orientation is not solely responsible for the reduced rate constant. Furthermore they showed that replacement of lysine-72 or lysine-79 has little effect on the electron transfer rate, even though these are likely binding sites for the cytochrome to the surface.[9] The proximity of the lysine 13 to the heme is discussed elsewhere.[10] Using the cytochrome *c* crystal structure, one can estimate a physical, 'through-space', distance of 5.8 Å from the lysine to the heme and a 'through-bond' distance of about 20 Å. The current work explores this chemically modified system RC9-K13A further, in order to determine whether the reduced rate constant arises from a change in the protein's reorganization energy or is caused by a change in the electron tunneling probability.

The electrochemical rate constant for the RC9-K13A mutant and the native rat cytochrome *c* were measured for two different SAM (self-assembled monolayer) coated electrodes. In the first case the electrodes were coated with COOH-terminated SAMs, and in the second case they were coated with mixed SAMs comprised of pyridine and alkane. In the first case, the findings are consistent with the earlier results of Niki et al. In the second case however, the mutant and native cytochrome *c* have similar standard electron transfer rate constants. This finding is consistent with adsorption of the protein to the SAM by axial coordination between the pyridine receptor and the protein's heme; [11] both electrochemical[11a] and spectroscopic[11b] studies demonstrate that the pyridine receptor binds directly with the heme unit of the protein. In addition, the similarity in the rate constant between the mutant and native form shows that the primary difference between the two cases is the nature of the link between the protein and the electrode.

6-2 EXPERIMENTAL DETAILS

Reagents and Materials. Water for the experiments was purified by using a Barnstead-Nanopure system and had a resistivity of 18 MΩ-cm. All mercaptoalkanes were purchased from Aldrich and used without further purification. 4-mercaptobenzoic acid (97%), 3-mercaptopropionic acid (99%), 6-Mercapto-1-hexanol, 11-bromo-1-undecanol (98%), 12-mercapto-1-dodecanol (98+ %), 1-nonadecanol, isonicotinic acid (99%), docosanedioic acid (85%), were purchased from Aldrich. All pyridine derivatives were synthesized in the manner reported earlier. [11,12]

Cytochrome *c* (Sigma C 7752, from horse heart, minimum 95% based on molecular weight 12,384) was purified using a cation exchange column (CM-52, carboxymethyl-cellulose

from Whatman) in a manner described previously.[11,12] Rat cytochrome *c* (from rat heart, C7892, 95% based on molecular weight 12,132) was purchased from Sigma and used without purification. The preparation of RC9-K13A rat cytochrome *c* mutant was reported elsewhere.[13] All cytochromes were stored under an argon atmosphere in a freezer until use.

Electrode Preparation. Details on the preparation and characterization of the gold electrode can be found elsewhere. A brief outline of the procedure is given here. A gold wire (0.5 mm diameter, 99.99%) was cleaned by reflux in nitric acid (68-70%) at 130 °C for a few hours and then was washed with deionized water. The tip of the gold wire was heated and annealed in a gas flame to form a ball of about 0.06-0.12 cm surface area.

Chemically modified electrodes were prepared by immersion in an ethanol or THF solution that contained 0.1 mM $HS(CH_2)_nOOC(C_5H_4N)$ and 0.9 mM $HS(CH_2)_{n-2}CH_3$, where n specifies the methylene chain length. The electrode remained in this solution for one day to form the mixed SAM. The electrode was removed from the solution, rinsed with absolute ethanol (or THF), then rinsed with the supporting buffer solution (20 mM phosphate buffer pH 7), and finally dried by a stream of argon gas. The electrode was characterized, as previously, and then immersed in a solution containing 100 μM cytochrome *c* and 20 mM phosphate buffer (purged with argon gas) for 30 to 60 min. This procedure immobilizes the cytochrome *c* on the SAM-coated electrode.

The electrodes were rinsed with the supporting buffer solution and immersed in a three electrode electrochemical cell that contained a buffer solution with no cytochrome *c*. Voltammetry was performed on these electrodes.

Electrochemical Measurements. Electrochemical measurements were performed by using an EG&G PAR-283 potentiostat that was controlled by a PC computer running version 4.3

of PARC's 270 software and a GPIB board. The three-electrode cell was composed of a platinum spiral counter electrode, an Ag/AgCl (3 M NaCl) reference electrode, and the SAM-coated Au as a working electrode. The voltammetry measurements were performed in 20 mM phosphate buffer solution (pH of 7.0) under an argon atmosphere. The potentiostat applies a staircase waveform rather than a true analog signal. For these experiments the voltage increment was either 1 or 2 mV and the scan rate ranged from tens of mV/sec to 60 V/sec. In each case, the current was sampled during the last $1/4^{th}$ of the potential increment's time window, which is appropriate for relatively high scan rate and proper kinetic analysis.

The uncompensated resistance (R_u) in the 20 mM buffer solution during the voltammetry measurements can sometimes be important for the data analysis at high scan rates. The measured R_u in these studies ranges from 200 to 500 ohms, depending on the distance between electrodes, the geometry, and the electrode areas. The calibrated peak potential in this work was corrected by the following equation

$$E_c(t) = E_a(t) - i(t) \cdot R_u \qquad 6\text{-}1$$

where $E_c(t)$ is the calibrated potential, $E_a(t)$ is the applied (apparent) potential, i(t) is the current of the voltammogram. An average resistance of R_u = 300 ohms was used. Because of the low currents in this study, the electron transfer rate constants obtained both from the apparent and corrected peak potentials differ little.

For an electron transfer rate constant measurement by cyclic voltammetry, the method is limited in its time resolution by the RC characteristics of the electrode. With the small diameter (*ca*.1 mm) gold ball electrodes used in this work, rate constants can be measured up to 10,000 s^{-1}.

6-3 RESULTS

The protein was adsorbed on the surface in two different ways (see Figure 6- 1). The case 1 method adsorbed the protein electrostatically to electrodes that were coated with a monolayer thick film of carboxyl-terminated alkanethiols. This method is well established.[14] The case 2 method adsorbed the protein onto mixed monolayer films, comprised of pyridine-terminated alkanethiols and alkanethiols. Previous work presents AC impedance, electrochemistry, and STM studies of the case 2 SAMs and the adsorbed protein.[11] In both cases the solution was pH =7 with 20 mM phosphate buffer.

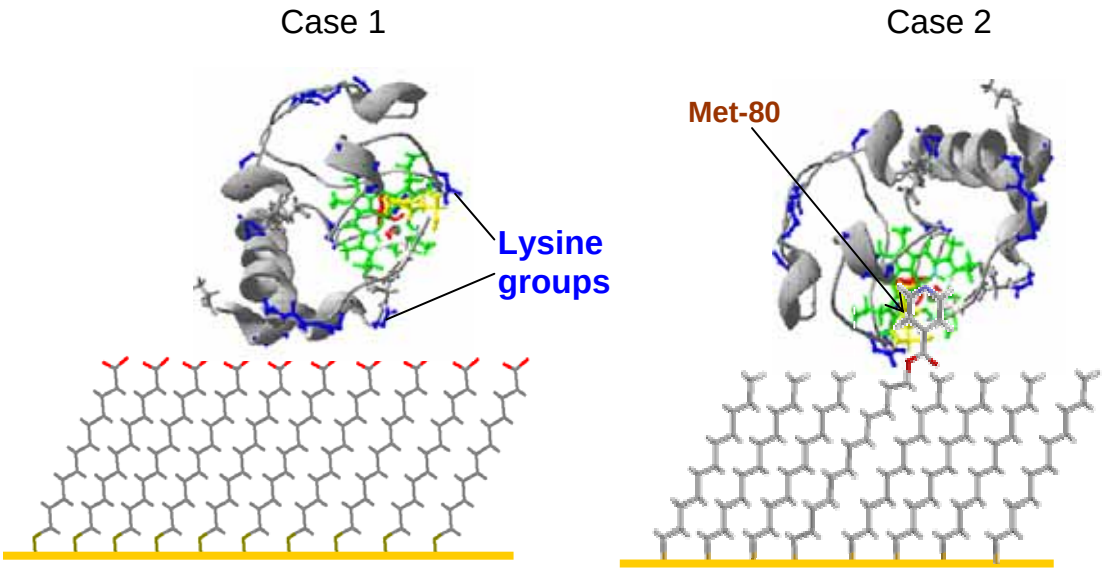

Figure 6- 1 Cytochrome *c* adsorption on self-assembled monolayers. Case 1: electrostatic adsorption on carboxylic acid SAM. Case 2: Ligand immobilized cytochrome *c* on pyridine terminated mixed SAM

Cyclic Voltammetry and Electron Transfer Rate Constant

Rat heart cytochrome *c* and the mutant K13A were immobilized on gold electrodes that were modified using the pyridine receptors. The adsorbed cytochrome *c*'s redox response was studied by using cyclic voltammetry over the potential range from -0.8V to 0.4V. A signature for

immobilization of the protein by the pyridine is a negative shift of its redox potential (for horse heart cytochrome *c* it shifts to -0.172 V *versus* Ag/AgCl). This value is indicative of the replacement of the heme's axial methionine ligand with the pyridine, under conditions that do not unfold the entire redox center. [10,11]

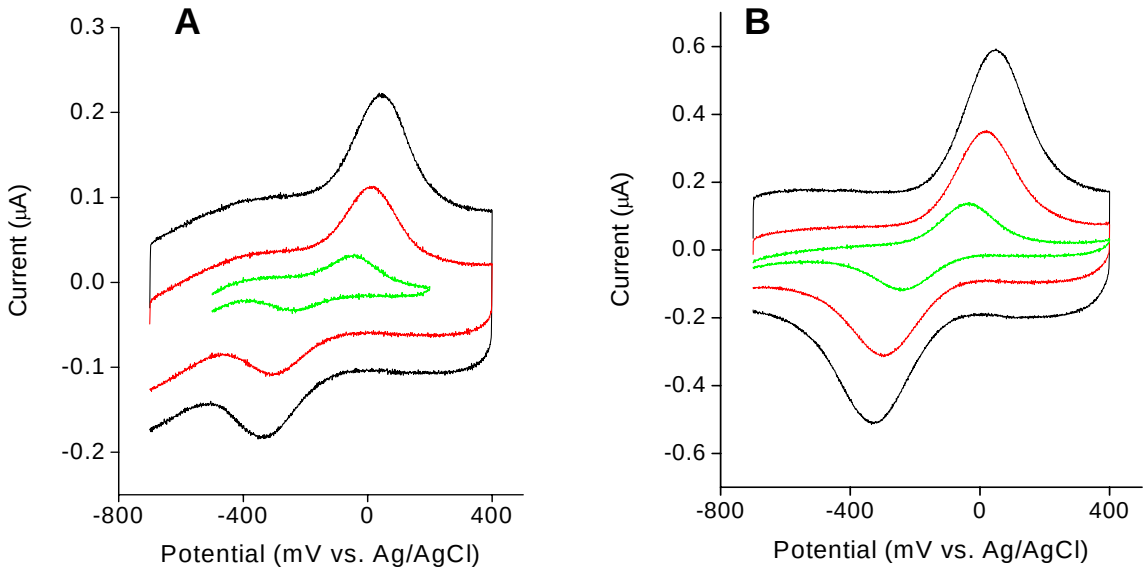

Figure 6- 2 Representative cyclic voltammagrams of native rat cytochrome *c* and rat mutant K13A immobilized on C20Py/C19 mixed monolayer modified gold electrodes. Panel A is for native cytochrome *c*; Panel B is for rat mutant K13A, the scan rates are 0.2 V/sec (green), 0.6 V/sec (red) and 1.0 V/sec (black), respectively.

Figure 6- 2 shows representative cyclic voltammograms of rat heart cytochrome *c* (panel A) and the mutant (panel B) immobilized on a gold electrode with C20OOC-Py/C19 alkanethiol mixed SAMs. The data present well-defined peaks with a formal potential at -0.147±0.006 V for native cytochrome *c* and -0.146±0.011 V for the mutant cytochrome *c*. These data also show the increase in peak separation with the increase in voltage scan rate. The supplemental material shows the linear relationship between the peak current (I_p) and scan rate (v). This latter

dependence confirms that the protein is adsorbed on the electrode surface, rather than diffusing in solution.

The rate constant was determined by fitting of the peak potential shift as a function of the scan rate to the classical Marcus theory, in the manner described previously.[11,15] In this analysis a reorganization energy of 0.58 eV was applied to obtain the standard electron transfer rate constant (*vide infra*) under the assumption that the reaction's symmetry factor is 0.5. Simulations of the cyclic voltammograms indicate that a symmetry factor of 0.46 for mutant K13A and 0.41 for native rat cytochrome c are more appropriate, however the comparisons between data sets is facilitated by approximating the symmetry factor by the value 0.5. This choice does not effect the reported rate constants very strongly. For example, the mutant's anodic electron transfer rate constant is 0.63 s^{-1} and its cathodic electron transfer rate constant is 0.60 s^{-1} when using a symmetry factor of 0.46. These rate constants are very close to the 0.62 s^{-1} value obtained from the factor 0.5.

Table 6-1 Electron transfer rate constant of rat heart cytochrome *c* and the mutant K13A adsorbed on different electrodes

Systems	Native Cytochrome *c*		Mutant K13A	
	k_{et}^0 (s^{-1})	# Trials	k_{et}^0 (s^{-1})	# Trials
C6Py/C5			789 ± 155	3
C11Py/C10	903 ± 130	3	816 ± 122	4
C12Py/C11	770 ± 42	3	737 ± 103	3
C16Py/C15	55.3 ± 2.1	3	80 ± 16	5
C20Py/C19	0.62 ± 0.03	3	0.73 ± 0.12	4
C3COOH	920 ± 60	2	0.13 ± 0.04	2
(C_6H_4)COOH	570 ± 45	5	0.20 ± 0.06	2
C5COOH	680 ± 68	5	0.0035 ± 0.001	4
C10COOH	19 ± 7.2	4		

Note: Errors indicated for the rate constant represents one standard deviation from the average value found for the different trials.

The standard heterogeneous rate constants k^0_{et} for the different systems of the native cytochrome *c* and mutant are summarized in Table 6-1. These data are in good agreement with the findings of earlier work.[2,10,18]

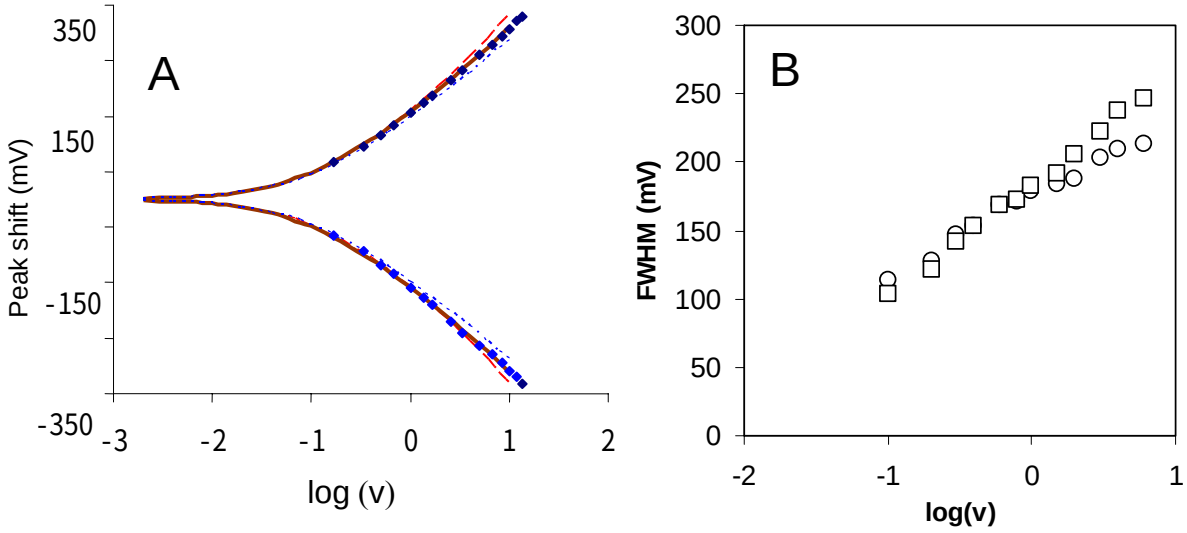

Figure 6- 3 Panel A shows the experimental peak shift for native rat cytochrome *c* plotted vs. log(*v*), where *v* is the voltage scan rate. The three curves are calculated from the Marcus model at reorganization energies: a) 0.30 eV red dashed curve; b) 0.58 eV solid curve, and c) 0.90 eV dotted curve. The best fit is at k_{et}^0 =0.62 s^{-1} and reorganization λ=0.58 eV Panel B shows the increase in the full-width at half maximum for the voltammogram as a function of the scan rate (squares are the reduction wave and circles are the oxidation wave)

Reorganization Energy Measurement

In principle, the reorganization energy of the cytochrome *c* and mutant can be obtained by fitting the peak shift with voltage scan rate to the Marcus model. In practice one must access high voltage scan rates so that significant overvoltage is probed.[16] By studying thick films, thereby slowing the electron transfer rate, and accessing higher scan rates the reorganization energy for the pyridine immobilized protein was probed. Figure 6- 3 shows data for the peak shift versus the voltage scan rate of the native rat cytochrome *c* immobilized on C20Py/C19 mixed film. At slow enough scan rates the peak separation should go to zero. Because of signal-

to-noise this limit was not reached for the C20Py films, however very small peak separations were found the shorter alkanethiols (e.g., 5 mV for C12Py/C11 - see ref. 18 and Supplemental Information). Figure 6- 3 B shows how the voltammogram width changes with scan rate. At slow scan rates, where the voltammogram is reversible, the width should be 91 mV and it increases as the scan rate makes the electron transfer process more irreversible. Note that high scan rates show that the reduction wave is broadened, as compared to the oxidation wave. This feature may reflect the importance of conformational changes at higher scan rates (see reference 11b).

Three different fits, corresponding to λ values of 0.3 eV, 0.58 eV, and 0.9 eV, of the Marcus model to the data in Figure 3A are shown. The best fit occurs for λ=0.58 eV and a standard electron transfer rate constant, k^0= 0.62 s^{-1}. By using this analysis, the reorganization energy of both native rat cytochrome *c* and the mutant K13A cytochrome *c* can be determined. These results are summarized in Table 6-2. An average reorganization energy of 0.6 eV for mutant K13A and 0.6 eV for native cytochrome *c* are obtained. These reorganization energies are similar to those reported for native cytochrome *c* in solution.[17] The error in determining the reorganization energy is between 0.1 and 0.2 eV; see the Supplemental Information for quantitative details.

Table 6-2 Summary of reorganization energy measurements of rat heart cytochrome *c* and mutant K13A obtained from immobilization on C20Py/C19 mixed monolayer films.

	Mutant K13A Cytochrome *c*			Native Cytochrome *c*		
Trial	k^0 (s^{-1})	λ (eV)	$E^{0'}$(mV)	k^0 (s^{-1})	λ (eV)	$E^{0'}$(mV)
1	0.82	0.50	-150	0.60	0.62	-141
2	0.85	0.45	-157	0.65	0.55	-153
3	0.66	0.70	-132	0.62	0.58	-148
4	0.60	0.65	-145			
Avg.	0.73±0.12	0.58±0.12	-146±11	0.62±0.03	0.58±0.04	-147±6

Note: Errors indicated for the rate constant represents one standard deviation from the average value found for the different trials.

Distance Dependence of Electron Transfer

The protein's electron transfer rate constant was measured as a function of distance from the electrode surface. The distance between the protein and the electrode was systematically varied by changing the thickness of the SAM. Figure 6- 4 presents the distance dependence of the measured electron transfer rate constant of rat heart cytochrome *c* and K13A mutant immobilized on pyridine systems. The data are similar to the results obtained for horse heart cytochrome *c* earlier (also shown).[11,18] Data are also shown for the proteins adsorbed on carboxylate terminated.

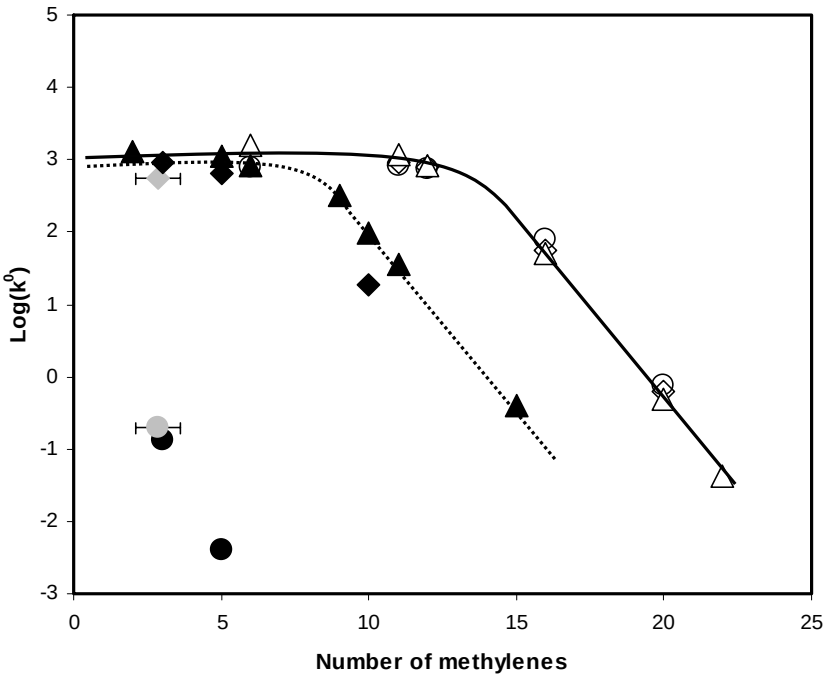

Figure 6- 4 The measured electron transfer rate constant of surface immobilized rat heart cytochrome *c* and its K13A mutant is plotted as a function of SAM thickness. The unfilled symbols represent pyridine immobilized cytochrome *c*: the triangle for native horse heart cytochrome *c*, the circle for mutant K13A, and the diamond for native rat cytochrome *c*. The filled symbols represent electrostatic adsorption by carboxylic acid films: the black diamond is native rat cytochrome *c*, the black circle is the K13A mutant, and the black triangle is horse heart cytochrome *c* [19]. The gray symbols are for a $S(C_6H_4)COOH$ monolayer and the bar shows the uncertainty in assigning it a length equivalent to some number of methylenes. The solid curve and the dashed curve represent the distance dependence of cytochrome c with the pyridine and carboxylic acid system, respectively.

For the pyridine-terminated films (open symbols), the native rat cytochrome *c* and the K13A cytochrome *c* rate constants are within 15% of each other, and they show a qualitatively similar dependence on the SAM thickness. The data display a plateau region at short donor-acceptor separations, which demonstrates that the two proteins have similar rate constants in this solvent controlled regime.[10,18] At large separations the electron transfer rate constant displays an exponential dependence on the charge-transfer distance with a decay coefficient of 1.12 per methylene for the native cytochrome and 1.16 per methylene for the mutant (dashed line). This distance dependence is similar to that found in other tunneling studies with saturated hydrocarbons and is a signature for nonadiabatic electron transfer. For a more detailed discussion and analysis of the electron transfer in these two regimes (plateau region and tunneling region) see references 10 and 18.

In contrast to the SAMs with pyridine receptors, the carboxyl-terminated monolayers display different rate constants for the native and mutant forms of cytochrome *c*. At short film thickness the native cytochrome *c* approaches the limiting (plateau) value[19] observed for the pyridine tethered protein. In contrast, the mutant cytochrome *c* never reaches this value, and its rate constant is consistently lower (by orders of magnitude) than the native cytochrome. Although the data for the mutant form appears to fall off exponentially with distance, no fit is shown through the data because of the few number of points.[20] This observation agrees with the findings reported earlier.

6-4 DISCUSSION

The data clearly show that the method of binding the cytochrome *c* to the monolayer film can be used to modify the electron transfer rate constant by changing the electron tunneling pathway. For the electrostatic binding mode (case 1 in Figure 6- 1), the electron transfer rate constant of the native cytochrome *c* differs by five orders of magnitude from that found for the K13A mutant. In this protein assembly the outer surface of the protein contacts the outer surface of the SAM so that electrons must tunnel through a portion of the protein's peptide chain to reach the redox center. In contrast, the immobilization of the cytochrome *c* by direct linkage of the protein's heme unit with the SAMs pyridine receptor has similar rate constants for the mutant and the native protein. This similarity results because the electron tunneling pathway, along the alkane tether of the pyridinal receptor, is the same in these two cases. Furthermore, the dependence of this electron transfer rate constant on the length of the alkane tether is qualitatively similar to that found for horse heart cytochrome *c*, even though the apparent redox potentials differ by 25 mV.

The reorganization energy of the cytochrome *c* could be determined for the slower electron transfer rate constants. In these cases the reorganization energy was found to be about 0.6 eV, and to vary little between the mutant and native form, or the method of immobilization. In fact this value of the reorganization energy is similar to that reported for cytochrome *c* in free solution.[17] The similarity of the reorganization energies for the mutant and native forms, when pyridine ligated, suggests that the mutation has little impact on the reorganization energy. Surprisingly, the pyridine ligated native form has a reorganization energy similar to that found for the native form when not ligated implying that the pyridine ligation does not strongly modify or control the reorganization energy. This observation is consistent with other studies which

conclude that the reorganization energy in cytochrome c is primarily 'outer sphere' and arises from small contributions of many different protein and solvent modes.[21] Although the error in the reorganization energy could be as high as 0.2 eV, such a difference would change the standard rate constant by less than one order of magnitude, as compared to the four to five order of magnitude difference between the two immobilizations of the mutant protein. These findings argue against an energy effect causing the dramatic decrease in the rate constant for the lysine 13 when it is adsorbed onto carboxylate films.

6-5 CONCLUSION

These studies support the conclusion that the reduced electron transfer rate constant for the K13A mutant adsorbed on carboxylate films results from a blocking of an efficient electron tunneling pathway. When adsorbed onto the carboxylate films, the electron must tunnel through the protein to reach the heme. When adsorbed through the pyridine receptors, the electron tunnels through the artificial tether and is not impacted by changes in the native protein's electron transfer pathways.

Supplemental Information

Here we provide an assessment of the error associated with the rate constant and reorganization energy determination; full-widths at half height and the peak shifts for the mutant voltammogram as a function of the scan speed, along with a table of FWHM data for different monolayer films; and the dependence of the current on scan speed.

1. χ square analysis:

In Figure 6-3 of the paper, we fit the experimentally observed peak shifts to the Marcus model predictions to obtain the standard electron transfer rate constant and reorganization energy. The reliability of the fit and parameter values were assessed through a goodness of fit, χ-square, error analysis. The chi-square is defined as[22]

$$\chi^2 = \frac{1}{2n-2}\sum_{i}^{2n}\left(\frac{\left|E^i_{Pthe} - E^i_{P\exp}\right|}{\sigma}\right)^2$$

in which n is the total cyclic voltammograms used in the analysis, *i* represents the i^{th} scan with a specific scan rate, Ep^i_{the} and E^i_{pexp} represent a theoretical peak position (oxidation or reduction) and experimental peak position (oxidation or reduction) for the i^{th} scan rate. σ is the error of peak position determination during analysis of the raw data. The peak positions were determined for each voltammogram by subtracting a baseline, identifying the peak position, and then correcting for iR drop. The estimated error in this determination is 2 to 4 mV.

The parameters, reorganization energy λ and standard rate constant k^0, are determined by minimizing the χ^2. Figure S1 plots the χ^2 value as a function of the standard rate constant for different values of the reorganization energy. It is evident from these graphs that the best fit value of k^0 is relatively insensitive (varies by only about 15% with reorganization energy

changes of 0.2 eV) to the choice of reorganization energy. The optimized electron transfer rate constant and χ^2 value, at each of the reorganization energies, is reported in Table 6-S1. It is evident from these results that the best fit reorganization energy lies near 0.6 eV. By adjusting both parameters in the fit we find a reorganization energy of 0.58 eV and a standard rate constant of 0.62 s^{-1}.

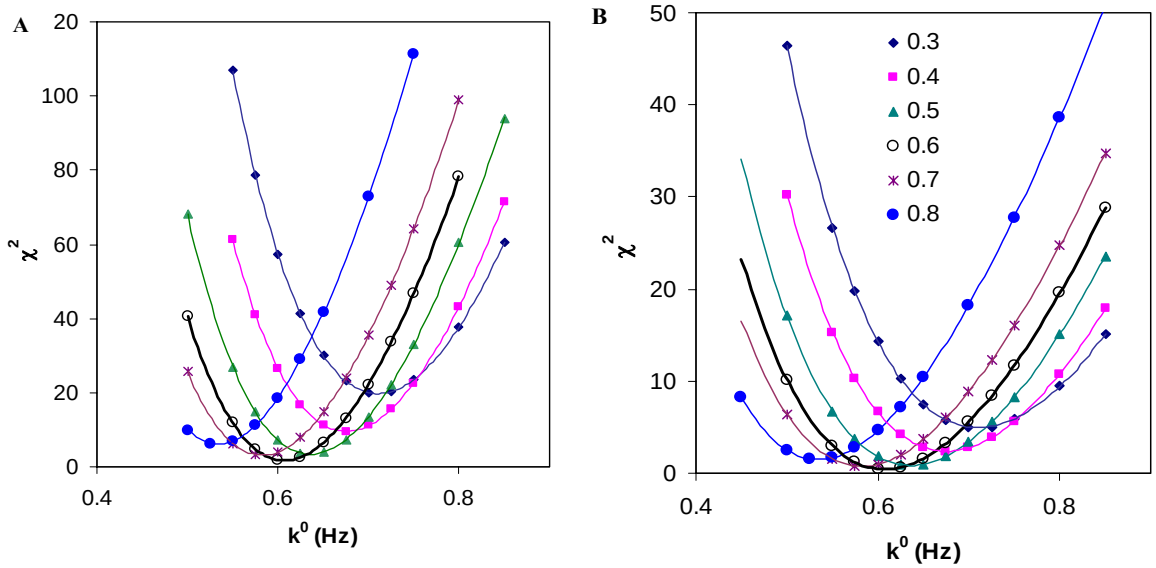

Fig. S1. χ^2 analysis of the reorganization energy λ and standard electron transfer rate constant k^0. Panel A shows the case for σ= 2 mV, and panel B shows the case for σ=4 mV.

Table 6-S1: The standard rate constant k^0, reorganization energy λ, and χ^2 values at the best fits with the assigned peak errors.

k^0	λ	σ = 2 mV	σ = 4 mV
		χ^2_{min}	χ^2_{min}
0.71	0.3	19.9	5.0
0.68	0.4	9.7	2.3
0.64	0.5	3.3	0.83
0.61	0.6	1.7	0.43
0.58	0.7	3.0	0.79
0. 53	0.8	6.0	1.54

To assess the significance of the χ^2 value, it must be normalized in the proper manner; that is the standard deviation σ for the peak assignments must be known. Yet this error will have an element of subjectivity to it because of the data analysis procedure and intrinsic features of the measurement. Assuming that the standard deviation of 2 mV is the correct one, the probability of a χ^2 value greater than 1.7 is only about 2% and values greater than 2.5 is only 0.05 %. Assuming that the standard deviation of 4 mV is the correct one, the probability of a χ^2 value larger than 1 is 46% and a χ^2 value larger than 2 is 0.4%. Hence, a realistic error in the reorganization energy assignment is about 0.1 eV, although it could be as high as 0.2 eV in some cases.

2. FWHM analysis

Figure 6-S2 shows the analogue of Figure 6-3 in the paper for the mutant system. The similarity between the data sets indicates that the pyridyl ligation is similar in both cases. Table 6-S2 shows the FWHM of the oxidation and reduction waves for the voltammograms obtained on different thickness films at the lowest scan rate studied. A fully reversible process has a FWHM of 90.6 mV and a peak separation of zero.

Table 6-S2**:** the FWHM* (mV) of the oxidation and reduction waves for the voltammograms obtained on different thickness films at low scan rates. The redox reactions are quasireversible.

Samples	Scan rate (V/sec)	Native rat cyt. C FWHM (mV)		peak separations	Mutant K13A FWHM (mV)		peak separations
		Oxidation	Reduction	E_{pO}-E_{pR} (mV)	Oxidation	Reduction	E_{pO}-E_{pR} (mV)
C11Py/C10	4	104	98.6	8±2	105	100	9±2
C12Py/C11	2	106	97.6	5±2	101	97	6±2
C16Py/C15	1	108	101	25±3	107	102	20±3

* The deviation for FWHM is about ±3 mV.

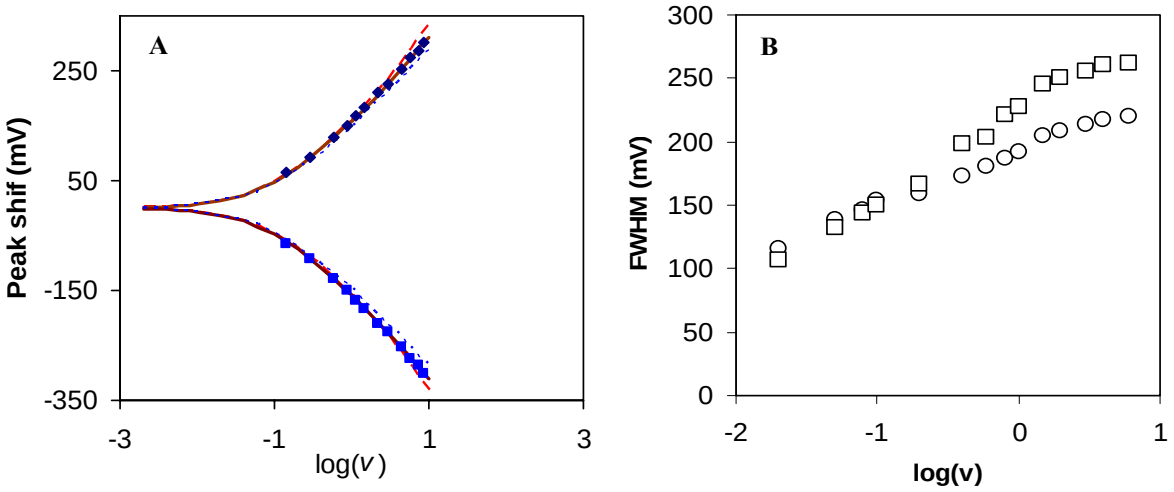

Figure S2. Panel A shows the experimental peak shift for mutant K13A rat cytochrome c plotted vs. log(v) is the voltage scan rate. The three curves are calculated from the Marcus model at reorganization energies: a) 0.3 eV red dashed curve; b) 0.6 eV solid curve, and c) 0.9 eV dotted curve. The best fit is at k_{et}^{0}=0.60 s-1 and reorganization energy 0.65 eV. Panel B shows the increase in the full-width at half maximum for the voltammogram as a function of the scan rate (squares are reduction wave and circles are the oxidation wave).

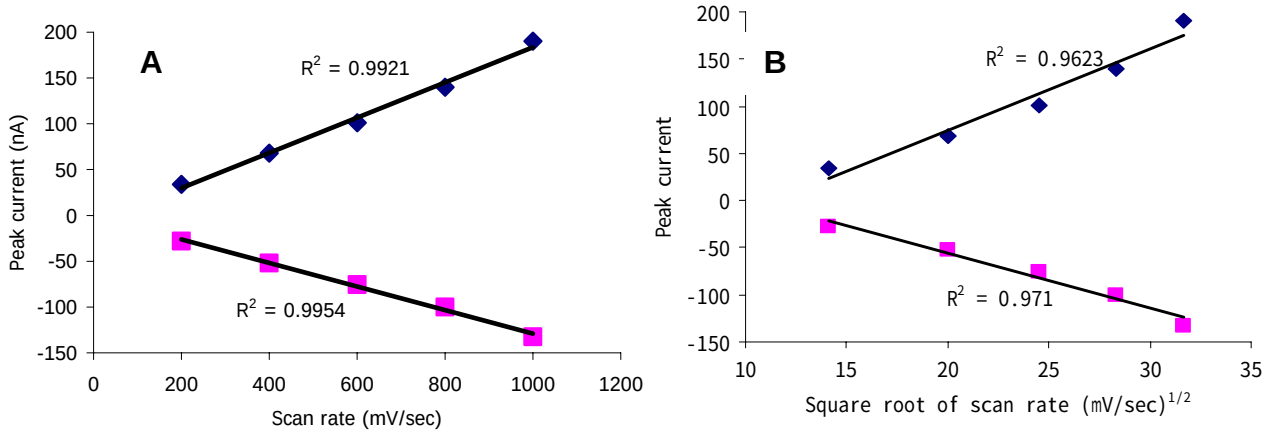

Figure S3 – The figure compares a plot of peak current versus scan rate to that of peak current versus the square root of scan rate. See text for details.

3. Current versus voltage dependence

The relationship of scan rate (v) vs. peak current (Ip) should be linear for immobilized protein and vary as the square root of peak current for freely diffusing protein. Figure S3 shows this dependence for the mutant K13A on C20Py/C19 SAMs. Panel A shows the linear relationship of scan rate with the peak current (the R^2 is 0.992, 0.995 for anodic and cathodic peak currents, respectively). Panel B shows the same data versus the square root of scan rate with the peak currents, (R^2 is 0.962, 0.971 for anodic and cathodic peak currents, respectively). Similar results were obtained for the native rat cytochrome c on the pyridine systems.

BIBLIOGRAPHY

[1] a) Willner, I.; Katz E. *Angew. Chem. Int. Ed.* **2000**, *39*, 1180; b) Willner, I.; Willner, B. *Trends in Biotech* **2001**, *19*, 222.

[2] Niki, K.; Hardy, W. R.; Hill, M. G.; Li, H.; Sprinkle, J. R.; Margoliash, E.; Fujita, K.; Tanimura, R.; Nakamura, N.; Ohno, H.; Richards, J. H.; Gray, H. B. *J. Phys. Chem. B.*, **2003**, 107, 9947

[3] a) Oevering, H.; Paddon-Row, M. N.; Heppener, M.; Oliver, A. M.; Costaris, E.; Verhoeven, J. W.; Hush, N. S. *J. Am. Chem. Soc.* **1987**, *109*, 3258; b) Closs, G. L.; Calcaterra, L. T.; Green, N. J.; Penfield, K. W.; Miller, J. R. *J. Phys. Chem.* **1986**, *90*, 3673; c) Helms, A.; Heiler, D.; McLendon, G. *J. Am. Chem. Soc.* **1992**, *114*, 6227; d) Helms, A.; Heiler, D.; McClendon G. *J. Am. Chem. Soc.* **1991**, *113*, 4325; e) Sakata, Y.; Tsue, H.; O'Neil, M. P.; Wiederrecht, G. P.; Wasielewski, M. R. *J. Am. Chem. Soc.* **1994**, *116*, 6904; f)) Penfield, K. W.; Miller, J. R.; Paddon-Row, M. N.; Cotsaris, E.; Oliver, A. M.; Hush, N. S. *J. Am.Chem. Soc.* **1987**, *109*, 5063; g) Pispisa, B.; Venanzi, M.; Palleschi, A. *J. Chem. Soc. Far. Trans*. **1994**, *90*, 435; h) Finckh, P.; Heitele, H.; Volk, M.; Michel-Beyerle, M. E. *J. Phys. Chem.* **1988**, *92*, 6584; i) Wasielewski, M. R.; Niemczyk, M. P.; Johnson, D. G.; Svec, W. A.; Minsek, D. W. *Tetrahedron* **1989**, *45*, 4785; j) Zehnacker, A.; Lahmani, F.; Van Walree, C. A.; Jenneskens, L. W. *J. Phys. Chem. A*. **2000**, *104*, 1377.

[4] Waldeck, D.H.; Zimmt, M.B. J. Phys. Chem. B. **2003**, *107* 3580.

[5] a) Jones, M. L.; Kurnikov, I. V.; Beratan, D. N. *J. Phys. Chem. A* **2002**, *106*, 2002, and references therein; b) Gray, H. B.; Winkler, J. R. *Ann. Rev. Biochem*. **1996**, *65*, 537.

[6] Moser, C.C.; Keske, J. M.; Warncke, K.; Farid, R. S.; Dutton, P.L. *Nature* **1992**, *355*, 796.

[7] Napper, A. M.; Liu, H.; Waldeck, D. H. *J. Phys. Chem. B* **2001,** *105*, 7699.

[8] Yamamoto, H.; Waldeck, D.H. J. Phys. Chem. B **2002,** *106,* 7469.

[9] These observations are consistent with the reduced enzyme activity of cytochrome *c* oxidase in the presence of the lysine-13 modified protein. See a) J.L. Theodorakis; E.A.E. Garber; J. McCracken; J.

Peisach; A. Schejter, E. Margoliash Biochim. Biophys. Acta, 1995, 1252, 103-113; b) Theodorakis, J. L.; Armes, L. G.; Margoliash, E. *Biochim. Biophys. Acta* **1995**, *1252*, 114; c) for diagram of binding by H.T. Smith; A.J. Ahmed; F. Millett J. Biol.. Chem. 1981, 256, 4984.

[10] Khoshtariya, D. E.; Wei, J.; Liu, Haiying; Yue, H.J., Waldeck, D. H., *J. Am. Chem. Soc.* **2003**, *125,* 7704.

[11] The primary evidence for the direct ligation between the pyridine and the heme unit is the negative shift in redox potential and the Raman spectra for the adsorbed protein. See a) Wei, J.; Liu, H.; Dick, A.; Yamamoto, H.; He, Y.; Waldeck, D. H. *J. Am. Chem. Soc.* **2002**, *124*, 9591; b) Murgida, D. H.; Hildebrandt, P.; Wei, J.; He, Y.-F.; Liu, H.; Waldeck, D. H., *J. Phys. Chem. B.,* **2004,** 108, 2261.

[12] Yamamoto, H.; Liu, H-Y.; Waldeck, D. H. *Chem. Commun.* **2001,** 1032.

13 Niki, K.; Pressler, K. R., Sprinkle, J. R., Li, H., Margoliash, E., *Russian J. of Electrochemistry*, **2002**, 38 (1) 74-78.

[14] a) Song, S.; Clark, R. A.; Bowden, E. F.; Tarlov, M. J. *J. Phys. Chem.* **1993**, *97*, 6364; b) Avila, A.; Gregory, B. W.; Niki, K.; Cotton, T. M. *J. Phys. Chem. B* **2000**, *104*, 2759.

[15] Napper, A. M.; Liu, H.; Waldeck, D. H. *J. Phys. Chem. B* **2001**, *105*, 7699.

[16] (a) Finklea, H. O. In *Electroanalytical Chemistry*; Bard, A. J., Rubinstein, I., Eds.; Marcel Dekker: New York, 1996; Vol. 19, p 109. (b) Chidsey, C. E. D. *Science* **1991**, *251*, 919. (c) Miller, C. J. In *Physical Methods in Electrochemistry*; Rubinstein, I., Ed. Wiley: New York, 1995; p 27.

[17] (a) Terrettaz, S.; Cheung, J.; Miller, C. J. *J. Am. Chem. Soc.* **1996**, *118*, 7857. (b) Winkler, J. R.; DiBilio, A. J.; Farrow, N. A.; Richards, J. H.; Gray, H. B. *Pure Appl. Chem.* **1999**, *71*, 1753.

[18] Wei, J.; Liu, H.-Y., Khoshtariya, D.E.; Yamamoto, H.; Dick, A.; Waldeck, D. H. *Angewandte Chem.,* **2002**, *41*, 4700.

[19] Feng, Z. Q.; Imabayashi, S.; Kakuichi, T.; Niki, K. *Chem. Soc. Faraday Trans.* **1997**, *93*, 1367.

[20] Attempts to adsorb the protein onto thinner films, gave a faradaic response but the apparent redox potential of the protein was shifted considerably from the other data. Because those results are suspect they are not included. Attempts to study thicker films were not fruitful because the signal is too weak.

[21] a) Sigfridsson, E.; Olsson, M. H. M. ; Ryde, U. *J. Phys. Chem. B* **2001** *105*, 5546; b) Muegge, I. ; Qi, P. X.; Wand, A. J.; Chu, Z. T.; Warshel, A. *J. Phys. Chem. B* **1997** *101*, 825; c) Lewgrand, N.; Boudon, A.; Simmonneaux, G. *Inorg. Chem.* **1996** *35* , 1627. d) Basu, G., Kitao, A.; Kuki, A.; Go, N. *J. Phys Chem. B* **1998,** *102*, 2085.

[22] Taylor, JR An Introduction to Error Analysis, Chapter 12, p261, 2nd edition, University Science Books, **1997**

CHAPTER 7 MOLECULAR CHIRALITY AND CHARGE HELICITY IN CHARGE TRANSFER THROUGH THROUGH SELF-ASSEMBLED CHIRAL MONOLAYERS[δ]

The effect of molecular chirality and charge helicity on electron transmissions is explored by photoelectrochemistry. Chiral scaffold molecules with a chromophore, 10,15,20-triphenyl-21,23H-porphyrin (H_2TPP), are self-assembled to gold surfaces by thiols to form a monolayer. The monolayer is characterized by UV-visible spectroscopy, electrochemistry, ellipsometry, contact angle, and scanning tunneling microscopy (STM) measurements. The cathodic photocurrent under illumination with a right or left circularly polarized light displays an asymmetry in magnitude with respect to a definite molecular chirality (left or right handedness). Induced circular dichroism of porphyrin aggregates, orbital angular momentum interaction in electron transfer as a superexchange model, are proposed as possible mechanisms for the asymmetry of photocurrents.

7-1. INTRODUCTION

The primary process of electron transfer underlies many chemical and biological reactions and is of primary importance in many technologies. Consequently, the nature of electron transfer (its dependence on energetics, nuclear degrees of freedom, and electronic coupling) has been under experimental and theoretical study for many years[1]. Despite these

[δ] This work is going to be submitted for publication coauthored by J. J. Wei, C. Schafmeister, G. Bird, A. Paul, R. Naaman, and D. H. Waldeck.

efforts, little attention has focused on the influence of chirality on electron transfer. This work examines the effect of molecular chirality on the photocurrent in film coated electrodes.

On a fundamental level, spin-polarized electrons have been used to perform chemistry and are implicated in the origin of chiral selectivity in biology[2]. Molecular chirality can be used to introduce a new control parameter for spin-sensitive devices. Naaman reported the first investigation of spin dependent electron transmission through thin chiral monolayer films and more recently observed an asymmetry for electron transmission through monolayers L (or D) polyalanine films.[3] The magnitude of the effect is 10^3 to 10^4 times larger than the chiral selectivity found for the interaction of polarized electrons with molecules that are not organized into two-dimensional arrays[4,5,6,7]. The observed asymmetry[8] in the transmission of polarized electrons changes from -0.09±0.02 to +0.10±0.02 upon changing the molecular handedness. Importantly, this 10% effect is induced by a 15% polarization of the initial photoelectron distribution. Thus, the selectivity to the incoming helicity of the electrons is as large as 70% and, within experimental error, could reach almost 100%.

In photoemission, the electron wavefunction can be delocalized among many chiral molecules in the film, whereas tunneling electrons are more localized. Hence, it is interesting to ask if such large effects are possible. Spin polarized tunneling has been observed in Metal-Oxide-GaAs (MOS) structures with an asymmetry of the order of 1% [9]. In these studies the polarized distribution of carriers is generated in the GaAs by circularly polarized light and tunneling occurs through a thin Al_2O_3 (2 to 20 nm) on Al. These findings show that it is possible to create the polarized distribution of charge carriers and observe asymmetry in electron tunneling.

In order to explore effect of molecular chirality, we studied how the photocurrent at surface modified gold electrodes depends on the light polarization. Although such systems have been constructed previously, the effects of chirality and spin polarization have not been explored. For example, Morita *et al.*[10] placed helical peptides on gold electrodes through thiol links and attached a carbazolyl chromophore to the outer end of the helix. Under photoexcitation of the chromophore, an electron is transferred to an acceptor (e.g., methylviologen), and the carbazolyl cation is reduced by the gold electrode. By measuring the dependence of the photocurrent on the polarization of the light field, the asymmetry in the electronic coupling can be evaluated quantitatively, as with the photoemission studies. We studied the asymmetry in photocurrent through films composed of porphyrins which are covelantly attached to chiral molecules.

7-2. EXPERIMENTAL SECTION

Materials: 5-(4-Carboxyphenyl)-10,15,20-triphenyl-21,23H-porphyrin (H_2TPP) (98%) was purchased from Porphyrin Systems GbR, in Germany. 4-Mercapto-1-butanol, 6-Mercapto-1-hexanol, 4-(dimethylamino)pyridine (DMAP, 99%), Triethanolamine (TEOA, 98%), Methyl viologen dichloride hydrate ($MV^{+/2+}$, 99%), Triethylamine (TEA, 99%), 1-[3-(dimethylamino)propyl]-3-ethylcarbodiimide (EDC, 98%), 1-Hydroxy-benzotriazole (HOBT, 99%) Trifluoroacetic acid (TFA, 99%) were purchased from Aldrich. TEA was distilled before use. Chloroform and acetonitrile (ACN 99.8%) are purchased from Aldrich. Absolute ethanol was purchased from Pharmco Products, Inc. Singly distilled water was purified by using a Barnstead-Nanopure system and had a resistivity of 18 MΩ-cm.

Scheme 7-1 shows the chiral scaffold molecules (L-Cys-(SS-Bb)$_4$-Porph (SS1), D-Cys-(RR-Bb)$_4$-Porph (RR1)) with their covalently linked porphyrin chromophore. The details of

preparation of the scaffold were reported previously[11]. The HPLC-MS data of cysteine and porphyrin attached scaffold we used in this work are reported in the supplemental information.

Scheme 7-1:

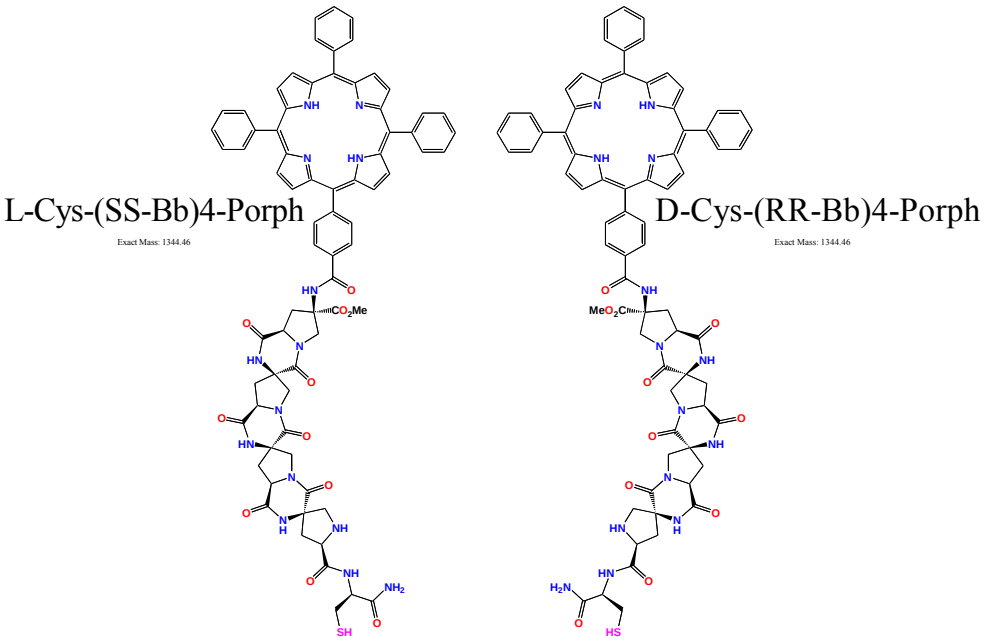

Evaporated gold slides were purchased from EMF Corp. The slides are coated with 1,000 angstroms Au on top of 50 angstroms Ti binder layer on 0.7 inch x 0.7 inch x 0.062 inch edges cut float glass.

Scaffold monolayer preparation: The gold slides were cleaned by inmersion into "piranha" (1:3 of H_2O_2 and 98% H_2SO_4) (**caution: this solution is dangerous**) for a few minutes, then rinsed by a large amount of deionized water (18MΩ), followed by ethanol, and then dried under an argon gas stream. The contact angle of the clean gold surfaces was checked with a small drop of water and was found to range from 55 to 65º. To self-assemble chiral scaffold helical structure onto the gold surface, the molecules were dissolved in a solution with

80%ACN/20%H_2O/0.1%TFA acid at a concentration of about 100 μM. The gold slides were incubated for 1-2 days for pure monolayer preparation at room temperature. These SAM coated gold slides were rinsed with 80%ACN/20%H_2O/0.1%TFA acid solvent before use. To prepare a mixed SAM of the scaffold/porphyrin and an alkanethiol C12 ($HS(CH_2)_{11}CH_3$), the pure scaffold SAM gold slide was immersed in a 80%ACN/20%H_2O/0.1%TFA solution with 1 mM concentration of C12 alkanethiol for a few (2-6) hours.

CD Spectroscopy: Circular dichroism spectroscopy was used to characterize the conformation of the scaffold molecules in solution. Room temperature circular dichroism spectra were obtained from a JASCO J-715 Spectrometer using a cell with a 1 cm optical path length.

UV-Visible Absorption Spectroscopy: The UV-Visible absorption of the free porphyrin and the porphyrin-scaffolds (L-Cys-(SS-Bb)$_4$-Porph, D-Cys-(RR-Bb)$_4$-Porph) were measured by using Agilent 8435 single beam UV-visible spectrometer. The beam was transmitted trough a 1 cm optical path length cell and the light absorption or transmission spectra were collected and recorded.

The surface UV-Visible absorption spectroscopy is performed by putting a gold coated (200 angstroms on glass, EMF Corp.) transparent slide at the light beam pathway. UV-visible spectra of the porphyrin scaffold SAM modified gold slides were recorded on the Agilent 8435 UV-visible spectrometer in a transmission mode.

Thickness Measurement: The SAM thickness was measured with a Gaertner L-117 Null ellipsometer. A linearly polarized He-Ne laser with wavelength 632.8 nm was used in the

measurement at incident angle 70º. The analyzer (A) can detect the change in the phase angle (Δ) and the amplitude change (Ψ) of the light after reflection from the sample. Refractive indexes of n1=1 for air, n2=1.45 for the organic molecular monolayer, and n3=0.166+3.22i for gold were used to calculate the thickness of films. The measurements were carried out at least three times at different locations for each sample, and the results are reported as an average of the measurements.

Contact Angle Measurement: Contact angles were measured with sessile water drops using a home-made setup and a microscopy goniometer at room temperature in air with humidity of 20-35%. Nearly all measurements were performed with drops that had a total volume of 10-20 microliters. The static contact angles after a water drop was made on the substrate and the syringe needle was no longer touching the drop. Measurements were carried out for at least three drops and averaged. Each drop was made on a new spot of the substrate for each sample.

STM Imaging: For the STM studies a Au(111) facet of a single crystalline bead (prepared by the Clavilier's method [12]) was used as the substrate. It was cleaned by immersion in hot piranha solution (1:3 H_2O_2 and H_2SO_4) for 5 min, followed by immersion in hot HNO_3 for 30 minutes. After each step the sample was rinsed by ultrasonication in ultrapure water (>18 MΩ-cm). The crystal was hydrogen flame annealed, and allowed to cool down to room temperature in air. The procedure for SAM formation on the Au (111) bead for STM was the same as the samples prepared for other experiments.

Cyclic Voltammetry Measurements: Cyclic voltammetry of electrodes modified with the porphyrin SAMs was carried out with a CHI180B potentiostat, which was USB connected and controlled by a Pentium computer running CHI software. The three electrode cell was composed of a platinum spiral counter electrode, an Ag/AgCl (3 M NaCl) reference electrode, and the porphyrin modified Au slide as a working electrode. The blocking behavior of the SAM modified electrodes were performed in a 0.5 M KCl and 1mM of $[Fe(CN)_6]^{3-/4-}$ solution.[13] The porphyrin coverage of the modified gold electrodes were estimated by performing cyclic voltammetry in 0.1 M of n-Bu_4NPF_6 in CH_2ClCH_2Cl or CH_2Cl_2 solution bubbled with argon gas.

Photocurrent Measurements: Photocurrent measurements of the porphyrins were performed using an amperometric (*i* versus *t*) technique through a CHI180B potentiostat. The same three electrode cell was used for the current measurement and the potential applied on the working electrode was controlled. For cathodic photocurrent measurements, a 10 mM MV^+ with saturated oxygen as electron acceptors and 0.1 M Na_2SO_4 aqueous solution was used as electrolyte solution. For anodic photocurrent measurements, 0.1 M Na_2SO_4, 0.1% TFA aqueous solution with bubbled argon gas was used as an electrolyte solution and contained 50 mM TEOA as an electron donor. For the wavelength dependent photocurrent measurements, a tungsten-halogen lamp of 25 mW was used as a light source and bandpass filters were used to control the wavelength from 200 nm to 800 nm. The energy of irradiation was measured by a power/energy meter (Newport, US).

For the polarization studies, a blue laser (He-Cd laser, Omnichrome) source with wavelength 440 nm was used as the excitation light, by way of a window in the electrochemical cell that was directly opposite to the gold slide electrode (see Figure 7- 1). In Figure 7- 1, an

optical setup was assembled to get either left/right circular polarized light or linear polarized light. A tilted quarter-wave plate (Alphalas Gmbh, Germany) behind a linearly polarizer serves as a circular polarizer to generate the left or right circular polarized light[14]. For each measurement, the energy was measured and recorded before and after the photocurrent measurement. During the measurements, the power-meter can be used to block the light beam. A generated photocurrent was recorded by a PC through a CHI180B potentiostat.

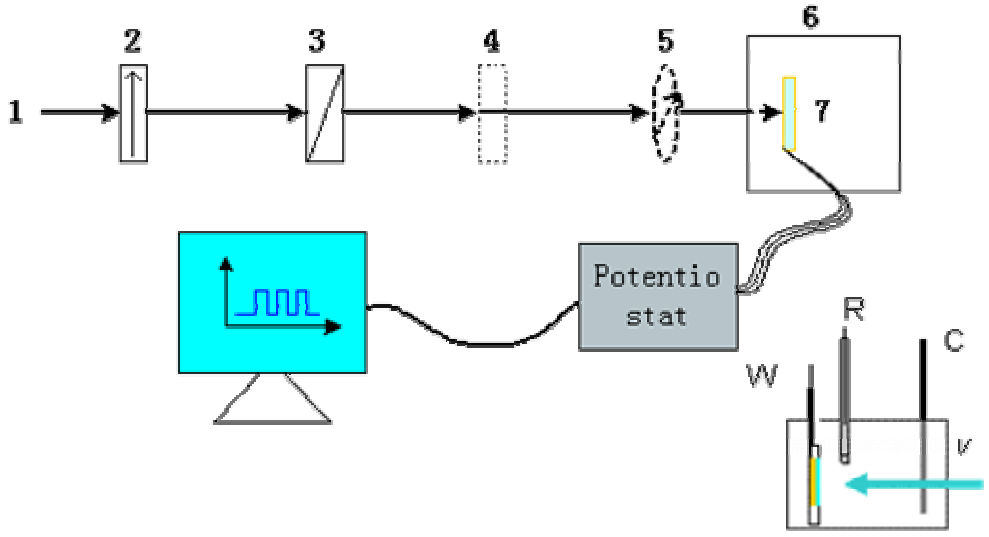

Figure 7- 1 A schematic diagram for the photocurrent and optical set-up for obtaining helicity (spin polarization). The components are 1-He-Cd laser source; 2-a linear polarizer; 3-a tilted quarter wave plate as circular polarizer; 4- a linear polarizer, if needed in the control experiments; 5-power meter for measuring light energy; 6-Faraday cage; 7-sample cell. 7 is a three-electrode cell as shown, W-working electrode; R-reference electrode, Ag/AgCl; C-counter electrode, Pt wire.

7-3. RESULTS

7-3-1. Characterization of Scaffold Molecules in Solution

Figure 7- 2 shows the absorption spectra of the SS1 and RR1 compounds in 80%ACN/20%H_2O/0.1%TFA acid solution. No significant peak shift is found in the Soret bands (λ_{max}=435 nm) and Q bands (649 nm for original porphyrin and 650 nm for scaffold porphyrins) in comparison to the free porphyrin (H_2TPP). This result suggests no significant change of the porphyrin electronic structure in SS1 and RR1. The Soret band at 435 nm is typical of a free base tetraphenylporphyrin (H_4TPP^{2+}) under acidic conditions (trifluoroacetic acid, TFA). The Q band shift to 650 nm corresponds to charge transition between the phenyls and the porphyrin ring. These results are consistent with previous semiempirical calculations[15] and experiments[16]. The Soret band shifts red in acidic acetonitrile solutions compared with dichloromethane solutions, paralleling changes from the brilliant green of the TFA solutions to reddish color of dichloromethane solutions.

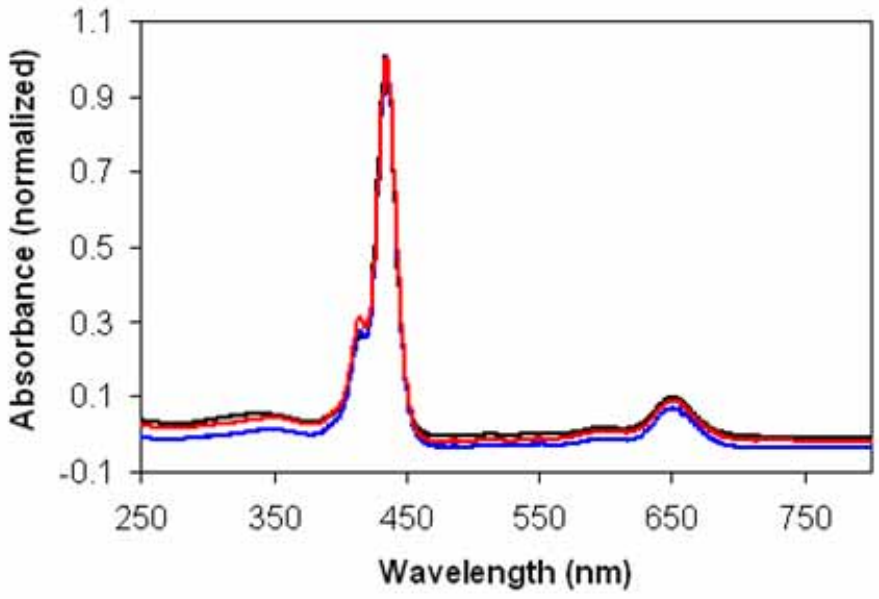

Figure 7- 2 Absorption spectra of porphyrin only (black), and RR1 (red) or SS1 (blue) scaffold with porphyrins attached in 80%ACN/20%H_2O/0.1%TFA acid solvent.

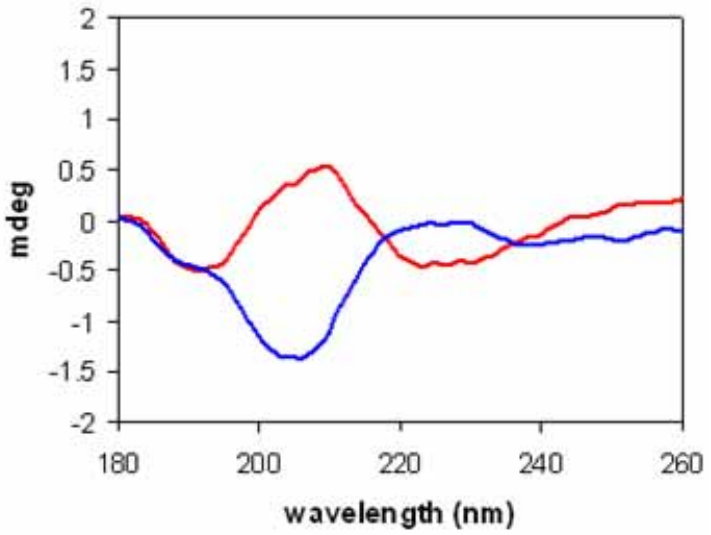

Figure 7- 3 CD spectra of chiral scaffold molecules, a) red (SS1, scaffold) and b) blue (RR1, scaffold).

CD spectra can reveal the helicity properties of a chiral molecule's electronic states. Figure 7- 3 shows CD spectra of the two porphyrin scaffolds for transitions observed in the far UV region (180-260 nm). It is well known that the transitions in a polypeptide involve the nonbonding electrons on the oxygen of the carbonyl group and the nearest nitrogen atoms. These transitions are $\pi \rightarrow \pi^*$ and $\pi \rightarrow \pi^*$. Normally, the $n \rightarrow \pi^*$ transition, analogous to that in ketones with lower intensity, occurs at the lower energy and depends on the extent of hydrogen bonding to the oxygen lone pairs, whereas the $\pi \rightarrow \pi^*$ transition, dominated by the carbonyl π-bond and affected by the involvement of nitrogen in the π orbitals occurs at higher energies ranging from 190 to 210 nm with change in conformation.[17] Hence we assign the peak at 225 nm in Figure 7- 3 to the $n \rightarrow \pi^*$ transitions in the scaffold chain, and the peak centered at 205 to the $\pi \rightarrow \pi^*$ transitions. The weak negative $n \rightarrow \pi^*$ band at 225 nm and strong positive $\pi \rightarrow \pi^*$ transition at 205 nm for the SS1 suggest a structure like β sheet with a β-turn in the

scaffold structure. The reversed signals of RR1 scaffold indicate an enantiomeric structure for the SS1 scaffold in the solution.

7-3-2. Characterization of RR1 and SS1 Films on Au

Contact angle and thickness: Table 7- 1 reports the static contact angles formed with pure water and the ellipsometrically determined thickness of SAMs composed of the 4-mer chiral scaffold porphyrin SAMs. The SAM coated gold surfaces are more hydrophobic than the bare gold slides contact angle (60±5º), presumably because of the hydrophobic nature of the terminal porphyrin. No difference in hydrophobicity with the chirality of the scaffold could be detected. The ellipsometric thicknesses for the films, 2.7 nm ± 0.5 nm for the 4-mer SS and 3.2 nm ± 0.4 nm for the 4-mer RR scaffold, are less than the length (3.1 nm) of optimized (energy minimized) 4-mer scaffold porphyrins. It was found that the thickness of the scaffold SAM increased if it was incubated in a 1 mM C12 alkanethiol at 80%ACN/20%H_2O/0.1%TFA solution for a few hours. For example, the thickness of a pure 4-mer SS scaffold SAM (2.8 nm) increased to 3.2 nm after 6 hours in a 1 mM C12 alkanethiol at 80%ACN/20%H_2O/0.1%TFA solution, and the contact angle of water increased from 80º to 92º. These results suggest that the scaffold molecules may not be compactly assembled at the surface, perhaps because of steric hindrance around the porphyrins.[18]

Table 7- 1 Summary of contact angle and thickness of the scaffold porphyrin derivatives SAMs at gold electrodes. Errors are one-standard deviations.

	SAMs of **SS1**	SAMs of **RR1**
Contact Angle (degree)	78 ± 5	76 ± 5
Thickness (nm)	2.7 ± 0.5	3.2 ± 0.4

Cyclic voltammetry: Voltammetry was used to characterize the electrochemical reaction of adsorbed scaffold porphyrin at gold slides with a surface area of *ca* 0.3 cm^2. Figure 7- 4 shows voltammagrams that were obtained at a scan rate of 0.4 V/sec and 0.2V/sec in a 0.2 M n-Bu_4NPF_6/CH_2Cl_2 solution. The porphyrin displays two strong oxidation peaks at around 1.12 V and 1.36 V vs Ag/AgCl reference electrodes at smaller scan rate (0.05 mV/sec). These two oxidation peaks are a characteristic signature for the porphyrin used in this research. The lack of reduction peaks at low scan rates arises from the instability of the oxidized porphyrin radicals in the solution.[19] The two oxidation peaks became weaker after multiple scans at a slow scan rate for quite a while (30 minutes) and finally disappeared, implying desorption or an inactivity of the resultant scaffold porphyrins. Similar voltammetry was observed from both SS1 and RR1 films (exposure area is 0.3 cm^2).

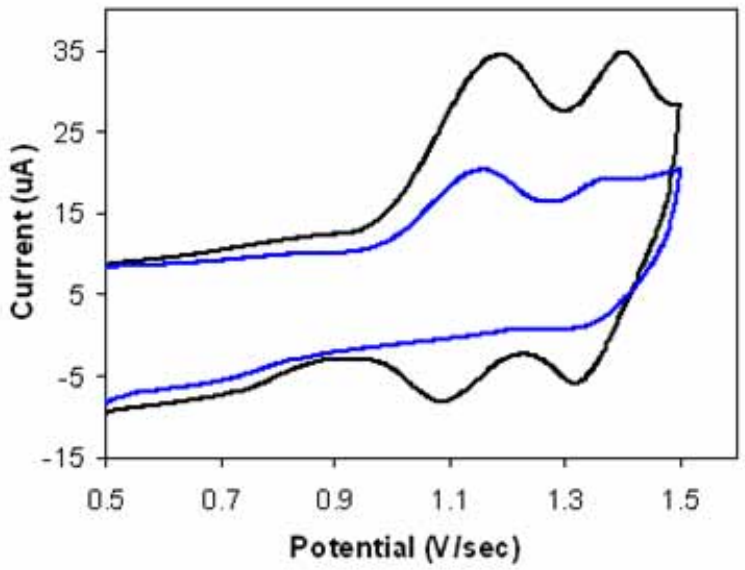

Figure 7- 4 Cylic voltammograms of porphyrin scaffold (RR1) film on a gold slide electrode, the experiment was carried out in n-Bu_4NPF_6/CH_2Cl_2 solution with saturated argon gas. The scan rate is 0.4 V/sec (black) and 0.2 V/sec (blue), Pt as counter electrode, and Ag/AgCl as reference electrode.

The surface concentration (electrochemical active species) of scaffold porphyrins was estimated by the amount of charge in the first oxidation peak and by the relationship between the peak current and scan rate. The two methods gave consistent results. Integration of the current peaks provide coverages (after correcting for surface roughness factor 1.2) of 4.6± 0.2 $\times 10^{-11}$mol/cm^2 for SS1 and 6.7±0.15 $\times 10^{-11}$ mol/cm^2 for RR1, almost the same as the coverage of alkane linked porphyrin on ITO [20] and gold electrodes[21]. This fractional coverage should be taken as a lower bound, since not all porphyrins at the surface are necessarily electrochemically active. Assuming that the porphyrin is in a planar conformation and has a circular shape with a 17.0 Å diameter, each porphyrin has an area of about 2.26 nm^2. For a compact porphyrin monolayer, the calculated coverage should be about 7.3×10^{-11}mol/cm^2. These results indicate that the RR1 material has a slightly more compact monolayer structure, consistent with the ellipsometric thickness measurements.

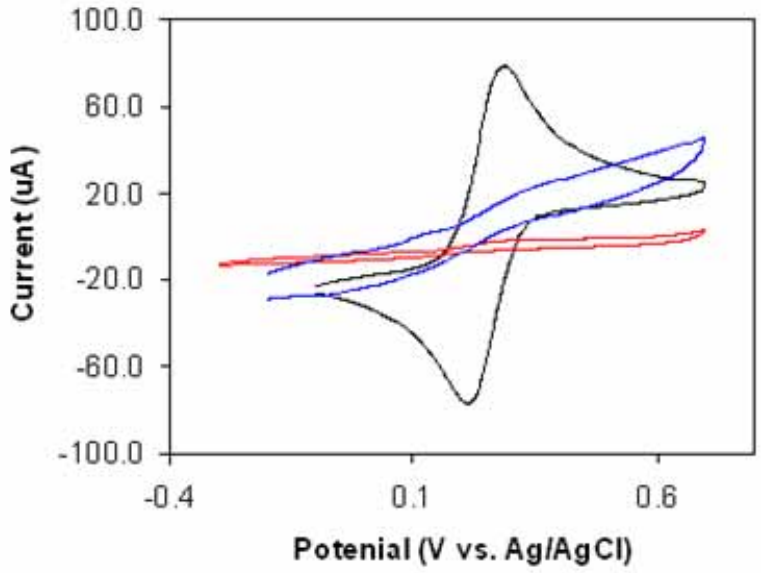

Figure 7- 5 Voltammograms are shown for three different electrodes in contact with an equimolar (1 mM) $Fe(CN)_6^{3-/4-}$ solution (black is bare gold electrode; blue is 4-mer-SS porphyrin-film electrode; red is 4-mer-RR-porphyrin-film electrode).

Current Blocking Behavior of the SAMs: The compactness of the monolayer films was probed by investigating how well they block faradaic current in an equimolar (1 mM) $Fe(CN)_6^{3-/4-}$ and 0.5 M KCl solution at a 100 mV/s scan (see Figure 7- 5). The bare gold electrode shows a typical faradaic response (black curve). In contrast, the scaffold porphyrins coated gold electrodes show a reduced current which is found commonly for insulating organic film coated electrodes. The blocking behavior indicates that the films inhibit the penetration of the ferricyanide and ferrocyanide redox species. A better blocking behavior was observed from the RR1 coated electrodes than the SS1 coated electrodes, implying a more tightly packed RR1 film than SS1 film.

Microscopy: Scanning tunneling microscopy (STM) was used to directly image the structures of the scaffold porphyrins at a gold surface. In Figure 7- 6, Panel A shows a topographic image for an electrode that has a pure film of the scaffold porphyrin adsorbed on the surface. Panel B shows the features of a cross-section through a domain in the image. The bright spot (domain) analyzed here is typical and has a width of 3-4 nm and a height of 2.2 nm. The vertical/height length scale shown here for the images is compressed over the actual physical height. The reasons for this artificial compression when observing alkanethiols have been discussed by others[22]. These dimensions imply an aggregate of about two scaffold porphyrin molecules. A statistical analysis of the image in Figure 7- 6 gives a domain coverage of 70% (roughly), larger than the coverage estimated from cyclic voltammagrams. It is evident from the image that the scaffold porphyrin form aggregates (nano-domains) but its dependence on preparation and solvent conditions has not yet been investigated.

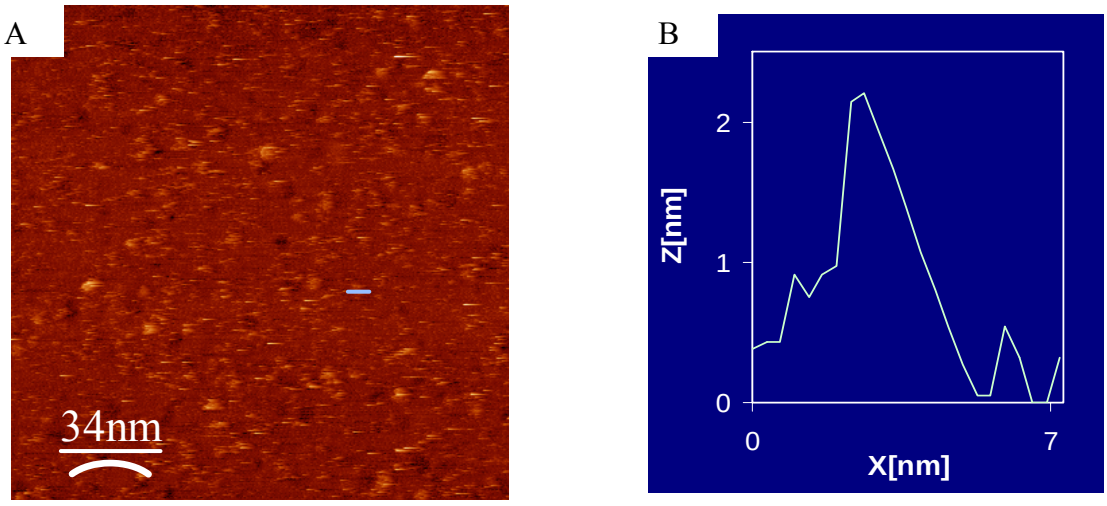

Figure 7- 6 STM images for pure scaffold (4-mer SS) porphyrin SAMs at gold surface. Panel A shows an actual topographic image for an electrode that has scaffold porphyrin adsorbed on the surface; Panel B shows the features of a cross-section.

UV-Visible Spectra of SAMs and Photocurrent Action Spectra: The action spectrum of scaffold porphyrins at gold electrodes was obtained by measuring the cathodic photocurrent under irradiation with light, whose wavelength was selected with bandpass filters. Figure 7- 7 shows the photocurrent action spectrum of an RR1 SAM, and the inset shows its absorbance spectra under different conditions. The greatest photocurrent is observed in the wavelength range of 400 to 450 nm, the Soret band region. The inset shows the spectrum of the porphyrin in 80%ACN/20%H_2O/0.1%TFA acid solvent (black curve), and the spectrum of the RR1 SAM in contact with the 80%ACN/20%H_2O/0.1%TFA acid solvent (blue curve). The films display a broadened Soret band (compared to the solution porphyrin). The photocurrent action spectrum and the absorption spectrum of scaffold porphyrins at the gold surface demonstrate that the porphyrin is the photoactive species responsible for the photocurrent generation.

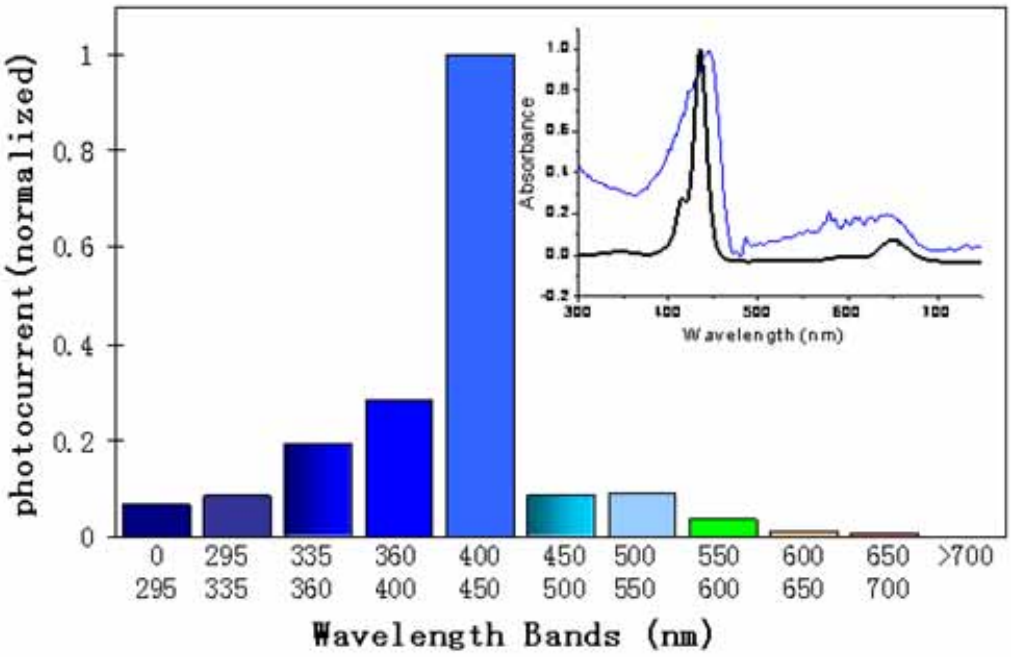

Figure 7- 7 A photocurrent action spectrum, the photocurrent is normalized to the maximum magnitude. The inserted graphic is the UV-visible spectra of scaffold porphyrins (RR1) in 80%ACN/20%H_2O/0.1%TFA acid solvent (black curve), the scaffold assembled at a gold coated transparent slide in a transmission mode in 80%ACN/20%H_2O/0.1%TFA acid solvent (blue curve), The spectra are normalized to Soret band absorbance for comparison, and the actual absorbance of the surface spectra is about 0.05 at surface.

The broadened Soret band of the porphyrins in the SAMs may have a number of possible origins, such as incompletely diprotonated free tetraphenylporphyrins[15,16] or interactions between porphyrins in the layer, either side-by-side (J aggregation, red shift) or face-to-face (H aggregation, blue shift)[23]. The Soret band (447) nm of the porphyrin scaffold films in 80%ACN/20%H_2O/0.1%TFA acid solvent is red shifted by about 12 nm, and is broadened compared to the spectra in solution. This red shift suggests a side by side interaction between porphyrins, suggesting the presence of J-aggregates, porphyrin monomers and/or weak interaction among porphyrins in the monolayer, which have been studied in the time resolved fluorescence by others.

Photoelectrochemical Characterization: Photoelectrochemical measurements were performed in a 0.1 M Na_2SO_4 aqueous electrolyte solution containing 10 mM methyl viologen (MV^+) and saturated oxygen as electron acceptors. A cathodic photocurrent from the porphyrin modified gold electrode was observed immediately upon irradiation by a 435 nm laser beam with a power of 1.35 mW at an applied voltage bias 0.0 V versus Ag/AgCl (3.0 M KCl) reference electrode. A time profile of the raw photocurrent for the SS1 SAM is shown in Figure 7- 8A at voltage bias 0.0 V. The dark current in cathodic photocurrent measurements changes positively with the voltage bias change from 0 to 0.6 V, indicating that the **SS1** SAM is not so compact. Nevertheless, the magnitude of photocurrent was stable, reproducible, and consistent with analogous systems reported earlier.[24] The photocurrent was linear in light intensity for laser powers <3.0 mW. Figure 7- 8B shows the voltage dependence of the photocurrent, which decreases monotonically with increasing positive bias. These results demonstrate that the electron flows from the gold electrode to the electrolyte through the scaffold porphyrin SAMs.

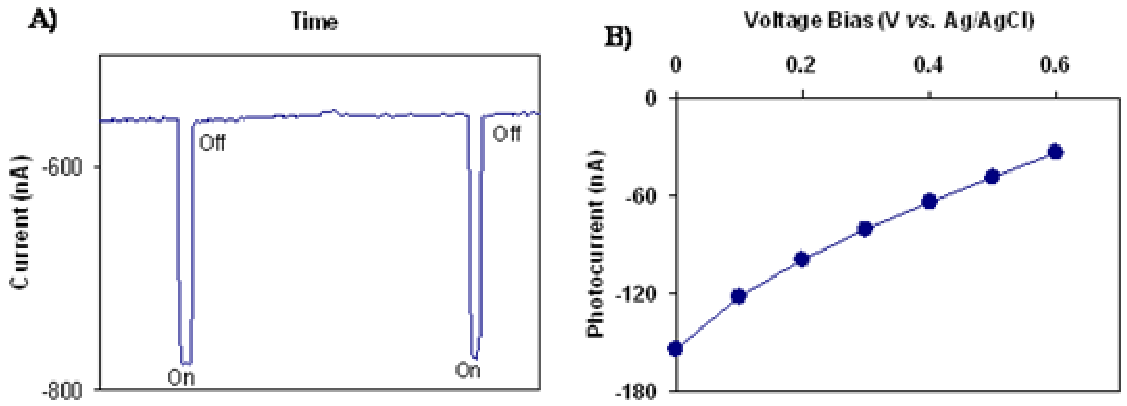

Figure 7- 8 A): Representative photoelectrochemical responses from the SS scaffold porphyrin SAM modified Au electrode at an applied voltage bias 0.0 V in a three-electrode cell (counter: Pt; reference: Ag/AgCl); B): The voltage bias dependent photocurrents for the Au-Porphyrin/$MV^{+/2+}$/Pt system. The wavelength of laser beam is 435 nm. The power of laser beam is 1.35 mW. The photocurrent in panel B is defined as $I_{photo}=I_{on}-I_{off}$

Similar wavelength responses and voltage dependencies were found for the RR1 and SS1 SAMs at gold electrodes. The average photocurrent generated at voltage bias 0.0 V under a laser beam with power of 1.35 mW was 230±50 nA and 320±50 nA for the and RRR1 scaffold pophyrin films, respectively. The photocurrent quantum yields[25], evaluated by a ratio of the number of generated charges to the number of incident photons, were 0.97% and 1.35% for and RRR1 SAMs, respectively, at gold surface. In addition, no photocurrent was observed from the bare gold electrodes under the irradiation with the laser beam. The photoelectrochemical characterization confirms that excitation of the porphyrin is responsible for photocurrent generation.

7-3-3. Asymmetry of Photocurrents and Charge Transfer with Helicities

Asymmetry of Photocurrent: To study the effect of molecular chirality and electron helicity on the electron transfer, photocurrent generated under irradiation with circularly polarized light (either right circularly polarized light, RCP, or left circularly polarized light, LCP) was examined for both SS1 and RR1 SAMs. Figure 7- 9 shows representative photocurrent spectra generated under the illumination with circular polarized light for the two chiral scaffold pophyrins at gold electrodes. The RCP or LCP polarizations were obtained by rotating a 1/4 wave plate at a specific tilt angle (see experimental section for details). The incident light intensity was measured for every illumination. For the SS1 scaffold porphyrins, the magnitude of photocurrent under LCP irradiation is slightly larger than that under RCP irradiation as shown in Figure 7- 9A. In contrast, the RR1 scaffold porphyins have a larger photocurrent under RCP irradiation than that under LCP irradiation (Figure 7- 9B). Although the preference is small, less than 1 %, it was highly reproducible for a given sample and stable over a period of many hours. In some cases,

measurements were performed over more than one day on the same electrode and found to be reproducible.

About ten electrodes for each sample type (RR1 and SS1) were studied under the same conditions and the propensities of the asymmetry in photocurrents were measured. Control experiments, using a linearly polarized laser beam, showed no asymmetry propensity.

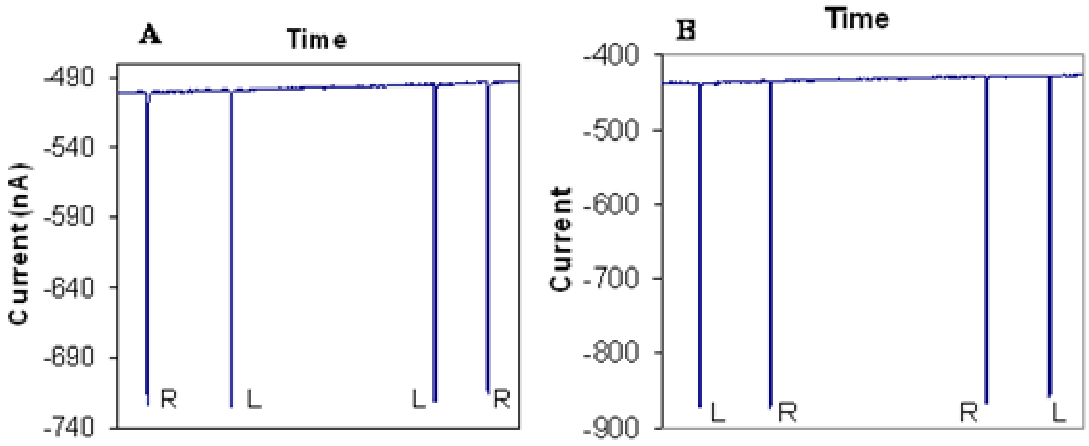

Figure 7- 9 Representative photocurrent spectra generated under circular polarized light for A) SS1 and B) RR1 scaffold porphyrins at gold electrodes. R and L represent right circularly polarized light and left circularly polarized light illumination, respectively. Voltage bias 0.0 V. The light energy was measured to be 1.3-1.4 mW.

Asymmetry Factor for Electron Transfer: An asymmetry factor *A* for the electron transfer was defined as

$$A = \frac{j(\sigma+) - j(\sigma-)}{j(\sigma+) + j(\sigma-)} \qquad 7\text{-}1$$

in which *j(σ+)* and *j(σ-)* are photocurrent intensities (normalized to light power) for RCP and LCP illumination at the same electrode, respectively. We can calculate the asymmetry factor for each pair by irradiation with RCP and LCP light. For the SS1 scaffold (4-mer) we obtain an

average asymmetry factor of -0.0048, and for the RR1 scaffold (4-mer) we obtain an average asymmetry factor of +0.0051.

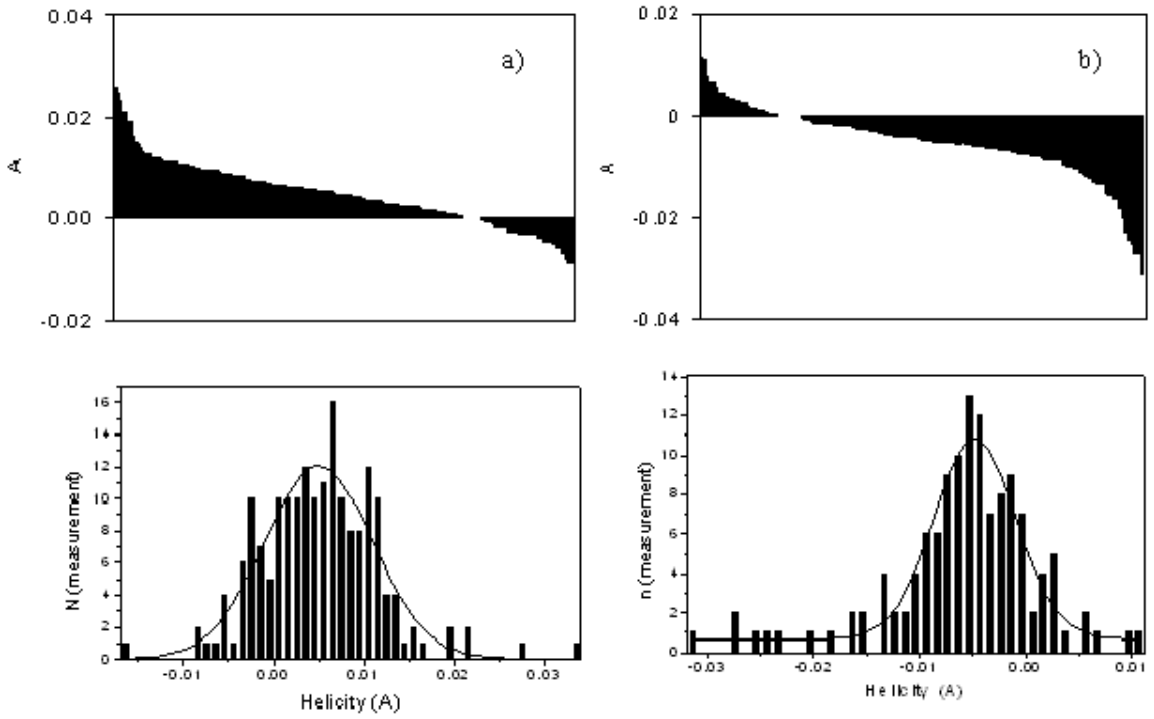

Figure 7- 10 Distributions of asymmetry factors and statistic analysis of the helicities. Where a) and b) respectively present the distributions of the asymmetry factors in a descending sort for RR1 and SS1 scaffold porphyrin electrodes, and c) and d) are the histograms of the number of observations vs. the observed ranges of asymmetry factors, corresponding to a) and b) respectively.

Figure 7- 10 plots the asymmetry factor obtained for all of the experiments. Panels a) and b) show the distribution (a descending sort) of asymmetry factors for RR1 and SS1 films, respectively. The asymmetry factors of the RR1 scaffold range from -0.016 to 0.032 and most of them are of positive values, whereas the asymmetry factor of SS1 scaffold range from –0.033 to 0.012 and most of them are of negative values. Panels c) and d) show a histogram (bin size of 0.001) for the asymmetry factors. A Gaussian function (solid curve in c and d) is fit to the distribution. This fit yields a standard deviation of 0.006 for the asymmetry factor of the RR1

scaffold and 0.004 for that of the SS1 scaffold. This analysis gives a 68% confidence level corresponding to the range of 0.0051±0.006 for the helicity of RR1 scaffold and -0.0048±0.004 for that of SS1 scaffold in this study. [26]

7-4. DISCUSSION

Structure of Scaffold Porphyrins at Gold Surface: The films formed by the SS1 and RR1 materials on gold were characterized through electrochemistry, STM, surface spectroscopy, ellipsometry, and contact angle measurements. The coverage obtained from the cyclic voltammetry indicates a well compact structure of RR1 scaffold pophyrins at gold surface, whereas a poorer packed monolayer structure of SS1 scaffold porphyrins for some uncovered reasons (the steric hindrance of porphyrins and the steric structure or orientation of the link chain). The thickness and contact angle measurements indicate monolayer structure with an organized orientation of scaffold molecules, but may be tilted from the surface to some extent. The STM image in Figure 6 demonstrates that the scaffold porphyrins form domains with areas of about 9 to 20 nm^2. A similar structure for porphyrin materials has been observed in alkanethiol monolayers on gold. The broadened and shifted Soret band (see Figure 7- 7) suggests some aggregation and interaction between the porphyrins.

Mechanism of Photocurrent Generation and Electron Transfer: Figure 7- 8 demonstrates that the photocurrent is generated by illumination of the porphyrin Soret band. The mechanism of photocurrent generation from the porphyrin at gold electrodes was established by Imahori et al[19, 24], and the current findings are consistent with that mechanism.

Figure 7- 11 summarizes the mechanism for cathodic photocurrent generation. Approximating the excited singlet and triplet state energies (relative to the ground state) of porphyrin at the gold surface by their solution values, their redox potentials are estimated to be -0.9 V for $^1TPP^*/TPP^+$ and -0.4 V for $^3TPP^*/TPP^+$, using a potential of 1.1 V versus Ag/AgCl for the ground state. In the cathodic photocurrent measurements, the electron acceptors, methyl

viologen (MV^{2+}/MV^{+}) and oxygen (O_2/O_2^{-}), have redox potentials of -0.62 V and -0.48 V, respectively. Thus the photoinduced electron transfer only occurs from the excited singlet porphyrin to MV^{2+} and/or O_2. The reduced acceptors, MV^{+} and O_2^{-}, can either reduce the porphyrin cation radicals or diffuse to the Pt counter electrode to generate a cathodic photocurrent. Those cation radicals that do not undergo recombination with the electron acceptors are reduced by electrons from the gold electrode. This phenomenon explains why the magnitude of the cathodic photocurrent depends on the applied voltage.

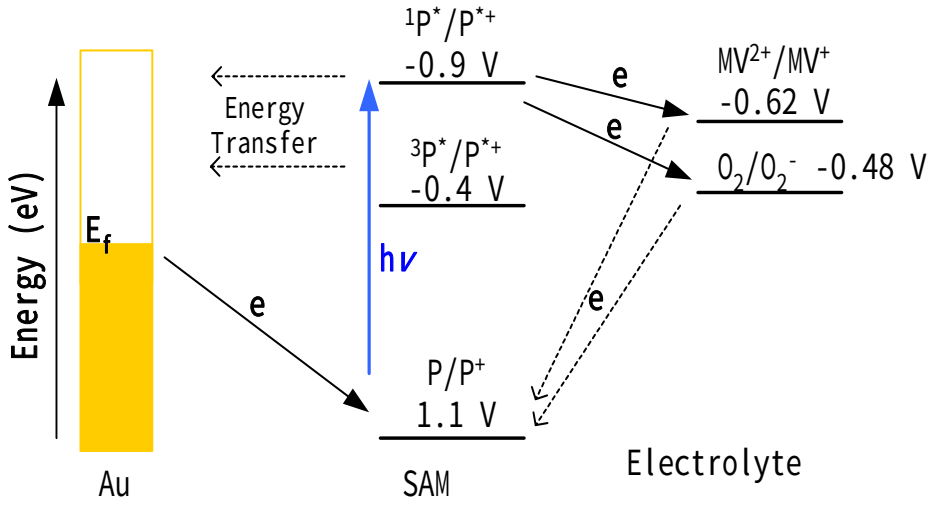

Figure 7- 11 This diagram is for cathodic photocurrent, and diagram B is for the anodic photocurrent. P represents the porphyrin attached.

The photocurrent generation process can be divided to be three steps, i.e. the charge tunneling from gold to the HOMO of the pophyrin, the photo-excitation from HOMO to excited states (LUMO), and the charge transfer from the LUMO of the porphyrin to the electron acceptors in solution. If the charge transfer from the LUMO to solution is faster than the charge tunneling through scaffold chain, the magnitude of photocurrent depends on the efficiency of charge tunneling through the scaffold linker[27]. Whereas when the electron tunneling through the

scaffold chain is more efficient than the charge transfer to the acceptor in solution, the later step will limit the magnitude of the photocurrent. The photoexcitation of porphyrin and its subsequent relaxation are most likely the fastest steps in the process. In this case, energy transfer quenching of the excited singlet porphyrin by the metal electrode would control the quantum yield of photocurrent generation.[19,24] Previous studies of H_2TPP both in various organic solvents[28] and surfaces[24,29] have found that the lifetime of excited singlet state of H_2TPP is tens of picoseconds for porphyrins linked by alkanethiol at gold surfaces, compared to 10 nanoseconds in bulk solvents. The lifetime of excited singlet electrons may play an important role, not only in the photocurrent generation, but also the importance of the interaction between the 'helicity' of the porphyrin excited state and the scaffold's chirality. In particular, the fast population relaxation of the porphyrin means that the photocurrent arises from short-lived excited states that may retain significant polarization from the exciting light field. Possible mechanisms for the electron helicity to bridge chirality interaction will be discussed below.

Electronic Helicities of Excited Porphyrins: It is well known that if a molecule is electronically excited by absorption of a photon, its angular momentum changes because the photon carries angular momentum (spin 1). The generation of circularly polarized light selects photons with a particular component of their angular momentum (spin orientation).[30] The transfer of the light field's polarization to molecules is well established, e.g., circular polarized molecular fluorescence[31]and circular dichroism spectroscopy. Earlier work has demonstrated the generation of electron spin polarization by circularly polarized light in photoemission at surfaces,[32] electron scattering of gas phase,[33] and other fundamental studies.[34] In this work, the asymmetry of photocurrent, generated by irradiation of porphyrin chromophores with circular polarized light,

could arise from electron transfer (electron tunneling) that depends on the charge carrier (electron or hole) polarization.

The observed asymmetry propensities in Figure 7- 10 and their correspondence with the chiral scaffold-linked porphyrin demonstrate a relationship between electron helicity (spin polarization) and molecular chirality in the electron transfer. For cathodic photocurrent, the electronic helicity induced by left circularly polarized light facilitates charge transport through the SS1 scaffold, while it retards that charge transfer through the RR1 scaffold. On the other hand, the right circular polarized light enhances photocurrent through the RR1 scaffold chain and decreases photocurrent through the SS1 scaffold. This result uncovers a coupling between the electronic state's spin polarization and the molecular chirality, presumably because of the electronic dissymmetry in the superexchange pathways.

Possible Mechanisms for electron (or hole) helicity and molecular chirality coupling in electron transfer: Common theoretical treatments of superexchange do not address whether molecular chirality is important, and often such models use simple nearest neighbor couplings which may not incorporate the overall chirality of the molecule (or electronic wavefunction) in a clear way. Three different mechanisms might explain the phenomenon that we observe: 1) circular dichroism of the layers, 2) a dependence on the orbital polarization of the porphyrin, or 3) a dependence on the spin polarization of the electron.

1. Circular Dichroism:

The absorption spectra in solution have Soret bands (B bands) for the SS1 and RR1 porphyrin monomers. However, the SS1 (and RR1) porphyrin's Soret band does not display a CD signal. The broadened and red shifted Soret band for the films suggest a side by side

interaction between porphyrins at the surface, *J*-aggregation of porphyrin complexes. The spectrum in the film is consistent with studies on various bis- and multiporphyrin systems[35], and the exciton coupling theory[36] for porphyrin complexes[37,38]. The Soret band (B band) of a porphyrin monomer has two components whose transition dipoles are oriented perpendicular to each other (Figure 7- 2). In the porphyrin aggregate, the exciton interaction splits the B bands and they have opposite behavior in CD experiments because their dipoles are perpendicular.

Because of the different chirality of the scaffolds, the porphyrin-porphyrin interaction may have a different "sense" that arises from the geometry of packing and gives rise to different CD signals. This kind of induced electronic "helicity" has been reported from porphyrin assemblies on DNA[39], bis-porphyrin derivatives[37,] a helical cyanine dye J-aggregate induced by DNA-templates[40], and other chiral induced systems[41]. If this occurs in the SAM film, then the differential absorption of the circularly polarized exciting light could give rise to differential excited state populations. This dichroism could then give rise to the asymmetry in the photocurrent measurements.

2. Orbital Angular Momentum:

In the case of metal-centered or diprotonated porphyrins, the inner perimeter of the ring of porphyrins is a 16 atom, 18 π-electron aromatic system with a D_{4h} point group symmetry.[42] A 4-obital-model[43] accounts for porphyrins' optical properties, the Soret band arises from two $\pi \rightarrow \pi^*$ electronic transitions between the two highest occupied molecular orbitals (HOMO) to the lowest unoccupied molecular orbitals (LUMO) involving changes in orbital angular momentum of $\Delta M_L = \pm 1$. For a porphyrin monomer of the symmetry D_{4h}, the two HOMO's energy level are so close that they can be viewed as essentially degenerate. For a given circularly

polarized light (either LCP or RCP) illumination, the excitation of porphyrins at the Soret band results in a nonequilibrium (helicity) of orbital angular momentum at both the HOMO and LUMO. For instance, the RCP irradiation of the porphyrin only causes a transition involving change in orbital angular momentum of +1.

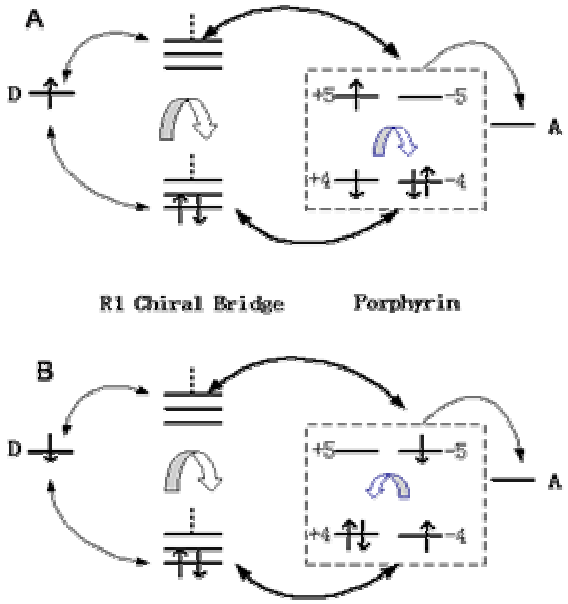

Figure 7- 12 A diagram illustrates a superexchange interaction in a RR1 chiral bridge system with Right (panel A) or Left (panel B) circularly polarized light. D is electron donor (Au electrode), A is electron acceptor. The thin line arrows (two ends) present donor-bridge coupling, the thick line arrows represent porphyrin-bridge coupling. The block arrows present the bridge handedness or excitation light helicity.

Assuming that the charge tunneling step in the photocurrent generation process is the limit of magnitude of photocurrent, the influence of the electronic helicity on the coupling to the chiral bridge unit may provide an alternative explanation for asymmetry in the photocurrent by way of a bridge-mediated superexchange mechanism[44]. Often, one uses the superexchange mechanism to describe electron transfer as a one-particle process, i.e. an electron transfers through available unoccupied orbitals and/or a "hole" passes through the manifold of filled orbitals. In this model, the electronic coupling arises from not only the nearest neighbor

couplings, but also by non-nearest-neighbor interactions[45] which are particularly important for long bridge systems. If the electronic chirality of the bridge and the porphyrin orbital are different, then their coupling may be different than if they are the same symmetry.

Figure 7- 12 illustrates this hypothesis for a right handed bridge-porphyrin system. When the porphyrins are excited with RCP, a transition with a change of +1 angular momentum occurs, and generates an excitation of the orbital with positive angular momentum. The porphyrin orbitals interact differently with the right handedness bridge orbitals than with the left handed bridge orbitals. In contrast to RCP light, LCP light should cause an opposite effect since they excite the opposite porphyrin orbitals. Whether the right handed porphyrin couples more strongly with a right handed bridge than a left handed bridge is not known, however, these experiments indicate the donor bridge states of the same chirality couple more strongly. For the right handed bridge, the magnitude of photocurrent is stronger under irradiation with RCP light than that with LCP, while for the left handed bridge, the magnitude of photocurrent is larger under irradiation with LCP light than that with RCP. The observed asymmetry can be ascribed to the difference of electronic couplings from the orbital interaction between the chiral bridge and the orbital "helicity" of porphyrins.

3. Electron Spin Polarization:

As discussed in the introduction, excitation of a Au film can generate spin polarized electrons and the spin polarization injection of electrons in solids has been well studied[30,46]. The photocurrent data reveal that the photocurrent arises from electronic excitation of the porphyrins; the photocurrent generation appears to arise from singlet state of the excited porphyrins which can't be spin polarized. Hence, this mechanism is discounted here.

7-5. CONCLUSIONS

Porphyrins on chiral scaffolds have been assembled on gold electrodes, and the effects of molecular chirality and the light helicity on the photocurrent generation have been studied. The photocurrent displays asymmetry when the chiral monolayer is irradiated by left and right circularly polarized light. The asymmetry factor obtained for a right handed monolayer is 0.0051±0.006 and for a left handed monolayer is -0.0048±0.004 with confidence of 68%. Experimental and theoretical studies on the coupling of electron helicity and molecular chirality in the gas phase have shown asymmetry factors to be 10^{-3}-10^{-4} for oriented molecules and 10^{-4}-10^{-5} for unoriented molecules[47]. The asymmetry factors obtained in this work with the orientated chiral chain are one order greater than those found from electron scattering in gas phase but less than that of the photoemission through multiple chiral LB film.

Two explanations are proposed for the phenomena. Porphyrin-porphyrin interaction in the film could cause a preferential absorption, circular dichroism, in the layer, which is reflected in the photocurrent. Alternatively, the orbital polarization of the excited porphyrin and its effects on the superexchange coupling could explain the asymmetry.

The relaxation of the orbital polarization should affect the importance of electron helicity on the coupling to the chiral bridge. If the orbital polarization relaxes rapidly, the nonequilibrium distribution will become depolarized and the influence of molecular chirality will be weak. In the limit of fast relaxation, the value of asymmetry factors would be small.[34] However, to better understand the mechanism of the observation, further theoretical and experimental work is needed.

BIBLIOGRAPHY

1 a) *Electron-Transfer from Isolated Molecules to Biomolecules Adv. Chem. Phys*. J. Jortner and M. Bixon eds. Vols. 106 and 107 (Wiley, NY, **1999**); b) Kuznetsov, A. M. *Charge transfer in Physics, Chemistry and Biology*; (Gordon & Breach, NY, **1995**)

2 Avalos, M., Babiano, R. P., Cintas, J. L. Jiménez, Palacios, J. C. and Barron, L. D. *Chem. Rev.* **1998,** 98, 2391

3 Ray, K., Ananthavel, S.P., Waldeck, D.H., Naaman, R. *Science***, 1999**, 283, 814

4 Bonner, W. A., *Chirality*, **2000**, 12**,** 114 and references therein;

5 a) Nolting, C., Mayer, S., Kessler, J., *J. Phys. B: At. Mol. Opt. Phys.* **1997**, 30**,** 5491, b) Mayer, S.; Nolting, C. Kessler, J. J. Phys. B, **1996**, 29, 3497-3511; c) Mayer, S., Kessler, J., *Phys. Rev. Lett.* **1995,** 74**,** 4803.

6 a) Beerlage, M. J. M., Farago, P.S., Vanderwiel, M.J. *J. Phys. B : At. Mol. Phys*. **1981**, 14**,** 3245, b) Hegstrom, R. A., Rein, D.W., Sandars, P.G.H., *J. Chem. Phys.* **1980**, 73, 2329; c) Ulbricht, T. L. V., Vester, F., *Tetrahedron* **1962,** 18**,** 629-637; d) Bonner, W. A., Van Dort, M. A., Yearian, M. R. *Nature* **1975**, 258**,** 419-421.

7 a) Blum, K., Thompson, D. G., *Adv. Atomic, Molecular and Optical Physics* **1997**, 38, 39; b) Johnston, C., Blum, K., Thompson, D., *J. Phys. B: At. Mol. Opt. Phys.* **1993**, 26, 965; c) Thompson, D.G., Kinnin, M., *J. Phys. B: At. Mol. Opt. Phys.* **1995**, 28, 2473; d) Smith, I.M., Thompson, D. G., Blum, K., *J. Phys. B: At. Mol. Opt. Phys*. 1998, 31**,** 4029.

8 The asymmetry parameter is defined as $A \equiv \frac{I(+P) - I(-P)}{I(+P) + I(-P)}$ where I(+P) and I(-P) are the transmission of the electron beam (or photocurrent) with spin angular momentum oriented parallel (+) and antiparallel (-) to its velocity vector.

9 Prins, M. W. J., van Kempen, H., de Groot, R. A., van Roy, W. and De *Boeck* J., *J. Phys. Condens. Matter* **1995,** 7 (1) 9447.

10 Morita, T., Kimura, S., Kobayashi, S., Imanishi, Y. *J. Am. Chem. Soc.* **2000**, 122 2850.

11 Levins C. G. and Schafmeister, C. E. T*J. Am. Chem. Soc.***2003**, *125*, 4702-4703.

12 Clavilier, J. *J. Electroanal. Chem*., **1980**. *107*, 205

13 Wei, J. J.; Liu, H. Y.; Dick, A. R.; Yamamoto, H.; He, Y. F.; Waldeck, D. H. *J. Am. Chem. Soc.* **2002**, *124*, 9591-9599.

14 a) Hecht, E. 1987, *Optics*, 2nd ed. Reading, MA: Addison-Wesley Publishing Co.; b) Yariv, A.; Yeh, P., 1984. *Optical Waves in Crystals.* New York: John Wiley and Sons

15. Vitasovic, M.; Gouterman, M.; Linschitz, H. *J. Porphyrins Phthalocyanines,* **2001**, *5*, 191-197

16 Ingar H. Wasbotten,† Jeanet Conradie,‡ and Abhik Ghosh*, *J. Phys. Chem. B* **2003**, *107,* 3613-3623.

17 a) Rodger, A.; Norden, B., *Circular Dichroism and Linear Dichroism*; Oxford University Press, Chapter 2, Chapter 6, 1997; b) Fasman, G. D., Edt. Circular Dichroism and The Conformational Analysis of Biomolecules.

18 Imahori, H.; Norieda, H.; Ozawa, S.; Ushida, K.; Yamada, H.; Azuma, T.; Tamaki, K.; Sakata, Y. *Langmuir*, **1998**, 14, 5335-5338

19 Yamada, H.; Imahori, H.; Nishimura, Y.; Yamazaki, I.; Ahn, TK.; Kim, SK.; Kim, D.; Fukuzumi S. *J. Am. Chem. Soc.* **2002**, *124*, 9129-9139.

20 Hasobe, T.; Imahori, H.; Yamada, H.; Sato, T.; Ohkubo, K.; Fukuzumi, S. *Nano Letter,* **2003**, 3, 409-412.

21 Boeckl, M.S.; Bramblett, A.L.; Hauch, K.D.; Sasaki, T.; Ratner, B.D.; and Rogers, Jr. J. W. *Langmuir*, **2000**, *16,* 5644-5653

22 a) Weiss, P. S.; Bumm, L.A.; Dunbar, T.D.; Burgin, T.P.; Tour, J.M.; Allara, D.L. Ann. N. Y. Acad. Sci. **1998**, 852, 145; b) Gorman, C.B.; Carrol, R.L.; He, Y.; Tian, F.; Fuierer, R. *Langmuir* **2000**,16, 6312.

23 a) Akins, D. L.; O¬ zcüelik, S.; Zhu, H.-R.; Guo, C. *J. Phys. Chem.* **1996**, *100*, 14390. b) Maiti, N. C.; Mazumdar, S.; Periasamy, N. *J. Phys. Chem. B* **1998**, *102*, 1528. c) Khairutdinov, R. F.; Serpone, N. *J. Phys. Chem. B* **1999**, *103*, 761.d) Osuka, A.; Maruyama, K. *J. Am. Chem. Soc.* **1988**, *110*, 4454.

24 Imahori, H; Norieda, H.; Nishimura, Y.; Yamazaki, I; Higuchi, K.; Kato, N.; Motohiro, T.; Yamada, H.; Tamaki, K.; Arimura, M.; Sakata.; Y. *J. Phys. Chem. B* **2000**, *104,* 1253-1260

25 The equation for the quantum yield is $\phi = N_{out}/N_{in} = (I_p hc/AP_i e\lambda)$, where *Nout* is the charge generated, *Nin* is the number of incident photons, *Ip* is the measured photocurrent, *h* is Plank constant, c is light velocity, *Pl* is the power of light beam, *e* is elementary charge, λ is the wavelength of light, A is the absorbance factor at surface at Soret band and here a value of 0.05 is used including reflection.

26 Taylor, J. R. An introduction of Error Analysis 2nd et. 1997, 149

27 a) Wei, JJ.; Liu, HY,; KhoshtariyaTaT, DE.; Yamamoto, H.; Dick, A.; Waldeck, DH. *Angewandte Chem, Int. Ed.*, **2002,** 41, 4700-4703, b) Khoshtariya, D. E.; Wei, JJ.; Liu, Hy; Yue, HJ., Waldeck, DH., *J. Am. Chem. Soc*., **2003,** 125, 7704-7714, c) Napper, A. M.; Liu, H.Y.; and Waldeck, D. H. *J. Phys. CHem.* B **2001,** 105, 7699-7707.

28 a) Chirvony, V.S.; Hoek, A.; Galievsky, V. A.; Sazanovich, I. V.; Schaafsma, T. J.; Holten, D. *J. Phys. Chem.* B **2000**, 104, 9909-9917, b) Gentemann, S.; Medforth, C. J.; Forsyth, T. P.; Nurco, D. J.; Smith, K. M.; Fajer, J.; Holten, D. *J. Am. Chem. Soc.* **1994**, *116*, 7363.

29 a) Dick, H. A.; Bolton, J. R.; Picard, G.; Munger, G.; Leblanc, R. M. *Langmuir* **1988**, *4*, 133. b) Imahori, H. Norieda, H.; Yamada, H.; Nishimura, Y.; Yamazaki, I.; Sakata,Y and Fukuzumi, S. *J. Am. Chem. Soc.* **2001,** *123,* 100-110

30 Meier, F.; Zakharchenya, B.P. Optical Orientation: Modern Problems in Condensed Matter Sciences. **1984**.

[31] A) Green, A. S.; Gallup, G. A.; Rosenberry, M. A.; and Gay, T. J. *Phys. Review Lett*. **2004**, 92 (9) 093201 b) Fiederling, R.; Keim, M.; Reiscjer, G.; Ossau, W.; Schmidt, G.; Waag, A.; Molenkamp, L.W., *Nature*, **1999**, 420, 787-790.

[32] Starke, K.; Kaduvela, A. P.; Liu, Y.; Johnson, P. D.; Van Hove, m. A.; Fadley, C. S.; Chakarian, V.; Chaban, E. E.; Meigs, G.; and Chen, C. T. *Phys. Review* B, **1996**, 53, R10544.

[33] a) Heinzmann, U.; Schonhense, G.; and Kessler, J. *Phys. Rev. Lett.* **1979**, 42, 1603; b) Schonhense, G.; Ayers, A.; Friess, U.; Schafers, F.; and U. Heinzmann, *Phys. Rev. Lett.* **1985**, 54, 547

[34] a) Ivchenko, E. L. and Pikus, G. E. *Superlattices and Other Heterostructures. Symmetry and Optical Phenomena* (Springer, Berlin, 1997) b) Prinz, G. A. Spin Transport. *Phys. Today* **1995**, 48 (4) 58-63

[35] (a) Arnold, D. P. *Synlett* **1999**, 296. (b) Anderson, H. L. *Chem. Commun.***1999**, 2323. (c) Kuciauskas, D.; Liddell, P. A.; Lin, S.; Johnson, T. E.; Weghorn, S. J.; Lindsey, J. S.; Moore, A. L.; Moore, T. A.; Gust, D. *J. Am. Chem. Soc.* **1999**, *121*, 8604. (d) Ruhlmann, L.; Lobstein, S.; Gross, M.; Giraudeau, A. *J. Org. Chem.* **1999**, *64*, 1352. (e) Ogawa, T.; Nishimoto, Y.; Yoshida, N.; Ono, N.; Osuka, A. *Angew. Chem., Int. Ed.* **1999**, *38*, 176.

[36] Kasha, M.; Rawls, H. R.; El-Bayoumi, M. A. *Pure Appl. Chem.* **1965**, *11*, 371.

[37] a) Pescitelli, G.; Gabriel, S.; Wang,Y.; Fleischhauer, J.; Woody, RW.; Berova, N. *J. Am. Chem. Soc***. 2003**, 125, 7613-7628; b) Borovkov, V. V.; Lintuluoto, J. M.; Fujiki, M.; Inoue, Y. *J. Am. Chem. Soc.* **2000**, *122*, 4403-4407; (c) Borovkov, V. V.; Lintuluoto, J. M.; Sugeta, H.; Fujiki, M.; Arakawa, R.; Inoue, Y. *J. Am. Chem. Soc.* **2002**, *124*, 2993-3006. d) Lintuluoto, J. M.; Borovkov, V. V.; Inoue, Y. *J. Am. Chem. Soc.* **2002**, *124*, 13676-13677. Borovkov, V. V.; Lintuluoto, J. M.; Inoue, Y. *J. Phys. Chem. A* **2000**, *104*, 9213-9219. (e) Borovkov, V. V.; Lintuluoto, J. M.; Inoue, Y. *Org. Lett.* **2000**, *2*, 1565-1568, f) Borovkov, V. V.; Lintuluoto, J. M.; Inoue, Y. *J. Am. Chem. Soc.* **2001**, *123*, 2979-2989.

[38] a) Pasternack, RF.; Giannetto, A.; Pagano, P.; Gibbs, EJ. *J. Am. Chem. Soc.* **1991,** 113**,** 7799-7800; b) Ogoshi, H.; Mizutani, T. *Acc. Chem. Res.* **1998**, *31*, 81-89. c) Ogoshi, H.; Mizutani, T.; Hayashi, T.; Kuroda, Y. In *The Porphyrin Handbook*;Kadish, K. M., Smith, K. M., Guilard, R., Eds.; Academic Press: San Diego,2000; Vol. 6, pp 280-340. d) Weiss, J. *J. Inclusion Phenom. Macrocyclic Chem.* **2001**, *40*, 1-22. e) Kurtan, T.; Nesnas, N.; Koehn, F. E.; Li, Y.-Q.; Nakanishi, K.; Berova, N.J. Am. Chem. Soc. **2001**, 123, 5974-5982

[39] a) Gibbs, E. J.; Tinoco, I., Jr.; Maestre, M.; Ellinas, P. A,; Pasternack, R. F. *Biochem. Biophys.* Res. Commun. **1988**, *157,*350. b) Gibbs, E. J.; Maurer, M. C.; Zhang, J. H.; Reiff, W. M.; Hill, D. T.; Malicka-Blaszkiewicz, M.: McKinnie, R. E.; Liu, H. Q.; Pasternack, R. F. *J.* Inorg. *Biochrm.* **1988**, *32,* 39. c)

Pasternack, R. F.; Brigandi, R. A,; Abrams, M. J.; Williams, A. P.; Gibbs, E. *J. Inorg. Chem.* **1990**, *29,* 4483

[40] Wang, M.; Silva, G. L.; Armitage, B. A. *J. Am. Chem. Soc.* **2000**, *122*, 9977

[41] (a) Hirschberg, J. H. K. K.; Brunsveld, L.; Ramzi, A.; Vekemans, J. A. J. M.; Sijbesma, R. P.; Meijer, E. W. *Nature* **2000**, *407*, 167. (b) Matsui, H.; Kushi, S.; Matsumoto, S.; Akazome, M.; Ogura, K. *Bull. Chem. Soc. Jpn.* **2000**, *73*, 991

[42] a) Moffitt, W.J., *J. Chem. Phys.* **1954**, 22, 320; b) Moffitt, W.J., *J. Chem. Phys*. **1954**, 22, 1820.

[43] Gouterman, M. J. In The Porphyrins, Dolphin, D. Edt.; Academic Press; New York, V0l 3, Part A Ch. 1, and reference therein;

[44] McConnell, H. M. *J. Chem. Phys.* **1961**, *35*, 508.

[45] Newton, MD., *Chem. Rev.* **1991**, 767-792 and reference herein.

[46] Zutic, I.; Fabian, J., Sarma, S. Das, *Rev. Mod. Phys*., **2004,** 76, 323-410

[47] a) Musigmann , K.; Blum, K.; Thompson, D.G. *J. Phys. B: At. Mol. Opt. Phys.* **2001**, 34, 2679-2696. b) Musigmann, M.; Bussa;;a, A.; Blum, K.; Thompson, D.G. *J. Phys. B: At. Mol. Opt. Phys.* **1999**, 4117-4128. c)Campbell, D. M.; Farago, P.S., *J. Phys. B*, **1987**, 21, 5133; d) Rich, A.; Van House, J.; Hegstrom, R.A., *Phys. Rev. Lett.* **1982**, 48, 1341.

CHAPTER 8 CONCLUDING REMARKS

It is a challenge to understand the electron transfer reaction in biological processes, especially in vivo or in vitro. Heterogeneous studies provide an approach to study electron transfer reaction in many biomaterials or biological reaction centers. In this work, cytochromes c and porphyrins were attached to metal surfaces with delicately designed self-assembled structures, and the electron transfer of the supramolecular assemblies was explored, specifically, on how the electron transfer reaction changes with the distance and the structures.

A novel strategy for cytochrome c immobilization by nitrogen ligands (pyridine, imidazole, and nitrile group) engineeringed monolayer at gold/silver surface was described and characterized in Chapter 2, and Chapter 3. Cytochorme c was immobilized on the monolayer by direct "wiring" of the protein's heme through the replacement of met-80 group, one of cytochrome c's native heme ligands, by a nitrogen ligand. The negative formal potential shifts of the wired cytochrome c were reasonably in agreement with results obtained from heme axial coordinate replacement studies in solution. The electron transfer rate constant of the three-ligand systems was measured by using cylic voltammetry, a traditional, powerful electrochemical technique. The faster rate constant, compared to cytochorme c adsorbed on carboxlic acid systems with same length chain, indicated a direct heme link or close interaction, resulting in a stronger electron coupling between the protein and electrode. Scanning tunneling microscopy (STM) studies illustrated the immobilization of cytochrome c at the monolayer modified electrode.

In Chapter 3, Surface enhanced resonance Raman (SERR) spectroscopy studies demonstrated that the pyridine groups were able to substitute for the natural axial ligand Met-80 group of cytochrome c immobilized on the mixed pyridine terminated monolayers on silver electrodes. Detailed analysis of the spectra reveal that the adsorbed cytochrome c forms a potential-dependent coordination equilibrium with a predominant five-coordinated high spin state in the reduced form and six-coordinated low spin state prevailing in the oxidized state, This finding indicates a more stable cytochrome c complex in the ferric state than in the ferrous form. No evidence for a denatured structure, or significant protein unfolding, was observed from the spectroscopy study after the ligand replacement. The SERR, electrochemical and STM studies suggest that the protein is most likely in a uniform orientation or a confined configuration with respect to the plane of the electrode. Hence, the ligand "wired" protein provides a model system to investigate aspects of electron transfer between biomolecules and metal electrodes.

The electron transfer studied in Chapter 6 compare native rat cytochrome c and its mutant K13A and suggest that the route of heme-ligand acceptor-SAM is the dominated ET pathway for heme "wired" system, different from the protein absorbed on –COOH in which the electron must tunnel through the protein to reach the heme. The electron transfer rate constant differed little between the native protein and the mutant adsorbed through the pyridine receptors, whereas they differ by five orders of magnitude when adsorbed on the –COOH system. The reduced electron transfer rate constant for the mutant adsorbed on –COOH films results from the blocking of an efficient electron tunneling pathway (Lys13 group). The reorganization energy was estimated by fitting to Marcus theory and found to be 0.6±0.2 eV for both the native protein and its mutant in Chapter 6, in agreement with other studies of natural cytochrome c in solutions. These results

supply evidence to support the protein in the manner of heme "wiring" at the ligand films without denaturation.

Chapter 4 and Chapter 5 explored the electron transfer mechanism of pyridine "wired" cytochrome c at gold surfaces. The electron transfer rate constants display an exponential dependence on distance at large thickness films, but show a plateau region at short donor-acceptor separations. Similar responses were observed for cytochrome c absorbed on –COOH terminated SAMs, however, the transition point from the plateau region to the exponential dependence region for the pyridine system is larger than that for the –COOH system. At large distance, both systems obey the electron tunneling mechanism with a distance decay factor about 1.2 per CH_2 group, but at a given number methylene, such as 16, the rate constant is significantly larger for pyridine system than for –COOH systems, indicating a larger electronic coupling (tunneling probability). Detailed studies and analysis of the electron transfer (by changing the distance between the protein and gold electrode, the composition of the SAMs chains, and the solvent conditions (viscoscity, deuterium isotope)) demonstrate that the rate constant changes from a mechanism controlled by solvent friction at short distance to one controlled by electron tunneling at long distance.

Chapter 7 decribed systems to investigate the importance of molecular chirality and charge helicity was studied in the charge transfer through self-assembled helical monolayers. A chiral molecular scaffold (S or D) with base-free porphyrin attached was self-assembled to a gold surface through a thiol in a cysteine group. Photocurrent was measured under irradiation with circularly polarized light (either left or right). The electron transmission shows an asymmetrical response from the two light polarizations, namely the magnitude of the light energy normalized photocurrent was different from the left to right circular polarization light. The asymmetry factor

of average value about 0.5% for a definite chiral chain was obtained with respect to right and left circularly polarized lights. A statistica analysis of data gave 68% confidence of the asymmetry factor with range 0.51±0.5% for the R scaffold and -0.48±0.4% for S scaffold. The asymmetrical studies demonstrated the interaction between the molecular chirality and charge helicity in the charge transmission. Two hypothesized mechanisms, circular dichroism from the porphyrin aggregates in the film, and orbital polarization in a superexchange model for electron tunneling, are proposed to explain the asymmetry in the photocurrent. To get insight to the mechanism of interaction of molecular chirality and charge helicity, both theoretical and experimental work are needed in the future.

APPENDICES

A. ELECTROCHEMICAL PRINCIPLES

1. Cyclic voltammetry

Cyclic voltammetry (CV) is an important analytical technique used in electrochemistry, and a powerful tool for studying electron transfer. Cyclic voltammograms probe the electron transfer during reduction and oxidation reactions by measuring a current-voltage curve. Cyclic voltammetry is typically carried out in a three-electrode cell, containing a working electrode, a reference electrode, and a counter electrode (Figure A-1). In cyclic voltammetry, the potential of the working electrode is cycled from a starting potential to a final potential as a linear function of time (Figure A-2a). The potential change rate with time is referred as the scan rate (ν). When the applied voltage reaches the potential of the redox reaction's potential, the electron transfer between the working electrode and redox group can occur. In addition, this method takes advantage of the fact that the electron transfer reaction, which occurs in the forward scan, can be probed again in the reverse scan.

A cyclic voltammogram for the case of a redox group absorbed on the working electrode surface is presented in Figure A-2b. As the potential sweeps from negative to positive, the reduced redox group loses electrons and becomes oxidized. The anodic (oxidative) peak current occurs at the point where the redox potential is sufficiently positive for almost all reductants to be oxidized, then the current decays. When the potential gets to the final point, one scans back

negatively. In the reverse scan, a cathodic (reductive) current is produced with a peak shape similar to the anodic current, but reversed sign. Provided that the coverage of the absorbed redox species is independent of the potential within the scan range, and the reaction is Nernstian, one finds the peak current i_p to be

$$i_p = \frac{n^2 F^2}{4RT} vN \qquad \text{(A-1)}$$

where n is the number of electrons transferred, F is Faraday's constant, v is the voltage scan rate, and N is the moles of redox active sites on the surface. In this limit, the peak potential is independent of the scan rate and abides by the Nernst equation. The total width at half-height of either the cathodic or anodic peak is given by

$$\Delta E_{p,1/2} = 3.53 \frac{RT}{nF} = 90.6/n \quad \text{(mV) at 25 °C} \qquad \text{(A-2)}$$

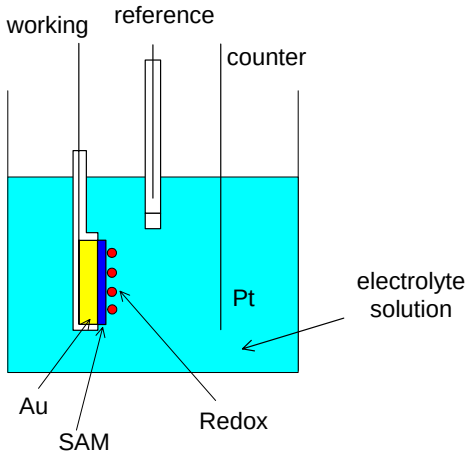

Figure A-1 a three-electrode cell
for cyclic voltammetry

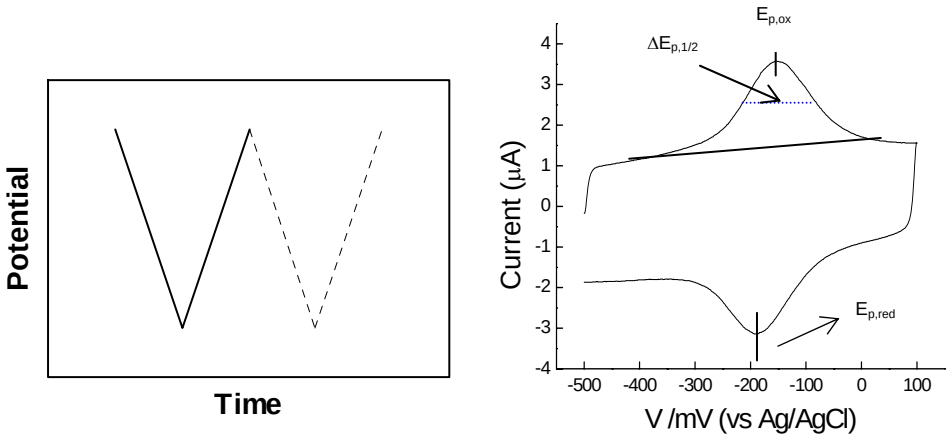

Figure A-2 a) cyclic potential scan; b) a typical cyclic voltammogram of cytochrome c immobilized on a pyridine-terminated alkanethiol SAMs on gold electrode, 10 V/sec scan rate.

The irreversible response of an absorbed redox species on the surface is different from the reversible case, because it depends on the kinetics of electron transfer. First, give a physical description of what happens as the scan rate increase, the peak current is given by

$$i_{p,red} = \frac{\alpha n_a F^2 v}{2.718RT} N \quad \text{and} \quad i_{p,ox} = \frac{(1-\alpha) n_a F^2 v}{2.718RT} N \qquad \text{(A-3)}$$

in which α is electron transfer coefficient (symmetry factor), v is scan rate, and n_a the "effective" number of electrons transferred from a single redox molecule, for cytochrome c n_a=1. Second, the wave (peak) of current response shifts from the reversible value, depending on the scan rate, and the peak potential is determined by

$$E_{p,red} = E^{0'} - \frac{RT}{\alpha n_a F} \ln\left(\frac{\alpha n_a F v}{RTk^0}\right) \qquad \text{for reduction or}$$

$$E_{p,ox} = E^{0'} - \frac{RT}{(1-\alpha) n_a F} \ln \frac{\alpha n_a F v}{RTk^0} \qquad \text{for oxidation} \qquad \text{(A-4)}$$

where k^0 is the standard electron transfer rate constant at the formal potential. The total width at half-height of cathodic and anodic peak is given by

$$\Delta E_{pred,1/2} = 2.44\frac{RT}{\alpha n_a F} = \frac{62.5}{\alpha n_a} \quad \text{(mV)} \quad \text{for reduction and}$$

$$\Delta E_{pox,1/2} = \frac{62.5}{(1-\alpha)n_a} \quad \text{(mV)} \quad \text{for oxidation at 25 °C} \qquad \text{(A-5)}$$

From the relationship between the peak position and the scan rate, a formalism developed by Laviron [1] can be used to calculate the rate constant of electron transfer. In this model, the overpotential is assumed to be much smaller than the solvent reorganization energy (peak separation is smaller than 200 mV). In this limit, from Eq. A-4 the rate constant for the reaction can be determined from the equation,

$$\log k^0 = \alpha\log(1-\alpha) + (1-\alpha)\log\alpha - \log\left(\frac{RT}{n_a F v}\right) - \frac{\alpha(1-\alpha)n_a F\Delta E_p}{2.3RT} \qquad \text{(A-6)}$$

where ΔE_p is the peak separation of reduction and oxidation. This model is consistent with Marcus theory of electron transfer at $e\eta << \lambda, k_B T << \lambda$ (see equation 1-14), and the electron-transfer rate constant follows the reversed exponential dependences on overpotential η. Because the reorganization energy of cytochrome c in buffer solution is around 0.6 eV [39,a] and even higher after substitution of Met-80 by imidazole ligand in this study [39, b], the electron transfer through short alkanethiol SAMs will comply with both Laviron and Marcus prediction. The electron transfer reaches maximum at $e\eta = \lambda$, and decreases at larger overpotential η, hence equation A-6 is no longer applicable.

2. AC impedance

AC-impedance spectroscopy is an important and powerful method for studying surface processes. In this research, AC impedance is used to characterize the self-assembled monolayers by obtaining the capacitance of the SAMs on a gold electrode in an electrochemical cell. By

modeling the monolayer as a parallel plate capacitor, one can obtain an effective thickness for the SAMs.

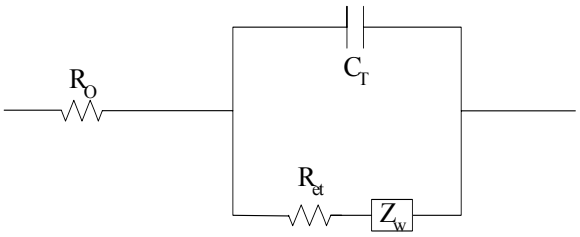

Figure A- 1 Equivalent circuit of an electrochemical cell

Impedance is a measure of the ability of a circuit to resist the flow of electrical current, and defined as

$$Z = \frac{E(t)}{I(t)} \qquad \text{(A-7)}$$

where E(t) and I(t) are voltage and current at time *t*, respectively. Usually, in a circuit there are different components that have different expressions for their impedance. For a resistor, Z=R=E/I, and for a capacitor, Z=(E(t)/I(t)=E(t)/CdE/dt=1/jωC, where ω is the frequency of ac voltage, j is $\sqrt{-1}$, and C is the capacitance.

Electrochemical impedance can be measured by applying an AC potential to an electrochemical cell and measuring the current through the cell. Figure A-3 presents an equivalent circuit of an electrochemical cell with a coated working electrode, i.e. SAM. R_O is the resistance of solution in the cell; C_T is the total capacitance of the coated monolayer and double layer. Due to the electron transfer reaction, there are impedances, R_{et} (electron transfer resistance or polarization resistance) and Z_w (the Warburg impedance or mass transfer impedance), parallel to the capacitance of C_T in the SAMs and double layer. Using the relationship of the impedance of circuit elements in both parallel and series combinations, the total impedance of this circuit is

$$Z_T = R_\Omega + \frac{\frac{1}{j\omega C}(R_{et} + Z_w)}{\frac{1}{j\omega C} + R_{et} + Z_w} = R_\Omega - j\left(\frac{R_{et} + Z_w}{(R_{et} + Z_w)C_T\omega - j}\right) \qquad \text{(A-8)}$$

At high frequency, the Warburg impedance is not important and can be ignored, then

$$Z_T = R_\Omega - j\left(\frac{R_{et}}{R_{et}C_T\omega - j}\right) \qquad \text{(A-9)}$$

Z_T has real and imaginary parts, which are given by

$$Z_{\mathrm{Re}} = R_\Omega + \frac{R_{et}}{1 + \omega^2 C_T^2 R_{et}^2} \qquad \text{(A-10) and}$$

$$Z_{\mathrm{Im}} = \frac{\omega C_T R_{et}^2}{1 + \omega^2 C_T^2 R_{et}^2} \qquad \text{(A-11)}$$

From equation A-10 and A-11, one finds that

$$(Z_{\mathrm{Re}} - R_\Omega - R_{et}/2)^2 + Z_{\mathrm{Im}}{}^2 = (R_{et}/2)^2 \qquad \text{(A-12)}$$

Thus, a plot of Z_{Im} *vs.* Z_{Re} (Nyquist Diagram) gives a semi circular graph with a center point at Z_{Im}=0, $Z_{\mathrm{Re}} = R_\Omega + R_{et}/2$, and a radius of $R_{et}/2$.

At low frequency, ω close to zero, Z_T is given by

$$Z_T = R_\Omega + R_{et} + Z_W \qquad \text{(A-13)}$$

Z_w is defined as $Z_w = \sigma/\omega^{1/2} - j\sigma/\omega^{1/2}$ and σ is the Warburg coefficient constant, which characterizes the mass transfer control. One can find the relationship between Z_{Im} and Z_{Re} to be.

$$Z_{\mathrm{Im}} = Z_{\mathrm{Re}} - R_\Omega - R_{et} + 2\sigma C_T \qquad \text{(A-14)}$$

Hence, the plot of Z_{Im} *vs.* Z_{Re} is a line with unit slope.

In an actual electrochemical cell measurement, the impedance is a combination of charge transfer kinetics and mass transport. Figure A-4 is a simulated Nyquist plot for a Mixed Control Circuit (from diffusion control to kinetic control) electrochemical cell impedance measurement,

where the circular part is controlled by charge transfer kinetics at high frequency, and the linear part is controlled by diffusion processes at low frequency. Analyzing the curve, one is able to get the parameters of the circuit, C_T, R_Ω, R_{et}, etc.

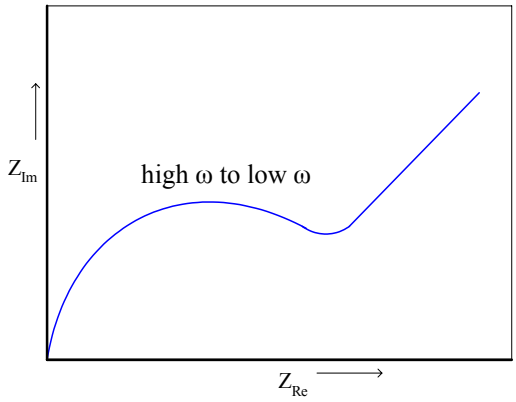

Figure A- 4 Nyquist plot for mixed control circuit

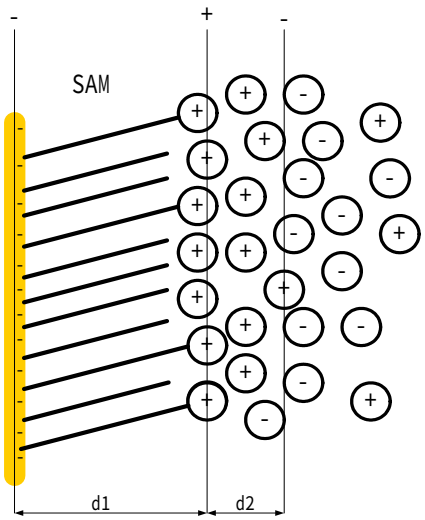

Figure A-5 A schematic diagram of a defect free monolayer and double layer structure

We are able to characterize the thickness of a self-assembled monolayer film on the electrode by the capacitance that is obtained from the AC impedance measurement. In the measurement, the DC potential is set at 0 mV at the equilibration, the AC sine wave amplitude is set as 5 mV, and frequency ranges from 100 kHz to 50 mHz. For a SAM modified electrode, the cell's impedance is controlled by charge transfer at high frequency and mass diffusion at low frequency (similar to Figure A-4).

Figure A-5 presents a schematic diagram of a defect free monolayers and double layer at a gold electrode. The capacitance C_T is a combination of two parts, the SAMs' capacitance and double layer capacitance related by

$$\frac{1}{C_T} = \frac{1}{C_S} + \frac{1}{C_d} \qquad \text{(A-15)}$$

C_s is capacitance of SAMs and C_d is capacitance of double layer. According to the Helmholtz theory for the electrical double layer, and using a simple parallel plate model, the capacitance per unit area is given by [2]

$$C = \frac{\varepsilon_0 \varepsilon A}{d} \qquad \text{(A-16)}$$

where d is the thickness of the SAM, ε_0 is the vacuum permittivity constant and ε is the relative dielectric constant ranging 2.3~2.6. The double layer thickness is dependent on different ions and $d1>>d2$ when the length of alkanethiol is long enough (the number of methylene is n≥9) and thus $C_d>>C_s$. The distance between the two sheets of charges is well approximated by the monolayer thickness and the diffuse charge double layer in the solution becomes insignificant. The measured capacitance C_T can be simply treated as C_s. Hence, for a defect-free SAM, the capacitance is mainly dependent on the thickness of the monolayer. In fact, when n≥9, the capacitance is inversely proportional to the length of the alkyl chain and independent of the electrolyte.

B. PROGRAMING MARCUS THEORY FOR ELECTRON TRANFER RATE CONSTANT

The basic idea for this program is to simulate the cyclic voltammograms of redox species adsorbed at solid electrodes based on the Marcus formula. We can obtain peak separations (or peak shift ΔE from the formal potential) with respect to the values of $\log(k_0/v)$ (k_0 is the rate constant, v is the scan rates). The experimental voltammograms provide a series of scan rate *vs.* peak shift. To obtain the rate constant, we guess a k_0 of the experimental system and fit the $\log(k_0/v)$-ΔE to those values obtained from Marcus model. The guessed k_0 which has the best fitting to the theory is the electron transfer rate constant.

We use Mathcad to simulate the voltammogram. The example given below shows a CV simulation at a reorganization energy 0.1 eV, a given rate constant 5 Hz, and three scan rates at 0.1, 1.0, 10.0 V/sec. From the data sheet, one can obtain the peak shifts at individual scan rates. More CVs can be simulated. It is easy to get a series of $\log(k_0/v)$- ΔE at different reorganization energy.

Some parameters.

$F := 96485.3$ C/mol is the Faraday constant

$R := 8.31451$ J/mol-K is the gas constant

$T := 300$ K is the temperature

$$thV := \frac{R \cdot T}{F} \qquad thV = 0.026 \quad V \qquad \frac{1}{thV} = 38.681 \quad 1/V$$

For a given reorganization energy and prefactor, we can calculate electron transfer rate constant (k_0) through the Marcus formulism:

A. First let us calculate the rate constant using the Marcus model.

$prefactor := 1$

$$ox0int(\lambda, x) := \exp\left[\frac{-\left(-x - \frac{\lambda}{thV}\right)^2}{4 \cdot \frac{\lambda}{thV}}\right] \cdot \left(\frac{\exp(x)}{1 + \exp(x)}\right) \qquad red0int(\lambda, x) := \frac{\exp\left[\frac{-\left(\frac{\lambda}{thV} - x\right)^2}{4 \cdot \frac{\lambda}{thV}}\right]}{(1 + \exp(x))}$$

$$k0ox(\lambda) := \frac{thV \cdot prefactor}{\sqrt{\lambda}} \cdot \int_{-100}^{100} ox0int(\lambda, x)\, dx \qquad k0red(\lambda) := \frac{thV \cdot prefactor}{\sqrt{\lambda}} \cdot \int_{-100}^{100} red0int(\lambda, x)\, dx$$

$k0ox(0.1) = 0.069$ $k0red(0.1) = 0.069$

For a given rate constant, we can obtain the reaction rate at specific overpotential:

$$k0 := 5 \quad \text{Hz}$$

$$oxint(\eta, \lambda, x) := \exp\left[\frac{-\left(\frac{\eta}{thV} - x - \frac{\lambda}{thV}\right)^2}{4 \cdot \frac{\lambda}{thV}}\right] \cdot \left(\frac{\exp(x)}{1 + \exp(x)}\right) \qquad redint(\eta, \lambda, x) := \frac{\exp\left[\frac{-\left(\frac{\lambda}{thV} + \frac{\eta}{thV} - x\right)^2}{4 \cdot \frac{\lambda}{thV}}\right]}{1 + \exp(x)}$$

$$kox(\eta, \lambda) := k0 \cdot \frac{\int_{-100}^{100} oxint(\eta, \lambda, x)\, dx}{\int_{-100}^{100} ox0int(\lambda, x)\, dx} \qquad kred(\eta, \lambda) := k0 \cdot \frac{\int_{-100}^{100} redint(\eta, \lambda, x)\, dx}{\int_{-100}^{100} red0int(\lambda, x)\, dx}$$

$$\eta := -2, -1.9 .. 2.0$$

$$sum(\eta, \lambda) := kred(\eta, \lambda) + kox(\eta, \lambda)$$

$$\eta 0 := -0.15 \qquad \delta := 0.005 \qquad nu1 := 0.1 \qquad nu2 := 1.0 \qquad nu3 := 10.0$$

$$Rinit := \exp\left(\frac{\eta 0}{thV}\right) \qquad finit := \frac{1}{1 + Rinit} \qquad \Delta t1 := \frac{\delta}{nu1} \qquad \Delta t2 := \frac{\delta}{nu2} \qquad \Delta t3 := \frac{\delta}{nu3}$$

$$finit = 0.997$$

Next we can obtain the CV curve. This program loop gives three voltammograms at three scan rates: 0.1 V/sec, 1.0V/sec, and 10.0 V/sec

$$
\begin{aligned}
F := \;& CV \leftarrow 0 \\
& finit1 \leftarrow \frac{1}{1 + Rinit} \\
& finit2 \leftarrow \frac{1}{1 + Rinit} \\
& finit3 \leftarrow \frac{1}{1 + Rinit} \\
& \text{for } m \in 0..199 \\
& \quad CV_{m,0} \leftarrow \delta \cdot m + \eta 0 \\
& \quad ftarg \leftarrow \frac{1}{1 + Rinit \cdot \exp\left(m \cdot \frac{\delta}{thV}\right)} \\
& \quad CV_{m,1} \leftarrow \left(\frac{thV}{\delta}\right) \cdot (ftarg - finit1) \cdot \left(1 - \exp\left(-sum\left(CV_{m,0}, 0.1\right) \cdot \Delta t1\right)\right) \\
& \quad CV_{m,2} \leftarrow \left(\frac{thV}{\delta}\right) \cdot (ftarg - finit2) \cdot \left(1 - \exp\left(-sum\left(CV_{m,0}, 0.1\right) \cdot \Delta t2\right)\right) \\
& \quad CV_{m,3} \leftarrow \left(\frac{thV}{\delta}\right) \cdot (ftarg - finit3) \cdot \left(1 - \exp\left(-sum\left(CV_{m,0}, 0.1\right) \cdot \Delta t3\right)\right) \\
& \quad finit1 \leftarrow finit1 + CV_{m,1} \cdot \frac{\delta}{thV} \\
& \quad finit2 \leftarrow finit2 + CV_{m,2} \cdot \frac{\delta}{thV} \\
& \quad finit3 \leftarrow finit3 + CV_{m,3} \cdot \frac{\delta}{thV} \\
& CV
\end{aligned}
$$

Three simulated CVs (reduction peaks only):

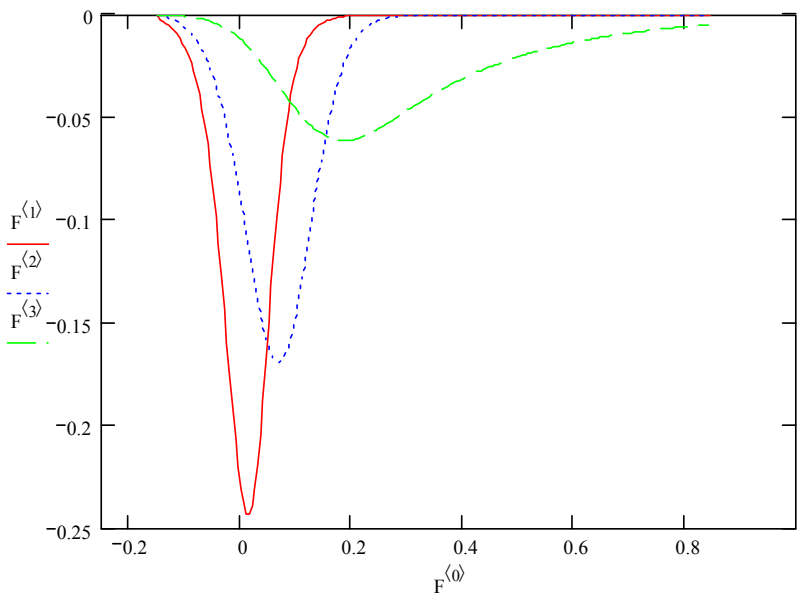

The data sheet of *i-V:*

F =

	0	1	2	3
0	-0.15	0	0	0
1	-0.145	-2.543?0 -3	-4.502?0 -4	-4.804?0 -5
2	-0.14	-3.623?0 -3	-9.095?0 -4	-1.025?0 -4
3	-0.135	-4.496?0 -3	-1.392?0 -3	-1.645?0 -4
4	-0.13	-5.449?0 -3	-1.911?0 -3	-2.35?0 -4
5	-0.125	-6.57?0 -3	-2.48?0 -3	-3.152?0 -4
6	-0.12	-7.908?0 -3	-3.115?0 -3	-4.067?0 -4
7	-0.115	-9.506?0 -3	-3.83?0 -3	-5.109?0 -4
8	-0.11	-0.011	-4.642?0 -3	-6.294?0 -4
9	-0.105	-0.014	-5.569?0 -3	-7.643?0 -4
10	-0.1	-0.016	-6.63?0 -3	-9.176?0 -4
11	-0.095	-0.02	-7.844?0 -3	-1.091?0 -3
12	-0.09	-0.023	-9.235?0 -3	-1.288?0 -3
13	-0.085	-0.028	-0.011	-1.511?0 -3
14	-0.08	-0.033	-0.013	-1.762?0 -3
15	-0.075	-0.039	-0.015	-2.044?0 -3

C. PRINCIPLES OF ELLIPSOMETRY AND THE PROGRAM FOR CALCULATING FILM THICKNESS MEASURED BY ELLIPSOMETER

1. Ellipsometer Instructions

Measurement[3]:

1. Turn on laser using the on-off key on the side, the light from the laser should come on immediately. For best results allow ~15 minutes for the laser to warm up.
2. The Analyzer and polarizer should be set to a 70°angle of incidence, (70° recommended). Both should be set to the same angle and clamped in place. [If not, To change the angle of incidence, (a) Loosen the large knob (clamp screw) on the back of the arm (behind the instrument). (b) Support the arm and pull the small knob (locating pin). When setting up the polarizer arm, support it under a drum, not under the laser. (c) With the pin pulled out, move the arm to near the new setting. Release the pin and continue the arm until the pin engages. Tighten the clamp and screw (Caution: never lower either arm to 90° setting without first lowering the sample stage as far as it will go, since the microspot optics will hit. To prevent this, the 90° locating pin hole is blocked. The 90° setting is only used for checking instrument alignment and for this the block may be removed),
3. Place the wafer to be measured on the sample stage. For accurate measurements the wafer should be flat on the sample stage. (usually vacuum pump helps but this system does not have it)
4. Adjust the gain knob to give an extinction reading meter reading between 150-200.

5. Rotate the analyzer (right drum) slowly in the red numbered region (0°-90°) to get a minimum reading on the meter.
6. Then rotate the polarizer (left drum) slowly in the red region (315°-135°) to get a lower minimum reading. The numerical value of the meter reading is not important, **only that it be a minimum**.
7. Return to the analyzer (right hand) and slowly rotate the drum to give a new minimum. This should be within the red region and search for a new minimum.
8. Return to the polarizer (left hand) and slowly rotate to give a lower meter reading. (The meter gain may be adjusted to keep the meter reading between 25 and 100)
9. Work back and forth between analyzer and polarizer to get the lowest possible meter reading. The analyzer and polarizer reading correspond to extinction.
10. Record the analyzer and polarizer settings, A(1) and P(1), respectively.
11. Set the polarizer to P(1) + 90°.
12. Set the analyzer to 180°-A(1).
13. Again work back and forth between analyzer and polarizer to get the lowest possible meter readings (extinction).
14. Record the polarizer and analyzer settings for the second extinction, P(2) and A(2). To obtain accurate measurements, these values should not differ by more than 4° from the values computed in 11 and 12.
15. Calculate ψ and Δ using the following equations

    The angles ψ and Δ are related to the measured angles, P1, A1, P2, A2 in the following way: $\Delta=3\pi/2-2P1=5\pi/2-2=2\pi-P1-P2$; $\psi=\pi-A2=(A1-A2+\pi)2$

    Usually I use, $\Delta=2\pi-P1-P2$ and $\psi=\pi-A2$

2. Theoretical Background on Ellipsometry [3,4]

One of the applications of ellipsometry is to analyze the thicknesses of thin films or monolayers at surfaces. Ellipsometry relies on the use of linearly polarized light and elliptically polarized light. For instance, light may be represented by the equations of a sine wave;

$$E_x = A_x \sin(\omega t + \phi_x)$$

$$E_y = A_y \sin(\omega t + \phi_y)$$

E_x is the electric field in the *x* direction, E_y is the electric field in the y direction, A_x is the amplitude in the *x* direction and A_y is the amplitude in the *y* direction, *t* is time, ϕ is the phase angle, ω, is 2πν, where ν is the frequency.

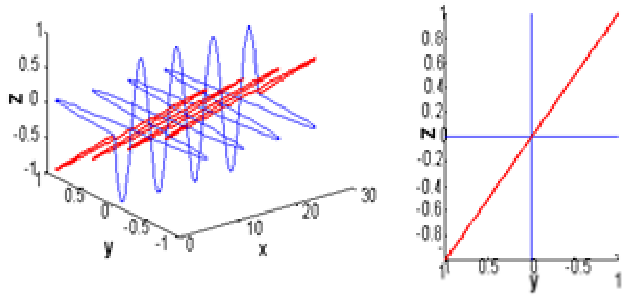

Figure A-6 Figure shows that when two sine waves of equal amplitude and phase are combined, linearly polarized light is obtained.

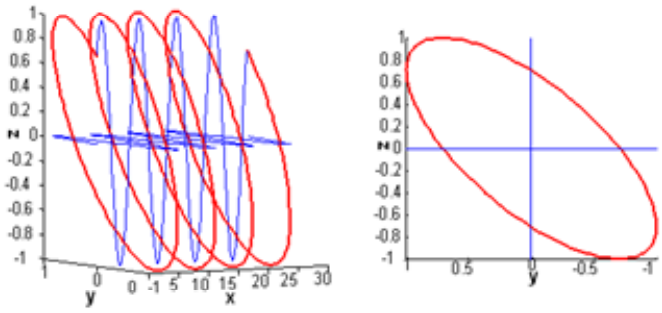

Figure A-7 shows that when there is a phase change, ϕ=45° between two perpendicular waves, the resultant wave is an elliptically polarized light.

Ellipsometry employs incident linearly polarized light. These are divided into two components: p-polarized light (E_p) in the plane of incidence and s-polarized light (E_s) perpendicular to the plane of incidence reflect from a surface. There will be a change in the *phase* and *amplitude* of the outgoing E_p and E_s components (therefore producing an elliptical light wave) upon reflection.

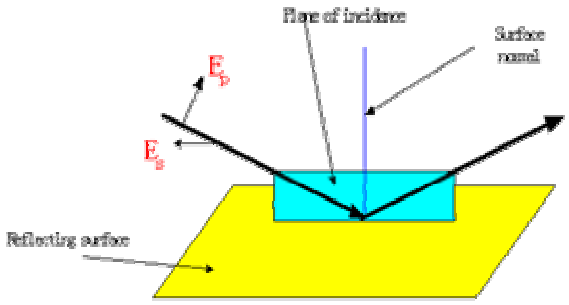

Figure A-8 shows a linearly polarized light of two components E_p and E_s reflected from a surface.

In practice and for simplicity of equations, an ellipsometer is set up in the following way to detect the change in the *phase angle* (Δ) and the *amplitude change* (ψ) upon reflection.

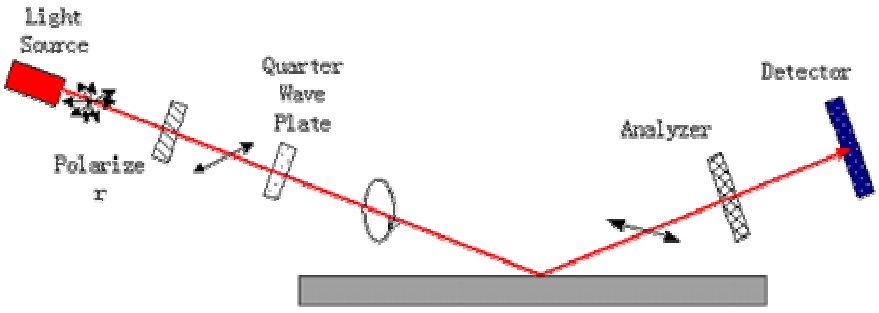

Figure A-9 shows an instrumental set-up of an actual ellipsometer.

A schematic diagram of an ellipsometer (Figure A-9) shows a beam of light as it passes through a nulling spectrometer. Since many light sources (other than lasers) emit light that has components with electric fields oriented in all directions perpendicular to the direction of travel, a polarizer is used to orient all the electric field in one direction or clean up non-linear light components to obtain a linearly polarized light. An ellipsometer often uses a monochromatic light of a He-Ne laser of wavelength, λ=632.8 nm. Therefore, if a linearly polarized light makes a reflection at the metal surface, there will be a shift of the *phases* and *amplitudes* of both p and s components (electric vectors, parallel (p) and perpendicular (s) to the plane of incidence). However, in this case, an optical element called the Quarter-Wave-Plate (QWP) is set at an angle 45° with respect to the plane of incidence (fixed) to produce an elliptical polarized light before reflection from the sample. Then both the polarizer (P) and the analyzer (A) are rotated until a minimum signal is obtained. This minimum signal is detected if the light reflected from the surface is linearly polarized; that is, when both polarizations, p and s are in phase. Therefore a null measurement results in two parameters, the angular setting of the polarizer prism, P, in the incident beam and the angular setting of the analyzing prism, A, in the reflected beam.

Experimentally, there are ideal zones of obtaining P and A and these are used to calculate Δ and ψ; Angles Δ and ψ are related to the measured angles P_1, A_1, P_2 and A_2 (experimentally two different positions of A and P are obtained for a minimum signal) as follows:

$$\Delta=3\pi/2-2P_1=5\pi/2-2P_2=2\pi-P_1-P_2$$

$$\psi=A_1=\pi-A_2=(A_1-A_2+\pi)/2$$

One can relate Δ and ψ to the thickness of a film or a monolayer at the surface (this will work well if the two materials, substrate and grafted material have different refractive indices) by the following equation:

$$\rho = \frac{r_p}{r_s} = \tan \psi \exp(i\Delta)$$

where ρ is the ratio of Fresnel Reflection Coefficients r_p and r_s and within it contains the thickness term

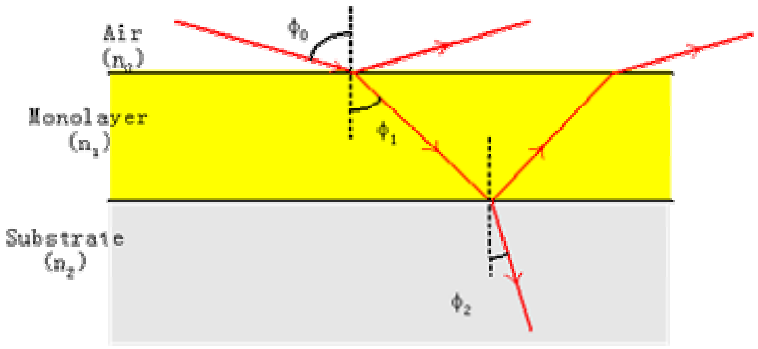

Figure A-10 shows a two layer model used for ellipsometry.

In calculating the thickness of the monolayers grafted on a silicon substrate a two-layer model (Figure A-9) was used where the ambient air has a refractive index n_0 (1), the monolayer has a refractive index n_1 and the silicon substrate n_2 (e.g. 3.875-0.018*i for Si).

Therefore, the reflection ellipsometry of an ambient-film-substrate relies on the overall difference in *amplitude* attenuation and *phase* shift experienced by p and s components upon reflection. These *phase* and *amplitude* differences of p and s-polarizations are given by Fresnel reflection coefficients r_p and r_s. An ellipsometer measures the ratios of these coefficients r_p and r_s *i.e.* relative *phase* change, Δ, and the relative *amplitude* change, tan Ψ.

Ellipsometry equations used to calculate the thickness of the monolayer.

Snell's law is given by:

$$n_0 \sin \phi_0 = n_1 \sin \phi_1 = n_2 \sin \phi_2$$

We can calculate ϕ_1 and ϕ_2 using Snell's laws:

$$\phi_1 = a \sin\left(\frac{n_0}{n_1} \sin \phi_0\right) \quad \& ; \phi_2 = a \sin\left(\frac{n_0}{n_2} \sin \phi_0\right)$$

Fresnel Reflection Coefficients at the 0-1 and 1-2 interfaces:

$$r_{01\,p} = \frac{n_1 \cos \phi_0 - n_0 \cos \phi_1}{n_1 \cos \phi_0 + n_0 \cos \phi_1} \quad \text{and} \quad r_{01\,s} = \frac{n_0 \cos \phi_0 - n_1 \cos \phi_1}{n_0 \cos \phi_0 + n_1 \cos \phi_1}$$

$$r_{12\,p} = \frac{n_2 \cos \phi_1 - n_1 \cos \phi_2}{n_2 \cos \phi_1 + n_1 \cos \phi_2} \quad \text{and} \quad r_{12\,s} = \frac{n_1 \cos \phi_1 - n_2 \cos \phi_2}{n_1 \cos \phi_1 + n_2 \cos \phi_2}$$

$$R_s = \frac{r_{01\,s} + r_{12\,s} e^{-j2\beta}}{1 + r_{01\,s} r_{12\,p} e^{-j2\beta}} \quad \text{and} \quad R_p = \frac{r_{01\,p} + r_{12\,p} e^{-j2\beta}}{1 + r_{01\,p} r_{12\,p} e^{-j2\beta}}$$

where, $\beta = 2\pi\left(\frac{d_1}{\lambda}\right) n_1 \cos \phi_1$, $\quad \rho_r = \frac{R_p}{R_s}$

If we substitute for R_p and R_s, we obtain;

$$\tan \psi e^{j\Delta} = \rho = \frac{r_{01\,p} + r_{12\,p} e^{-j2\beta}}{1 + r_{01\,p} r_{12\,p} e^{-j2\beta}} \times \frac{1 + r_{01\,s} r_{12\,s} e^{-j2\beta}}{r_{01\,s} + r_{12\,s} e^{-j2\beta}}$$

3. The program in Mathcad for film thickness at gold substrate

Parameters

Refractive Index

Air $n0 := 1$

SAM $n1 := 1.45$ for DNA SAM or alkane is 1.45, ref. Herne, TM. Tarlov, MJ.*JACS*, 1997 119, 8916-8920

Substrate (gold) $n2 := 0.166 - 3.22i$

Laser wavelength: $\lambda := 632.8\ nm$

Angle of incidence $\phi 0 := 70 \cdot \frac{\pi}{180}$

Experimental Results: (all angle change from degree to Radians by multiply $\frac{\pi}{180}$)

$p1 := 82.3 \cdot \frac{\pi}{180}$ $A1 := 43.6 \cdot \frac{\pi}{180}$

$p2 := 172.8 \cdot \frac{\pi}{180}$ $A2 := 136.5 \cdot \frac{\pi}{180}$

Calculating parameters from experimental results for obtaining thickness

$\Delta := 2\pi - p1 - p2$ $\Psi := \pi - A2$

$\tan(\Psi) \cdot e^{i \cdot \Delta} = -0.244 + 0.917i$

Calculating Refractive angle at 0-1 and 1-2 interfaces

$$\phi 1 := \operatorname{asin}\left[\left(\sin(\phi 0)\right)\cdot\left(\frac{n0}{n1}\right)\right]$$

$$\phi 2 := \operatorname{asin}\left[\left(\sin(\phi 0)\right)\cdot\left(\frac{n0}{n2}\right)\right]$$

Fresnel reflection coefficients at 0-1 and 1-2 interfaces

$$r01p := \frac{\left(n1\cdot\cos(\phi 0) - n0\cdot\cos(\phi 1)\right)}{n1\cdot\cos(\phi 0) + n0\cdot\cos(\phi 1)}$$

$$r01s := \frac{\left(n0\cdot\cos(\phi 0) - n1\cdot\cos(\phi 1)\right)}{n0\cdot\cos(\phi 0) + n1\cdot\cos(\phi 1)}$$

$$r12p := \frac{\left(n2\cdot\cos(\phi 1) - n1\cdot\cos(\phi 2)\right)}{n2\cdot\cos(\phi 1) + n1\cdot\cos(\phi 2)}$$

$$r12s := \frac{\left(n1\cdot\cos(\phi 1) - n2\cdot\cos(\phi 2)\right)}{n1\cdot\cos(\phi 1) + n2\cdot\cos(\phi 2)}$$

$$\rho(d1) := \frac{\begin{bmatrix} r01p + r12p \cdot e^{-i \cdot 2 \cdot \left[2 \cdot \pi \cdot \left(\frac{d1}{\lambda}\right) \cdot n1 \cdot \cos(\phi 1)\right]} \end{bmatrix} \cdot \begin{bmatrix} 1 + r01s \cdot r12s \cdot e^{-i \cdot 2 \cdot \left[2 \cdot \pi \cdot \left(\frac{d1}{\lambda}\right) \cdot n1 \cdot \cos(\phi 1)\right]} \end{bmatrix}}{\begin{bmatrix} 1 + r01p \cdot r12p \cdot e^{-i \cdot 2 \cdot \left[2 \cdot \pi \cdot \left(\frac{d1}{\lambda}\right) \cdot n1 \cdot \cos(\phi 1)\right]} \end{bmatrix} \cdot \begin{bmatrix} r01s + r12s \cdot e^{-i \cdot 2 \cdot \left[2 \cdot \pi \cdot \left(\frac{d1}{\lambda}\right) \cdot n1 \cdot \cos(\phi 1)\right]} \end{bmatrix}}$$

Define a function f(d)=0, using the built-in root function to get the solution,
Be aware that, to make the caculation in a real number formulism, the complex number have transfer to be angle with unit Radian.

$$f(d1) := \arg\left(\tan(\Psi) \cdot e^{i \cdot \Delta}\right) - \arg(\rho(d1))$$

Enter a guss value for the solution (modify as necessary)

$$d1 := 0.0016 \quad nm$$

$$soln := root(f(d1), d1) \qquad \Delta = 1.831$$

Real Solution of f(d1)

$$\arg\left(\tan(\Psi) \cdot e^{i \cdot \Delta}\right) = 1.831$$

$$soln = 2.959 \times 10^{-3} \quad nm \qquad \arg(\rho(soln)) = 1.831$$

$$g(d1) := \operatorname{atan}\left(\left|\tan(\Psi)\cdot e^{i\cdot\Delta}\right|\right) - \operatorname{atan}\left(\left|\rho(d1)\right|\right)$$

$d1 := 0.1$ nm

$soln := root(g(d1), d1)$

$\Psi =$ ▮

$\operatorname{atan}\left(\left|\tan(\Psi)\cdot e^{i\cdot\Delta}\right|\right) =$ ▮

Real Solution of f(d1)

$soln =$ ▮ nm

$\operatorname{atan}\left(\left|\rho(soln)\right|\right) =$ ▮

$d1 := -10 .. 10$

$q(d1) := \left(\left|f(d1)\right|\right)^2 + \left(\left|g(d1)\right|\right)^2$

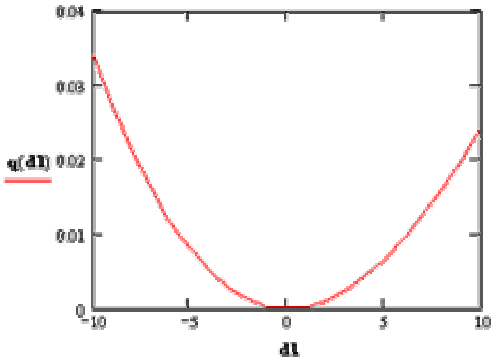

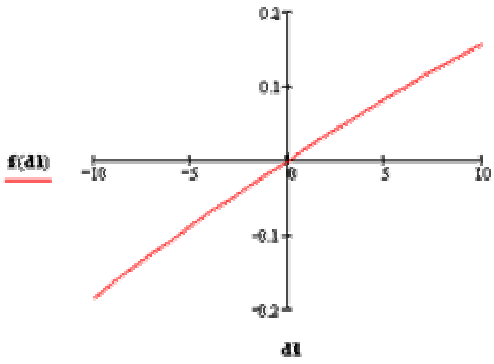

BIBLIOGRAPHY

[1] Laviron, E., *J. Electroanal. Chem.*, **1979**, 101, 19-28

[2] (a) Porter, MD; Bright, TB; Allara, DL; Chidsey, CED, *J. Am. Chem. Soc.* **1987**, 109, 3559; (b) Liu, Y. -P.; Newton, M. D. *J. Phys. Chem*. **1994**, 98, 7162. (c) Smalley, J. F.; Feldberg, S. W.; Chidsey, C. E. D.; Linford, M. R.; Newton, M. D.; Liu, Y. -P. *J. Phys. Chem*. **1995**, 99, 13141-13149.

[3] This manual is copied from Al-Maawali, S PhD thesis, University of Pittsburgh

[4] a)R.M.A. Azzam and N.M. Bashara, *Ellipsometry and Polarized Light* ,North-Holland publishing Company, Amsterdam,1977 (especially, pp-283-288,270-274); b) Harland G. Tompkins, *A user's Guide to ELLIPSOMETRY*, Academic Press, INC, 1993